Finite Element Analysis and Design Optimisation of Shaded Pole Induction Motors

By

Dawei Zhou

A Thesis submitted in partial fulfilment of the requirement of the University of Abertay Dundee for the degree of Doctor of Philosophy

March 2001

I Certify that this thesis is the true and accurate version of the thesis approved by the examiners.

Signed: [redacted]
(Director of Studies)

Date: 22/8/01

Declaration

I hereby declare that this work has not previously been accepted in substance for any other award and is not being currently submitted in candidature for any other degree. I further declare that except where stated the work presented in thesis is original and was performed by the author at the University of Abertay Dundee.

Signed: 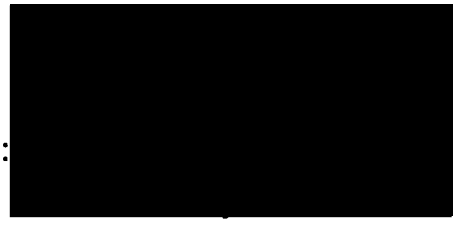

Date: 28 June 2001

Acknowledgements

The work presented in this thesis was carried out at School of Science & Engineering, University of Abertay Dundee, under the supervision of Dr. C. B. Rajanathan.

I wish to express my gratitude to Dr. C. B. Rajanathan who gives me guidance and advice till the last moment of his life. His spirit of hard working and conscientiousness encouraged me to complete my study.

I would also sincerely like to thank Professor P. F. Martin, Head of School of Science & Engineering, for his valuable advice and genuine encouragement throughout the study, especially in final period of my study. Without his support, this research could not have been accomplished.

Gratitude is also given to Mr. A. T. Sapeluk, Dr. C. S. Ozveren, Dr. C. Main for their helpful discussion and assistance concerning the technical aspects of the research. Also gratefulness to Mr. I. Longair, Head of the division, for his support to research.

Financial support by the University of Abertay Dundee is gratefully acknowledged.

Finally, my debt of gratitude to my family, especially to my wife, Mrs Feng Tang, for her patience, understanding and wholehearted support during the past years.

Abstract

In the area of performance analysis of the Shaded Pole Induction Motors (SPIMs), much research has been done with different equivalent circuit models, but the results are generally not satisfactory. The emergence of Finite Element (FE) methods provides an opportunity to take a fresh look at the design of SPIMs and this forms the backbone of my research.

In the research, a more accurate two-dimensional time-stepping eddy-current FE model was developed. The multi-slice technique, justified as the more efficient way to consider the effect of a skewed rotor, has been adopted in the model. For the first time, the end-ring resistance was investigated under the condition that the end-ring current distributes itself non-sinusoidally along the circumferential direction in the end-ring area. An instantaneous non-uniform end-ring resistance model was therefore presented and coupled with the two-dimensional multi-slice FE model. Thus, compared with using the normal two-dimensional FE model, the three-dimensional nature of electric machines, e.g. the skew and end-ring, could be considered more properly by using the proposed FE Model. Meanwhile, the harmonics, the skin effect and the saturation of the permeable parts can all be taken into account with the new model.

On the other hand, in order to reduce the computing time required by the time-stepping technique, a variable step size method was adopted and a more reliable method of estimating the truncation error of time-stepping has been developed. Additionally, by coupling the external circuits equations directly to the field equations, the time cost was further reduced and the performance of a SPIM including current and torque might be obtained immediately after the systems equations were solved.

With the developed two-dimensional FE model, the effects of variation of design parameters, including air gap profile, pole bridge, the skew, rotor slot number and closed-slot rotor, have been investigated. By introducing a new harmonic analysis method based directly on the time-stepping finite element method, the effect of different designs on the spatial harmonic in the air gap field and the time harmonic in the rotor-bar current can be learned.

The optimisation technique was applied to the design of SPIMs in order to obtain a proper combination of the design variables. A more efficient global-local hybrid search algorithm that combines the Genetic Algorithm with the direct search method was proposed in this study. To meet the demand of either speed or accuracy, a multi-slice fixed-mesh model of SPIMs was built up and used to calculate of the motor performance, the objective function of the optimisation. Because the optimisation program was based on FE analysis directly, an automatic re-mesh scheme depending on the optimisation variables was required and therefore developed in this research as well. A great performance improvement was achieved when applying the proposed optimisation method to maximising the starting torque.

Finally, In order to validate the result of the two-dimensional, multi-slice FE model proposed, a PC-based experimental rig has been set up. With this test rig, two SPIMs have been tested in both the steady state and the transient state and the measuring results proved the accuracy of the analysis model developed in the study.

List of Symbols

∇	Laplace operator
[U]	unit diagonal matrix.
A, *A*	vector potential (Wb/m)
A_e	cross-sectional area of the end ring (m^2)
B, *B*	magnetic flux density (T)
B_b	amplitude of flux density of the backward rotating fields (T)
B_f	amplitude of flux density of the forward rotating fields (T)
B_n, B_t	normal and tangential components of the flux density (T)
C_i	volume-charge density (C/m^3)
D	electric flux density (C/m^2)
DF	distortion factor
DF_n	distortion factor of the n^{th} order harmonic
df_n, df_t	normal and tangential components of the force density (N/m)
D_r	mean diameter of the end ring (mm)
E	electric field strength (V/m)
e_z	unit vector parallel to the z-axis
f	frequency (Hz)
$f(x)$	objective function of optimisation
F, *F*	force (N)
H	magnetic field strength (A·m)
H1	thickness of the slot-bridge of closed-slot (mm)
H2	length of the middle part of rotor slot (mm)
I, *i*	Current (A)

$\mathbf{J}$, J	free current density (A/m^2)
K	ratio between the air-gap length under the step air-gap and that under other part of air-gap
k_{ring}	correction factor to consider the non-uniform current distribution in a wide end ring.
L	leakage reactance (H)
l_z	length of solution region in the z-direction (m)
n	rotor speed (rev/min)
N_b	number of rotor bars
N_c	turns of coil of one pole (turns)
p	pole number
R	resistance (Ω)
$R1$	radius of the upper half circle of a rotor slot (mm)
$R2$	radius of the lower half circle of a rotor slot (mm)
Rr	outer radius of rotor (mm)
$Rs1$	radius of step air gap (mm)
S	area (m^2)
Skew	skewed angle of the rotor bar measured in slot
$\mathbf{T}$	Maxwell stress tensor
T	temperature (^{o}C)
t	time (s)
T, T_M	output mechanical torque (N.m)
THD	total harmonic distortion
Turns	turns of the stator coil
V	electrical potential (V)
$\mathbf{v}$, v	velocity of a conductor with respect to B (m/s)
V_b	source voltage applied to the terminal of the region (V)
W_c	magnetic co-energy stored in the whole study region (J)
Δ_e	area of a triangle element (mm)
Δt	time step size (s)
Ω	study region

α	length of the step air-gap measured in electrical degree
δ_{Share}	sharing distance of the niching Genetic Algorithm
ε	error
ϕ	flux (Wb)
ϕ_m	flux through the main portion of a pole (Wb)
ϕ_s	flux through the portion of shaded-ring (Wb)
μ	magnetic permeability (H/m)
ν	magnetic reluctivity (m/H)
θ	spatial angle (^{o})
ρ	free charge density (C/m^3)
σ	electrical conductivity $(\Omega \cdot m)^{-1}$
ω	angular frequency of power supply (rad/s)

Table of Contents

1 INTRODUCTION

1. 1 Shaded-Pole Induction Motors

Millions of Shaded-Pole Induction Motors (SPIMs) are made every year with power ratings ranging from a fraction of a watt to about 150W. Due to their simple construction, low cost and maintenance-free operation, SPIMs are used in an extremely wide variety of applications: small electrical appliances such as rotisseries, fans of all kinds, humidifiers and slide projectors; household appliances, e.g. discharge pump motors in washing machines and roller-driven motors in ironing machines; and small business machines including photocopy machines, vending machines and advertising display. In particular, the direct drive to the drum for spinning in washing machines and to the compressor in refrigerators has become a classical application for large two- or four-pole SPIMs with power ratings from 60W to 150W [Veinott, 1986]. In the sub-fractional range, they are often regarded as the most cost-effective solution.

SPIMs have the simplest structure of all induction motors. In the normal form of construction, laminated salient poles are used and a pre-wound stator coil is fitted over them. The shaded-ring, an auxiliary short-circuited winding, consists of a single turn placed around a portion of the main pole. Sometimes two or three shaded-rings are used on each pole with each ring surrounding a different fraction of the main-pole face. The rotor of SPIMs is a squirrel-cage rotor. A typical structure of a 2-pole SPIM is shown in Fig. 1.1 although construction may vary considerably in detail for different purposes.

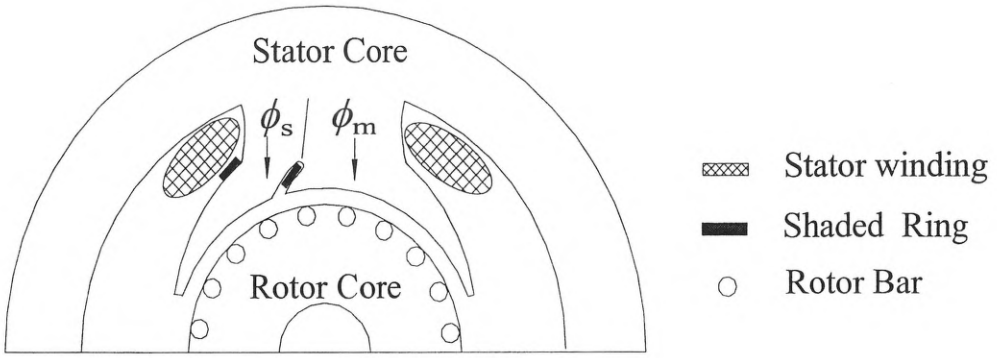

Fig. 1.1 Structure diagram of a 2-pole SPIM with single shaded-ring

The picture of a real stator and rotor of a 4-pole 50W SPIM is shown in Fig. 1.2. The large skew angle of the rotor-bars can be clearly observed in the picture.

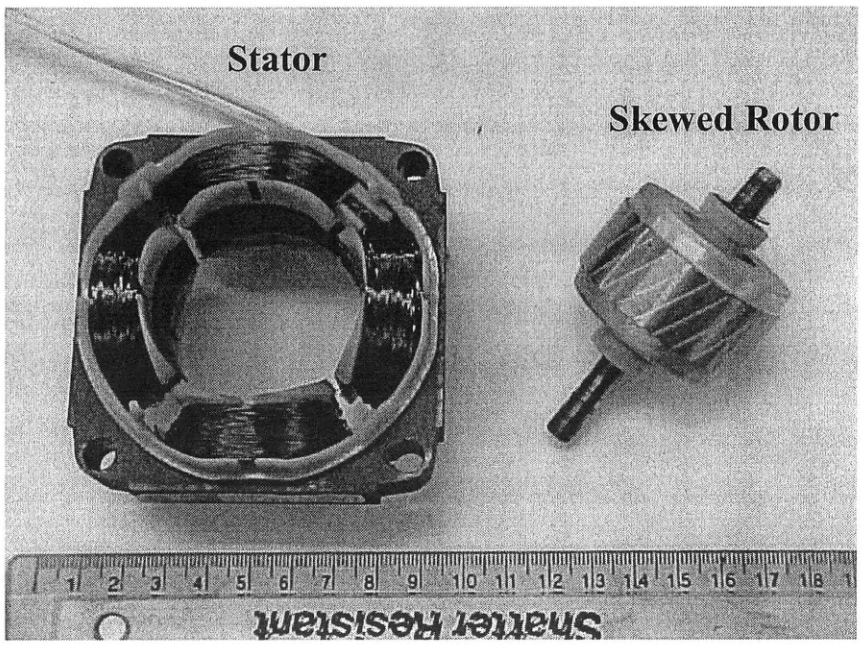

Fig. 1.2 The stator and rotor of a 4-pole 50W SPIM (Model T)
(The ruler is marked in centimetres)

SPIMs are driven by the action of a rotating magnetic field built up by the primary winding and shaded-rings displaced asymmetrically in space. Since the shaded ring is not excited by the external source, the method to obtain the rotating magnetic field is slightly

different from that of symmetric three- or two-phase induction motors. According to Veinott's explanation [1959] , an elementary understanding of the action of the rotating field of SPIMs may be gained from studying the variation of flux in different portions of the main pole. Consider the moment when the current flowing in the stator coil is zero but is just starting to increase positively. In the un-shaded portion of the main pole, the flux ϕ_m is set up in phase with the stator winding current. In the shaded area, the change of flux induces a voltage in the shading-ring, therefore an inductive current is caused to flow in the shading ring. According to the Lenz's law, the flux due to the induced current always opposes the previous flux. Thus, the build up of ϕ_S, the flux in the shaded area, is delayed by the induced current in the shading-ring. Furthermore, when the current in the stator coil begins to decrease, the flux ϕ_m starts to decrease immediately, but the flux ϕ_S does not decrease in phase with ϕ_m because the induced current in the shading-ring by the decreasing flux acts to oppose the change of flux ϕ_S and hence to maintain the flux in the shaded pole area. Therefore, flux ϕ_S always lags behind ϕ_m in time. Consequently, a rotating flux in the air gap is produced by the shaded winding and the main stator winding which have currents at different phase angle and displaced in the space. Since the rotating flux always moves from the main pole toward the shading-rings, the direction of rotation of a SPIM is from the un-shaded pole to the shaded portion of the pole.

Due to the use of the salient pole, the asymmetric displacement of the two windings and the non-uniform air gap, there are abundant spatial harmonics in the air gap field and time harmonics in the rotor-bar currents. Because of these abundant harmonics, the torque-speed characteristic of this kind of motor is usually unfavourable and not easy to predict accurately. When the speed variation of SPIMs is required, a phase control scheme with a triac or a pair of thyristors is most frequently adopted introducing more time harmonics in the stator current. Under these condition, the calculation of the torque performance is a major issue in the design of SPIMs and more attention needs to be paid to it.

Additionally, compared with other kinds of single-phase induction motors, SPIMs suffer the drawbacks of lower efficiency. Usually, the efficiency of SPIMs is not be beyond 30% [Veinott, 1959].

1. 2 Analysis Models of SPIMs

In order to improve the performance of the SPIMs, many papers have been published covering the area of developing analysis models and studying their performance characteristics after Trickey [1936] presented the earliest theoretical analysis. However, due to the asymmetrical windings, non-uniform air gap, spatial harmonics in the field and time harmonics in rotor-bar current, which generally do not simultaneously appear in other kinds of induction motors, the analysis of SPIMs is usually considered the most complicated. The analysis models of SPIMs proposed previously are roughly divided into two main categories: equivalent circuit models and finite element (FE) models.

1.2.1 Equivalent Circuit Models

Over the past 50 years, most published papers on SPIMs are based on equivalent circuit methods. In Chang's well-known paper [1951], the techniques to evaluate the spatial harmonic effects on motors with a constant air gap were presented by assuming a 90 electrical degree displacement between the shaded and unshaded portion of the poles and neglecting the effect of saliency. Usually, the accuracy of his model is not considered good enough because the actual shaded-rings are not always displaced at 90 electrical degrees. Chang's model was further developed by Bulter and Wallace [1969] with a generalised method to predict the motor performance with two shading rings per pole and arbitrary angles between the main coil and shading rings. A different model introduced by Kron [1950] tried to consider both the air gap variation and the magnetic-motive force (MMF) variation, but Kron did not give the method used for calculating the various constants in his model. The model employing the d-q axis theory by Dasai and Mathew [1971], similar to Kron's approach, was successfully used to compute the transient performance of motors with one shading ring per pole. In order to study the effect of the air gap profile, Eastham [1973] and Williamson [1977, 1978] developed a model for the direct solution of air gap field equations. The rotating-field theory, which can be applied for many shading rings per pole as well as an arbitrary reluctance augmented air gap, was

applied to SPIMs analysis by Trutt [1981]. Using an improved model, the harmonic effects were considered by Guru using rotating-field theory [1983]. By integrating a set of non-linear differential equations of the rotor and stator circuits with a numerical method, Perret and Poloujadoff [1976] proposed a new model to consider the saturation for steady state analysis. This numerical method was further developed by using a step-by-step method for SPIMs with non-uniform air gaps and non-sinusoidally distributed windings by Poloujadoff [1982]. Lock [1984, 1984, 1987] successfully applied an improved Poloujadoff model to predict the performance of SPIMs under transient states and variable speed states with phase-controlled circuits.

Although all these proposed equivalent circuit models are different, the following assumptions are usually made to derive the equivalent circuit equations.

(a) Harmonics are either ignored or considered with the superposition method. Therefore, the harmonic torque can not be calculated accurately.
(b) Saturation of the material is not considered in most proposed models, so the leakage reactance in the equivalent circuit cannot be obtained correctly.
(c) The effect of eddy currents is neglected. The iron loss is estimated from the experimental results.
(d) No magnetic bridge is considered.
(e) Skin effect is ignored and all the resistances and reactances of the equivalent circuit are assumed independent of the magnitude and frequency of the current.
(f) The effect of rotor slotting is neglected. The torque ripple due to the slotting is always neglected.

Due to the above assumptions, the results of the proposed models. e.g. torque/speed performance, are generally not satisfactory and are suitable only for a certain operated cases or structures. To improve the accuracy of equivalent circuit models, many empirical factors have to be used. These empirical factors are inevitably based on the personal experiences of the designer. Local factors, such as saturation and skin effect, are very difficult to account for by the analytical approaches. Therefore, more researchers now tend to apply the finite element method to the analysis of SPIMs.

1.2.2 Finite Element Models

After Chari [1971] pioneered the application of the finite element method in calculating the electromagnetic field, the finite element method has become the main tool to compute the magnetic fields in electrical machines. With the finite element method, the designer can solve problems that are hard to solve by analytical approaches, e.g. the harmonics' effect and the complicated three-dimensional magnetic field. The actual flux distribution can be found when the source current is defined. The saturation in different parts, e.g. the pole-bridge and the closed-slot, can be considered properly. The skin effect, which is essential for the starting performance, can also be investigated without the overall correction factors required by equivalent circuit models.

The field models of finite element analysis for different kinds of induction motors are all based upon Maxwell's equations. The variations of finite element models result from the different simplifying assumptions and the different external circuit equations.

The earliest form of finite element models for induction motors are known as fixed-mesh models because the rotor mesh employed by these models is stationary with respect to the stator mesh. Such models were initially developed for the determination of the performance of a sinusoidally excited machine operating at a constant speed. With these models, all the currents and field variables are assumed to vary sinusoidally in time and complex variables can be used. For such a model, the effect of rotor movement is considered using appropriate slip-frequency transformations. For these models, The field equation is defined as

$$\nabla \times \nu \nabla \times \vec{\mathbf{A}} = \vec{\mathbf{J}} \tag{1.1}$$

in which the arrows indicate complex quantities. The use of complex analysis implies that the field solution does not need to be time-stepped, giving a massive saving in computing time compared with the time-stepping method introduced next.

The main disadvantages resulting from the assumption of sinusoidal variation are that the effect of the harmonics has to be ignored and that the magnetic saturation has to be considered by using the time-averaged reluctivity for each non-linear element. To

overcome these drawbacks, a time-stepping model is usually adopted, in which the rotor rotation is simulated by rotating the rotor mesh with respect to the stator mesh. The field equation of this method can be defined as

$$\nabla \times \nu \nabla \times \mathbf{A} = \mathbf{J}. \tag{1.2}$$

The time-stepping models have a number of attractive advantages that are listed as below;

(a) All the non-sinusoidal quantities and source supply are able to be considered, therefore the harmonic torque can be taken into account correctly.

(b) Local iron saturation may be represented by an instantaneous value rather than the time-averaged one, so the local torque and the iron loss can be predicted more accurately.

(c) The effect of slotting in the rotor and stator to the air gap profile can be calculated and the torque ripple can be considered properly

(d) Dynamic performance, e.g. starting process, can be modelled easily.

However, against these advantages, the time-stepping model requires computing time two or more orders of magnitude greater than their fixed-mesh counterparts.

The field model of an induction motor is a three-dimensional problem. However at present, the three-dimensional (3D) finite element model is still the biggest challenge for electrical machines design. Due to the complicated mathematical model, the huge amount of computing cost and the requirement for a 3D pre- and post-processor, the 3D field model of a induction motor, especially the 3D time-stepping model, remains much more difficult to handle. Usually, the 3D model is simplified to a two-dimensional (2D) model by neglecting structure variation along the z-axis direction, e.g. the skew, rotor end-ring, stator hang-out and radial ventilation ducts, and by adopting the assumption that the vector potential consists only of an axial component.

With a 2D time-stepping FE model, both the steady state and transient characteristics of induction motors with unskewed rotors can be calculated with a high degree of accuracy [Arkkio, 1987; Salon, 1995]. However, for the SPIMs in which the skew plays an important role in reducing the effects of the spatial harmonics present in the air gap, the 2D approximation of the electromagnetic field of SPIMs cannot produce a satisfactory

result. Therefore, a more efficient alternative should be adopted. In recent years, the 2D non-linear, multi-slice, time-stepping, moving-mesh finite element model has been applied for several kinds of electrical machines [Piriou, 1990; Boualem, 1994; Williamson, 1995; Ho, 1997]. It presents a chance to take the skew into account.

Besides the skew, the end-ring effect is always ignored or is considered together with the lump resistance and reactance in the external circuit. However, the previous investigations using 2D or 3D finite element model [Kametani, 1996; Smith, 1997; Yamazaki, 1998] have proved that the effect of the end-ring on harmonics and machine performance should be taken into account.

Normally, the SPIM is voltage-driven, so all the source currents are unknown before the field is solved. However, the magnetic field of the SPIM is also not defined before the exciting current is known. Therefore, the external circuits and the magnetic field are coupled with each other. To solve such a coupled problem two different methods, the circuit model and the eddy-current model, are usually used. In the circuit method, the performance of the induction motor is based upon the traditional equivalent circuit approach. The finite element method, as a complement to the circuit method, is used only to compute the parameters of the equivalent circuit. All the stator and rotor currents are calculated outside the solution of the field equations [Williamson, 1985; Akbaba, 1992]. With this model, the eddy current, the skin effect and the harmonics cannot be considered properly. As to the eddy-current model, the characteristics of an electrical machine are determined directly by the distribution of the magnetic field and the current density. The stator and rotor-bar currents are decided by coupling the external circuit with the field equation either directly or indirectly. The skin effect is ready to be investigated and the harmonics can be included using the time-stepping method [Shen, 1985; Strangas, 1985; Arkkio, 1987; Vassent, 1991; Salon, 1995].

1. 3 Optimisation Design of SPIMs

When design engineers are asked to design an electrical machine to meet a given

specification, e.g. starting torque, unit volume or less material, they have to produce an initial draft according to their experience and existing machine designs. By comparing the performance of the designed machine with the given specification, the designer must then adjust some design variables to produce a revised design and analyse its performance. If the new design does not satisfy the required performance, the designer should adjust the design variables and re-calculate. The procedure of adjusting–analysing–comparing has to be repeated until a final design that satisfies all the requirements is obtained.

With such a design procedure, the quality of the final design depends mainly on the designer's experience. A good draft may be obtained by an experienced designer, even so they are not necessarily sure whether their design is the best one under the given conditions. To help the designer to get the best design, it is necessary to introduce the optimisation technique into the design procedure. However, for the electrical motor design, its optimisation is a highly non-linear problem with a rigorous feasible area. Although the conventional deterministic methods converge very fast, their results rely on the initial design and cannot ensure that the result obtained is the global optimisation result, the best solution under the given condition. For the modern optimisation method, such as Genetic Algorithms and Simulated Annealing, which usually can produce the global optimisation, a low convergence speed prevents their being used in normal machine design. Thus, the study of optimisation search algorithm for electrical machines has been one of interest in recent years [Simkin, 1992; Hameyer, 1994; Hameyer, 1996; Bianchi, 1998; Uler, 1996; Salujian, 1998; Mohammed, 1992; Lowther, 1993; Rong, 1994; Dym, 1991; Li, 1990; Kamper, 1996; Brisset, 1998; Williamson, 1996; Brandstater, 1998].

Additionally, in order to obtain a reliable optimisation result, the accurate evaluation of the objective function is another essential element. For the optimisation of SPIMs, if the performance calculation is not accurate enough, the optimisation search algorithm will be misled to a wrong direction. Since the equivalent circuit model is considered not accurate enough, this kind of model has been less used in electrical machine optimisation recently and a more accurate analysis model such as the finite element model is required. However, for the time-stepping method, the computing cost is still unacceptable for the

optimisation of SPIMs even in the two-dimensional situation. Thus, a suitable finite element model that can keep a balance between the accuracy and the computing time is required for the optimisation of SPIMs.

In the area of the SPIMs optimisation, no attention has been given recently to an overall (both stator and rotor) optimum design except for Yokozuka's research [1983]. In Yokozuka's paper, the performance analysis in the optimum design procedure is still performed by means of the equivalent circuit model that is not very accurate.

1. 4 About this Project

This research project was initially suggested by the Turk Electric Company (Turkey) which is the leading company in Europe making single-phase induction motors. The SPIM is one of their main products. The improvement in performance of the machine is continuously required by motor users. However, the engineers in the company's research and develop department do not have an accurate, reliable and convenient tool to carry out the analysis of this kind of machine. Therefore, the objective of this co-operative research was proposed three years ago. According to the original agreement, the Turk Electric Company supported their present designs and several motor samples for analysis and testing. With the finite element analysis and optimisation tools developed in this project, the optimum design arising from this research would be manufactured and tested using the full facilities of the Turkish company. Unfortunately, the company reformed its organisation last year and the research and develop department was removed. Hence it will not be possible to manufacture the prototype design, although the validation of the proposed 2D multi-slice time-stepping finite element model has been proved by the experimental results of the motor samples and the optimum design is ready to be produced using the optimisation program developed in this research.

1. 5 Major Aspects of the Research

In this research, the main tasks are to build up an accurate two-dimensional finite element model, investigating the effect of design parameter variations on SPIMs' characteristics and developing a suitable analysis model and a search algorithm for the optimisation of SPIMs. The major research work completed can be summarised as follows.

1. The GINO-based pre- and post-processors, which were previously developed by one of author's supervisors, Dr. Rajanathan, have been modified and transferred from the DEC Alpha mainframe to a PC platform to suit the PC-based finite element solver.

2. The 2D, time-stepping, non-linear eddy-current solver, which couples the external circuit equations to field equations, has been built up. In this research, both the indirect coupling and direct coupling methods were examined. In order to reduce the computing time of the time-stepping method, a variable step size method was investigated, which depends on estimating the truncation error of time-stepping. Additionally, by combining the Moving Band method with the Sliding Surface method, the continuous rotor movement can be simulated. Hence, both the steady state and transient characteristics of SPIMs can be studied.

3. To consider the 3D nature of SPIMs, e.g. the skew and end-ring, an improved 2D finite element was developed. In the proposed model, the multi-slice technique which was known to be the more efficient way of considering the effect of a skewed rotor has been introduced into the 2D FE model of SPIMs. As to the end-ring, for the first time, the end-ring resistance was investigated under the condition that the end-ring current distributes itself non-sinusoidally along the circumferential direction in the end-ring area. An instantaneous non-uniform end-ring resistance model was therefore adopted in the new model. Additionally, the external circuit equations were coupled directly to the field equations. Thus, the iteration of performance calculation is unnecessary and once the system equations are solved, the performance of a SPIM including current and torque can be obtained.

4. With the 2D multi-slice FE model coupled with uneven end-ring resistance, the

effects of variation of several design parameters including air gap profile, pole bridge, the skew, rotor slot number and closed-slot rotor have been examined. In order to learn the effect of different designs on the spatial harmonics in the air gap field and the time harmonics in the rotor-bar current, a harmonic analysis method based directly on the time-stepping finite element method was developed in this research.

5. Before applying the optimisation technique to the design of SPIMs, several kinds of optimisation search algorithms were investigated. A more efficient hybrid search algorithm which combines the Genetic Algorithms with the direct search method was proposed in this study. In order to meet the demand for both speed and accuracy, a multi-slice fixed-mesh model of SPIMs was built up and used for the calculation of the objective function in the optimisation procedure. Because the optimisation program is based on FE analysis directly, an automatic remesh scheme depending on the optimisation variables is necessary and therefore has been developed in this research as well. The proposed optimisation model for SPIMs design was tested by the optimisation design for maximum starting torque in this study.

6. In order to validate the result of the 2D, multi-slice finite element model proposed in this study, a PC-based experimental rig has been built. Using this test rig, two different designs of SPIMs have been tested and both the steady state and the transient state characteristics were investigated.

In this research, no commercial software was used. All the programs including the 2D multi-slice finite element solver of SPIMs and the improved hybrid global–local search algorithm were coded in FORTRAN by the author except that the pre-post processor were a modification of Dr. C. B. Rajanathan's design.

1. 6 Outline of the Thesis

This research involves a vast field ranging from electromagnetic field theory to optimisation search algorithms and form the derivation of mathematical equations to

computer program coding. To introduce them in detail, this thesis is divided into eight chapters, arranged as follows.

The previous section of this chapter introduced the operating principle of SPIMs. Different analysis tools for the SPIMs developed in the past have been investigated and the necessity of optimisation design is explained as well.

Starting from the original Maxwell equations, the partial differential equation of the magnetic field of electrical machines is derived for the 2D situation in chapter 2. To formulate the field equations into finite element terms, the Galerkin method is applied. Using the Backward Difference approach, the time-dependent field equations are discretised in the time domain. Finally, particular attention is given to the procedure of linearising the stiffness matrix equations using the Newton–Raphson method.

In chapter 3, the system equations describing the 2D, eddy-current time-stepping FE model of SPIMs are derived. To couple the external circuit equation to the field equation, both the indirect method and the direct method are discussed. Then, the linearised global system equations are presented. In order to study the SPIMs at different speeds or in the transient state, a hybrid method combining the Sliding Surface model with the Moving Band model is proposed to improve the convenience and quality of the rebuilt mesh as rotor mesh is rotated at each time step. The variable step-size method, which can significantly save computing time in the time-stepping FE method, is another interesting point in this chapter. By using the Neville's extrapolation process, the truncation error due to the time-stepping is estimated more accurately. Hence, the step size can be adjusted automatically according to the difference in vector potential between Neville's Algorithm and the Backward Difference method. The proposed method is tested by simulating a SPIM under the locked-rotor state and the results are compared with an existing variable step size model. In the final part of chapter 3, three different methods for calculating the electromagnetic force or torque are examined and the equation of torque calculation based on Maxwell's stress tensor is derived.

Although the multi-slice model has been successfully used in other kinds of electrical

motors, no detail of its application to SPIMs is available at present. Hence, to take the effect of the skew into account, the multi-slice model of a SPIM is introduced in chapter 4 and the procedure for deducing the governing system equations, which couple the field and external circuit equations directly, is described in detail. Besides the skewed rotor, the effect of the end-ring is also studied in this chapter. By using the finite element method to compute the electric field of the end-ring in the 2D situation, the resistance between two adjacent rotor bars can be calculated precisely. The influence of non-uniform end-ring resistance on the SPIM's performance is investigated by coupling it with the 2D multi-slice finite element model. In the final section of this chapter, to verify the validity of the proposed model, both the steady state and transient performances of two typical SPIMs are investigated with the 2D multi-slice approach that can consider the effect of skew and the end-ring. The results are compared with the experimental data showing the advantages of the proposed model.

In chapter 5, using the proposed 2D multi-slice time-stepping method, the effect of design parameter changes on SPIMs' performance is investigated. The parameters including air gap profile, pole bridge, the skew and the closed-slot rotor are usually difficult to analyse with the equivalent circuit method. In order to learn the effect of parameter variation on the field harmonics, a harmonic analysis method based on the time-stepping FE method is firstly introduced before the results of predicted performance with varying parameters are given.

The FE-based optimisation process applied to the design of the SPIMs is introduced in chapter 6. In this chapter, the different optimisation methods are first investigated. Based upon Genetic Algorithms and the Modified Hook–Jeeves' method, a more efficient and reliable hybrid optimisation method is proposed. A parameterised automatic remeshing scheme, which is driven by a few geometrical design parameters, is introduced to meet the requirement of the FE analysis program when the machine geometry is changed. In order to keep balance between speed and accuracy, a multi-slice sinusoidal approximation (fixed–mesh) FE model is examined and employed to estimate the performance of SPIMs. In the final section of chapter 6, the proposed optimisation program, combined with the approximation FE model, is tested by the optimisation of the

design of a SPIM, and the maximum starting torque is set as the optimisation object.

In chapter 7, a PC-based data acquisition system is developed and the detail of both the hardware and software of the test rig is explained. With this test rig, two types of SPIMs have been tested in both the steady state and the transient state. The results and analysis of testing are given in the final section of this chapter. In this chapter, the method of measuring torque-speed performance is another interesting point. Different measuring methods for torque measuring in both the steady state and transient state are examined.

In the final chapter, the achievements of the whole research are summarised briefly. Further work on developing the finite element method in the analysis SPIMs is indicated.

2 THEORY OF ELECTROMAGNETIC FIELDS AND TIME-STEPPING FINITE ELEMENT METHOD

2. 1 Introduction

Magnetic field computation is the core problem in electrical machine design. The accuracy of electrical machine analysis depends on knowledge of the electromagnetic field. Although Maxwell's equations offer a very accurate description for the magnetic field in electrical machines, there is still no universal analytical method that can be used to solve the field equations because of complicated geometry and non-linear material. As to the conventional analysis method, the magnetic field of an electrical machine is calculated approximately with the equivalent circuit models. All these models are normally based on the rough estimation of the magnetic field and are derived with some given assumptions: for instance, supplied by sinusoidal voltage, ignoring the saturation of the iron core and the effect of harmonics. Once these assumptions are not satisfied, the results of the model will be far outside what is acceptable. For different kinds of induction motor or different operational surroundings, different models have to be applied. Therefore, many equivalent circuit models have been developed for the analysis the performances of induction motors in steady state or transient. Even so, for SPIMs, there is still no reliable model that can be applied for the analysis of the transient state or locked-rotor operation.

The finite element technique, originally introduced by Chari and Silverter [1971] for the solution of the field equation, has become the most important tool in the analysis of the complicated electromagnetic fields of electrical machines. This method has proved to be the most efficient one in analysing accurately the performance of different kinds of electrical devices with complicated geometry. Although much more attention has been paid to the 3D finite element models due to the growth of computer capacity, the computing time for solving the 3D model with the time-stepping method is still too expensive. Therefore, in this study, the field model of SPIMs is simplified to two-dimensions. In order to consider the geometrical variation along the shaft of the machine, e.g. skewed-rotor, the 2D multi-slice model has been applied.

In this chapter, starting from the original Maxwell's equations, the partial differential equations for the magnetic field of electrical machines are derived for the 2D situation. Next, the Galerkin method, one of the Weighted Residuals methods [Binns, 1992], is applied to formulate the field equations in finite element terms. With the time difference approach, the time-dependent field equations are discretized in the time domain. Finally, particular attention is given to the procedure of linearizing the stiffness matrix equation by the Newton–Raphson method. Overall, the whole chapter focuses on introducing the background of the non-linear time-stepping finite element method.

2. 2 Equations of Time-dependent Electromagnetic Field

In this section, the differential equation in the term of vector potential is derived from Maxwell's equation, which aims to give the basic theoretical background of the time-dependent electromagnetic field.

The electromagnetic field, central to the analysis of electrical machine, is governed by a set of equations defining the curl and divergence of the field quantities. These equations

are known as the Maxwell's equations. Written in the form of differential equations, Maxwell's equations can be expressed as follows.

$$\nabla \times \mathbf{H} = \mathbf{J} + \frac{\partial \mathbf{D}}{\partial t} \tag{2.1}$$

$$\nabla \times \mathbf{E} = -\frac{\partial \mathbf{B}}{\partial t} \tag{2.2}$$

$$\nabla \cdot \mathbf{D} = \rho \tag{2.3}$$

$$\nabla \cdot \mathbf{B} = 0 \tag{2.4}$$

where **D** denotes the electric flux density and **E** the electric field strength. **B** is the magnetic flux density, **H** the magnetic field strength, ρ the free charge density and **J** the free current density in the region.

At the frequencies encountered in electrical machines, the wavelengths of the electromagnetic fields are very large compared with the physical dimension of the electrical machine, and the polarisation and displacement currents are very small compared with the free current density **J**. On the other hand, there is usually no free charge in the electrical machine, so the free charge density ρ is zero. In this case, Maxwell's equations for the electrical machine are simplified to:

$$\nabla \times \mathbf{H} = \mathbf{J} \tag{2.5}$$

$$\nabla \times \mathbf{E} = -\frac{\partial \mathbf{B}}{\partial t} \tag{2.6}$$

$$\nabla \cdot \mathbf{B} = 0. \tag{2.7}$$

Combining these equations with material characteristic equations gives

$$\mathbf{H} = \nu \mathbf{B} \tag{2.8}$$

$$\mathbf{J} = \sigma \mathbf{E} \tag{2.9}$$

where ν is the reluctivity of the material and σ the conductivity. Meanwhile, the current density **J** satisfies the continuity equation

$$\nabla \cdot \mathbf{J} = 0. \tag{2.10}$$

Using the magnetic vector potential **A** defined by

$$\mathbf{B} = \nabla \times \mathbf{A} \tag{2.11}$$

and electrical potential V, the following equation is derived from (2.6)

$$\mathbf{E} = -\frac{\partial \mathbf{A}}{\partial t} - \nabla V . \tag{2.12}$$

In (2.12) neither **A** nor V is completely defined since the gradient of an arbitrary scalar function can be added to **A** and the time derivative of the same function can be subtracted from V without affecting the physical quantities **E** and **B**. The uniqueness of the solution can only be ensured by specifying the divergence of **A** together with the necessary boundary condition. Normally, the 'Coulomb gauge' condition, $\nabla \cdot \mathbf{A} = 0$, is adopted [Binns, 1992].

Thus, the field equations in terms of current density, vector potential and scalar potential can be rewritten

$$\nabla \times \nu \nabla \times \mathbf{A} = \mathbf{J} \tag{2.13}$$

$$\mathbf{J} = \sigma(\frac{\partial \mathbf{A}}{\partial t} + \nabla V) . \tag{2.14}$$

In the general three-dimensional situation, the vector potential, **A**, and scalar potential, V, depend on the three spatial coordinates and time, so there are four unknown components. When the magnetic model of electrical machines is reduced to two dimensions, in which the geometry and material are independent of the z-coordinate, the field equations becomes much easier to solve. In the two-dimensional model, the vector potential and the current density can be defined as

$$\mathbf{A} = A(x, y, t)\mathbf{e}_z \tag{2.15}$$

$$\mathbf{J} = J(x, y, t)\mathbf{e}_z \tag{2.16}$$

where $\mathbf{e}_z$ is the unit vector parallel to the z-axis.

Therefore, the field equation (2.13) becomes

$$\frac{\partial}{\partial x}(\nu \frac{\partial A}{\partial x}) + \frac{\partial}{\partial y}(\nu \frac{\partial A}{\partial y}) = J . \tag{2.17}$$

In the two-dimensional model, because the vector potential and current density are constant along the z-axis, the scalar potential must be a linear function of the z-coordinate

to satisfy (2.14). Thus, the scalar potential difference between the ends of the conductor can be calculated by

$$\nabla V = \frac{V_b}{l_z} \tag{2.18}$$

where l_z = length of solution region in z-direction

V_b = source voltage applied to the terminal of the region

In an electrical machine there is relative rotation between the stator and rotor. The current density in the conductor moving with relative velocity **v** is generated by the Lorentz force and is computed by

$$\mathbf{J}_v = \sigma(\mathbf{v} \times \mathbf{B}) = \sigma(\mathbf{v} \times \nabla \times \mathbf{A}) \tag{2.19}$$

where **v** is the velocity of the conductor with respect to **B**.

Thus, in two-dimension, the current density, J, can generally be calculated with the following equation.

$$J = \sigma \frac{V_b}{l_z} - \sigma \frac{\partial A}{\partial t} - \sigma v \times B \tag{2.20}$$

In (2.20), the current density in conductor clearly consists of three parts which are called source current density, eddy-current density and motion-induced current density respectively. The first term is due to the external applied source, the second is due to the induced electric field produced by the time-varying magnetic flux, and the third due to motion-induced or 'motional' voltage. The three parts of J are distinguished only in pure mathematics, while the different components cannot be separated by experiment.

For the finite element method, if the velocity-relevant term is included in the field equation, the symmetry of the final system equations will be destroyed [Binns, 1992]. Thus, a more complete asymmetrical linear equation solver is needed. Additionally, the introduction of the velocity term may lead to severe numerical instability of the system equations if its magnitude is larger than the magnitude of the second order derivative term $\nabla^2 \mathbf{A}$. To avoid such problems, the time-stepping method is adopted in this study. With the time-stepping method, by employing a frame of reference which is fixed with

respect to the component under consideration (stator or rotor), the relative velocity v for each time step becomes zero. Therefore, the electromagnetic effects of motion can be taken into account by rotating the rotor by a spatial angle $\Delta\theta$ in a time step Δt and computing the whole change $\partial A/\partial t$ in (2.20) without separating it into 'transformer' and 'motional' components [Rajanathan, 1996]. Thus, for the time-stepping method, equation (2.13) is usually simplified to

$$\frac{\partial}{\partial x}(\nu\frac{\partial A}{\partial x})+\frac{\partial}{\partial y}(\nu\frac{\partial A}{\partial y})=\sigma(\frac{V_b}{l_z}-\frac{\partial A}{\partial t}). \tag{2.21}$$

In the above equation, the vector potential, A, and the source voltage, V_b, applied to the study region are time-dependent. If the magnetic field under consideration consists only of magnetically linear materials, all the field quantities will vary sinusoidally in the steady state when a sinusoidally varying source (voltage or current) is applied. In this situation, the time-dependence can be eliminated from (2.21) by using complex variables:

$$\frac{\partial}{\partial x}(\nu\frac{\partial \vec{A}}{\partial x})+\frac{\partial}{\partial y}(\nu\frac{\partial \vec{A}}{\partial y})=\sigma(\frac{\vec{V}_b}{l_z}-j\omega\vec{A}) \tag{2.22}$$

where the ω is the angular frequency of the time variation. Employing appropriate slip-frequency transformations, the rotor movement can be considered with a fixed rotor mesh.

2. 3 Finite Element Solution of Field Equation with Galerkin Formulation

There are two commonly used formulations for the solution of a field problem by the finite element method. The first one is to apply a variational principle corresponding to the defining field equations. With this method, an energy-related functional is formed from the partial differential equations modelling the field. The approximate solution of the field is given as a minimised point of the energy functional. However, this approach is only suitable for the problem whose field can be described by the elliptic partial different equation. Thus, an alternative formulation based on the weighted residuals method, e.g.

the Galerkin procedure, was proposed. This method has a wider applicability and is easy to apply to the problem whose functional cannot be found. In this thesis the Galerkin formulation is preferred and used in discretization of the field equation (2.21).

The field equation which governs the region Ω with boundary condition Γ is rewritten so that the right side of equation is zero:

$$G(x, y, A) = 0. \tag{2.23}$$

Submitting an approximate solution $\hat{A}$ into (2.23), a residual R is obtained since $A \neq \hat{A}$.

$$G(x, y, \hat{A}) = R. \tag{2.24}$$

According to the method of weighted residuals, the integral of the projection of the residual R on a specified weighting function, W, should be zero over the region Ω.

$$\int_{\Omega} RW dxdy = 0 \tag{2.25}$$

For the Galerkin formulation, the weight function, W, is chosen to have the same form as the finite element shape function, so the final finite element equations will be the same as that derived with the variational method in the cases where the functional can be found [Chari, 1971].

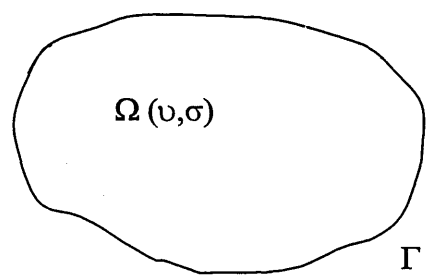

Fig. 2.1 Region being modelled

Substituting an approximation $\hat{A}$ and multiplying by a weight function W, the integration of (2.21) over the region Ω is

$$\iint_{\Omega} \left(W \left[\frac{\partial}{\partial x} \nu \frac{\partial \hat{A}}{\partial x} + \frac{\partial}{\partial y} \nu \frac{\partial \hat{A}}{\partial y} \right] - (W\sigma \frac{V_b}{l_z} - W\sigma \frac{\partial \hat{A}}{\partial t}) \right) dxdy = 0. \tag{2.26}$$

Integrating the first term in (2.26),

$$\iint_{\Omega} W\left[\frac{\partial}{\partial x}\nu\frac{\partial \hat{A}}{\partial x}+\frac{\partial}{\partial y}\nu\frac{\partial \hat{A}}{\partial y}\right]dxdy=\iint_{\Omega}\nu\left(\frac{\partial W}{\partial x}\frac{\partial \hat{A}}{\partial x}+\frac{\partial W}{\partial y}\frac{\partial \hat{A}}{\partial y}\right)dxdy-\frac{\partial \hat{A}}{\partial n}\oint_{\Gamma}\nu W d\Gamma \quad (2.27)$$

where $\frac{\partial \hat{A}}{\partial n}$ denotes the normal gradient of the vector potential on the boundary Γ.

With the finite element method, the whole study region Ω is meshed by a large number of small triangles, so the surface integrals in (2.26) are replaced by summations of the integrals over the small elements Ω^e, which yields

$$\sum_{N}\left\{\iint_{e}\nu^{e}\left(\frac{\partial W^{e}}{\partial x}\frac{\partial \hat{A}^{e}}{\partial x}+\frac{\partial W^{e}}{\partial y}\frac{\partial \hat{A}^{e}}{\partial y}\right)dxdy-\oint_{\Gamma}\nu^{e}\frac{\partial \hat{A}^{e}}{\partial n}W^{e}d\Gamma\right.$$
$$\left.-\iint_{e}W^{e}\sigma^{e}\frac{V_b^{e}}{l_z}dxdy+\iint_{e}W^{e}\sigma^{e}\frac{\partial \hat{A}^{e}}{\partial t}dxdy\right\}=0 \quad (2.28)$$

where N is the total number of the elements in region Ω.

In the field of an electrical machine the value of the boundary nodes is assumed to be a constant value, e.g. zero; in other words, the normal gradient of the vector potential on boundary Γ, $\frac{\partial \hat{A}^{e}}{\partial n}$ is set to be zero. Therefore, the line integral over the boundary in (2.28) becomes zero and can be neglected.

In this study, the first order, triangular finite elements Ω^e shown in Fig. 2.2 were used to mesh the solution region Ω.

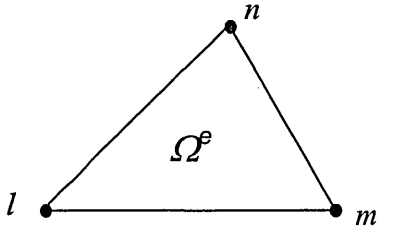

Fig. 2.2 Vertex notation for first order triangle element

For the first order element, the potential varies linearly in the element. With this assumption, the vector potential at any point in the element can be expressed as

$$\begin{aligned}\hat{A}^e(t) &= \begin{pmatrix} N_l & N_m & N_n \end{pmatrix} \begin{pmatrix} A_l(t) \\ A_m(t) \\ A_n(t) \end{pmatrix} \\ &= \sum N_i A_i(t) \qquad i = l, m, n \end{aligned} \tag{2.29}$$

where $A_l(t)$, $A_m(t)$ and $A_n(t)$ are the approximations of the nodal vector potential at the vertices of triangle mesh. N_l, N_m and N_n are the shape functions and can be calculated using following equations.

$$N_l = \frac{a_l + b_l x + c_l y}{\Delta_e} \tag{2.30a}$$

$$N_m = \frac{a_m + b_m x + c_m y}{\Delta_e} \tag{2.30b}$$

$$N_n = \frac{a_n + b_n x + c_n y}{\Delta_e} \tag{2.30c}$$

where Δ_e is the area of the triangle element

$$\Delta_e = \frac{1}{2}\begin{vmatrix} 1 & x_l & y_l \\ 1 & x_m & y_m \\ 1 & x_n & y_n \end{vmatrix} \tag{2.31a}$$

The geometric coefficient $\{a_l, b_l, c_l\}$ can be evaluated by

$$\begin{cases} a_l = x_m y_n - x_n y_m \\ b_l = y_m - y_n \\ c_l = x_n - x_m \end{cases}. \tag{2.32}$$

Similarly, $\{a_m, b_m, c_m\}$ and $\{a_n, b_n, c_n\}$ can be calculated as well.

Therefore, the derivatives of the approximation $\hat{A}$ with respect to x and y become

$$\begin{cases} \dfrac{\partial \hat{A}_e}{\partial x} = \dfrac{1}{2\Delta_e}\begin{pmatrix} b_l & b_m & b_n \end{pmatrix} \begin{pmatrix} A_l(t) \\ A_m(t) \\ A_n(t) \end{pmatrix} \\ \dfrac{\partial \hat{A}_e}{\partial y} = \dfrac{1}{2\Delta_e}\begin{pmatrix} c_l & c_m & c_n \end{pmatrix} \begin{pmatrix} A_l(t) \\ A_m(t) \\ A_n(t) \end{pmatrix} \end{cases}. \tag{2.33}$$

For the Galerkin method, the weighting function is the shape function itself, so

$$W^e = \begin{pmatrix} N_l \\ N_m \\ N_n \end{pmatrix} \tag{2.34}$$

Taking derivatives of W^e with respect to x and y, one obtains

$$\begin{cases} \dfrac{\partial W^e}{\partial x} = \dfrac{1}{2\Delta_e}\begin{pmatrix} b_l \\ b_m \\ b_n \end{pmatrix} \\ \dfrac{\partial W^e}{\partial y} = \dfrac{1}{2\Delta_e}\begin{pmatrix} c_l \\ c_m \\ c_n \end{pmatrix} \end{cases} . \tag{2.35}$$

Substituting (2.33) and (2.32) into first term of (2.28), we get

$$\begin{aligned} \iint_e \nu^e \left(\frac{\partial W^e}{\partial x}\frac{\partial \hat{A}^e}{\partial x} + \frac{\partial W^e}{\partial y}\frac{\partial \hat{A}^e}{\partial y} \right) dxdy &= \nu^e \left(\frac{\partial W^e}{\partial x}\frac{\partial \hat{A}^e}{\partial x} + \frac{\partial W^e}{\partial y}\frac{\partial \hat{A}^e}{\partial y} \right) \iint_e dxdy \\ &= \nu^e \begin{pmatrix} s_{e,ll} & s_{e,lm} & s_{e,ln} \\ s_{e,ml} & s_{e,mm} & s_{e,mn} \\ s_{e,nl} & s_{e,nm} & s_{e,nn} \end{pmatrix} \begin{pmatrix} A_l(t) \\ A_m(t) \\ A_n(t) \end{pmatrix} \end{aligned} \tag{2.36}$$

where

$$s_{e,ij} = \frac{1}{4\Delta_e}(b_i b_j + c_i c_j) \qquad \begin{cases} i = l,m,n \\ j = l,m,n \end{cases} . \tag{2.37}$$

Substituting (2.29) and (2.34) into(2.28), the third integral item becomes

$$\begin{aligned} \iint W^e \sigma^e \frac{V_b^e}{l_Z} dxdy &= \sigma^e \frac{V_b^e}{l_Z} \iint \begin{pmatrix} N_l \\ N_m \\ N_n \end{pmatrix} dxdy \\ &= \sigma^e \frac{V_b^e}{l_Z} \cdot \frac{\Delta_e}{3} \begin{pmatrix} 1 \\ 1 \\ 1 \end{pmatrix} \end{aligned} . \tag{2.38}$$

The final item in (2.28) can be simplified as well;

$$\iint_e W^e \sigma^e \frac{\partial \hat{A}^e}{\partial t} dxdy = \left(\sigma^e \iint \begin{pmatrix} N_l \\ N_m \\ N_n \end{pmatrix} (N_l \quad N_m \quad N_n) dxdy \right) \begin{pmatrix} \frac{\partial A_l(t)}{\partial t} \\ \frac{\partial A_m(t)}{\partial t} \\ \frac{\partial A_n(t)}{\partial t} \end{pmatrix}$$
$$= \begin{pmatrix} t_{ll} & t_{ml} & t_{ln} \\ t_{lm} & t_{mm} & t_{mn} \\ t_{\ln} & t_{mn} & t_{nn} \end{pmatrix} \begin{pmatrix} \frac{\partial A_l(t)}{\partial t} \\ \frac{\partial A_m(t)}{\partial t} \\ \frac{\partial A_n(t)}{\partial t} \end{pmatrix} \tag{2.39}$$

where

$$t_{e,ij} == \begin{cases} \frac{\sigma \Delta_e}{6} & i = j \\ \frac{\sigma \Delta_e}{12} & i \neq j \end{cases} . \tag{2.40}$$

With (2.36), (2.38) and (2.39), (2.28) can alternatively be rewritten in matrix form:

$$\sum_e \left[\nu [\mathbf{S}]_e \{A(t)\} \right] + [\mathbf{T}]_e \left\{ \frac{\partial A(t)}{\partial t} \right\} - [\mathbf{Q}]_e \frac{V_b}{l_z} = \{0\} . \tag{2.41}$$

In the above equation, Σ_e indicates summation over all of the finite elements in the solution region and the subscript e means that the matrix refers to a particular element. Typical entries in these matrices are calculated with (2.37), (2.40) and

$$Q_{e,i} = \frac{\sigma \Delta_e}{3} \tag{2.42}$$

Usually, when the time-stepping method is used, it is only necessary to deform the elements in free space (air gap) and the conductivity, σ, in such elements is zero, which nullifies the contribution of the [**T**], [**Q**] matrixes in (2.41). Hence, only [**S**] is time-dependent and requires re-evaluation at each time step.

After applying the Galerkin formulation, the field diffusion equation is finally changed into a set of time-dependent non-linear equations:

$$\nu[\mathbf{S}]\{A(t)\}+[\mathbf{T}]\left\{\frac{\partial A(t)}{\partial t}\right\}-[\mathbf{Q}]_e\frac{V_b}{l_z}=\{\mathbf{0}\}. \tag{2.43}$$

In (2.43) the terminal voltage V_b is unknown before the field equations are solved since the external circuit of SPIMs is coupled with the magnetic field for SPIMs.

2. 4 Time Discretion of Field Equation

The field equation (2.21) is a parabolic partial differential equation. As mentioned in section 2.2, for linear materials with sinusoidal source supply only, the time differential term in (2.21) can be replaced by using complex variables. However, due to the non-linear material used, the field quantities do not vary sinusoidally even under the excitation of a sinusoidal source supply, so abundant harmonics result in the field of SPIMs. Under these conditions, the sinusoidal approximation cannot give an accurate result. Usually, the time-stepping method, which can handle the non-sinusoidal field quantities, is considered the most suitable method. On the other hand, with the time-stepping method, the performance in the transient state can be taken into account as well.

One of the most frequently used methods for the electromagnetic field computation is the finite difference type of time-discretization algorithm, which can be generally described by the following equation:

$$\beta\{\frac{\partial A}{\partial t}\}^{t+\Delta t}+(1-\beta)\{\frac{\partial A}{\partial t}\}^{t}=\frac{\{A\}^{t+\Delta t}-\{A\}^{t}}{\Delta t}. \tag{2.44}$$

The value of the constant β, which determines the performance of the time-discretization algorithm, can vary from zero to one. In particular,

$\beta=0$ Forward Difference type

$\beta=1$ Backward Difference type

$\beta=1/2$ Crank-Nicholson Difference type.

Among these three methods, the Backward Difference type, in which β equals one, was considered very stable and simple [Salon, 1995; Rajanathan, 1996] and was adopted in this study as well. So, one obtains

$$\{\frac{\partial A}{\partial t}\}^{t+\Delta t} = \frac{\{A\}^{t+\Delta t} - \{A\}^{t}}{\Delta t}. \tag{2.45}$$

Hence, Equation (2.43) is changed accordingly to

$$\nu[\mathbf{S}]\{\mathbf{A}\}^{t+\Delta t} + [\mathbf{T}]\frac{\{\mathbf{A}\}^{t+\Delta t} - \{\mathbf{A}\}^{t}}{\Delta t} - [\mathbf{Q}]_e \frac{V_b^{t+\Delta t}}{l_z} = \{\mathbf{0}\}. \tag{2.46}$$

By denoting $n+1$ for time $t+\Delta t$, n for time t, and rearranging the term to isolate the t+Δt, we obtain

$$\left[\nu[\mathbf{S}] + \frac{[\mathbf{T}]}{\Delta t}\right]\{\mathbf{A}\}^{(n+1)} - [\mathbf{Q}]\frac{V_b^{(n+1)}}{l_z} = \frac{[\mathbf{T}]}{\Delta t}\{\mathbf{A}\}^{(n)}. \tag{2.47}$$

2. 5 Linearisation of the Field Equation

For the analysis of electrical machines, the field problem is always non-linear due to the presence of ferromagnetic material. The reluctivity, ν, in (2.21) is a function of the flux density, B, and hence of the vector potential, A. To linearise equation (2.21), different iteration methods are available. Among these methods, the Newton–Raphson method first applied by Chari & Silvester [1971] is considered the most efficient one.

To apply the Newton–Raphson method, (2.47) is rewritten to functional form

$$\left\{Y(A_i^{(n+1)}, V_b^{(n+1)})\right\} = \left[\nu[\mathbf{S}] + \frac{[\mathbf{T}]}{\Delta t}\right]\{\mathbf{A}\}^{(n+1)} - [\mathbf{Q}]_e \frac{V_b^{(n+1)}}{l_z} - \frac{[\mathbf{T}]}{\Delta t}\{\mathbf{A}\}^{(n)} = 0 \tag{2.48}$$

where $\{\mathbf{A}\}^{(n+1)}$ and $V_b^{(n+1)}$ are unknown at time $n+1$, while the vector potential of time n, $\{\mathbf{A}\}^{(n)}$, is known. Equation (2.48) can be expanded around $\{\mathbf{A}\}^{(n)}$ in a Taylor series in which only the first order term is kept, so it yields

$$\left\{\frac{\partial Y_i}{\partial A_i}\right\}\left\{A_i^{(n+1)}-A_i^{(n)}\right\}+\left\{\frac{\partial Y_i}{\partial V_b}\right\}\left\{V_b^{(n+1)}-V_b^{(n)}\right\}=-\left\{Y(A_i^{(n+1)}),V_b^{(n+1)}\right\}. \tag{2.49}$$

Considering the above equations in only one element, we obtain equation in matrix form:

$$\left(\nu\begin{pmatrix}s_{ll} & s_{lm} & s_{ln}\\ s_{ml} & s_{mm} & s_{mn}\\ s_{nl} & s_{nm} & s_{nn}\end{pmatrix}+\begin{pmatrix}t_{ll} & t_{ml} & t_{ln}\\ t_{lm} & t_{mm} & t_{mn}\\ t_{\ln} & t_{mn} & t_{nn}\end{pmatrix}\right)\begin{pmatrix}A_l\\ A_m\\ A_n\end{pmatrix}-\frac{1}{l_z}\begin{pmatrix}q_l\\ q_m\\ q_n\end{pmatrix}V_b-\begin{pmatrix}d_l\\ d_m\\ d_n\end{pmatrix}=0 \tag{2.50}$$

where
$$\begin{cases} s_{ij}=\dfrac{1}{4\Delta_e}(b_ib_j+c_ic_j)\\ t_{ij}=\begin{cases}\dfrac{\sigma\Delta_e}{6\Delta t} & i=j\\ \dfrac{\sigma\Delta_e}{12\Delta t} & i\neq j\end{cases}\\ q_i=\dfrac{\sigma\Delta_e}{3}\\ d_i=\sum\dfrac{t_{ij}}{\Delta t}A_{ij}^{(n)}\end{cases}$$

and A_i denotes the $A_i^{(n+1)}$, V_b is the $V_b^{(n+1)}$.

Let F represent the first equation. G and H represent the 2nd and 3rd :

$$F=\left(\nu\begin{pmatrix}s_{ll} & s_{lm} & s_{ln}\end{pmatrix}+\begin{pmatrix}t_{ll} & t_{lm} & t_{ln}\end{pmatrix}\right)\begin{pmatrix}A_l\\ A_m\\ A_n\end{pmatrix}-\frac{q_l}{l_z}V_b-d_l \tag{2.51a}$$

$$G=\left(\nu\begin{pmatrix}s_{ml} & s_{mm} & s_{mn}\end{pmatrix}+\begin{pmatrix}t_{ml} & t_{mm} & t_{mn}\end{pmatrix}\right)\begin{pmatrix}A_l\\ A_m\\ A_n\end{pmatrix}-\frac{q_m}{l_z}V_b-d_m \tag{2.51b}$$

$$H=\left(\nu\begin{pmatrix}s_{nl} & s_{nm} & s_{nn}\end{pmatrix}+\begin{pmatrix}s_{nl} & s_{nm} & s_{nn}\end{pmatrix}\right)\begin{pmatrix}A_l\\ A_m\\ A_n\end{pmatrix}-\frac{q_n}{l_z}V_b-d_n. \tag{2.51c}$$

To find the derivative necessary for the Newton–Raphson method, we differentiate the above equations with respect to the nodal vector potential. For F this gives

$$\frac{\partial F}{\partial A_l} = (\nu s_{ll} + t_{ll}) + (s_{ll}A_l + s_{lm}A_l + s_{\ln}A_n)\frac{\partial \nu}{\partial A_l} \tag{2.52a}$$

$$\frac{\partial F}{\partial A_m} = (\nu s_{ml} + t_{ml}) + (s_{ml}A_l + s_{mm}A_m + s_{mn}A_n)\frac{\partial \nu}{\partial A_m} \tag{2.52b}$$

$$\frac{\partial F}{\partial A_n} = (\nu s_{nl} + t_{nl}) + (s_{nl}A_l + s_{nm}A_m + s_{nn}A_n)\frac{\partial \nu}{\partial A_n} \tag{2.52c}$$

$$\frac{\partial F}{\partial V_b} = -\frac{q_l}{l_z} \tag{2.52d}$$

So the Newton–Raphson equation for F is given as

$$\frac{\partial F}{\partial A_l}\Delta A_l + \frac{\partial F}{\partial A_m}\Delta A_m + \frac{\partial F}{\partial A_n}\Delta A_n + + \frac{\partial F}{\partial V_b}\Delta V_b = -F(A_l, A_m, A_n, V_b) \tag{2.53}$$

According to the chain rule, $\dfrac{\partial \nu}{\partial A_l} = \dfrac{\partial \nu}{\partial B^2}\dfrac{\partial B^2}{\partial A_l}$

and by defining $FL = (s_{ll}A_l + s_{lm}A_m + s_{ln}A_n)$, equation 1.19 becomes

$$(\nu s_{ll} + t_{lli})\Delta A_l + (\nu s_{lm} + t_{lm})\Delta A_m + (\nu s_{ln} + t_{ln})\Delta A_n + FL\frac{\partial \nu}{\partial B^2}\left(\frac{\partial B^2}{\partial A_l}\Delta A_l + \frac{\partial B^2}{\partial A_m}\Delta A_m + \frac{\partial B^2}{\partial A_n}\Delta A_n\right) - \frac{q_i}{l_z}\Delta V_b = -F \tag{2.54}$$

Rewritten in matrix form, the above equation is changed into

$$\left((\nu s_{ll} + t_{ll}) \quad (\nu s_{lm} + t_{lm}) \quad (\nu s_{ln} + t_{ln})\right)\begin{pmatrix}\Delta A_l \\ \Delta A_m \\ \Delta A_n\end{pmatrix} + FL * \frac{\partial \nu}{\partial B^2}\begin{pmatrix}\frac{\partial B^2}{\partial A_l} & \frac{\partial B^2}{\partial A_m} & \frac{\partial B^2}{\partial A_n}\end{pmatrix}\begin{pmatrix}\Delta A_l \\ \Delta A_m \\ \Delta A_n\end{pmatrix} - \frac{q_i}{l_z}\Delta V_b = -F \tag{2.55}$$

And we can deal with the equations for G and H in the same way to get the whole element equation of the Newton–Raphson form:

$$\left(\nu\begin{pmatrix} s_{ll} & s_{lm} & s_{ln} \\ s_{ml} & s_{mm} & s_{mn} \\ s_{nl} & s_{nm} & s_{nn} \end{pmatrix}+\begin{pmatrix} t_{ll} & t_{ml} & t_{ln} \\ t_{lm} & t_{mm} & t_{mn} \\ t_{ln} & t_{mn} & t_{nn} \end{pmatrix}\right)\begin{pmatrix} \Delta A_l \\ \Delta A_m \\ \Delta A_n \end{pmatrix}+\frac{\partial \nu}{\partial B^2}\begin{pmatrix} FL & FL & FL \\ FM & FM & FM \\ FN & FN & FN \end{pmatrix}\begin{pmatrix} \frac{\partial B^2}{\partial A_l} & & \\ & \frac{\partial B^2}{\partial A_m} & \\ & & \frac{\partial B^2}{\partial A_n} \end{pmatrix}\begin{pmatrix} \Delta A_l \\ \Delta A_m \\ \Delta A_n \end{pmatrix}-\begin{pmatrix} q_l \\ q_m \\ q_n \end{pmatrix}\frac{\Delta V_b}{l_z}$$

$$=\left(\nu\begin{pmatrix} s_{ll} & s_{lm} & s_{ln} \\ s_{ml} & s_{mm} & s_{mn} \\ s_{nl} & s_{nm} & s_{nn} \end{pmatrix}+\begin{pmatrix} t_{ll} & t_{ml} & t_{ln} \\ t_{lm} & t_{mm} & t_{mn} \\ t_{ln} & t_{mn} & t_{nn} \end{pmatrix}\right)\begin{pmatrix} A_l \\ A_m \\ A_n \end{pmatrix}+-\frac{1}{l_z}\begin{pmatrix} q_l \\ q_m \\ q_n \end{pmatrix}V_b-\begin{pmatrix} d_l \\ d_m \\ d_n \end{pmatrix} \tag{2.56}$$

where

$$FL = s_{ll}A_l + s_{lm}A_m + s_{ln}A_n$$

$$FM = s_{ml}A_i + s_{mm}A_m + s_{mn}A_n$$

$$FN = s_{nl}A_l + s_{nm}A_m + s_{nn}A_n .$$

In (2.56), the $\frac{\partial \nu}{\partial B^2}$ term can be obtained from the B-H curve and $\frac{\partial B^2}{\partial A_l}$ can be evaluated with element geometry coefficients as well. Because

$$B^2 = (\frac{\partial A}{\partial x})^2 + (\frac{\partial A}{\partial y})^2 \tag{2.57}$$

and

$$A = \frac{a_l + b_l x + c_l y}{2\Delta_e}A_l + \frac{a_m + b_m x + c_m y}{2\Delta_e}A_m + \frac{a_n + b_n x + c_n y}{2\Delta_e}A_n \tag{2.58}$$

one obtains

$$\begin{cases} \frac{\partial A}{\partial x} = \frac{b_l A_l + b_m A_m + b_n A_n}{2\Delta_e} \\ \frac{\partial A}{\partial y} = \frac{c_l A_l + c_m A_m + c_n A_n}{2\Delta_e} \end{cases} \tag{2.59}$$

and $B^2 = \left(\frac{b_l A_l + b_m A_m + b_n A_n}{2\Delta_e}\right)^2 + \left(\frac{c_l A_l + c_m A_m + c_n A_n}{2\Delta_e}\right)^2 .$

Thus, we obtain

$$\frac{\partial B^2}{\partial A_l} = \frac{2b_l(b_l A_l + b_m A_m + b_n A_n) + c_l(c_l A_l + c_m A_m + c_n A_n)}{4\Delta_e^2} = \frac{2(s_{ll} A_l + s_{lm} A_m + s_{ln} A_n)}{\Delta_e} = \frac{2}{\Delta_e} FL \tag{2.60a}$$

The same procedure can apply to $\partial B^2 / \partial A_m$ and $\partial B^2 / \partial A_n$. Then we get

$$\frac{\partial B^2}{\partial A_m} = \frac{2}{\Delta_e} FM \qquad \frac{\partial B^2}{\partial A_n} = \frac{2}{\Delta_e} FN \tag{2.60b), (2.60c}$$

Substituting equation (2.60) into equation (2.56), the final equation yields

$$\left(\nu \begin{pmatrix} s_{ll} & s_{lm} & s_{ln} \\ s_{ml} & s_{mm} & s_{mn} \\ s_{nl} & s_{nm} & s_{nn} \end{pmatrix} + \begin{pmatrix} t_{ll} & t_{ml} & t_{ln} \\ t_{lm} & t_{mm} & t_{mn} \\ t_{ln} & t_{mn} & t_{nn} \end{pmatrix} \right) \begin{pmatrix} \Delta A_l \\ \Delta A_m \\ \Delta A_m \end{pmatrix} + \frac{\partial \nu}{\partial B^2} \begin{pmatrix} FL*FL & FL*FM & FL*FN \\ FM*FL & FM*FM & FM*FN \\ FN*FL & FN*FM & FN*FN \end{pmatrix} \begin{pmatrix} \Delta A_l \\ \Delta A_m \\ \Delta A_n \end{pmatrix} - \frac{1}{l_z} \begin{pmatrix} q_l \\ q_m \\ q_n \end{pmatrix} \Delta V_b$$
$$= \left(\nu \begin{pmatrix} s_{ll} & s_{lm} & s_{ln} \\ s_{ml} & s_{mm} & s_{mn} \\ s_{nl} & s_{nm} & s_{nn} \end{pmatrix} + \begin{pmatrix} t_{ll} & t_{ml} & t_{ln} \\ t_{lm} & t_{mm} & t_{mn} \\ t_{ln} & t_{mn} & t_{nn} \end{pmatrix} \right) \begin{pmatrix} A_l \\ A_m \\ A_n \end{pmatrix} - \frac{1}{l_z} \begin{pmatrix} q_l \\ q_m \\ q_n \end{pmatrix} V_b - \begin{pmatrix} d_l \\ d_m \\ d_n \end{pmatrix} = 0 \tag{2.61}$$

Therefore, assembling all elements in the solution region, (2.47) can be linearised:

$$\left[\nu[\mathbf{S}] + [\mathbf{G}] + \frac{[\mathbf{T}]}{\Delta t} \right] \{\Delta \mathbf{A}\}^{(n+1)} - [\mathbf{Q}]_e \frac{\Delta V_b}{l_z} = -\left[\nu[\mathbf{S}] + \frac{[\mathbf{T}]}{\Delta t} \right] \{\mathbf{A}\}^{(n+1)} - [\mathbf{Q}]_e \frac{V_b}{l_z} + \frac{[\mathbf{T}]}{\Delta t} \{\mathbf{A}\}^{(n)} \tag{2.62}$$

where $G = \frac{2}{\Delta_e} \frac{\partial \nu}{\partial B^2} \begin{pmatrix} FL*FL & FL*FM & FL*FN \\ FM*FL & FM*FM & FM*FN \\ FN*FL & FN*FM & FN*FN \end{pmatrix}$

Thus, after linearization, the coefficient matrix of the non-linear term, $\left[\nu[\boldsymbol{S}] + \frac{[\boldsymbol{T}]}{\Delta t} \right]$, is changed to $\left[\nu[\mathbf{S}] + [\mathbf{G}] + \frac{[\mathbf{T}]}{\Delta t} \right]$ called the Jacobian Matrix.

The process of applying the Newton–Raphson method to solve the non-linear field can be summarised as the following steps.

1. Assume an initial value of reluctivity for each element, $\nu_e = \nu_e^0$.
2. Evaluate the matrices **[S]** in (2.62) by using ν_e and assemble the matrix.
3. Apply the boundary condition and solve the field equation for ΔA_i vector.
4. Find the new $A_i^{(k+1)}$, by adding the ΔA_i to the previous value of A_i:

$$A_i^{(k+1)} = A_i^{(k)} + \Delta A_i. \tag{2.63}$$

5. Applying a convergence criterion:

$$err = \frac{\sum_i |\Delta A_i|^{k+1}}{\sum_i |A_i|^k} \leq \varepsilon \tag{2.64}$$

where the index i ranges over all nodes in the solution region, and the superscript k indicates the iteration number.

If equation (2.64) is satisfied at step five, which means *err* is smaller than ε, a positive small number, the Newton–Raphson iteration can be stopped and the final solution of the non-linear equation (2.62) is obtained. Otherwise, calculate the $\nu_e^{(k+1)}$ of each element according to the new $A_i^{(k+1)}$ and go to step two again.

It is found that no noticeable difference is observed in the terminal characteristics for values of ε smaller than 0.03, so the ε value used in the simulation program is between 0.01 and 0.03.

3 TWO-DIMENSIONAL EDDY-CURRENT TIME-STEPPING FINITE ELEMENT MODEL FOR SPIMS

3. 1 Introduction

The suitability of the finite element method for the analysis of electrical machines has long been recognised. Generally, the induction motor models for finite elements analysis can be divided into two broad categories: circuit models [Williamson, 1985, Akbaba, 1996] and eddy-current models [Arkkio, 1987, Boualem, 1994].

For the circuit models, the fields are described by (2.17). Using these models, all the currents in the field are assumed known before the field equation is solved. Thus, the system equations of this kind of model are quite easy to build up and solve. This model is very suitable for modelling the Switched Reluctance motors and DC Brushless motors in which all the currents in the study area have been defined. However, by using this kind of model for the induction motors, the skin effect in the conductors has to be ignored and the irregular harmonic currents in the field are difficult to be considered as well [Williamson, 1985]. On the other hand, in order to decide the currents in the field, the equivalent circuit equations for induction motor are usually employed by the circuit models, so the accuracy of circuit models are normally restricted by the equivalent circuit equations.

The eddy-current models depend on the field equation (2.21) and they have two primary advantages compared with the circuit model. First, the skin effects in the rotor-bar can be taken into account automatically in the starting procedure. Secondly, the abundant harmonics including the third-order, the fifth-order and other irregular harmonics can be considered properly when the time-stepping method is adopted. The harmonic torque, which play an important role in the performance of SPIMs, can be considered properly. In this research, the eddy-current time-stepping finite element model of SPIMs is studied.

Based on the electromagnetic field knowledge introduced in Chapter 2, a two-dimensional eddy-current time-stepping finite element model of SPIMs is built up in this chapter. For SPIMs driven by a voltage source, the external circuit equations are coupled with the field equations, both of which should be solved simultaneously. In this chapter, two methods, the indirect and the direct, are used to cope with the coupled problem. The final system equations are linearised with the Newton-Raphson method.

When the time-stepping method is applied, the finite element mesh should be rebuilt at each time step to simulate the continuous movement of rotor rotation. In order to know the performance during the whole speed range, the rotor speed is required to vary from zero to synchronous speed. Therefore, the advantages and disadvantages of the conventional re-mesh schemes, such as the Moving Band model and the Sliding Surface model, are investigated. Furthermore, a hybrid method combining the Sliding Surface model with the Moving Band model is proposed to improve the convenience and quality of the rebuilt mesh.

The computing cost is always expensive for the time-stepping method. In order to save calculation time, a variable step size method is required. However, to choose a suitable step size is always difficult for a variable step size method. In this study, by adopting a more accurate extrapolation process, Neville's Algorithm, to estimate the truncation error due to using the time-stepping method, the suitability of step size can be judged correctly. Hence, it becomes possible to adjust the time step size automatically according to the scale of the truncation error given by Neville's Algorithm and the Backward Difference

method. The proposed method is tested by simulating a SPIM under the locked-rotor state and the results are compared with a existing variable step size model.

In the final part of this chapter, three different methods to calculate the electromagnetic force or torque are explained. The equation of torque calculation based on Maxwell's stress tensor is derived. To obtain a more accurate solution, the criterion of choosing the integration contour is also given here.

3. 2 Eddy-current Time-Stepping Model of SPIMs

According to the discussion in the proceeding chapter, the eddy-current model of SPIMs can be described with (2.21) and is rewritten here again:

$$\frac{\partial}{\partial x}(\nu\frac{\partial A}{\partial x})+\frac{\partial}{\partial y}(\nu\frac{\partial A}{\partial y})=\sigma(\frac{V_b}{l_z}-\frac{\partial A}{\partial t}). \tag{3.1}$$

In the stator windings region, due to the fact that the stator coil normally consists of fine wires, the current density J_c in the stator coil is assumed uniform without considering the eddy-current effect. Therefore it can be expressed from the armature conductor current I_c as

$$J_C=\frac{N_c}{S_p}I_c \tag{3.2}$$

where N_c denotes the turns of coil of one pole and S_p is the cross-sectional area of one coil side.

In the rotor-bar region, the eddy-current should be taken into account, and the bar current consists of two parts, the eddy-current and the source current. So the current density J_b can be represented as

$$J_C = \sigma \frac{V_b}{l_z} - \sigma \frac{\partial A}{\partial t} \tag{3.3}$$

where

σ = electrical conductivity of bar

l_z = length of bar

V_b = source voltage applied to the bar terminal.

If the end-ring of the rotor cage is assumed as an ideal short circuit, in other words, the leakage reactance and the resistance of the end-ring of the cage rotor are ignored, the ends of rotor bars are all at the same potential. Consequently, the potential difference term, V_b, in (3.3) equals zero. This assumption makes the eddy-current model of the induction motor much simpler because the complex circuit equations of the rotor cage disappear from the final system equations. This model has been used successfully to simulate the single-phase induction motor operating in the motoring, generating and braking situations [Rajanathan, 1996]. However, for SPIMs, this model is too simple to get enough accuracy of the rotor cage current as the resistance of the end-ring has significant effect on the rotor current [Williamson & Mueller, 1992]. Therefore, in the following discussion, the terminal potential difference of the rotor bar, V_b, will be considered to increase the accuracy of FE Model.

With regard to the shaded-rings, we have two options. One is to treat it the same way as the stator winding by assuming that the current flowing through the shading ring is uniform. The other is using the eddy-current model that is similar to the rotor-bar model. The model without eddy-current effect will make coupling the electric circuit equation much simpler, especially in the multi-slice case, which will be explained in the next chapter. Normally, the thickness of the shading ring is much smaller compared with that of rotor bars. Therefore, in this study, the current of the shading ring is estimated without considering the effect of eddy current, so the current density of the shaded-ring, J_s, is calculated as

$$J_S = \frac{1}{S_S} I_S \tag{3.4}$$

where S_s denotes the cross-sectional area of shaded-ring.

For the SPIMs, because the iron core is laminated, the eddy currents in the iron core are neglected in our model. Therefore, in the iron region and air gap, the current density, J, equals zero.

Subject to the above assumptions, the model of SPIMs for finite elements can be defined:

$$\frac{\partial}{\partial x}(\nu\frac{\partial A}{\partial x})+\frac{\partial}{\partial y}(\nu\frac{\partial A}{\partial y})=\beta_n^c I_C+\beta_n^s I_S+\beta_n^b\left(\frac{V_b}{l_z}-\frac{\partial A}{\partial t}\right) \tag{3.5}$$

where

$$\beta_n^c(x,y)=\begin{cases}+\dfrac{N_C}{S_C} & \text{If point } (x, y) \text{ belongs to a positively oriented stator coil side of winding } n\\ -\dfrac{N_C}{S_C} & \text{If point } (x, y) \text{ belong to a negatively oriented stator coil side of winding } n\\ 0 & \text{Otherwise}\end{cases}$$

$$\beta_n^s(x,y)=\begin{cases}+\dfrac{1}{S_C} & \text{If point } (x, y) \text{ belongs to a positively oriented shaded ring side of winding n}\\ -\dfrac{1}{S_C} & \text{If point } (x, y) \text{ belongs to a negatively oriented shaded ring side of winding } n\\ 0 & \text{Otherwise}\end{cases}$$

$$\beta_n^s(x,y)=\begin{cases}1 & \text{If point } (x, y) \text{ belongs to rotor-bar n}\\ 0 & \text{Otherwise}\end{cases}$$

By applying the Galerkin procedure to equation (3.5), we can get the system equation in matrix form

$$\nu[\mathbf{S}]\{\mathbf{A}\}^{(n+1)}+[\mathbf{T}]\left\{\frac{\partial \mathbf{A}}{\partial t}\right\}^{(n+1)}-[\mathbf{Q}]\frac{\mathbf{V_b}}{l_z}-[\mathbf{D_C}]\{\mathbf{I_C}\}-[\mathbf{D}_S]\{\mathbf{I}_S\}=\{\mathbf{0}\} \tag{3.6}$$

where

$$S_{ij}=\frac{1}{4\Delta_e}(b_i b_j+c_i c_j) \tag{3.7a}$$

$$T_{ij}=\begin{cases}\beta_n^b\dfrac{\Delta_e}{6} & i=j\\ \beta_n^b\dfrac{\Delta_e}{12} & i\neq j\end{cases} \tag{3.7b}$$

$$Q_{ij} = \beta_n^b \frac{\sigma \Delta_e}{3} \tag{3.7c}$$

$$D_{c,ij} = \beta_n^C \frac{\Delta_e}{3} \tag{3.7d}$$

$$D_{S,ij} = \beta_n^S \frac{\Delta_e}{3}. \tag{3.7e}$$

According to the Backward Difference method, substituting (2.45) into (3.6), the field equation can be time-discretized.

$$\left(\nu[\mathbf{S}] + \frac{[\mathbf{T}]}{\Delta t}\right)\{\mathbf{A}\}^{(n+1)} - [\mathbf{Q}]\frac{\{\mathbf{V_b}\}^{(n+1)}}{l_z} - [\mathbf{D_C}]\{\mathbf{I_C}\}^{(n+1)} - [\mathbf{D}_S]\{\mathbf{I}_S\}^{(n+1)} = \frac{[\mathbf{T}]}{\Delta t}\{\mathbf{A}\}^{(n)} \tag{3.8}$$

3. 3 Coupling External Circuits to Field Equations

Since the SPIMs is supplied with a voltage source rather than a current source, the current in the stator coil and the shading ring are unknown before the field equations are solved. Meanwhile, the field distribution cannot be decided as the exciting currents are not defined. Therefore, the field equations and external circuit equations are coupled. Usually, two strategies are used to cope with this problem, one is called the indirect method [Williamson, 1985, Rajanathan, 1996], the other the direct method [Arkkio, 1987, Salon, 1995].

The indirect method, the one most frequently and successfully used in the simulation of the induction motor and actuator by the author's supervisor [Rajanathan, 1996], is based on an iterative procedure which finally gets the correct currents to match both circuit and field equations. The main advantage of this method is that it is easy to connect the non-linear circuit component without making the stiffness matrix more complex. In addition, by adopting the modified secant method [Rajanathan, 1996], the iteration steps can be significantly reduced. However, for the eddy-current FE model of the induction motor, the indirect method can only be used to solve the model assuming that the end-ring of the

rotor cage is an ideal short circuit, which makes the term of V_b/l_z disappear from field equation (3.5). The lower accuracy of the cage bar current is the main disadvantage of the indirect method being used for SPIMs. Compared with the direct coupling method, this method is easy to program, so it is explained here first.

3.3.1 Indirect Method of Coupling Circuit Equations

Using the indirect coupling method, since the terminal potential difference between adjacent rotor bars has to be ignored, the term V_b/l_z in field equation (3.5) becomes zero. The current density in the rotor region results only from the effect of the eddy current, so it can be coupled to the field equation automatically by calculating $\partial A/\partial t$. Therefore, the global system equation can be described as the following.

$$\left(\nu[\mathbf{S}]+\frac{[\mathbf{T}]}{\Delta t}\right)\{\mathbf{A}\}^{(n+1)}=[\mathbf{D_C}]\{\mathbf{I_C}\}^{(n+1)}+[\mathbf{D}_S]\{\mathbf{I}_S\}^{(n+1)}+\frac{[\mathbf{T}]}{\Delta t}\{\mathbf{A}\}^{(n)} \tag{3.9}$$

With the indirect coupling method, only three unknown variables of the external circuit equations of SPIMs need to be evaluated, which are the current in stator coil *Ic* and two shaded-ring currents I_{S1} and I_{S2}. The convergence of the iteration procedure can usually be secured with efficient search algorithms. The iteration procedure of the indirect coupling method includes the following stages.

1. Assuming the initial approximation currents of the stator and shaded-rings for time step $n+1$ are $I_{C0}^{(n+1)}$, $I_{S10}^{(n+1)}$ and $I_{S20}^{(n+1)}$, the current density in the stator and shaded-rings region can be obtained by applying equation (3.2) and (3.4) respectively.
2. Because all the source current is unknown, the field equation (3.9) can be solved, hence each nodal vector potential A_i is known.
3. Evaluate the induced potential difference by computing $d\phi/dt$.

4. Applying Backward Differences to time-discretise the circuit equation, the current in the stator and shaded-rings for iteration k loops, $I_C^{(n+1)}$, $I_{S1}^{(n+1)}$ and $I_{S2}^{(n+1)}$, can be obtained according to following equations

$$I_C^{(n+1)} = \frac{\Delta t}{R_C \Delta t + L_C}(V_C - \frac{d\Phi_C}{dt} + \frac{L_C}{\Delta t})I_C^{(n)} \tag{3.10a}$$

$$I_{S1,2}^{(n+1)} = \frac{\Delta t}{R_S \Delta t + L_S}(0 - \frac{d\Phi_{S1,2}}{dt} + \frac{L_S}{\Delta t})I_{S1,2}^{(n)}. \tag{3.10b}$$

5. Compare $I_C^{(n+1)}$, $I_{S1}^{(n+1)}$ and $I_{S2}^{(n+1)}$, with the approximation value $I_{C0}^{(n+1)}$, $I_{S10}^{(n+1)}$ and $I_{S20}^{(n+1)}$, and calculate the error with the following equation

$$err = ABS(\frac{I_C^{(n+1)} - I_{C0}^{(n+1)}}{I_{C0}^{(n+1)}}) + ABS(\frac{I_{S1}^{(n+1)} - I_{S10}^{(n+1)}}{I_{S10}^{(n+1)}}) + ABS(\frac{I_{S2}^{(n+1)} - I_{S20}^{(n+1)}}{I_{S20}^{(n+1)}}) \tag{3.11}$$

6. If the error is smaller than a positive number, e.g. 0.02–0.005, which means that obtained current $I_C^{(n+1)}$, $I_{S1}^{(n+1)}$ and $I_{S2}^{(n+1)}$ can satisfy both field and circuit equations, the iteration procedure stops. Otherwise, the new approximation current of stator and shaded-rings should be calculated again and the iteration form step two repeated.

Normally, the indirect coupling method takes much more time in finding the final I_C, I_{S1} and I_{S2} due to the low efficiency of the search scheme. By adopting the modified secant method to estimate the new approximation current for next iteration loop [Rajanathan, 1996], the convergence speed can be increased. The basic equation of the modified secant method can be written

$$I_k = I_{k-2} + (I_{k-1} - I_{k-2})\frac{V - V_{k-2}}{V_{k-1} - V_{k-2}} \tag{3.12}$$

where I_k, I_{k-1} and I_{k-2} are the approximation initial currents in iteration *k, k–1, k–2* loops, and V is the given supply voltage at step *k*; the V_{k-1} and V_{k-2} has been calculated at *k–1, k–2* iteration loops according to (3.10a) for the stator coil and (3.10b) for the shaded-rings respectively.

Besides the search scheme, the initial approximation currents for each time step are also important for the convergence speed. Thus, the second order discretized Newton algorithm expressed in (3.13) is adopted to obtain a good initial value for the iteration at each time-step.

$$I^{(n)} = I^{(n-1)} + (I^{(n-1)} - I^{(n-2)})\frac{V^{(n)} - V^{(n-1)}}{V^{(n-1)} - V^{(n-2)}} \tag{3.13}$$

where the $I^{(n-1)}$ and $I^{(n-2)}$ are the final calculated currents at time step $n-1$ and $n-2$ while $V^{(n)}$, $V^{(n-1)}$ and $V^{(n-2)}$ are the supply voltages at corresponding time step.

With above scheme, the convergence speed is increased notably and the average number of iteration loops is just five to six.

3.3.2 Direct Method of Coupling Circuit Equations

Compared with the indirect method, although the direct method makes the global system equations more complicate due to the addition of the external circuit equations, the better convergence and lower computing time make this method more suitable for solving the non-linear case which will arise in the Newton–Raphson iteration. In this study, the direct method to coupling the external circuit equations of SPIMs has been developed, which solves the field and circuit equations simultaneously. The global system equation has been derived in this section.

A) Stator winding equation

The external circuit equation of the stator winding is defined as

$$V_C = i_C R_C + \frac{d\phi}{dt} + L_C \frac{di_C}{dt} \tag{3.14}$$

where V_c: supply voltage

i_c: stator winding current

R_c: total resistance of stator winding

L_c: $L_c = L_{end} + L_{skew}$.

L_{end} denotes the reactance due to the leakage of end winding, and L_{skew} is the skew leakage reactance. In the two-dimensional model, the effect of winding overhang and skew can be taken into account, so the two reactance, L_{end} and L_{skew}, are evaluated by the traditional equivalent circuit model [Veinott, 1959].

The coupling between the magnetic and electric equation can be defined with the differentiation of flux linkage $d\phi/dt$, which can be expressed from the magnetic vector potential by

$$\frac{d\phi}{dt} = Ns\sum_{i=1}^{m}\frac{d_i N_c l_z}{S_C}\int_{s_C}\frac{dA}{dt}ds \tag{3.15}$$

where m is the number of coil sides connected by serial connection in the solution region and Ns is the number of symmetry sectors that the machine contains.

$$d_i = \begin{cases} +1 & \text{If coil belongs to a positively oriented coil side} \\ -1 & \text{If coil belongs to a negatively oriented coil side.} \end{cases}$$

Thus, equation (3.14) can be rewritten in term of vector potential, A, as

$$V_C = i_C R_C + Nsl_z\sum_{i=1}^{m}\beta_i^C\int_{s_C}\frac{dA}{dt}ds + L_C\frac{di_C}{dt} \tag{3.16}$$

With the time-stepping formulation, the time derivatives of the vector potential, A, and the stator winding current i_C are approximated by using the first-order differentiation of Backward Difference type, which yields

$$\begin{aligned} \left\{\frac{\partial A}{\partial t}\right\}^{t+\Delta t} &= \frac{\{A\}^{t+\Delta t} - \{A\}^{t}}{\Delta t} \\ \left\{\frac{\partial I_c}{\partial t}\right\}^{t+\Delta t} &= \frac{\{I_c\}^{t+\Delta t} - \{I_c\}^{t}}{\Delta t} \end{aligned} \tag{3.17}$$

where the Δt is the time step.

Substituting (3.17) into (3.16) and applying Galerkin formulation, the circuit equation of the stator winding is obtained:

$$V_c^{(n+1)} = I_c^{(n+1)} R_C + N s l_z \int_\Omega \left\{ \beta_i^C \sum_{i=1}^{N} \frac{\{A\}^{(n+1)} - \{A\}^{(n)}}{\Delta t} N_j \right\} d\Omega + L_C \frac{I_C^{(n+1)} - I_C^{(n)}}{\Delta t} \tag{3.18}$$

where Ω is the cross section of the solution field region.

If the vector column [A] is used, (3.18) is rewritten as

$$-[\mathbf{D_C}]^T \{\mathbf{A}\}^{(n+1)} - \frac{R_C \Delta t + L_C}{N_S l_z} \{\mathbf{I_C}\}^{(n+1)} = -[\mathbf{D_C}]^T \{\mathbf{A}\}^{(n)} - \frac{L_C}{N_S l_z} \{\mathbf{I_C}\}^{(n)} + \frac{\Delta t}{N_S l_z} \{\mathbf{V_C}\}^{(n+1)} \tag{3.19}$$

B) Rotor cage equations

The equivalent poly-phase circuit of Fig. 3.1 can be used to describe the relationship among the rotor bar current, i_b, the end ring current, i_e, and their corresponding voltage.

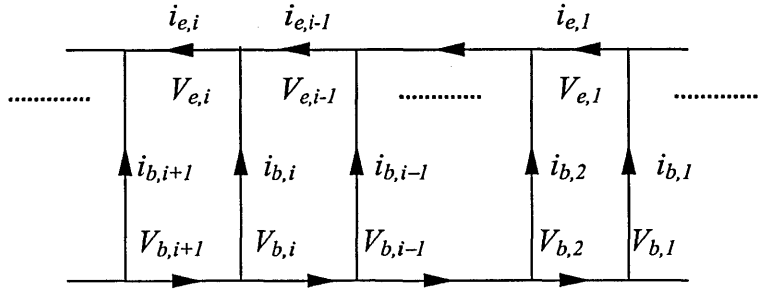

Fig. 3.1 The equivalent circuit of rotor bars and end-rings

Let R_e and L_e be respectively the resistance and the reactance between two adjacent rotor bars in the end-ring. The difference of the resistance and reactance among different portions of the end-ring was ignored in most models that had been proposed in the past [Strangas, 1985, Arkkio, 1987]. In this chapter, the difference is still ignored, and further discussion on this topic will be given in the next chapter.

According to Kirchhoff's law, for the rotor-bar i, the following equations hold

$$\begin{cases} V_{e,i} = -\dfrac{1}{2}(V_{b,i} - V_{b,i+1}) \\ i_{b,i} = i_{e,i} - i_{e,i-1} \\ V_{e,i} = i_{e,i} R_e + L_e \dfrac{di_{e,i}}{dt} \end{cases} \tag{3.20}$$

After time discretisation by applying the Backward Difference method, the last equation of (3.20) becomes

$$V_{e,i}^{(n+1)} = i_{e,i}^{(n+1)}(R_e + \frac{L_e}{\Delta t}) - \frac{L_e}{\Delta t} i_{e,i}^{(n)} . \tag{3.20b}$$

For the whole rotor cage, the circuit equation yields

$$\begin{cases} \{\mathbf{V_e}\}^{(n+1)} = -\frac{1}{2}[\mathbf{M}]\{\mathbf{V_b}\}^{(n+1)} \\ \{\mathbf{I_b}\}^{(n+1)} = [\mathbf{M}]^T\{\mathbf{I_e}\}^{(n+1)} \\ \{\mathbf{V_e}\}^{(n+1)} = \left(R_e + \frac{L_e}{\Delta t}\right)\{\mathbf{I_e}\}^{(n+1)} - \frac{L_e}{\Delta t}\{\mathbf{I_e}\}^{(n)} \end{cases} \tag{3.21a,b,c}$$

where

$$[\mathbf{M}] = \begin{pmatrix} 1 & -1 & & & \\ & 1 & -1 & & \\ & & \ddots & \ddots & \\ -1 & & & & 1 \end{pmatrix} \text{ and } [\mathbf{M}]^T = \begin{pmatrix} 1 & & & & -1 \\ -1 & 1 & & & \\ & \ddots & \ddots & & \\ & & & -1 & 1 \end{pmatrix}$$

In the previous section, the current density in the rotor-bar region was calculated by the equation (3.3). Thus the total current in rotor-bar i could be found by integrating (3.3) over the cross-section of bar i :

$$i_{b,i} = \iint_{bar,i} (\sigma \frac{V_b}{l_z} - \sigma \frac{\partial A}{\partial t}) dxdy \tag{3.22}$$

The first term of integration is constant, so we obtain

$$\iint_{bar,i} (\sigma \frac{V_b}{l_z}) dxdy = \sigma \frac{V_b}{l_z} \Delta_b = \frac{V_b}{R_b} \tag{3.23}$$

where Δ_b denotes the cross-sectional area of the bar, and R_b represents the DC resistance of the rotor bar. The second term (3.22) can also be calculated by applying the Galerkin procedure, which yields

$$\iint_{bar,i} (\sigma \frac{\partial A}{\partial t}) dxdy = \iint_{bar,i} (\sigma \frac{\partial A_i}{\partial t} N_j) dxdy = \sum_{bar,i} \beta_i^b \frac{\Delta_e}{3} \frac{\partial A_i}{\partial t} \tag{3.24}$$

Therefore the current in bar i, $\mathbf{I}_{b,i}$, can be expressed from vector potential [A] in matrix form:

$$[\mathbf{I}_{b,i}] = \frac{V_b}{R_b} - [\mathbf{Q}]^T_{bar,i} \left\{ \frac{dA_i}{dt} \right\}_{bar,i} . \tag{3.25}$$

So, the rotor-bar current $[\mathbf{I}_b]$ can be calculated by the following equation

$$[\mathbf{I}_b] = \frac{V_b}{R_b} - [\mathbf{Q}]^T \left\{ \frac{dA_i}{dt} \right\} . \tag{3.26}$$

Combing equations (3.21a), (3.21b) and (3.21c), the rotor-bar current $[\mathbf{I}_b]$ can be obtained from the bar terminal potential difference $[\mathbf{V}_b]$ by the following equation

$$\{\mathbf{I}_b\}^{(n+1)} = \left(\frac{\Delta t}{R_e \Delta t + L_e} \right) \left(\frac{1}{2} [\mathbf{M}]^T [\mathbf{M}] \{\mathbf{V}_b\}^{(n+1)} + \frac{L_e}{\Delta t} [\mathbf{M}]^T \{\mathbf{I}_e\}^{(n)} \right) \tag{3.27}$$

where $[\mathbf{M}]^T[\mathbf{M}] = \begin{pmatrix} 2 & -1 & & & -1 \\ -1 & 2 & -1 & & \\ & -1 & \ddots & & \\ & & & \ddots & -1 \\ -1 & & & -1 & 2 \end{pmatrix}$.

Substituting equation (3.27) into (3.26), the bar current term can be eliminated, thus equation (3.26) becomes

$$-[\mathbf{Q}]^T \left\{ \frac{dA_i}{dt} \right\}^{(n+1)} + \left(\frac{1}{R_b} [\mathbf{U}] + \frac{\Delta t}{2(R_e \Delta t + L_e)} [\mathbf{M}]^T [\mathbf{M}] \right) \{\mathbf{V}_b\}^{(n+1)} = \frac{L_e}{(R_e \Delta t + L_e)} [\mathbf{M}]^T \{\mathbf{I}_e\}^{(n)} \tag{3.28}$$

where $[\mathbf{U}]$ is the unit diagonal matrix. Applying the Backward Difference method to time-discretised the equation above, we obtain

$$-[\mathbf{Q}]^T \{\mathbf{A}\}^{(n+1)} + \Delta t [\mathbf{Y}] \{\mathbf{V}_b\}^{(n+1)} = \frac{L_e \Delta t}{(R_e \Delta t + L_e)} [\mathbf{M}]^T \{\mathbf{I}_e\}^{(n)} - [\mathbf{Q}]^T \{\mathbf{A}\}^{(n)} \tag{3.28a}$$

where $[\mathbf{Y}] = \left(\frac{1}{R_b} [\mathbf{U}] + \frac{\Delta t}{2(R_e \Delta t + L_e)} [\mathbf{M}]^T [\mathbf{M}] \right)$. The coefficient matrix $[\mathbf{Y}]$ is symmetric and positive.

C) Shaded-ring equation

Since the eddy-current effect is not taken into account, the shaded-ring circuit model is as same as that of the stator winding except that the source supply voltage of the shaded-ring is always zero. Thus, the shaded-ring circuit equation can be easily written as

$$i_S R_S + \frac{d\phi_S}{dt} + L_S \frac{di_S}{dt} = 0 \tag{3.29}$$

where $\frac{d\phi_S}{dt} = \sum_{i=1}^{m} \frac{d_i l_z}{S_S} \int_{S_S} \frac{dA}{dt} ds$.

Accordingly, rewriting equation (3.29) in matrix form, one obtains

$$-[\mathbf{D}_S]^T \{\mathbf{A}\}^{(n+1)} - \frac{R_S \Delta t + L_S}{l_z} \{\mathbf{I}_S\}^{(n+1)} = -[\mathbf{D}_S]^T \{\mathbf{A}\}^{(n)} - \frac{L_S}{l_z} \{\mathbf{I}_S\}^{(n)} \tag{3.29a}$$

where R_S is the DC resistance of the whole ring and the definition of $D_{S,ij}$ is given in (3.7).

For the shaded-ring, if the eddy-current model is adopted, the circuit equation will become very complex and the derivation procedure is very similar to that of the rotor cage. Here only the final results are given.

The electric circuit of the shaded-ring is shown in Fig. 3.2,

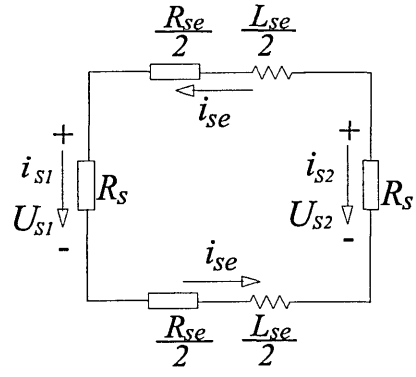

Fig. 3.2 The equivalent circuit of shaded-rings

and the circuit equations are

$$\left(\nu[\mathbf{S}] + \frac{[\mathbf{T}]}{\Delta t}\right)\{\mathbf{A}\}^{(n+1)} - [\mathbf{Q}_S]\frac{\mathbf{V_S}^{(n+1)}}{l_z} = \frac{[\mathbf{T}]}{\Delta t}\{\mathbf{A}\}^{(n)} \tag{3.30}$$

$$-[\mathbf{Q}_S]^T\{\mathbf{A}\}^{(n+1)} - [\mathbf{H}_S]\frac{\mathbf{V}_S}{l_z}^{(n+1)} = [\mathbf{P}_S][\mathbf{I}_S]^{(n)} - [\mathbf{Q}_S]^T\{\mathbf{A}\}^{(n)} \tag{3.31}$$

where

$$Q_{ij} = \beta_n^b \frac{\sigma\Delta_e}{3},$$

$$[\mathbf{H}_S] = \begin{pmatrix} -\left(1+\dfrac{R_S\Delta t}{R_{Se}\Delta t + L_{Se}}\right) & \dfrac{-R_S\Delta t}{R_{Se}\Delta t + L_{Se}} \\ \dfrac{R_S\Delta t}{R_{Se}\Delta t + L_{Se}} & \left(1+\dfrac{R_S\Delta t}{R_{Se}\Delta t + L_{Se}}\right) \end{pmatrix}$$

$$[\mathbf{P}_S] = \begin{pmatrix} \dfrac{-R_S\Delta t}{R_{Se}\Delta t + L_{Se}} \\ \dfrac{R_S\Delta t}{R_{Se}\Delta t + L_{Se}} \end{pmatrix}.$$

If we ignore the external and the end reactance of the shaded-ring, the matrices $[\mathbf{H}_s]$ and $[\mathbf{P}_s]$ will become

$$[\mathbf{H}_S] = \begin{pmatrix} -\left(1+\dfrac{R_S}{R_{Se}}\right) & \dfrac{-R_S}{R_{Se}} \\ \dfrac{R_S}{R_{Se}} & \left(1+\dfrac{R_S}{R_{Se}}\right) \end{pmatrix} \text{ and } [\mathbf{P}_S] = \begin{pmatrix} 0 \\ 0 \end{pmatrix}$$

A similar result can be found in the literature [Strangas, 1985], in which the external and end reactance are ignored as well.

Until now, the field and circuit equations have been available in time discretised form, which are

a) Field equation

$$F(\mathbf{A}_i, \mathbf{I}_{C,i}, \mathbf{I}_{Si}, \mathbf{V}_{b,i}) =$$

$$\left(\nu[\mathbf{S}] + \frac{[\mathbf{T}]}{\Delta t}\right)\{\mathbf{A}\}^{(n+1)} - [\mathbf{Q}]\frac{\{\mathbf{V}_b\}^{(n+1)}}{l_z} - [\mathbf{D}_C]\{\mathbf{I}_C\}^{(n+1)} - [\mathbf{D}_S]\{\mathbf{I}_S\}^{(n+1)} - \frac{[\mathbf{T}]}{\Delta t}\{\mathbf{A}\}^{(n)} = 0 \tag{3.32a}$$

b) Stator circuit equation

$$C(\mathbf{A}_i,\mathbf{I}_{C,i}) =$$

$$-[\mathbf{D}_C]^T\{\mathbf{A}\}^{(n+1)} - \frac{R_C\Delta t + L_C}{N_S l_z}\{\mathbf{I}_C\}^{(n+1)} - \left(-[\mathbf{D}_C]^T\{\mathbf{A}\}^{(n)} - \frac{L_C}{N_S l_z}\{\mathbf{I}_C\}^{(n)} + \frac{\Delta t}{N_S l_z}\{\mathbf{V}_C\}^{(n+1)}\right) \tag{3.32b}$$

c) Rotor cage equation

$$R(\mathbf{A}_i,\mathbf{V}_{b,i})$$

$$-\frac{[\mathbf{Q}]^T}{l_z}\{\mathbf{A}\}^{(n+1)} + \frac{\Delta t}{l_z}[\mathbf{Y}]\{\mathbf{V}_b\}^{(n+1)} - \frac{1}{l_z}\left(\frac{L_e\Delta t}{(R_e\Delta t + L_e)}\{\mathbf{I}_e\}^{(n)} - [\mathbf{Q}]^T\{\mathbf{A}\}^{(n)}\right) = 0 \tag{3.32c}$$

d) Shaded-ring equation

$$S(\mathbf{A}_i,\mathbf{I}_{S,i}) =$$

$$-[\mathbf{D}_S]^T\{\mathbf{A}\}^{(n+1)} - \frac{R_S\Delta t + L_S}{l_z}\{\mathbf{I}_S\}^{(n+1)} - \left(-[\mathbf{D}_S]^T\{\mathbf{A}\}^{(n)} - \frac{L_S}{l_z}\{\mathbf{I}_S\}^{(n)}\right) = 0 \tag{3.32d}$$

Applying the Newton–Raphson procedure to the above equations, one obtains

$$\begin{pmatrix} \left(\frac{\partial F_i}{\partial A_i}\right) & \left(\frac{\partial F_i}{\partial I_{C,i}}\right) & \left(\frac{\partial F_i}{\partial I_{S,i}}\right) & \left(\frac{\partial F_i}{\partial V_{b,i}}\right) \\ \left(\frac{\partial C_i}{\partial A_i}\right) & \left(\frac{\partial C_i}{\partial I_{C,i}}\right) & & \\ \left(\frac{\partial S_i}{\partial A_i}\right) & & \left(\frac{\partial S_i}{\partial I_{S,i}}\right) & \\ \left(\frac{\partial R_i}{\partial A_i}\right) & & & \left(\frac{\partial R_i}{\partial V_{b,i}}\right) \end{pmatrix} \begin{pmatrix} \{\Delta\mathbf{A}_i\} \\ \{\Delta\mathbf{I}_{C,i}\} \\ \{\Delta\mathbf{I}_{S,i}\} \\ \{\Delta\mathbf{V}_{b,i}\} \end{pmatrix} = \begin{pmatrix} F_i(A_i,I_{C,i},I_{S,i},V_{b,i}) \\ C_i(A_i,I_{C,i}) \\ S_i(A_i,I_{S,i}) \\ R_i(A_i,V_{b,i}) \end{pmatrix} \tag{3.33a}$$

Recalling equations (3.32a) to (3.32d), since all coefficient matrices in the function $F(A_i, I_C, I_S, V_b)$ except for the coefficient matrix of $\{A_i\}$ are linear, their Jacobian coefficient matrices are themselves. The Jacobian matrix of $\{dF_i/dA_i\}$, which can be found using the same procedure as in section 2.5, is $[\nu[\mathbf{S}]+[\mathbf{G}]+[\mathbf{T}]/\Delta t]$. The expression

of the new matrix [G] is defined in section 2.5 and can be calculated according to equation (2.62).

Thus, the linearised global system equations describing the whole problem can be rewritten as follows:

$$\begin{pmatrix} \left[\nu[\mathbf{S}]+[\mathbf{G}]+\frac{[\mathbf{T}]}{\Delta t}\right] & -[\mathbf{D_C}] & -[\mathbf{D}_S] & \frac{-[\mathbf{Q}]}{l_z} \\ -[\mathbf{D_C}]^{\mathrm{T}} & [\mathbf{Y_C}] & & \\ -[\mathbf{D}_S]^T & & [\mathbf{Y}_S] & \\ \frac{-[\mathbf{Q}]^T}{l_z} & & & [\mathbf{Y}_b] \end{pmatrix} \begin{pmatrix} \{\Delta\mathbf{A_i}\} \\ \{\Delta\mathbf{I_{C,i}}\} \\ \{\Delta\mathbf{I_{S,i}}\} \\ \{\Delta\mathbf{V_{b,i}}\} \end{pmatrix}^{(n+1)} =$$

$$-\begin{pmatrix} \left[\nu[\mathbf{S}]+\frac{[\mathbf{T}]}{\Delta t}\right] & -[\mathbf{D_C}] & -[\mathbf{D}_S] & \frac{-[\mathbf{Q}]}{l_z} \\ -[\mathbf{D_C}]^{\mathrm{T}} & [\mathbf{Y_C}] & & \\ -[\mathbf{D}_S]^T & & [\mathbf{Y}_S] & \\ \frac{-[\mathbf{Q}]^T}{l_z} & & & [\mathbf{Y}_b] \end{pmatrix} \begin{pmatrix} \{\mathbf{A_i}\} \\ \{\mathbf{I_{C,i}}\} \\ \{\mathbf{I_{S,i}}\} \\ \{\mathbf{V_{b,i}}\} \end{pmatrix}^{(n+1)} + \begin{pmatrix} \{\mathbf{N_A}\} \\ \{\mathbf{N_C}\} \\ \{\mathbf{N_S}\} \\ \{\mathbf{N_b}\} \end{pmatrix} \tag{3.33b}$$

where

$$\{\mathbf{Y_C}\} = -\frac{R_C\Delta t + L_C}{N_S l_z}[\mathbf{U}],\ \{\mathbf{Y_S}\} = -\frac{R_S\Delta t + L_S}{l_z}[\mathbf{U}],\ \{\mathbf{Y}_b\} = \frac{\Delta t}{l_z}[\mathbf{Y}],$$

and

$$\{\mathbf{N_A}\} = -\frac{[\mathbf{T}]}{\Delta t}\{\mathbf{A}\}^{(n)}$$

$$\{\mathbf{N_C}\} = -[\mathbf{D_C}]^T\{\mathbf{A}\}^{(n)} - \frac{L_C}{N_S l_z}\{\mathbf{I_C}\}^{(n)} + \frac{\Delta t}{N_S l_z}\{\mathbf{V_C}\}^{(n+1)}$$

$$\{\mathbf{N}_b\} = \frac{1}{l_z}\left(\frac{L_e\Delta t}{(R_e\Delta t + L_e)}\{\mathbf{M}\}^T\{\mathbf{I_e}\}^{(n)} - [\mathbf{Q}]^T\{\mathbf{A}\}^{(n)}\right)$$

$$\{\mathbf{N_S}\} = -[\mathbf{D}_S]^T\{\mathbf{A}\}^{(n)} - \frac{L_S}{l_z}\{\mathbf{I}_S\}^{(n)}$$

This global system matrix is symmetric and generally sparse, but the matrix is not positive because the matrices $[\mathbf{Y_c}]$ and $[\mathbf{Y_s}]$ are always negative while all the other diagonal entries in the system matrix are positive. Although Gausssian elimination (GE)

can still be used to solve the equations, the Incomplete Choleski Conjugate Gradient (ICCG) method, a more efficient linear equation solver, cannot be adopted because the ICGG method programs Choleski decomposition, which needs to take the root of the diagonal elements.

However, the system matrix can be made positive by adding auxiliary variables[Salon, 1995]. First, consider the stator winding circuit equation

$$-[\mathbf{D_C}]^T\{\Delta\mathbf{A}\}^{(n+1)}+[\mathbf{Y_C}]\{\Delta\mathbf{I_C}\}^{(n+1)}=-\left(-[\mathbf{D_C}]^T\{\mathbf{A}\}^{(n)}+[\mathbf{Y_C}]\{\mathbf{I_C}\}^{(n)}\right)+\{\mathbf{N_C}\} \tag{3.34}$$

By adding an auxiliary variable vector $\{\mathbf{I_{c,aux}}\}$, the equations (3.34) can be split into two equations as follows

$$\begin{aligned}-[\mathbf{D_C}]^T\{\Delta\mathbf{A}\}^{(n+1)}-[\mathbf{Y_C}]\{\Delta\mathbf{I_C}\}^{(n+1)}+2[\mathbf{Y_C}]\{\Delta\mathbf{I_{C,aux}}\}^{(n+1)}&=-\left(-[\mathbf{D_C}]^T\{\mathbf{A}\}^{(n)}+[\mathbf{Y_C}]\{\mathbf{I_C}\}^{(n)}\right)+\{\mathbf{N_C}\}\\ +[\mathbf{Y_C}]\{\Delta\mathbf{I_C}\}^{(n+1)}-2[\mathbf{Y_C}]\{\Delta\mathbf{I_{C,aux}}\}^{(n+1)}&=0\end{aligned} \tag{3.34a}$$

The same procedure can be applied to shaded-ring circuit equations. With the additional vectors $\{\mathbf{I_{c,aux}}\}$and $\{\mathbf{I_{s,aux}}\}$, the global system equation becomes

$$\begin{bmatrix}\left[\nu[\mathbf{S}]+[\mathbf{G}]+\frac{[\mathbf{T}]}{\Delta t}\right] & -[\mathbf{D_C}] & 0 & -[\mathbf{D}_S] & 0 & \frac{-[\mathbf{Q}]}{l_z}\\ -[\mathbf{D_C}]^{\mathrm{T}} & -[\mathbf{Y_C}] & 2[\mathbf{Y_C}] & & & \\ 0 & 2[\mathbf{Y_C}] & 2[\mathbf{Y_C}] & & & \\ -[\mathbf{D_C}]^{\mathrm{T}} & & & -[\mathbf{Y}_S] & 2[\mathbf{Y}_S] & \\ 0 & & & 2[\mathbf{Y}_S] & -2[\mathbf{Y}_S] & \\ \frac{-[\mathbf{Q}]^T}{l_z} & & & & & [\mathbf{Y}_b]\end{bmatrix}\begin{Bmatrix}\{\Delta\mathbf{A}\}\\ \{\Delta\mathbf{I}_C\}\\ \{\Delta\mathbf{I_{C,aux}}\}\\ \{\Delta\mathbf{I_S}\}\\ \{\Delta\mathbf{I_{S,aux}}\}\\ \{\Delta\mathbf{V_b}\}\end{Bmatrix}^{(n+1)}=$$

$$-\begin{bmatrix}\left[\nu[\mathbf{S}]+[\mathbf{G}]+\frac{[\mathbf{T}]}{\Delta t}\right] & -[\mathbf{D_C}] & 0 & -[\mathbf{D}_S] & 0 & \frac{-[\mathbf{Q}]}{l_z}\\ -[\mathbf{D_C}]^{\mathrm{T}} & -[\mathbf{Y_C}] & 0 & & & \\ 0 & 0 & 0 & & & \\ -[\mathbf{D_C}]^{\mathrm{T}} & & & -[\mathbf{Y}_S] & 0 & \\ 0 & & & 0 & 0 & \\ \frac{-[\mathbf{Q}]^T}{l_z} & & & & & [\mathbf{Y}_b]\end{bmatrix}\begin{Bmatrix}\{\mathbf{A}\}\\ \{\mathbf{I}_C\}\\ \{\mathbf{I_{C,aux}}\}\\ \{\mathbf{I_S}\}\\ \{\mathbf{I_{S,aux}}\}\\ \{\mathbf{V_b}\}\end{Bmatrix}^{(n+1)}+\begin{Bmatrix}\{\mathbf{N_A}\}\\ \{\mathbf{N_C}\}\\ 0\\ \{\mathbf{N_S}\}\\ 0\\ \{\mathbf{N_b}\}\end{Bmatrix} \tag{3.35}$$

Thus the linearised system equation, which couples both the circuit and field equations, is now sparse, symmetric and positive. It is ready to solve this equation using either the ICCG or the GE method.

3. 4 Rotor Movement

As mentioned in chapter 2, the reason why the velocity term is not introduced into the field equation directly is to avoid the asymmetrical system equations and to maintain their stability. Thus, the time-stepping method, which simulates the continuous movement of rotor rotation by a series of discrete step movements at each time point, is commonly used to analyse the performance of electromagnetic devices including rotating parts.

With the time-stepping method, the finite element mesh that covers the whole study domain should be rebuilt at each time step according to the rotor rotation. When the rotor is moving, the geometry of rotor and stator is fixed, so the re-mesh usually only occurs in the air gap. To rebuild the mesh according to the different rotor positions, the Moving Band model and Sliding Surface model are the most frequently used schemes among the different available approaches. In these two models, the full mesh of the solved domain is divided into four parts: the fixed stator mesh, the fixed rotor mesh, the stator side air gap mesh and the rotor side air gap mesh. These are shown in Fig. 3.3a and Fig. 3.3b.

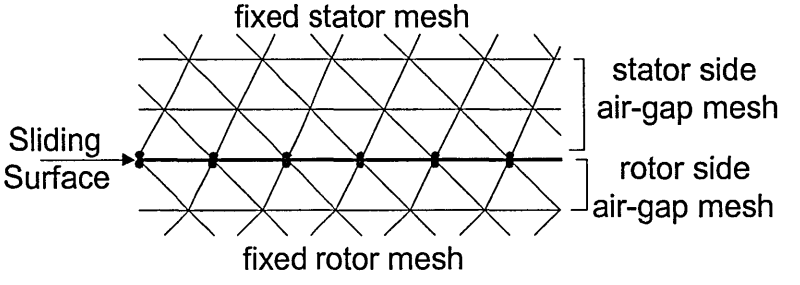

Fig. 3.3a Sliding Surface model

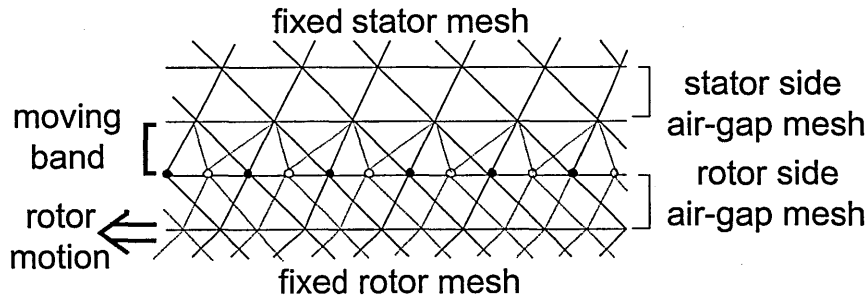

Fig. 3.3b Moving Band model

3.4.1 Sliding Surface Model

To use the Sliding Surface model, a set of uniform space nodes is introduced into the air gap. These nodes are put on the slip surface (line), which separates the stator side air gap mesh from rotor side air gap mesh. When half the cross-section of a SPIM is modelled with periodic boundary conditions, the spatial step size is decided by the spatial angle θ between two adjacent nodes where $\theta = \pi/(n\text{-}1)$ (n is the number of total slip nodes). Since the coinciding node pair on the different sides of the sliding surface should be matched in each time step, only discrete rotor movement is allowed. In other words, each spatial step of rotor movement should be an integral multiple of the angle θ.

Therefore, with the Sliding Surface model, the time step between two simulation positions, Δt, is variable when the rotor speed changes. For a constant rotor speed to be simulated, a suitable Δt can be decided by adjusting the number of slip nodes in the pre-processing stage. However, if the rotor speed is variable, for instance, from zero to synchronous speed, this solution is not applicable. The number of slip nodes that is suitable for high speed may make the Δt too big for the lower speed and hence becomes unsuitable. An example is given in Table 3.1. It can be observed that the time step at 200 rev/min is seven times bigger than that at 1400 rev/min if the same number of total slip nodes is used. In other words, if the time step at 200 rev/min speed remains as the same as that at 1400 rev/min, the number of nodes on the sliding surface should be 1260,

which is seven times finer than the original mesh, therefore the computing cost becomes too high to accept.

Table 3.1 Time step at various speeds

Speed (rev/min)	1400	1200	1000	800	600	400	200
Time Step (ms)	0.119	0.139	0.167	0.208	0.277	0.417	0.833

Note: In this study, the number of total slip nodes n is usually chosen at 181, therefore, the spatial $\theta = 180°/(n\text{-}1) = 1°$. The SPIM studied have 4 poles, so its synchronous speed is 1500 rev/min.

3.4.2 Moving Band Model

The Moving Band model simulates the rotor motion by distorting a band of air gap mesh (see Fig. 3.3b). In the moving band, one side belongs to the moving rotor, and another belongs to the stationary stator. Once the rotor moves by a small spatial step according to the rotor speed, the rotor mesh including the fixed rotor mesh and the rotor side air gap mesh rotates by the same spatial angle. All the element numbers, the node numbers and the logical connection of the whole mesh remain as same as that before rotating. With Moving Band model, the small rotor movement is realised by changing the shape of the mesh in the 'Moving Band'. To avoid introducing significant distortion of the moving band mesh, nodes on the sides of band must be reconnected after a certain spatial angle. The procedure of the reconnection is in fact the same as that of Sliding Surface model.

The distortion of the moving band mesh is the primary disadvantage of the Moving Band method. However, if the distortion in the band is kept within a limit of one mesh size in one layer, the distortion error is still within acceptable limits [Tsukerman, 1995].

3.4.3 The Hybrid Model

The advantage of the Sliding Surface method is the avoidance of mesh distortion during rotor movement. However, if the machine is at a low speed or at variable speed situation, this method requires a sufficiently fine nodes subdivision on the sliding surface. Hence the number of nodes becomes larger and the whole computing time is increased. In contrast, for the Moving Band model, the rotor rotation is discretized according to the time step Δt rather than the spatial angle θ. Hence at lower speeds, this model is more suitable and can avoid too fine node subdivision when the spatial step size of the rotation is smaller.

In this study, in order to calculate the performance in the transient state, e.g. the starting procedure, a hybrid method was adopted. This hybrid method is generated by combining the Sliding Surface model with the Moving Band model. When the rotor speed is low, the Moving Band method is adopted. The time step Δt is fixed and the spatial angle of rotor movement θ is decided by the instantaneous rotor speed. If the instantaneous speed increases to a certain value, e.g. 1000rpm (At this speed, the time step is considered small enough based on the calculation in Table 3.1), the Sliding Surface method is employed. Thus, the spatial angle of rotor movement is constant while the time step becomes variable at higher speed. With this hybrid method, a high level of accuracy can be obtained without excessively fine discretization with a great number of slip nodes, which would result in increased computing time.

This hybrid method is also readily implemented in the multi-slice model which is explained in the next chapter. The basic mesh of multi-slice model is also divided into the four parts shown in Fig. 3.3. This basic mesh is used to represent the first slice, and the other slices can be directly generated by rotating the rotor part in the basic mesh with a small angle that corresponds to the skew angle. Thus, the skewed rotor is described by a series of 2D unskewed slice. When the rotor moves, rotor parts of each mesh slice move with the same spatial step. Therefore, the geometrical difference between each slice can be maintained during rotor motion.

3. 5 Variable Step Size for Time-Stepping Method

The time-stepping finite element method, which can consider the effects of the saturation, the eddy current, the rotation of rotor and the harmonics conveniently, is regarded as the most accurate model for analysis of electrical machines. This method has been successfully applied to simulate the starting procedure and to analyse the performance of induction motors fed by the PWM inverter.

The time-stepping method is based on the time-discretisation principle in which $\partial A/\partial t$ is generally approximated by $\Delta A/\Delta t$. Moving $\partial A/\partial t$ to the left side, the field equation described by (3.5) can be rewritten as following:

$$\frac{\partial A}{\partial t} = f(A,t) \tag{3.36}$$

where $f(A,t)$ denotes for the other terms in equation (3.5).
Applying the Backward Difference method at the kth step, the approximate solution of (3.36), A_k^*, is therefore obtained:

$$A_k^* = A_{k-1} + (\Delta t) f(A_k^*, t_k) \tag{3.37}$$

where Δt is the step size and $\Delta t = t_k - t_{k-1}$.

Equation (3.37) can be rewritten in integration form, which gives

$$A_k = A_{k-1} + \int_{k-1}^{k} f(A,t)dt \tag{3.38}$$

For the above equation, using Taylor's expansion, the exact solution at time t_k, X_k, is obtained:

$$A_k = A_{k-1} + (\Delta t) f(A_k, t_k) + \frac{(\Delta t)^2}{2} A''(A_k, t_k) + \frac{(\Delta t)^3}{3} A'''(A_k, t_k) + \ldots \tag{3.39}$$

where the A'' and A''' are the second and third order derivative of A with respect to time t.

Comparing (3.37) with (3.39), the approximate solution A_k^* can be equal to the exact result A_k only when the higher order derivatives, such as A'' and A''', are all zero at the k^{th}

step. In other words, using the Backward Difference method, the exact result can be obtained only under the condition that A is a linear function of t during the small area $[t_{k-1}, t_k]$. The accuracy of the time-stepping method depends on the step size Δt directly. If the fine size, Δt, is used, a more accurate solution can be secured, but a large amount of computing time is required. On the contrary, if a large step is adopted the computing time is saved while the accuracy of the solution decreases. Hence, the choice of a suitable step size is critical for keeping a balance between the computing time and the accurate solution.

For most electromagnetic devices, such as induction motors, the variations of the quantities of the magnetic field and the external supply are usually near sinusoidal and their derivatives with time change at different rates during different periods. Taking a simple sinusoidal function shown in Fig. 3.4 (p. 58) as an example, the curve varies almost linearly during area AB, so the large step size can be applied without losing accuracy. For area BC, the slope changes very rapidly and a small step size is required to maintain the accuracy. Therefore, a variable step size method is proposed and considered as a good way to deal with the time-stepping finite element problem.

The essential problem of the variable step size method is to decide the step size before the field equations have been solved. To overcome this problem, Williamson [1985] chose the time step on the basis of maximum permitted change of flux linkage. In Vassent's study [1991], the variation of the time step is controlled by the error between the predicted and calculated values of rotor displacement. More recently, Brauer [1996] presented an implementation of adjusting the time step size for non-linear applications by monitoring the change of potential or reluctivity. With his method, the step size is doubled if the change of scalar potential approaches zero, and the bisection of the step size is activated when divergence occurs or when the change in incremental reluctivity dH/dB exceeds a specified limitation. All the above methods have been applied with different degrees of success, but they fail to provide the direct relationship between the truncation error and the step size. Ho [1997] has used the truncation error of vector

potential to control the step size directly. However, due to ignoring the variation of the second order derivative, the estimation of truncation error is correct only under linear situation.

In this study, a new approach to adjust the step size automatically has been used. With this method, the step size is determined according to the magnitude of the truncation error which is estimated by using the Neville's three-point extrapolation algorithm.

3.5.1 Neville's Extrapolation Algorithm and Truncation Error Estimate

Before introducing the procedure for controlling the step size, the Neville's three-point extrapolation algorithm is explained [Press, W. H. 1992].

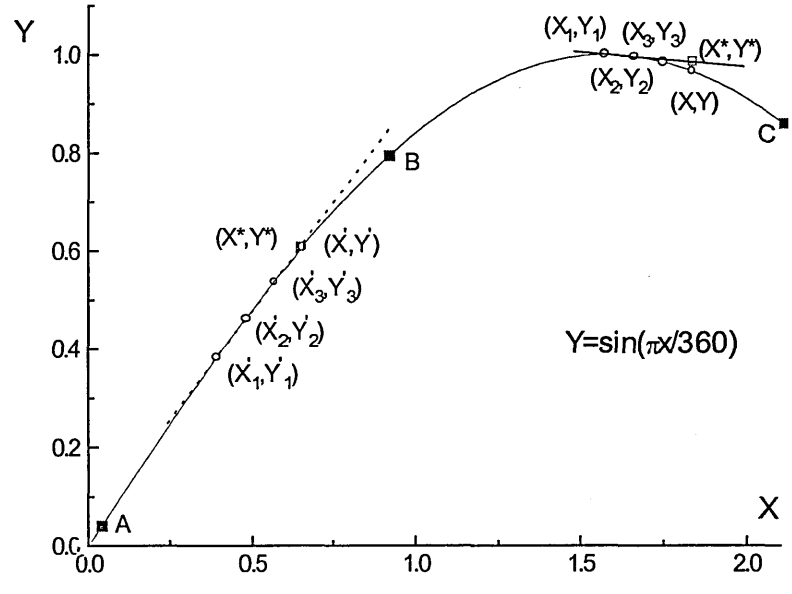

Fig. 3.4 Estimated truncation error given by the extrapolation algorithm

Neville's extrapolation algorithm is a recurrence procedure. For three points algorithms (N_p=3), the calculating procedure can be described by the following equations.

$$\begin{array}{lll} x_1 : y_1 = P_1 & & \\ & P_{12} & \\ x_2 : y_2 = P_2 & & P_{123} \\ & P_{23} & \\ x_3 : y_3 = P_3 & & \end{array} \tag{3.40}$$

where P_1, P_2 and P_3 are the values at x_1, x_2 *and* x_3. P_{12} are the value at x of the unique linear polynomial passing through both (x_1 y_1) and (x_2 y_2). P_{23} is defined similarly. P_{123} is defined as the value at x of the second-order degree polynomial passing through three points.

Neville's process is a recursive way of filling in the numbers in the table a column at a time, from left to right (Ref. to the equation 3.40). The 'daughter' (right-hand column) can be calculated according to two 'parents' (left-hand column) with following equation;

$$P_{i(i+1)\cdots(i+m)} = \frac{(x - x_{i+m})P_{i(i+1)\cdots(i+m-1)} + (x_i - x)P_{(i+1)(i+2)\cdots(i+m)}}{x_i - x_{i+m}} \tag{3.41}$$

where $m = N_p - 1$

The result of (3.41) is as the same as that calculated by Lagrange's polynomial formula. However, by keeping track of the small difference between parents and daughters, which is defined in (3.41), the result of Neville's algorithm can be more accurate.

$$\begin{aligned} C_{m,i} &= P_{i(i+1)\cdots(i+m)} - P_{i(i+1)\cdots(i+m-1)} \\ D_{m,i} &= P_{i(i+1)\cdots(i+m)} - P_{(i+1)\cdots(i+m-1)} \end{aligned} \tag{3.42}$$

The high order coefficients of $C_{m+1,i}$ and $D_{m+1,i}$ can be calculated as:

$$\begin{aligned} D_{m+1,i} &= \frac{(x_{i+m+1} - x)(C_{m,i+1} - D_{m,i})}{(x_i - x_{i+m+1})} \\ C_{m+1,i} &= \frac{(x_i - x)(C_{m,i+1} - D_{m,i})}{(x_i - x_{i+m+1})} \end{aligned} \tag{3.43}$$

The final P_{123} is equal to the sum of any y_i plus a set of C's or D's that form a path through the family tree to the rightmost daughter. At each level, m, $C_{m,i}$ and $D_{m,i}$ are the corrections to make the extrapolation one order higher [Press, W. H. 1992].

With extrapolation algorithms, e.g. Neville's algorithm and linear Backward Difference method, the function value of the next step can be estimated according to the value of the previous step points. The truncation error is used to measure the difference between the estimated value and the actual function value. Form the previous discussion, it is known that the scale of the truncation error depends on both the slope variation of the function curve and the discrete step size.

In Fig. 3.4, it is observed that the truncation error, ABS(X'Y' $-X^*Y^*$), is quite small in the linear part of the curve (AB) while the error, ABS(XY $-X^*Y^*$), increases significantly in the non-linear part (BC) with the same step size. However, in the area where the slope of the curve varies very rapidly, the truncation error can remain very small if a fine enough step size is employed. Therefore, by monitoring the truncation error variation, whether the step size chosen is a proper one can be determined accordingly.

However, in most cases, the actual function value can not be found. Thus, an alternative method to estimate the truncation error due to the time-stepping procedure is employed. With this method, two different extrapolation algorithms are used to estimate the function value of next step. Therefore, at the k^{th} step, the truncation error for a given step size, Err_k, can be calculated using following equation.

$$Err_k = \frac{1}{N}\sum_{i=1}^{N}\left|\frac{Y_k^* - Y_k^{\#}}{Y_k^{\#}}\right| * 100\% \tag{3.44}$$

where Y^*_k is the approximate solution given by the Neville's three-point extrapolation algorithm and $Y^{\#}_k$ is the approximate solution obtained with the Backward Difference method. The N is the total number of the vector potential variables of the finite element model studied.

Since the Neville's three-point algorithms is a second-order extrapolation algorithm, the variation of second derivative of the function can be considered. Therefore, its estimation

is usually regarded as more accurate compared with the linear Backward Difference method. The estimate error between two extrapolation methods becomes zero only when the function is linear. For non-linear function, the error depends on step size and the slope variation of the function curve. Therefore, it can be used to monitor the performance of the different step size.

For Ho's method, Y^*_k in (3.44) is given by the linear extrapolation algorithm which is

$$Y_k^* = Y_{k-1} + (X_k - X_{k-1})\frac{(Y_{k-1} - Y_{k-2})}{(X_{k-1} - X_{k-2})} \tag{3.45}$$

Compared with the Neville's three-point algorithm, his algorithm only uses the information of two points obtained previously and ignores the variation of second derivative.

3.5.2 Adjust Step Size According to the Estimate Error

According to the discussion in the previous section, the truncation error at each step can be used to detect whether the present step size is correct. Therefore, the step size can be determined by using this error as a criterion. Given a permitted limitation ε for the truncation error, the step size of the next step can be increased or doubled if the estimated error is smaller than ε, otherwise the step size should be decreased or bisected. One can adjust the step size according to scale of the truncation error.

In order to check the validity of the proposed method for the truncation error estimation, four different step sizes are used to simulate the locked rotor state of a 220V, 50Hz, 4-pole SPIM with 30 rotor slots. The basic step size is 0.144ms, so there are 140 steps per cycle. The largest step size is four times bigger than the basic one, thus only 35 steps are required for each cycle. All the step sizes are fixed during the simulation procedure.

Fig. 3.5 shows the simulated waveforms of the stator currents. All current curves for different step sizes almost overlap. The biggest difference occurs between the curve for the smallest step size and that of the largest step size when the curves reach the peaks, but it is still smaller than 2% which is usually ignored in most engineering computations. The same situation can also be observed in the variation of shaded-ring currents shown in Fig. 3.6. Therefore, one can draw the conclusion that the stator current and the shaded-ring currents are not sensitive to the step sizes if the mesh is the same. This conclusion can be used to explain the calculating results drawn from Williamson's work [1985], in which he obtained the same current accuracy with only 30 time steps per supply cycle, while the others have reported 100 –500 steps per cycle

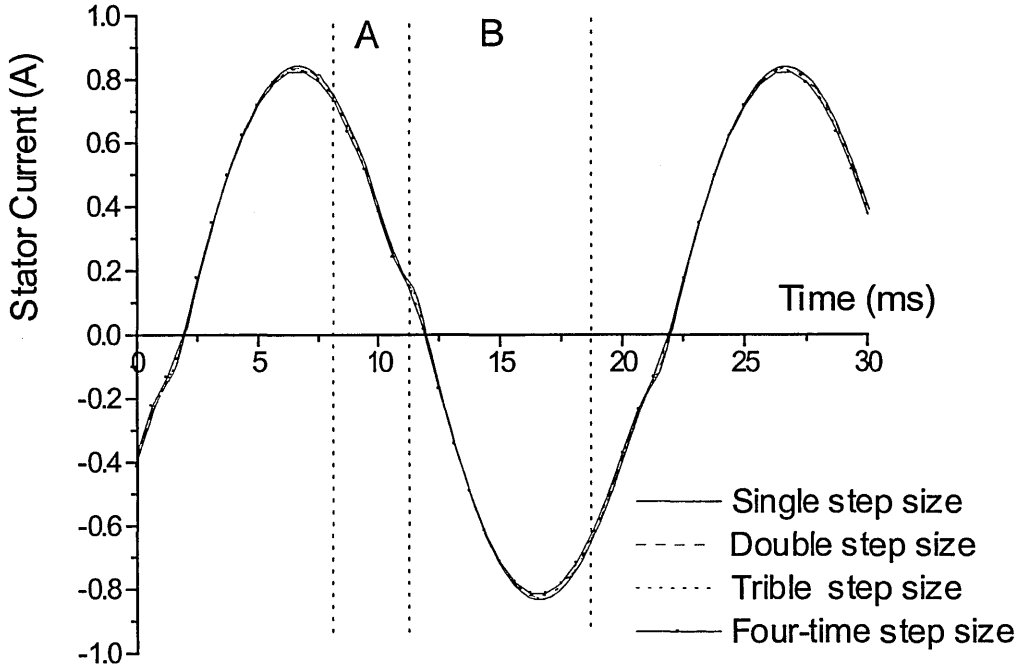

Fig. 3.5 Variation of stator current for different step sizes

[It can seen that the current curves for different step sizes almost overlap each other and hence their difference can not be clearly observed]

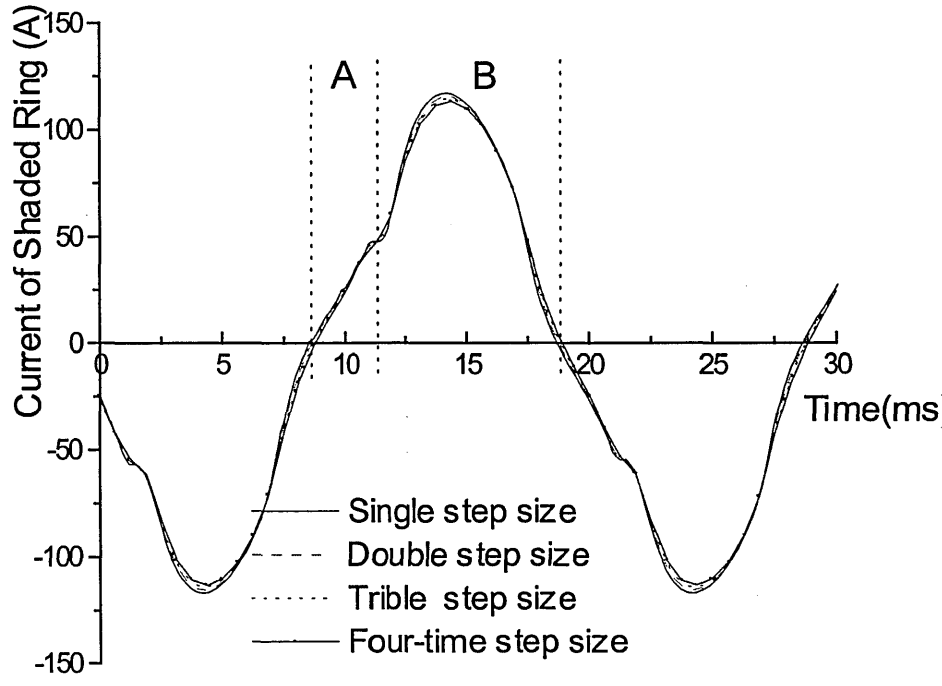

Fig. 3.6 Variation of shaded-ring current for different step sizes

However, the torque that is directly calculated from the field distribution by Maxwell's stress tensor becomes very sensitive to the variation in the step size. The difference in torque between each curve is clearly observed in Fig. 3.7. The average torque over one supply cycle given by the largest step size is 15 percent smaller than the average torque given by the basic step size. Therefore, if the torque is calculated from the field distribution directly, a smaller step size is usually needed.

Fig. 3.8 shows the variation of truncation error given by Neville's algorithm under different step sizes and Fig. 3.9 shows the result obtained by Ho's method. In this study, only the variation of vector potential of the nodes in the air gap elements is take into account when the truncation error is calculated, so the interrelation between the estimated error and the torque can be improved.

In Fig. 3.7 one can find that, for the two areas marked A and B respectively, the torque difference at the same time among each curve is different. In area A, all the torque curves nearly overlap which means the step size does not have much effect on the torque in this

area. However, in area B, the difference between the basic step curve and the largest step curve is quite significant. Referring to Fig. 3.8, the two areas can also be marked at same period. In period A the difference in the truncation errors between each curves is quite small, while in period B the truncation error for larger step size increases rapidly to a very significant level, which suggests that the linear approximate solution with such a big step size is now unacceptable. By comparing Fig. 3.7 and Fig.3.8, it is clear that the truncation error is a very sensitive to the field variation. Therefore, whether the step size is suitable can be judged reliably according to this error.

When Ho's method is applied to the truncation error estimate, the sensitivity of the error against the field variation is not good enough. Although in area B the difference in truncation error between these curves is also very notable, in area A the difference is still at a very significant level while there is almost no gap between the torque curves. Therefore, the truncation error given by Neville's algorithm is more accurate than the result given by Ho's method.

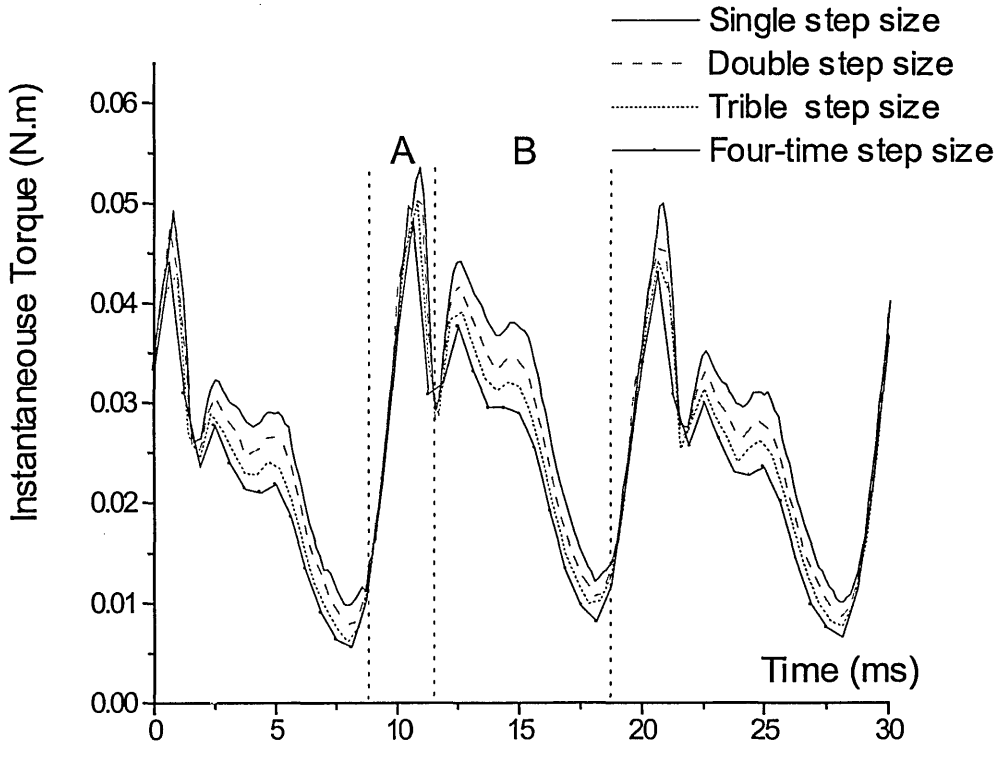

Fig. 3.7 Variation of mechanic torque calculated for different step sizes

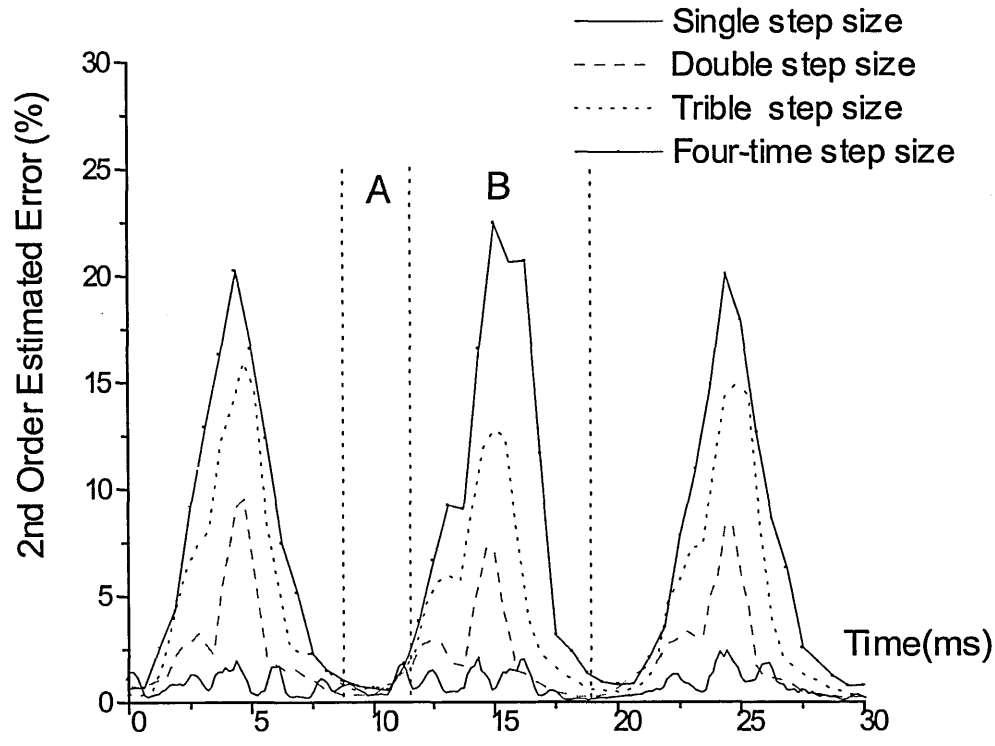

Fig. 3.8 Variation of estimated error given by Neville's algorithm for different step sizes

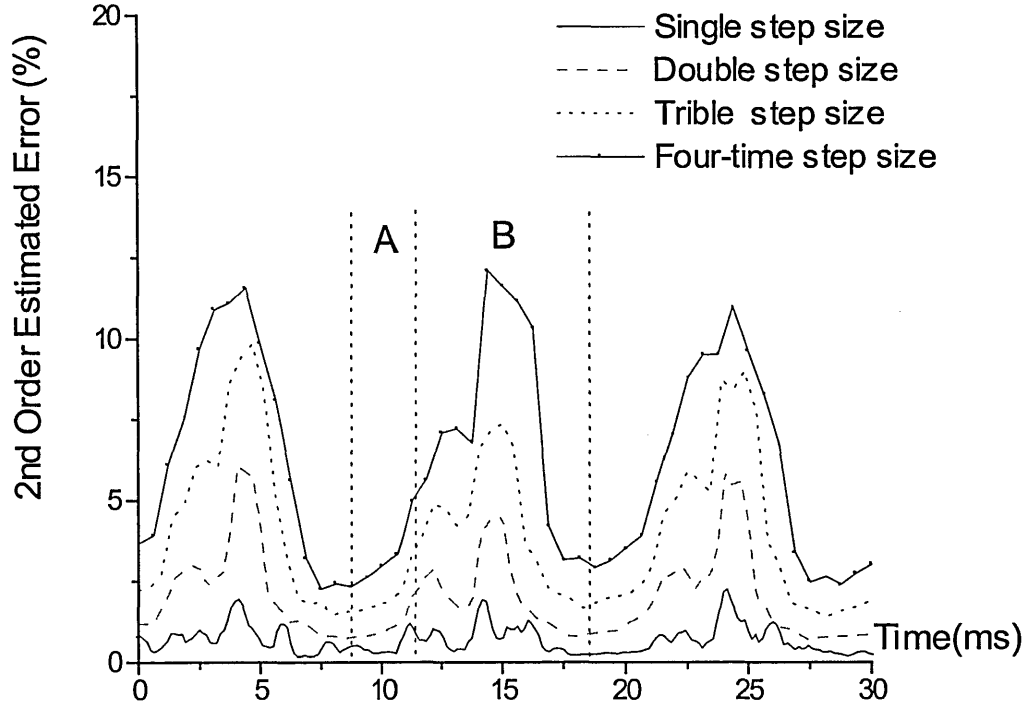

Fig. 3.9 Variation of estimated error given by Ho's method for different step sizes

Unlike the normal three-phase induction motor, the variation in frequency of the SPIMs' torque is twice of that of the supply source frequency, and the waveform of the torque includes many harmonics (Fig. 3.7). To secure the accuracy of the torque simulation only double step size is used when the truncation error is less than the given limit. In this case, the limit of the truncation error, ε, is set at 0.008.

With the truncation error, the process of adjusting step size becomes simple. At the k^{th} step, where k is bigger than 4, first, calculate the approximation solution Y_k* by Neville's three-point algorithm, then, estimate the truncation error by (3.45) since another approximation result, $Y_k^{\#}$, given by the Backward Difference method is already known. If the estimated error is greater than the limit, the basic step size is used, otherwise, the step size can be doubled. For the initial four steps, the basic step size is always used.

The waveform given by the variable step size method is shown in Fig. 3.10 together with the curves of the fixed step-size method. The variation of truncation error for variable step size method is shown in Fig. 3.11. By comparison of the torque curves in Fig. 3.10, the accuracy of the variable step size method can be appreciated. The same conclusion can also be drawn from the comparison of the variation in truncation errors. In Fig. 3.11 the estimated truncation error of variable step size method is less than that of fixed double steps.

With the variable step size method, the total step for a given time is reduced notably. In this case, the variable step process needs 604 steps while 834 steps are required by the process of basic step size for a 0.12s simulation time. Without losing the accuracy of the torque calculation, near 28% computing time has been saved by using variable step process. If this method were applied to other kinds of electrical machines which have smoother torque variation, more computing time would be saved.

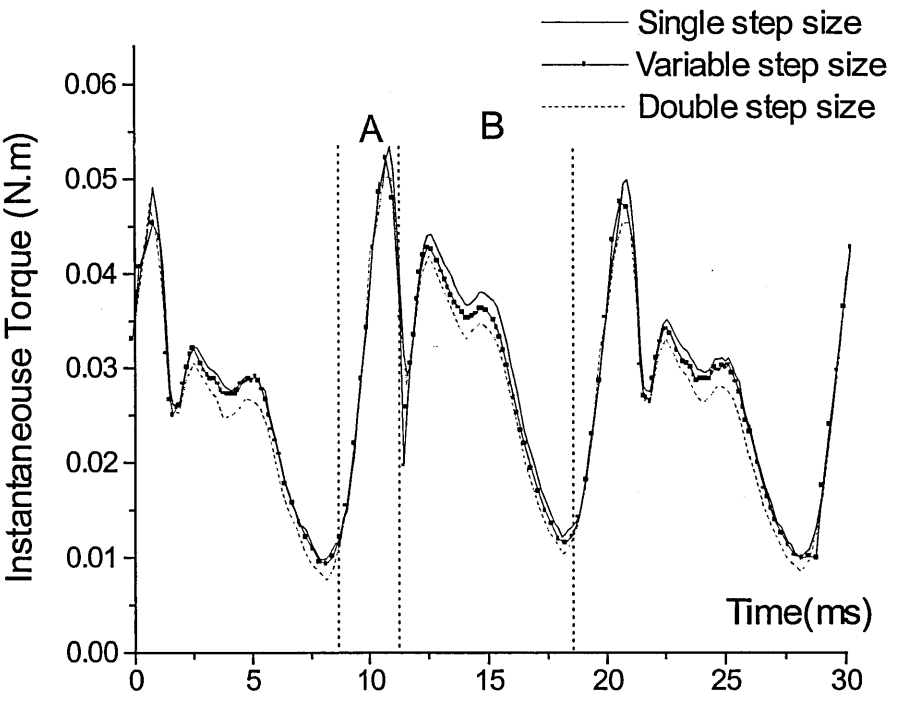

Fig. 3.10 Variation of mechanical torque for variable step size

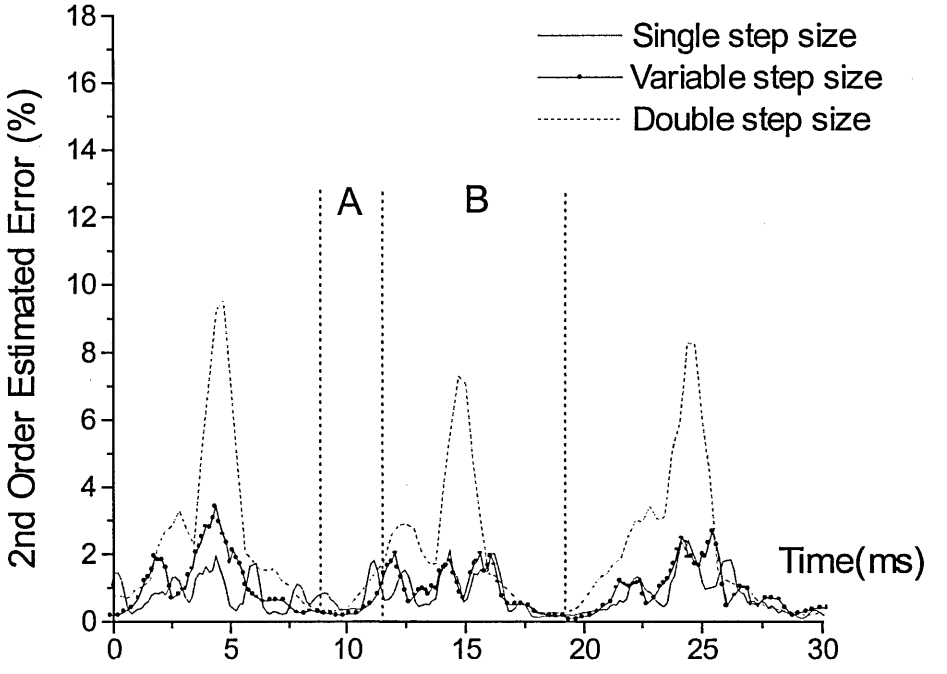

Fig. 3.11 Variation of truncation error given by variable step size

3. 6 Electromagnetic Force Calculation

In most cases, the purpose of a motor is to produce force or torque, so computing the force or torque and their variation with position or excitation are always the focus of the designer's interests. The electromagnetic force or torque developed in an electric machine can be obtained from the numerical field solution of the study region. The following three categories of force computation are the most popular methods.

- The Bil method (Ampere's Force Law)
- The Virtual Work method
- The Maxwell stress tensor

The basic formulation and computational implementation of these methods are briefly discussed below.

A) The Bil method

The general expression of the Bil method is very straight-forward.

$$d\mathbf{F} = i(d\mathbf{l} \times \mathbf{B}) \tag{3.46}$$

where **dl** is the length of the conductor carrying current, i, and the **B** is the local flux density.

This method is easy to apply for calculating forces between isolated conductors in the air [Gary, 1989] or torque in current-currying loops situated in magnetic fields [Cheng, 1989]. Apart from the very special motors designed with air gap winding or with air-core magnetic circuit, this method is only used to calculate the force on the end windings, because with this method, it is difficult to estimate the force on a body made of magnetic material, e.g. reluctance force between stator and rotor.

B) The Virtual Work method

The principle of the Virtual Work method depends on the relationship between force and energy provided by the principle of conservation of energy. The force acting on an object

can be found as the derivative of magnetic energy with respect to the position at constant flux linkage or the derivative of magnetic co-energy with respect to position at constant current. The second method (co-energy) is usually easier for the finite element model. Using co-energy method, two different field solutions which have a small displacement are solved under the condition of the same exciting currents, then the force along the displacement direction s can be evaluated as:

$$F = \frac{W_c^2 - W_c^1}{\Delta s} \tag{3.47}$$

where Δs is the small displacement between two positions. The W_c^1 and W_c^2 are the magnetic co-energy stored in whole study region Ω at each position and can be calculated with following equation.

$$W_c = \int_\Omega [\int_0^B HdB] d\Omega \tag{3.48}$$

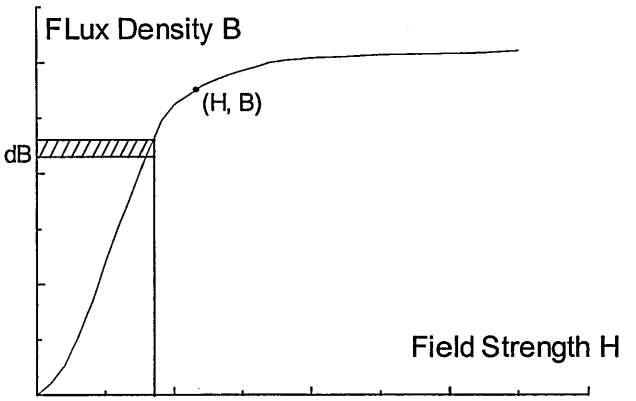

Fig. 3.12 Calculation of magnetic co-energy

When rotational displacements are considered, the torque T can be similarly evaluated by the following equation.

$$T = \frac{W_c^2 - W_c^1}{\Delta \theta} \tag{3.49}$$

Since the stored magnetic co-energy is a global quantity, the Virtual Work method is less sensitive to local error due to poor meshing or local round off. This method has been used in finite element analysis for many years, but it still suffers from many difficulties.

First, the result of this approach is mainly related to the accuracy of computing the magnetic co-energy difference (W_c^2 - W_c^1). Although the error in each of the two co-energy estimates is very small, the precision of their difference depends on the magnitude and sign of the two errors and may be very significant if the two errors have different signs. This problem becomes most acute when the difference of two estimates is only a very small percentage of the magnitude of the co-energy, since in such a case the effect of the round-off errors will be more severe.

Secondly, this approach usually requires a judicious choice of the positional displacement. If a small displacement is chosen, the co-energy value will be of very similar magnitude at two positions and a significant round-off error will occur when computing the difference. On the other hand, a large displacement may not be adequate to model the non-linear characteristic which represents the variation of magnetic co-energy with respect to position [McFee, 1987].

Finally, for the Virtual Work method, two field solutions are necessary. Therefore, for calculating the force at each position, twice the computing time is required to solve two different geometry or meshes. Coulomb [1983, 1984] proposed a method whereby co-energy can be directly differentiated with respect to virtual displacement, but his model is only suitable for the case in which the non-linear characteristic is not considering.

C) The Maxwell stress tensor

With the Maxwell stress tensor method the force and torque are directly calculated from the field distribution by integration of the force density over the surface s (for a three-dimensional problem) or a contour C (for a two-dimensional problem) surrounding the parts of interest. The general expression can be obtained using Ampere's force law and fictitious equivalent current distributions to replace magnetic material [Salon, 1995, Stratton, 1941]:

$$\mathbf{F} = \oiint_S \mathbf{T} d\mathbf{s} \tag{3.50}$$

where $\mathbf{T}$ is the Maxwell stress tensor with terms given by

$$\mathbf{T} = \begin{bmatrix} B_x H_x - BH/2 & B_x B_y & B_x B_z \\ B_y B_x & B_y H_y - BH/2 & B_y B_z \\ B_z B_x & B_z B_y & B_z H_z - BH/2 \end{bmatrix} \tag{3.51}$$

If the problem is limited in two-dimensional geometry, the integration (3.50) can be resolved into components of force density normal and tangential to the contour. The normal and tangential components of the force density are given by:

$$dF_t = \frac{1}{\mu} B_t B_n dl \tag{3.52}$$

$$dF_n = \frac{1}{2\mu}(B_n^2 - B_t^2) dl \tag{3.53}$$

where the *dl* is a differential length along the contour *C*. For the torque calculation, only the tangential component dF_t is summed along the contour specified.

Compared with the Virtual Work method, The Maxwell stress tensor method is easy to apply because only one field solution is required to evaluate the force or torque associated with the a given rotor position. However, this approach is highly sensitive to local error due to the poor meshing. Usually, this method requires a fine discretisation.

Of the three methods introduced above, the Virtual Work method and the Maxwell stress tensor method are more popularly used for the finite element analysis. Although lots of work has been done to improve these two methods, there are still no completely reliable solutions and the attempt to find out which of the force methods is "most accurate" is inconclusive [Mizia, 1988; Komeza, 1994; Salon, 1995]. The force and torque calculation is problem-dependent.

In this study, the Maxwell stress tensor is used. To obtain a more accurate solution, the integration contour is carefully chosen to satisfy the following rules recommended by Mizia [1988] and De Bortoli [1990].

1. The contour passing through the nodes must be avoided.
2. The contour should cross elements by joining the midpoints of two of their sides.
3. The contour should pass through the centres of elements.

4. The contour should be entirely placed in the air gap and not intersect magnetic materials or current-carrying elements.

Besides choosing the contour, extra consideration is given to the mesh geometry since the Maxwell stress tensor is also very sensitive to the density of discretisation and the symmetry of the mesh. A typical mesh of SPIMs used in this study is shown in Fig. 3.13. In the 0.4mm air gap, four layers elements are meshed. The integration contour zigzag crosses the elements in the layer shaded layer by joining the two midpoints of their sides (Fig. 3.14).

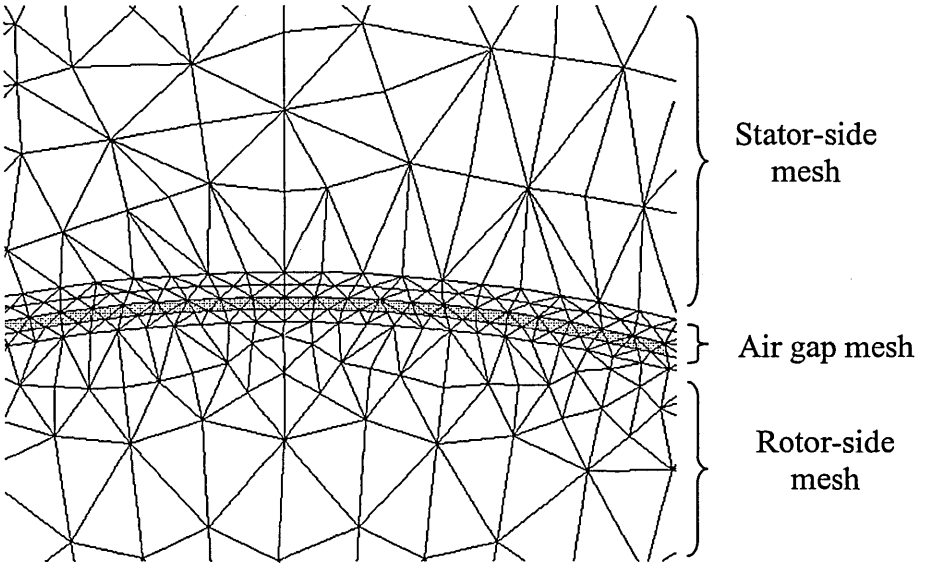

Fig. 3.13 Typical air gap mesh of SPIMs

Therefore, once the field distribution has been solved the components of flux density along the x-axis and y-axis can be calculated respectively by

$$\begin{cases} B_x = \dfrac{1}{2\Delta_e}(c_l A_l + c_m A_m + c_n A_n) \\ B_y = \dfrac{-1}{2\Delta_e}(b_l A_l + b_m A_m + b_n A_n) \end{cases} \tag{3.54}$$

where Δ_e is the area of the element and the geometric coefficients $\{b_l, b_m, b_n\}$ and $\{c_l, c_m, c_n\}$ can be estimated by (2.32).

Accordingly, the formulas for computing the normal and tangential components of the force density are given according to the location of each element (Fig. 3.14).

1. If the element is located in the first quadrant ($X_c > 0$ *and* $Y_c > 0$)

$$\begin{cases} B_t = -B_x \cos\theta + B_y \sin\theta \\ B_n = -B_x \sin\theta - B_y \cos\theta \end{cases} \tag{3.55a}$$

2. If the element is located in the second quadrant ($X_c < 0$ *and* $Y_c > 0$)

$$\begin{cases} B_t = -B_x \cos\theta - B_y \sin\theta \\ B_n = +B_x \sin\theta - B_y \cos\theta \end{cases} \tag{3.55b}$$

3. If the element is located in the third quadrant ($X_c < 0$ *and* $Y_c < 0$)

$$\begin{cases} B_t = -B_x \cos\theta - B_y \sin\theta \\ B_n = +B_x \sin\theta + B_y \cos\theta \end{cases} \tag{3.55c}$$

4. If the element is located in the forth quadrant ($X_c > 0$ *and* $Y_c < 0$)

$$\begin{cases} B_t = +B_x \cos\theta + B_y \sin\theta \\ B_n = -B_x \sin\theta + B_y \cos\theta \end{cases} \tag{3.55d}$$

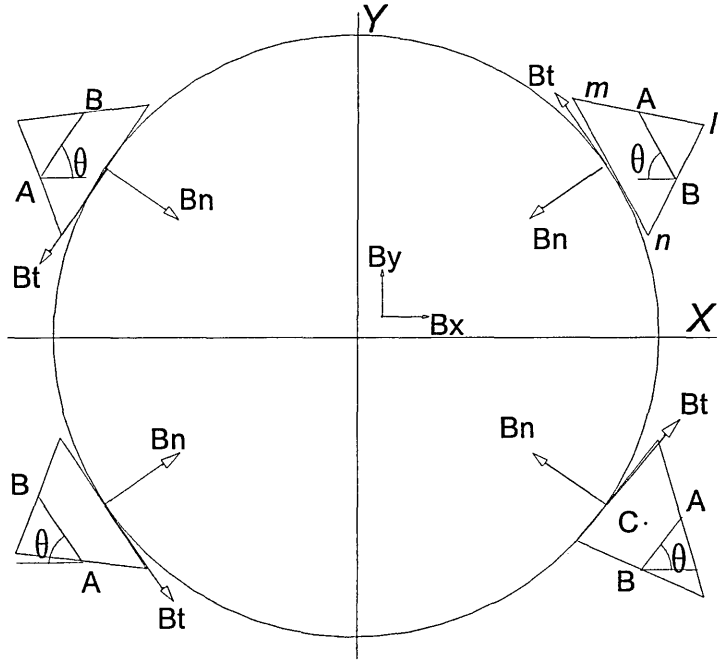

Fig. 3.14 Torque calculation using the Maxwell stress tensor

(Point A and B are the midpoint of each side. Point C is the centre of the element)

In (3.55), θ can be calculated using the coordinate of two midpoints A and B and the distance between A and B, l_{AB}.

$$\theta = \sin^{-1}\left(\frac{|y_A - y_B|}{l_{AB}}\right) \qquad \left(0 < \theta < 90^o\right) \tag{3.56}$$

Summing the tangential component of the Maxwell stress tensor over the N elements along the integration contour, the mechanical torque of rotor can be estimated from:

$$T = \sum_N \frac{1}{\mu_o} B_t B_n l_{AB} \ . \tag{3.57}$$

3. 7 Conclusion

The main contribution of this chapter was to develop a two-dimensional eddy-current time-stepping finite element model for SPIMs. With this model, the skin effect, saturation and harmonics can all be taken into account. Since the external circuit equations are coupled with the field equations in this model, the voltage-driven sources, such as the triac voltage controller and PWM inverter, can be considered directly. In addition, once this coupled system equations have been solved the performances of SPIMs, such as the stator current, shaded-ring current, torque, even the real rotor-bar current, are all known.

This chapter has also addressed two difficult aspects of the time-stepping method. One is the re-mesh algorithm and the other is the variable step size. Using the hybrid method which combines the Sliding Surface model with the Moving Band model, the convenience and quality of the rebuilt mesh has been improved over the whole range of machine speeds.

The core problem in using a variable step size is to judge whether the step size is suitable at every time step. By using Neville's Algorithm to estimate the truncation error due to

the time-stepping process, the variation of the field was reliably detected by the truncation error, therefore, a suitable step size can be determined accordingly. The validity of the proposed method for variable step size model was confirmed by the simulation results of a SPIM in the locked-rotor state. Compared with the existing method, the truncation error calculated by the proposed method is more sensitive and reliable to the variation of the field.

As to force/torque calculation which is always a focus of electromagnetic field calculation it has been examined in this chapter as well. The torque calculation equation for a SPIM based on Maxwell's stress tensor was derived and the criteria for choosing a suitable integration contour were proposed.

4 TWO-DIMENSIONAL MULTI-SLICE FINITE ELEMENT MODEL OF SPIMS

4. 1 Introduction

For the performance analysis of induction motors by the finite element method, the 2D model is the most popular due to its simplicity compared with its 3D rival. However, if a 2D model is used, the inherent 3D attributes of a real machine, such as the skewed rotor, the rotor end-ring and the overhang of the stator winding, are still difficult to be studied accurately.

Due to the abundant harmonics in the air gap, the skewed rotor is always employed in the SPIMs and the skew has a significant effect on their performance. With the 2D eddy-current model discussed in the previous chapter, the geometry of machine along the shaft is assumed non-variable, so the skew cannot be taken into account. In this case, the 3D finite element model can offer a more accurate prediction, but the 3D mesh for skewed rotor is far from easy to build up and the computing with the 3D time-stepping model is still a hard task. In order to deal with the problems of skewed rotor with the 2D model, some alternatives are developed. Among these methods, the multi-slice method [Piriou, 1990; Boualem, 1994; Williamson, 1995; Ho, 1997] is, in the author's opinion, a more efficient and more useful model.

Using this alternative method, the skewed rotor described by Fig. 4.1a is divided into a series of 2D unskewed sections, as shown in Fig. 4.1b, and each slice corresponds to the different position along the axial length of the machine. In every slice, since the rotor-bar is unskewed, there is no axial variation of magnetic field along the z-direction; thus the 2D finite element model can be used to calculate the flux distribution in each slice. Because the currents flowing in the stator coil, shaded-ring and rotor-bar are considered uniform in each slice, the fields of all slices are coupled and should be solved simultaneously.

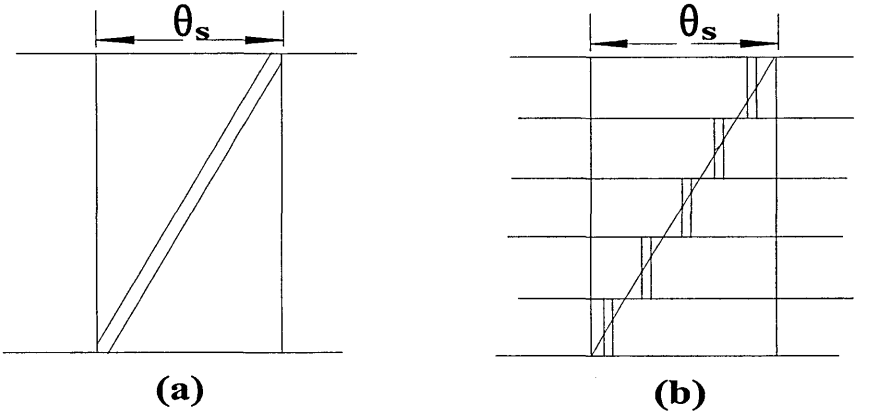

Fig. 4.1 Representation of skewed rotor-bar (θ_s is the skew angle)

The multi-slice finite element model was first applied to simulate a permanent magnet synchronous machine by Piriou [1990]. Boualem [1994] used this technology to simulate the steady state operation of a three-phase squirrel-cage rotor induction motor and his model was further developed and simplified by Ho [1997]. Using separate field and circuit equations, Williamson [1995] proposed a circuit multi-slice model to analyse the salient-pole synchronous generator and three-phase induction motor, but his method is usually suitable for the normal three-phase induction motors with fewer harmonics. Although these methods have been successfully used in different cases, no one has applied such a model for predicting the performances of the shaded-pole motors. Therefore, it is useful to study the SPIMs with the multi-slice technique. In this chapter, the governing system equation of multi-slice modelling for a shaded-pole induction motor is derived first. In this multi-slice model, the eddy-current time-stepping method was

adopted, so the model can include all the consequences of the rotor skew, skin effect, saturation and non-sinusoidal quantities. The external circuit equation is solved by coupling with the field equation directly; thus, once the system equation is solved, all performances at this time are known.

Besides the skew, the end-rings of the rotor cage in SPIMs can exert an appreciable influence over the performance of the machine because the end-rings contribute a significant proportion of the rotor impedance. However, in normal 2D or 2D multi-slice finite element models for an induction motor, the end-ring impedance is either neglected or considered as a lumped impedance coupled into the rotor circuit shown in Fig. 3.1.

In the latter situation, the end-ring resistance between two adjacent bars, $R_{e,i}$ is generally obtained by calculating the DC resistance along the mean circumference of the end-rings with Veinott's [1959] equation;

$$R_{e,i} = \frac{\pi D_r}{\sigma A_e N_b} \tag{4.1}$$

where D_r: the mean diameter of the end-ring.

σ : conductivity of end-ring

A_e: cross section area of end-ring

N_b : number of rotor bars

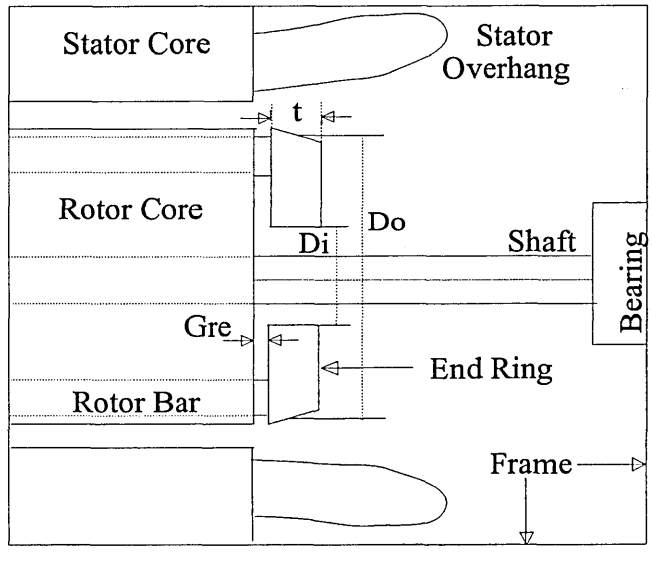

Fig. 4.2 A side elevation of the end-ring of a SPIM

This approach assumes that the currents in the end-ring distribute themselves uniformly along the radial direction. If the difference between D_o and D_i is small, which means that the end-ring is very narrow in the radial direction, this assumption is considered acceptable. However, if the end-ring is wide compared with the pole pitch, such an assumption is not justified because the currents entering from the rotor bars have to travel quite a distance radially before they start to travel along the circumference.

Trichey [1936] and Wilimason [1986] have studied the effect of current distribution in the end-rings, and their results show that Veinott's equation can lead to poor accuracy in the case of a machine with wide end-ring, particularly when the pole number is high. However, their proposed models can only be used to calculate the resistance of the whole end-ring. Both of the two methods assume that the distribution of rotor-bar currents is sinusoidal along the circumference direction, and this condition cannot be satisfied for SPIMs. Therefore, in this study, a more accurate method to calculate the resistance between two adjacent bars has been used which is based on electric field analysis using the finite element model. The detail of this method is given in the second section of this chapter.

As to the calculation of the leakage reactance of the end-ring, both the analytical approximation and the 2D finite element method have been tried with different assumptions [Kovacs, 1982; Williamson, 1995; De Weerdt, 1995]. However, it is found that the accuracy of the leakage reactance of the end-ring mainly depends on the assumed permeability of rotor core, stator core, frame and shaft. The reactance varies over a wide range with a different boundary condition and permeability assumption. In contrast to the end-ring resistance which is less affected by the surrounding parts, it is considered that a more accurate result for the reactance of the end-ring may only be obtained by using 3D finite element model. In this study, the reactance of the end-ring was computed by using the modal current together with the images method [Williamson, 1995].

The eddy-current time-stepping multi-slice finite element model of SPIMs is considered as a fairly precise model for the analysing the performance of SPIMs. To verify the validity of the proposed model, both the steady and transient state performances of a

typical SPIM are investigated with the 2D multi-slice approach proposed in this study. The SPIMs supplied by the triac-controlled non-sinusoidal voltage source is studied as well in this chapter. The results are compared with the experimental data showing the advantages of the proposed model.

4. 2 Two-dimensional Multi-slice Finite Element Model of SPIMs

Using the multi-slice model, the skewed rotor is divided into a series of 2D unskewed slices and each slice rotates a certain angle to correspond to its position along the axial length of the machine. Because there is no axial variation of the magnetic field along the z-direction, the magnetic field in each slice can be described by the 2D finite element directly. However, due to the continuity of the currents flowing in the conductor in the study region, the fields equations of all slices have to be solved simultaneously.

A) Field equation

The field equation in the S_i^{th} slice is

$$\frac{\partial}{\partial x}(\nu\frac{\partial A^{Si}}{\partial x})+\frac{\partial}{\partial y}(\nu\frac{\partial A^{Si}}{\partial y})=\beta_n^{C,Si}J_C^{Si}+\beta_n^{S,Si}J_S^{S}+\beta_n^{b,Si}\left(\frac{V_b^{Si}}{l_z}-\frac{\partial A^{Si}}{\partial t}\right) \tag{4.2}$$

In equation (4.2), if the slice sequence number S_i is disregarded, the definition of $\beta_n^{C,Si}$, $\beta_n^{S,Si}$ and $\beta_n^{b,Si}$ is the same as (3.5) in chapter 3. Assuming the currents of stator and shaded-rings are uniform without considering the effect of eddy current, the current density in the stator and shaded-ring regions in each slice, J_C^{Si} and J_S^{Si}, can be calculated using the following equation.

$$J_C^{Si}=J_C=\frac{N_c}{S_p}I_c \tag{4.3}$$

$$J_S^{Si} = J_S = \frac{N_c}{S_p} I_S \tag{4.4}$$

By applying the Galerkin procedure to (4.2), one can get the field equation in the S_i^{th} slice in matrix form:

$$\nu[\mathbf{S}^{Si}]\{\mathbf{A}^{Si}\}^{(n+1)} + [\mathbf{T}^{Si}]\left\{\frac{\partial \mathbf{A}^{Si}}{\partial t}\right\}^{(n+1)} - [\mathbf{Q}^{Si}]\frac{\mathbf{V}_b^{Si}}{l_{z,Si}} - [\mathbf{D}_C^{Si}]\{\mathbf{I}_C\} - [\mathbf{D}_S^{Si}]\{\mathbf{I}_S\} = \{\mathbf{0}\} \tag{4.5}$$

where

$$S_{ij}^{Si} = \frac{1}{4\Delta_e}(b_i b_j + c_i c_j) \tag{4.5a}$$

$$T_{ij}^{Si} = \begin{cases} \beta_n^{b,Si}\dfrac{\Delta_e}{6} & i = j \\ \beta_n^{b,Si}\dfrac{\Delta_e}{12} & i \neq j \end{cases} \tag{4.5b}$$

$$Q_{ij}^{Si} = \beta_n^{b,Si}\frac{\sigma\Delta_e}{3} \tag{4.5c}$$

$$D_{C,ij}^{Si} = \beta_n^{C,Si}\frac{\Delta_e}{3} \tag{4.5d}$$

$$D_{S,ij}^{Si} = \beta_n^{S,Si}\frac{\Delta_e}{3}. \tag{4.5e}$$

The field equation can be time-discretized using the Backward Difference method introduced in chapter 2. Substituting (2.45) into (4.2), one obtains

$$\left(\nu[\mathbf{S}^{Si}] + \frac{[\mathbf{T}^{Si}]}{\Delta t}\right)\{\mathbf{A}^{Si}\}^{(n+1)} - [\mathbf{Q}^{Si}]\frac{\{\mathbf{V}_b^{Si}\}^{(n+1)}}{l_z} - [\mathbf{D}_C^{Si}]\{\mathbf{I}_C\}^{(n+1)} - [\mathbf{D}_S^{Si}]\{\mathbf{I}_S\}^{(n+1)} = \frac{[\mathbf{T}^{Si}]}{\Delta t}\{\mathbf{A}^{Si}\}^{(n)} \tag{4.6}$$

Since the reluctivity, ν, depends on the magnitude of the flux density which is a function of vector potential A, equation (4.6) is non-linear.

B) Stator winding circuit equation

For all the *Ms* slices, the current flowing in the coil remains same and the current satisfies the stator circuit equation (4.7),

$$V_C = i_C R_C + \frac{d\phi}{dt} + L_C \frac{di_C}{dt} \tag{4.7}$$

where the total differentiation of flux linkage $d\phi/dt$ is the summation of all Ms slices.

For each slice, its $d\phi^{Si}/dt$ can be expressed from the magnetic vector potential in the same way as for the 2D case by

$$\frac{d\phi^{Si}}{dt} = Ns\sum_{i=1}^{m}\frac{d_i N_c l_z^{Si}}{S_p}\int\frac{dA^{Si}}{dt}ds \tag{4.8}$$

where $l_z^{Si} = l_z/Ms$ if the slices are divided uniformly in the z-direction.

Therefore, the total differentiation of flux linkage $d\phi/dt$ in (4.7) can be calculated.

$$\frac{d\phi}{dt} = \sum_{j=1}^{Ms}\frac{d\phi^{Si}}{dt} = \sum_{j=1}^{Ms} Ns\sum_{i=1}^{m}\frac{d_i N_c l_z^{Si}}{S_p}\int\frac{dA^{Si}}{dt}ds = Nsl_z^{Si}\sum_{i=1}^{m}\beta_i^{C,Si}\left\{\sum_{i=1}^{N}\frac{dA^{Si}}{dt}N_j\right\}d\Omega^{Si} \tag{4.9}$$

where Ω^{Si} is the cross-sectional area of state winding of the slice Si.

Substituting equation (4.9) into (4.7) and applying the Backward Difference time-discretization method, equation (4.7) can be rewritten in matrix form:

$$\begin{aligned}\left(-\left[\mathbf{D}_C^{S1}\right]^T\ -\left[\mathbf{D}_C^{S2}\right]^T\ \cdots\ -\left[\mathbf{D}_C^{Ms}\right]^T\right)\begin{pmatrix}\{\mathbf{A}^{S1}\}\\ \{\mathbf{A}^{S2}\}\\ \vdots\\ \{\mathbf{A}^{Ms}\}\end{pmatrix}^{(n+1)} - \frac{R_C\Delta t + L_C}{N_S l_z}\{\mathbf{I_C}\}^{(n+1)} \\ = \left(-\left[\mathbf{D}_C^{S1}\right]^T\ -\left[\mathbf{D}_C^{S2}\right]^T\ \cdots\ -\left[\mathbf{D}_C^{Ms}\right]^T\right)\begin{pmatrix}\{\mathbf{A}^{S1}\}\\ \{\mathbf{A}^{S2}\}\\ \vdots\\ \{\mathbf{A}^{Ms}\}\end{pmatrix}^{(n)} - \frac{L_C}{N_S l_z}\{\mathbf{I_C}\}^{(n)} + \frac{\Delta t}{N_S l_z}\{\mathbf{V_C}\}^{(n+1)}\end{aligned} \tag{4.10}$$

C) Shaded-ring circuit equation

The model of the shaded-ring is the same as the stator winding model except that the external voltage supply of the shaded-ring is zero, therefore, one can write the shaded-rings circuit equation similarly:

$$\begin{aligned}\left(-\left[\mathbf{D}_S^{S1}\right]^T \quad -\left[\mathbf{D}_S^{S2}\right]^T \quad \cdots \quad -\left[\mathbf{D}_S^{Ms}\right]^T\right)\begin{pmatrix}\{\mathbf{A}^{S1}\}\\ \{\mathbf{A}^{S2}\}\\ \vdots\\ \{\mathbf{A}^{Ms}\}\end{pmatrix}^{(n+1)} - \frac{R_C\Delta t + L_C}{N_S l_z}\{\mathbf{I}_S\}^{(n+1)} \\ = \left(-\left[\mathbf{D}_S^{S1}\right]^T \quad -\left[\mathbf{D}_S^{S2}\right]^T \quad \cdots \quad -\left[\mathbf{D}_S^{Ms}\right]^T\right)\begin{pmatrix}\{\mathbf{A}^{S1}\}\\ \{\mathbf{A}^{S2}\}\\ \vdots\\ \{\mathbf{A}^{Ms}\}\end{pmatrix}^{(n)} - \frac{L_S}{N_S l_z}\{\mathbf{I}_S\}^{(n)}\end{aligned} \tag{4.11}$$

D) Rotor cage circuit equations

The whole bar terminal potential difference $\{V_b\}$ can be obtained by adding all the potential difference of each slice together;

$$\{\mathbf{V_b}\} = \{\mathbf{V_b^{S1}}\} + \{\mathbf{V_b^{S2}}\} + \cdots \quad \cdots + \{\mathbf{V_b^{Ms}}\} = \sum_{i=1}^{Ms}\{\mathbf{V_b^{Si}}\} \tag{4.12}$$

The current in the same bar in different slice is uniform, therefore it can be calculated as:

$$\{\mathbf{i_b}\} = \{\mathbf{i_b^{s_1}}\} = \{\mathbf{i_b^{s_2}}\} = \cdots = \{\mathbf{i_b^{Si}}\}. \tag{4.13}$$

For each slice, the following equation must be satisfied

$$i_{b,i}^{Si} = \sigma \iint_{bar,i}\left(\frac{V_b^{Si}}{l_z^{Si}} - \frac{\partial A^{Si}}{\partial t}\right)dxdy \tag{4.14}$$

Referring to the same equation (3.22) in chapter 3, a similar result is yielded:

$$\iint_{bar,i}(\sigma\frac{V_b^{Si}}{l_z^{Si}} - \sigma\frac{\partial A}{\partial t})dxdy = \sigma\frac{V_b^{Si}}{l_z^{Si}}\Delta_b - \iint_{bar,i}(\sigma\frac{\partial A_i^{Si}}{\partial t}N_j)dxdy = \frac{V_b^{Si}}{R_b^{Si}} - \sum_{bar,i}\beta_i^b\frac{\Delta_e}{3}\frac{\partial A_i}{\partial t} \tag{4.15}$$

where R_b^{Si} represents the DC resistance of the rotor-bar in the S_i^{th} slice. Therefore, the rotor-bar current $[I_b]$ can be expressed from vector potential $[A_i]$ in matrix form:

$$\{I_b^{Si}\} = \frac{\{V_{b,i}^{Si}\}}{R_b^{Si}} - [Q^{Si}]^T\left\{\frac{dA_i^{Si}}{dt}\right\} \tag{4.16}$$

In the multi-slice model, the equation describing the relationship between bar current, end-ring current and the total terminal potential difference are still available. Substituting equation (4.12) and (4.13) into equation (3.27), one can obtain:

$$\begin{aligned}\{\mathbf{I_b}\}^{(n+1)} &= \{\mathbf{I}_b^{S1}\}^{(n+1)} = \{\mathbf{I}_b^{S2}\}^{(n+1)} \ldots = \{\mathbf{I}_b^{Ms}\}^{(n+1)} \\ &= \left(\frac{\Delta t}{R_e\Delta t + L_e}\right)\left(\frac{1}{2}[\mathbf{M}]^T[\mathbf{M}]\sum_{Si=1}^{Ms}\{\mathbf{V}_b^{Si}\}^{(n+1)} + \frac{L_e}{\Delta t}[\mathbf{M}]^T\{\mathbf{I_e}\}^{(n)}\right)\end{aligned} \tag{4.17}$$

Substituting equation (4.17) into (4.16), the bar current term can be eliminated. Applying the Backward Difference method to (4.16) and assembling all the *Ms* sliced together, the equations describing the rotor-bar for all slices are obtained:

$$\begin{aligned}&\begin{pmatrix}-[\mathbf{Q}^{S1}]^T & & & \\ & -[\mathbf{Q}^{S2}]^T & & \\ & & \ddots & \\ & & & -[\mathbf{Q}^{Ms}]^T\end{pmatrix}\begin{pmatrix}\mathbf{A}_i^{S1}\\ \mathbf{A}_i^{S2}\\ \vdots\\ \mathbf{A}_i^{Ms}\end{pmatrix}^{(n+1)} + \begin{pmatrix}\mathbf{Y}_{1,1} & \mathbf{Y}_{1,2} & \cdots & \mathbf{Y}_{1,Ms}\\ \mathbf{Y}_{1,2} & \mathbf{Y}_{1,2} & \cdots & \mathbf{Y}_{1,Ms}\\ \vdots & \vdots & \ddots & \vdots\\ \mathbf{Y}_{1,Ms} & \mathbf{Y}_{1,Ms} & \cdots & \mathbf{Y}_{Ms,Ms}\end{pmatrix}\begin{pmatrix}\{\mathbf{V}_b^{S1}\}\\ \{\mathbf{V}_b^{S2}\}\\ \vdots\\ \{\mathbf{V}_b^{Ms}\}\end{pmatrix}^{(n+1)} \\ &= \begin{pmatrix}-[\mathbf{Q}^{S1}]^T & & & \\ & -[\mathbf{Q}^{S2}]^T & & \\ & & \ddots & \\ & & & -[\mathbf{Q}^{Ms}]^T\end{pmatrix}\begin{pmatrix}\mathbf{A}_i^{S1}\\ \mathbf{A}_i^{S2}\\ \vdots\\ \mathbf{A}_i^{Ms}\end{pmatrix}^{(n)} + \frac{L_e\Delta t}{(R_e\Delta t + L_e)}[\mathbf{M}]^T\begin{pmatrix}\{\mathbf{I}_e\}\\ \{\mathbf{I}_e\}\\ \{\mathbf{I}_e\}\\ \{\mathbf{I}_e\}\end{pmatrix}^{(n)}\end{aligned} \tag{4.18}$$

where

$$\mathbf{Y}_{i,j} = \begin{cases}\dfrac{\Delta t}{2(R_e\Delta t + L_e)}[\mathbf{M}]^T[\mathbf{M}] + \dfrac{[\mathbf{U}]}{R_b^{Si}} & i = j\\ \dfrac{\Delta t}{2(R_e\Delta t + L_e)}[\mathbf{M}]^T[\mathbf{M}] & i \neq j\end{cases}$$

Therefore, the field equation and the circuit equation of each slice are known, we can assemble them into a global equation:

$$\begin{pmatrix} [\mathbf{ST}^{S1}] & & \cdots & & -[\mathbf{D}_C^{S1}] & -[\mathbf{Q}_l^{S1}] & & & \\ & [\mathbf{ST}^{S2}] & & & -[\mathbf{D}_C^{S2}] & & -[\mathbf{Q}_l^{S2}] & & \\ \vdots & & \ddots & \vdots & \vdots & & & \ddots & \\ & & \cdots & [\mathbf{ST}^{Ms}] & -[\mathbf{D}_C^{Ms}] & & & & -[\mathbf{Q}_l^{Ms}] \\ -[\mathbf{D}_C^{S1}]^{\mathrm{T}} & -[\mathbf{D}_C^{S2}]^{\mathrm{T}} & \cdots & -[\mathbf{D}_C^{Ms}]^{\mathrm{T}} & [\mathbf{Y}_{\mathrm{C}}] & & & & \\ -[\mathbf{D}_S^{S1}]^{\mathrm{T}} & -[\mathbf{D}_S^{S2}]^{\mathrm{T}} & \cdots & -[\mathbf{D}_S^{Ms}]^{\mathrm{T}} & & [\mathbf{Y}_S] & & & \\ -[\mathbf{Q}_l^{S1}]^{T} & & \cdots & & & \begin{bmatrix}\mathbf{Y}'_{1,1}\\ \mathbf{Y}'_{1,2}\end{bmatrix} & \begin{bmatrix}\mathbf{Y}'_{1,2}\\ \mathbf{Y}'_{2,2}\end{bmatrix} & \cdots & \begin{bmatrix}\mathbf{Y}'_{1,Ms}\\ \mathbf{Y}'_{2,Ms}\end{bmatrix} \\ & -[\mathbf{Q}_l^{S1}]^{T} & & & & & & & \\ \vdots & & \ddots & \vdots & & \vdots & \vdots & \ddots & \vdots \\ & & \cdots & -[\mathbf{Q}_l^{S1}]^{T} & & \left[\mathbf{Y}'_{1,Ms}\right] & \left[\mathbf{Y}'_{2,Ms}\right] & \cdots & \left[\mathbf{Y}'_{Ms,Ms}\right] \end{pmatrix} \begin{pmatrix} \{\mathbf{A}^{\mathrm{S1}}\} \\ \{\mathbf{A}^{\mathrm{S2}}\} \\ \vdots \\ \{\mathbf{A}^{Ms}\} \\ \{\mathbf{I}_{\mathrm{C}}\} \\ \{\mathbf{I}_{\mathrm{S}}\} \\ \{\mathbf{V}_{\mathrm{b}}^{\mathrm{S1}}\} \\ \{\mathbf{V}_{\mathrm{b}}^{\mathrm{S2}}\} \\ \vdots \\ \{\mathbf{V}_{\mathrm{b}}^{Ms}\} \end{pmatrix} = \begin{pmatrix} \{\mathbf{N}_{\mathrm{A}}^{\mathrm{S1}}\} \\ \{\mathbf{N}_{\mathrm{A}}^{\mathrm{S2}}\} \\ \vdots \\ \{\mathbf{N}_{\mathrm{A}}^{Ms}\} \\ \{\mathbf{N}_{\mathrm{C}}\} \\ \{\mathbf{N}_{\mathrm{S}}\} \\ \{\mathbf{N}_{\mathrm{b}}^{\mathrm{S1}}\} \\ \{\mathbf{N}_{\mathrm{b}}^{\mathrm{S2}}\} \\ \vdots \\ \{\mathbf{N}_{\mathrm{b}}^{Ms}\} \end{pmatrix} \tag{4.19}$$

where

$$\left[\mathbf{ST}^{\mathrm{Si}}\right] = \nu[\mathbf{S}^{\mathrm{Si}}] + \frac{\left[\mathbf{T}^{\mathrm{Si}}\right]}{\Delta t}, \qquad \left[\mathbf{Q}_{\mathrm{l}}^{\mathrm{Si}}\right] = \frac{\left[\mathbf{Q}^{\mathrm{Si}}\right]}{l_z^{Si}},$$

$$\{Y_C\} = -\frac{R_C\Delta t + L_C}{N_S l_z}[U], \qquad \{Y_S\} = -\frac{R_S\Delta t + L_S}{l_z}[U], \qquad \left[Y'_{i,j}\right] = \frac{\left[Y_{i,j}\right]}{l_z^{Si}}$$

$$\{N_A^{Si}\} = -\frac{[T^{Si}]}{\Delta t}\{A^{Si}\}$$

$$\{N_C\} = -\sum_{Si=1}^{Ms}\left[D_C^{Si}\right]^T\left\{A^{Si}\right\}^{(n)} - \frac{L_C}{N_S l_z}\{I_C\}^{(n)} + \frac{\Delta t}{N_S l_z}\{V_C\}^{(n+1)}$$

$$\{N_S\} = -\sum_{Si=1}^{Mx}\left[D_S^{Si}\right]^T\left\{A^{Si}\right\}^{(n)} - \frac{L_S}{l_z}\{I_S\}^{(n)}$$

$$\{\mathbf{N}_b^{Si}\} = \frac{1}{l_z^{Si}}\left(-[\mathbf{Q}^{Si}]^T\left\{\mathbf{A}^{Si}\right\}^{(n)} + \frac{L_e\Delta t}{(R_e\Delta t + L_e)}[\mathbf{M}]^T\{\mathbf{I}_{\mathrm{e}}\}^{(n)}\right)$$

Since the coefficient matrices $\left[\mathbf{ST}^{\mathrm{Si}}\right] = \nu[\mathbf{S}^{\mathrm{Si}}] + \frac{\left[\mathbf{T}^{\mathrm{Si}}\right]}{\Delta t}$ are non-linear, the Newton–Raphson method has to be employed to linearize the globe equation. Thus, one obtains:

$$\begin{pmatrix} [\mathbf{STL}] & -[\mathbf{D}_{\mathrm{C}}] & -[\mathbf{D}_S] & -[\mathbf{Q}_l] \\ -[\mathbf{D}_{\mathrm{C}}]^{\mathrm{T}} & [\mathbf{Y}_{\mathrm{C}}] & & \\ -[\mathbf{D}_S]^T & & [\mathbf{Y}_S] & \\ -[\mathbf{Q}_l]^T & & & [\mathbf{Y}_b] \end{pmatrix}\begin{pmatrix} \{\Delta\mathbf{A}_{\mathrm{i}}\} \\ \{\Delta\mathbf{I}_{\mathrm{C,i}}\} \\ \{\Delta\mathbf{I}_{\mathrm{S,i}}\} \\ \{\Delta\mathbf{V}_{\mathrm{b,i}}\} \end{pmatrix} = -\begin{pmatrix} [\mathbf{ST}] & -[\mathbf{D}_{\mathrm{C}}] & -[\mathbf{D}_S] & -[\mathbf{Q}_l] \\ -[\mathbf{D}_{\mathrm{C}}]^{\mathrm{T}} & [\mathbf{Y}_{\mathrm{C}}] & & \\ -[\mathbf{D}_S]^T & & [\mathbf{Y}_S] & \\ -[\mathbf{Q}_l]^T & & & [\mathbf{Y}_b] \end{pmatrix}\begin{pmatrix} \{\mathbf{A}_{\mathrm{i}}\} \\ \{\mathbf{I}_{\mathrm{C,i}}\} \\ \{\mathbf{I}_{\mathrm{S,i}}\} \\ \{\mathbf{V}_{\mathrm{b,i}}\} \end{pmatrix} + \begin{pmatrix} \{\mathbf{N}_{\mathrm{A}}\} \\ \{\mathbf{N}_{\mathrm{C}}\} \\ \{\mathbf{N}_{\mathrm{S}}\} \\ \{\mathbf{N}_{\mathrm{b}}\} \end{pmatrix} \tag{4.20}$$

where $[\mathbf{STL}^{Si}] = \left[\nu[\mathbf{S}^{Si}] + [\mathbf{G}^{Si}] + \frac{[\mathbf{T}^{Si}]}{\Delta t} \right][\mathbf{U}]$

Obviously, the system equations which couple both circuit and field equations are now sparse and symmetric, but not positive. To make the equation positive, the same procedure discussed in chapter 3 can be applied by adding the auxiliary variable vector $[\mathbf{I}_{C,aux}]$ and $[\mathbf{I}_{S,aux}]$. Therefore, stator and shaded-ring circuit equations can be split into two positive equations.

4. 3 End-ring Resistance Calculation

When the conventional equivalent circuit model is applied for SPIMs design, the effect of the end-ring resistance is normally considered by adding an appropriate amount to the bar resistance. By equating the Joule losses in the real cage to those in an equivalent cage which carries the same current distribution but has a zero-resistance end-ring, the equivalent bar resistance, R_b', is derived under the condition that the currents in the rotor bars are distribute themselves sinusoidally along the circumference at any time:

$$R_b' = R_b + \frac{R_e}{2N_b \sin(\frac{2p\pi}{N_b})} \tag{4.21}$$

where R_b is the bar resistance, p denotes the pole number and R_e is the resistance of one complete end-ring.

To obtain R_e, the resistance of a complete end-ring, Veinott [1959] used a very simple equation assuming that the distribution of currents in the end-ring is uniform along the radial direction. By a combination of flux-mapping the current in the wide ring and other analytical means, Trickey [1936] proposed a correction factor k_{ring} to consider the non-uniform current distribution in a wide end-ring.

$$R_e = \frac{2\pi D_r}{\sigma A_e} k_{ring} \tag{4.22}$$

where $k_{ring} = \frac{p}{2}\left[\frac{1+(\frac{D_i}{D_r})^p}{1-(\frac{D_i}{D_r})^p}\right]\left(1-(\frac{D_i}{D_r})\right)$.

With a single-slot pitch finite element model, Williamson [1986] found that equation (4.22) yields an unacceptably large error when the pole number increases because of Trickey's assumption that the bar currents are injected into the end-ring in a smooth, sinusoidal distribution along circumferential direction. Although with Williamson's method, the "smooth" condition is not necessary, because of using the single-slot pitch finite element model, the assumption that the bar currents distribute themselves sinusoidally along the circumference direction is still essential when equation (4.21) is employed to transfer the end-ring resistance into an appropriate amount of bar resistance. Additionally, both Trickey and Williamson ignored the skin effect, so their results are effective only for the DC condition. In order to study the skin effect, a linearised model based on modal current technique was used by Kovacs [1982]. In this model, the end-ring was replaced by a long straight bus bar with the same cross-sectional area and the shaft was considered as an infinitely permeable plane. However, this model could not consider the non-uniform radial current distribution. A similar model was also used in Williamson's study [1993] to calculate both the resistance and reactance of rotor cage end-rings.

With the existing methods, the results of calculating the end-ring resistance are still not satisfactory. Normally, only one effect, either the non-uniform current distribution or the skin effect, can be taken into account.

When the finite element model has been employed in the analysis of SPIMs, the calculation of end-ring resistance has not received adequate attention in the 2D situation. Although, Williamson [1982], Stangas [1985], Arkkio [1987], Vassent [1991] and Ho [1997] all used the equivalent rotor circuit model similar to the one described in Fig. 3.1 to include the effect of the impedance of rotor cage end-rings, none of them has explained

how to calculate the end-ring resistance between two adjacent bars. In the equivalent rotor circuit model which was adopted by most researchers using the 2D or 2D multi-slice model, the end-ring resistance between each pair of adjacent bars was consider uniform. In other words, the non-uniform distribution in the end-ring was ignored.

In this section, the effect of the non-uniform current distribution on the end-ring resistance has been considered by computing the 2D electric field of the end-ring. The end-ring resistance is calculated from the Joule losses and the current in a slot pitch. Consequently, a new equivalent rotor circuit model with variable end-ring resistance is proposed and is coupled into the magnetic field equation. This rotor circuit model is updated by computing the electric field of the end-ring simultaneously at each time step.

4.3.1 Calculating End-ring Resistance by FE Method

The first finite element model for evaluating the end-ring resistance was proposed by Williamson [1985]. His model, in which the end-ring current distribution is studied only in one slot pitch area, has three main assumptions.

1. The thickness of the end-ring is small when compared to their radial width and to the pole pitch: With this assumption., the current flow in the end-rings is regarded as essentially two-dimensional.
2. The current in the intersection area of rotor bar, the cross-hatched area in Fig. 4.3, distributes itself uniformly, which means the skin effect is negligible.
3. The current distribution of rotor bars along the circumferential direction is considered sinusoidal at any time. This assumption is not efficacious for the induction machine, e.g. SPIMs in which abundant harmonic currents exist in the rotor currents.

In this study, only the first assumption remains because it is the fundamental assumption to evaluate the end-ring resistance under two-dimensional conditions. The other two assumptions are removed by using a full pole pitch finite element model, as shown in Fig. 4.3. Since this finite element model of the end-ring is coupled with the magnetic field of the whole stator and rotor core in this study, the current of each rotor-bar has been calculated after the magnetic field is solved. Thus, the circumferential distribution of rotor-bar currents is exactly known when the electric field equation of end-ring is built up. On the other hand, once the magnetic field is solved, the distribution of current density in each rotor-bar cross-sectional area is also available. Therefore, the assumption of uniform distribution in area 1 is also unnecessary and the uneven distribution of the rotor-bar current due to the skin effect can be taken into account.

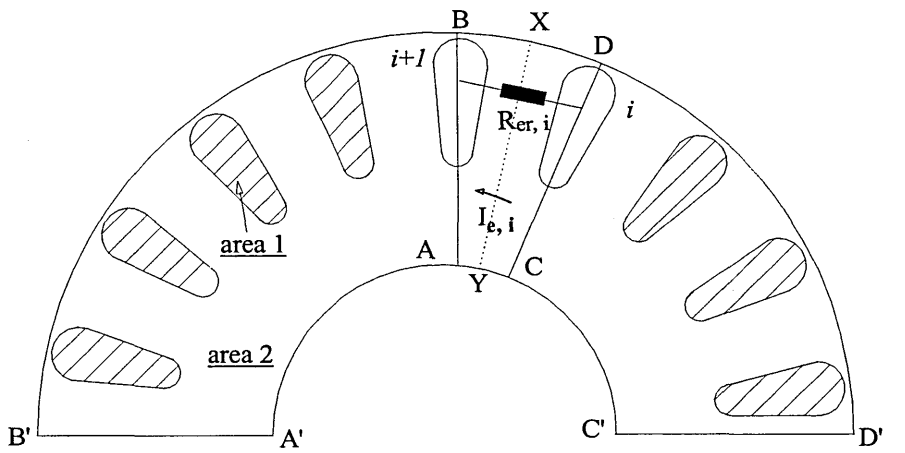

Fig. 4.3 Model used for finite element model for calculating end-ring resistance

So, the electrical field of the end-ring area shown in Fig. 4.3 is governed by [Rogers, 1954]

$$\nabla^2 \mathbf{V} = -\frac{C_i}{\sigma} \tag{4.23}$$

where V is the electrical potential and the C_i is the volume-charge density.

In the 2D situation, the above equation can be rewritten as

$$\begin{cases} \dfrac{\partial^2 V}{\partial^2 x}+\dfrac{\partial^2 V}{\partial^2 y}=-\dfrac{C_i}{\sigma} & area\ \ 1 \\ \dfrac{\partial^2 V}{\partial^2 x}+\dfrac{\partial^2 V}{\partial^2 y}=0 & area\ \ 2 \end{cases} \tag{4.24}$$

In this study, C_i can be calculated from

$$C_i=\frac{i_{b,i}}{t*S_b}. \tag{4.25}$$

In (4.25), t is the thickness of end-ring and S_b is the rotor-bar cross-sectional area. $i_{b,i}$ is the current of the i^{th} bar. Of cause, C_i can be exactly evaluated element by element according to the current density distribution in each rotor-bar which is already known once the magnetic field has been solved. Here, to demonstrate how the resistance between two adjacent bars is evaluated, the current distribution in each rotor-bar is assumed uniform temporarily.

As to the boundary conditions, the arcs A'ACC' and B'BDD' correspond to the inside and outside boundary of the end-ring. A homogeneous Neumann boundary condition, $\frac{\partial V}{\partial \vec{n}}=0$, is enforced along the two arcs.

After applying the Galerkin Formulation, the electrical field equation (4.24) can be transferred into the finite element format. The procedure is as same as that of dealing with the magnetic field, which has been demonstrated in Chapter 2. The final system equation of this electrical field is linear.

After the electrical field equation has been solved, the power loss in a slot pitch, $P_{e,i}$, is calculated by summing all the elements distributed in the i^{th} slot pitch area ACDB in Fig. 4.3.

$$\begin{aligned} P_{e,i} &= \sigma \int_{pitch\ \ i} \vec{E}_j^2 dv \\ &= \sigma * t \int_{pitch\ \ i} (E_x^2+E_y^2)dxdy \end{aligned} \tag{4.26}$$

where $E_x = \frac{-\partial V}{\partial x}$ and $E_y = \frac{-\partial V}{\partial y}$. dv is the volume of the small triangle element.

The current between bar $i+1$ and bar i can be evaluated by

$$i_{e,i} = t \int_{XY} \vec{J}_j \bullet \vec{n} dl \tag{4.27}$$

where $\vec{J}_j = \sigma \vec{E}_j$ is the current density in element j and $\vec{n}$ is the normal direction along the line XY in element j.

By equating Joule loss in the i^{th} slot pitch with those in a lumped resistance, the end-ring resistance between two adjacent bars, $R_{e,i}$, can be evaluated accordingly.

$$R_{e,i} = \frac{P_{e,i}}{i_{e,i}^2} \tag{4.28}$$

Using the finite element model introduced above, an end-ring with 26 rotor bars is studied (Model T). The parameters of the end-ring are given below.

$$t = 6mm,\ D_o = 41mm,\ D_i = 21mm,\ p = 4,\ \sigma = 2.1 \times 10^7 S/m$$

The uniform end-ring resistance between two adjacent bars, which is calculated using (4.1) and Trickey's correction factor k_{ring}, is $2.941 \times 10^6 \Omega$. Three cases, which have different mesh sizes and different rotor-bar current distributions, are investigated using the proposed finite element model.

Case_A	Case_B	CASE C
sinusoidal distribution*	sinusoidal distribution*	non-sinusoidal distribution**
fine mesh size (2860 elements, 1538 nodes)	normal mesh size (2028 elements, 1114 nodes)	normal mesh size

* When current distribution along the circumference is assumed sinusoidal, the current in the i^{th} bar, *Bar_current(i)*, is calculated by

$$Bar\_current(i) = 300 * \sin(\frac{2\pi i}{N_{bar}})$$

where N_{bar} is the number of rotor-bars in the model.

** Non-sinusoidal current distribution is a result obtained with the time-stepping method and is shown in Table 4.3

The electrical field of different cases is shown in Fig. 4.3 to Fig. 4.9. The results of the calculation of the end-ring resistance is shown in Table 4.1, Table 4.2 and Table 4.3.

Table 4.1 End-ring resistance calculated by finite element method (CASE A)

Slot Number	Bar Current (A)	End-ring Current (A)	Bar Current* (A)	Resistance(Ω)
1	139.41	469.15	139.41	2.2161E-6
2	246.89	222.26	246.89	4.5404E-6
3	297.81	-75.55	297.81	2.8883E-5
4	280.50	-356.05	280.50	2.7123E-6
5	198.93	-554.99	198.93	2.0189E-6
6	71.79	-626.78	71.79	1.9092E-6
7	-71.79	-554.99	-71.79	2.0151E-6
8	-198.93	-356.05	-198.94	2.7009E-6
9	-280.50	-75.55	-280.50	2.8820E-5
10	-297.81	222.26	-297.82	4.5610E-6
11	-246.89	469.15	-246.90	2.2226E-6
12	-139.41	608.57	-139.41	1.93320E-6
13	-9.0597E-5	608.57	-7.32422E-4	1.9297E-6

* The Bar Current is calculated as

Bar_current (i) = End_Ring_Current (i–1) – End_Ring_Current (i)*

*** Total copper loss due to the end-ring resistance = 5.8655 (W)

Table 4.2 End-ring resistance calculated by finite element method

Slot Number	Bar Current (A)	End-ring Current (A)	Bar Current* (A)	Resistance(Ω)	ERR (%)**
1	139.41	468.10	139.41	2.1368E-6	-3.576
2	246.89	221.20	246.89	4.8047E-6	5.820
3	297.81	-76.61	297.81	2.7202E-5	-5.819
4	280.50	-357.11	280.50	2.7961E-6	3.090
5	198.93	-556.04	198.93	1.9740E-6	-2.225
6	71.794	-627.84	71.795	1.947E-6	1.994
7	-71.794	-556.04	-71.794	1.9600E-6	-2.734
8	-198.93	-357.11	-198.93	2.7558E-6	-6.611
9	-280.50	-76.61	-280.50	2.6915E-5	2.030
10	-297.81	221.20	-297.81	4.7770E-6	4.735
11	-246.89	468.10	-246.89	2.1768E-6	-2.058
12	-139.41	607.51	-139.41	1.9723E-6	2.025
13	-9.0597E-5	607.51	7.9345E-4	1.9687E-6	2.024

** The ERR is difference of resistance between Case A and Case B.

*** Total copper loss due to the end-ring resistance = 5.8782(W)

Table 4.3 End-ring resistance calculated by finite element method

Slot Number	Bar Current (A)	End-ring Current (A)	Bar Current*(A)	Resistance(Ω)
1	-114.76	-311.90	-114.76	2.47357E-6
2	-223.31	-88.595	-223.31	1.64589E-5
3	-300.60	212.00	-300.60	4.06726E-6
4	-206.87	418.88	-206.87	2.18823E-6
5	-57.51	476.39	-57.51	1.87643E-6
6	18.41	457.97	18.41	1.96411E-6
7	75.81	382.17	75.81	2.10054E-6
8	170.80	211.37	170.80	3.96819E-6
9	272.12	-60.751	272.12	3.18432E-5
10	271.78	-332.53	271.78	2.60465E-6
11	124.41	-456.94	124.41	1.94317E-6
12	15.05	-471.99	15.05	1.93847E-6
13	-45.33	-426.66	-45.33	2.02879E-6

*** Total copper loss due to the end-ring resistance =3.870897 (W)

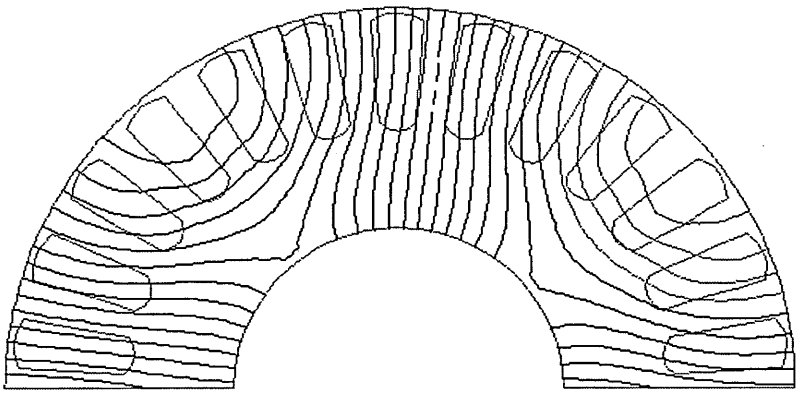

Fig. 4.4 Equipotential line of scalar electrical potential (V) (CASE A)

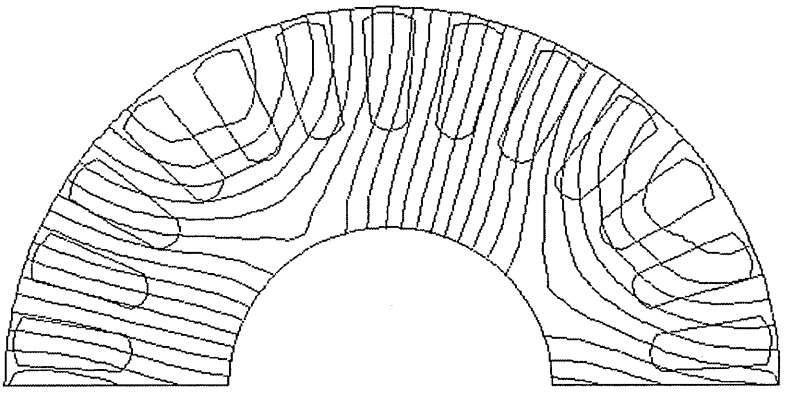

Fig. 4.5 Equipotential line of scalar electrical potential (V) (CASE C)

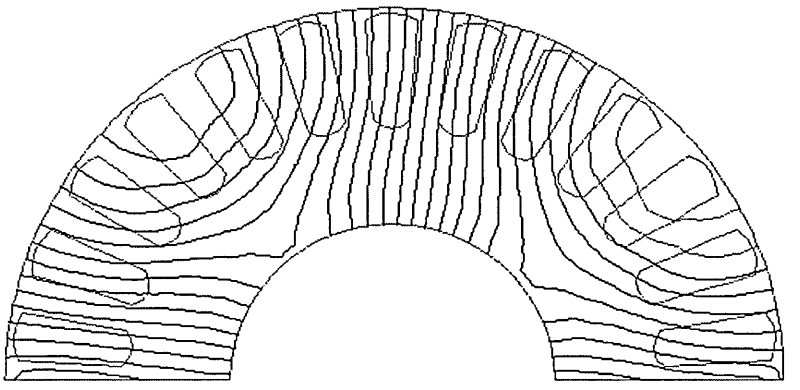

Fig. 4.6 Equipotential line of scalar electrical potential (V) (CASE B)

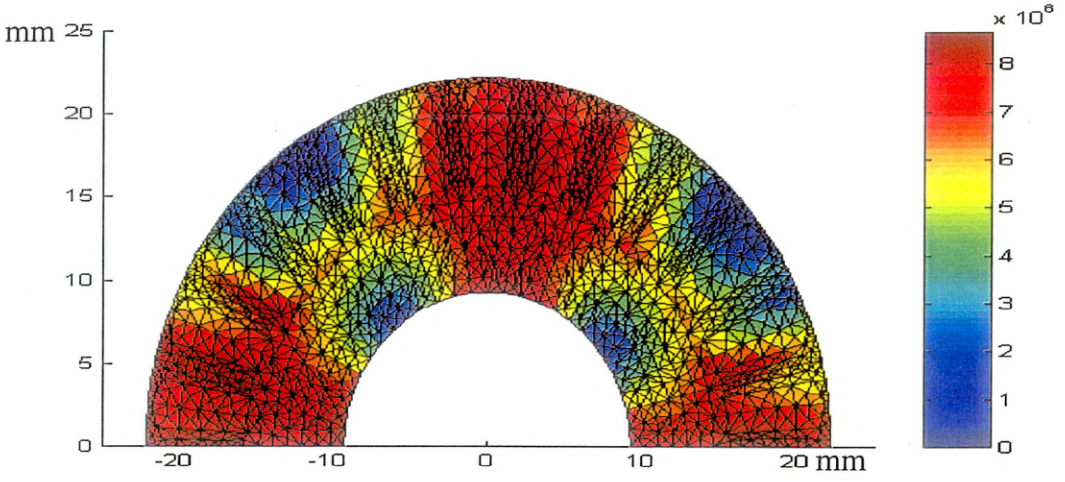

Fig. 4.7 Distribution of Current Density (A/m^2) (CASE A)

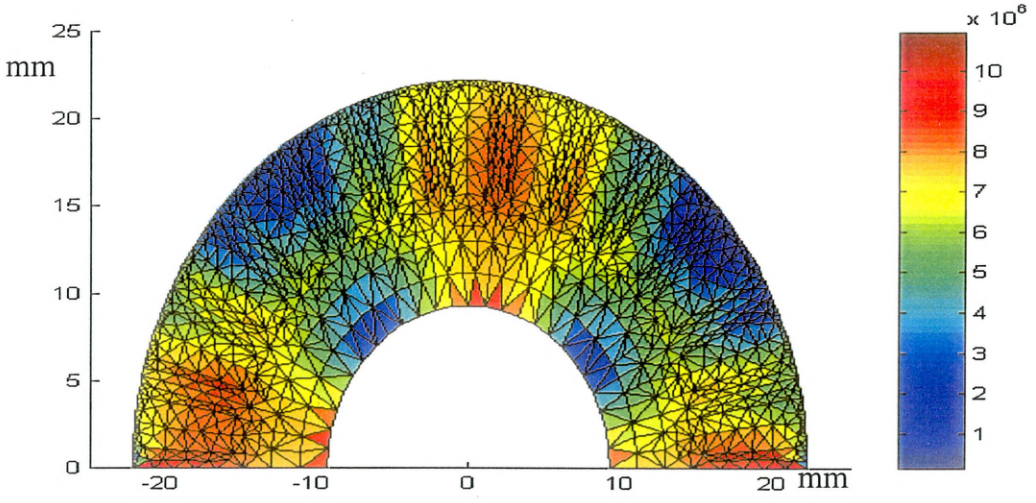

Fig. 4.8 Distribution of Current Density (A/m^2) (CASE B)

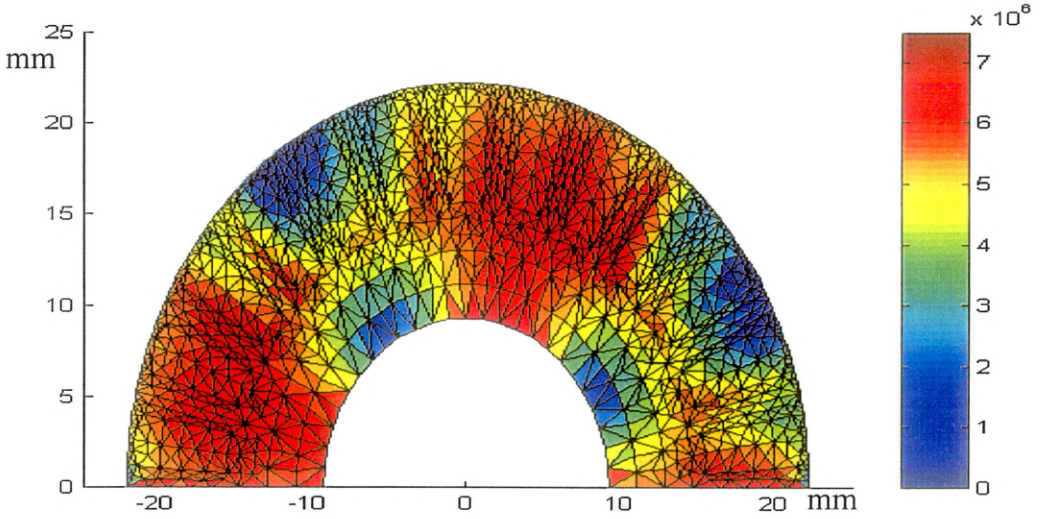

Fig. 4.9 Distribution of Current Density (A/m^2) (CASE C)

From the results shown in Table 4.1, Table 4.2 and Table 4.3, one can see that the variation of the end-ring resistance, $R_{e,i}$, along the circumferential direction is significant, even when the rotor-bar current is of sinusoidal distribution. The resistance, $R_{e,i}$, is determined by the distribution of the end-ring currents and should not be consiered as an uniform value

On the other hand, by comparing Table 4.1 and Table 4.2, it is found that the accuracy of the end-ring resistance calculated by the finite element method depends on the mesh size. Nevertheless, from the comparison between the end-ring resistance and the columnn *err* in Table 4.2, it can be seen that the difference in the calculated resistance between the two meshes is still in the acceptable range.

4.3.2 Coupling Calculation of End-Ring Resistance with 2D Multi-Slice FE Model

In this section, the end-ring resistance calculated by the finite element method will combine with the magnetic field analysis using the 2D multi-slice time-stepping FE model of the SPIM.

When the finite element model was applied for calculating the end-ring resistance in the previous section, the distribution of the rotor-bar current is assumed to be known. However, before the end-ring resistance has been evaluated, $R_{e,i}$, one of parameters in equivalent circuit of the rotor bar [Fig. 4.4], is undefined. Thus, the current in each rotor bar, i_b, cannot be determined. The calculation of the end-ring resistance and computing the magnetic field are coupled and should be solved at the same time.

In order to avoid too huge final global equations due to directly coupling the electrical field with the magnetic field and external circuit equations, an indirect coupling algorithm is employed in this study. The iteration procedure can be briefly described as follows.

1. Give an initial value of $R_{e,i}$.
2. Evaluate the magnetic field and external circuit equation to obtain the rotor-bar current $i_{e,i}$ by using the multi-slice finite element model.
3. Solve the electrical field of the end-ring with the current distribution obtained in step two. A new $R'_{e,i}$ is computed according to (4.28).
4. Replace $R_{e,i}$ in the rotor circuit with new $R'_{e,i}$, evaluate the magnetic field and external circuit equation again as step two so that a new rotor-bar current $i'_{e,i}$ is obtained.
5. Compare $i'_{e,i}$ with the original $i_{e,i}$. If the error between two values is in the acceptable range, the iteration is stopped. Otherwise, go back to step two with the new $R_{e,i}$ and $i_{e,i}$ according to the following equations.

$$\begin{cases} i_{e,i} = i'_{e,i} \\ R_{e,i} = \alpha * R'_{e,i} + (1-\alpha) R_{e,i} \qquad \alpha = 0.618 \end{cases} \tag{4.29}$$

The error of currents for all the rotor bars is given by

$$\varepsilon = \sum_{i=1}^{N} \left| \frac{i_{e,i} - i'_{e,i}}{i_{e,i}} \right| \times 100\% . \tag{4.30}$$

In the earlier discussion, the end-ring resistance R_e was always considered uniform in the rotor circuit, but in the above iteration procedure a new rotor circuit with the non-uniform end-ring resistance is required and is derived in this section first.

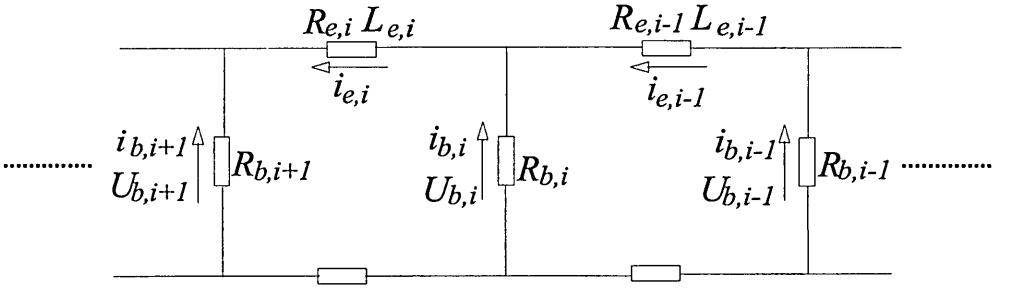

Fig. 4.10 Equivalent circuit model with non-uniform resistance of end-ring

Except for the non-uniform end-ring resistance $R_{e,i}$, the new equivalent rotor circuit shown in Fig. 4.10 is the same as the common model discussed in the previous chapter. $R_{e,i}$ and $L_{e,i}$ are the end-ring resistance and reactance between two adjacent rotor bars, bar i and $i+1$, and they have different values for different portions of the end-ring.

According to Kirchhoff's law, for the bar i, the following equations are obtained.

$$\begin{cases} V_{e,i} = -\dfrac{1}{2}(V_{b,i} - V_{b,i+1}) \\ i_{b,i} = i_{e,i} - i_{e,i-1} \\ V_{e,i} = i_{e,i}R_{e,i} + L_{e,i}\dfrac{di_{e,i}}{dt} \end{cases} \tag{4.31}$$

By applying the Backward Difference method at step $n+1$, the last equation in (4.31) is time-discretized and becomes,

$$i_{e,i}^{(n+1)} = \frac{\Delta t V_{r,i}^{(n+1)} + L_{e,i} i_{e,i}^{(n)}}{(\Delta t R_{e,i} + L_{e,i})}. \tag{4.31c}$$

For the whole rotor cage, the circuit equation is

$$\begin{cases} \{V_e\}^{(n+1)} = -\dfrac{1}{2}[M]\{V_b\}^{(n+1)} \\ \{I_b\}^{(n+1)} = [M]^T\{I_e\}^{(n+1)} \\ \{I_e\}^{(n+1)} = [ER]\{V_e\}^{(n+1)} + [ERL]\{I_e\}^{(n)} \end{cases} \tag{4.32a,b,c}$$

where $[ER] = \begin{pmatrix} ER_1 & & & & \\ & ER_2 & \ddots & & \\ & & \ddots & \ddots & \\ & & & & ER_n \end{pmatrix}$ and $[ERL] = \begin{pmatrix} ERL_1 & & & & \\ & ERL_2 & \ddots & & \\ & & \ddots & \ddots & \\ & & & & ERL_n \end{pmatrix}$.

and the elements in matrix $[ER]$ and $[ERL]$ are evaluated by the following two equations respectively.

$$ER_i = \frac{\Delta t}{(\Delta t R_{e,i} + L_{e,i})} \tag{4.33a}$$

$$ERL_i = \frac{L_{e,i}}{(\Delta t R_{e,i} + L_{e,i})} \tag{4.33b}$$

Combing (4.32a), (4.32b) and (4.32c), the term $[\mathbf{I_e}]$ and $[\mathbf{V_e}]$ can be eliminated. The rotor-bar current $[\mathbf{I_b}]$ is defined by the bar terminal potential difference $[\mathbf{V_b}]$.

$$\{\mathbf{I_b}\}^{(n+1)} = \frac{-1}{2}[\mathbf{M}]^T[\mathbf{ER}][\mathbf{M}]\{\mathbf{V_b}\}^{(n+1)} + [\mathbf{M}]^T[\mathbf{ERL}]\{\mathbf{I_e}\}^{(n)} \tag{4.34}$$

where $[M]^T[ER][M] = \begin{pmatrix} ER_1 + ER_n & -ER_1 & & & -ER_n \\ -ER_1 & ER_1 + ER_2 & -ER_2 & & \\ & -ER_2 & \ddots & \ddots & \\ & & & \ddots & -ER_{n-1} \\ -ER_n & & & -ER_{n-1} & ER_{n-1} + ER_n \end{pmatrix}$ and

$$[\mathbf{M}]^T[\mathbf{ERL}] = \begin{pmatrix} ERL_1 & 0 & & & -ERL_n \\ -ERL_1 & ERL_2 & 0 & & \\ & -ERL_2 & \ddots & \ddots & \\ & & & \ddots & \\ & & & -ERL_{n-1} & ERL_n \end{pmatrix}$$

Here, if the resistances and the reactances are considered uniform, the equation will be the same as (3.27).

For the 2D multi-slice model, (4.34) can be rewritten as

$$\begin{aligned} \{\mathbf{I_b}\}^{(n+1)} &= \{\mathbf{I}_b^{S1}\}^{(n+1)} = \{\mathbf{I}_b^{S2}\}^{(n+1)} \ldots = \{\mathbf{I}_b^{Ms}\}^{(n+1)} \\ &= \left(\frac{-1}{2}[\mathbf{M}]^T[\mathbf{ER}][\mathbf{M}]\sum_{Si=1}^{Ms}\{\mathbf{V}_b^{Si}\}^{(n+1)} + [\mathbf{M}]^T[\mathbf{ERL}]\{\mathbf{I_e}\}^{(n)}\right) \end{aligned} \tag{4.35}$$

Since the rotor-bar area is in the magnetic field, the rotor-bar current can be also determined by the vector potential and terminal voltage by (3.26) or (4.16). Thus, after submitting (4.34) into (3.26) or (4.16), the rotor-bar current can be eliminated from the final system equation.

When the non-uniform end-ring resistance is taken into account, the final system equation of the 2D multi-slice model, which couples the magnetic field equation and external

circuit equations, is similar to (4.19) in which the end-ring resistance is considered uniform, but $\mathbf{Y}_{i,j}$ and $\{\mathbf{N}_b^{Si}\}$ in equation (4.19) should be modified according to following equations.

$$\mathbf{Y}_{i,j} = \begin{cases} \frac{1}{2}[\mathbf{M}]^T[\mathbf{ER}][\mathbf{M}] + \frac{[\mathbf{U}]}{R_{b,}^{Si}} & i = j \\ \frac{1}{2}[\mathbf{M}]^T[\mathbf{ER}][\mathbf{M}] & i \neq j \end{cases} \tag{4.36a}$$

$$\{\mathbf{N}_b^{Si}\} = \frac{1}{l_z^{Si}}\left(-[\mathbf{Q}^{Si}]^T\{\mathbf{A}^{Si}\}^{(n)} + \Delta t[\mathbf{M}]^T[\mathbf{ERL}]\{\mathbf{I}_e\}^{(n)}\right) \tag{4.36b}$$

Using the proposed coupling algorithm and modified rotor circuit equation, the time-stepping finite element model of SPIMs using non-uniform end-ring resistance can now be investigated.

First, this model was used to examine the variation in end-ring resistance with time. When the time-stepping method is adopted, the distribution of rotor-bar currents can be decided with the proposed model at each time step, so the variation of resistance between the same adjacent bars can be also determined. Fig. 4.12 shows the variation of instantaneous resistance with time in the rotor-locked state with model T. It is seen that the scale of end-ring resistance variation with time is quite significant.

By using the model with non-uniform end-ring resistance, it was found that the coupling procedure usually converges after three or four times iteration. Consequently, for each time step, both the magnetic field of SPIMs and the electrical field of end-rings had to be repeated three or four times, so the computing cost due to using the non-uniform resistance model increased quite significantly. In order to reduce the computing cost, a simplified approach was presented. According to this approach, at each time step, the rotor-bar currents are first determined by using the end-ring resistance of the last time step. After comparing the variation of rotor-bar currents between two steps, the iteration procedure is started only when the rotor-bar currents vary violently. If the time-step is not big enough, only one calculation is usually needed. Therefore, the new approach does not need more time than the normal time-stepping method does.

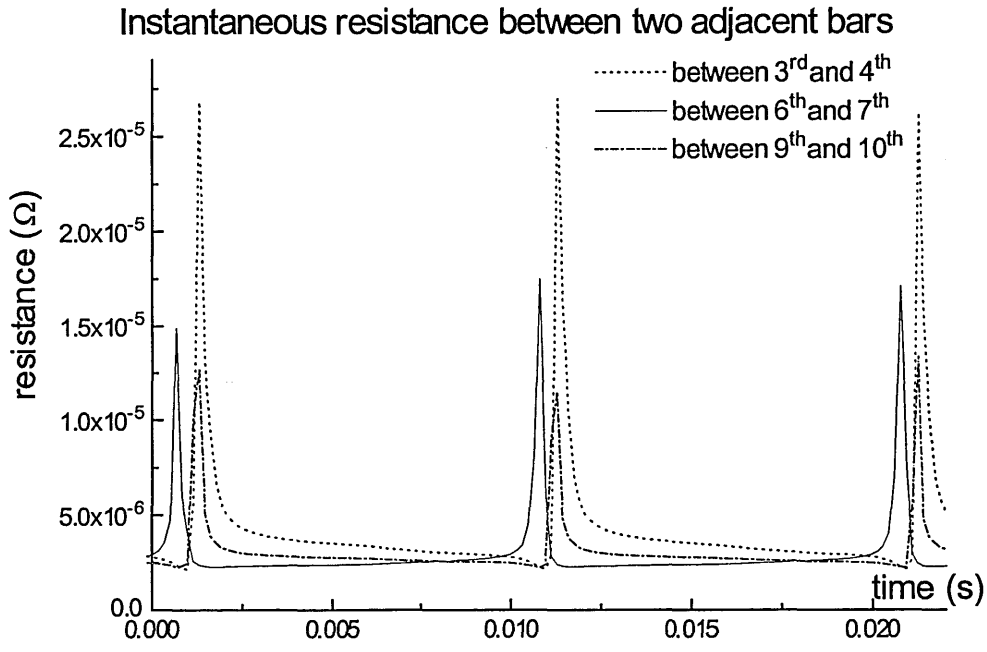

Fig. 4.11 Variation of instantaneous resistance among different bars with time (Model T in the rotor-locked state)

To learn the effect of the proposed model on the performance evaluation, the results for the stator current and output torque are compared with that of the model with uniform end-ring resistance and that of the simplified approach.

Comparing the results obtained with different end-ring resistance models in 2D situation (non-skew), which is shown in Fig. 4.12 to Fig. 4.13, one can see that:

1. The torque is very sensitive to the calculation model used for the end-ring resistance. The maximum torque obtained with the non-uniform end-ring resistance model is 10% more than that obtained by normal uniform resistance model,
2. The model for the end-ring resistance does not make a considerable difference on the stator current. The three curves resulting from the different models overlap each other in the whole speed range,
3. The simplified method is in good agreement with the iteration procedure in most situations.

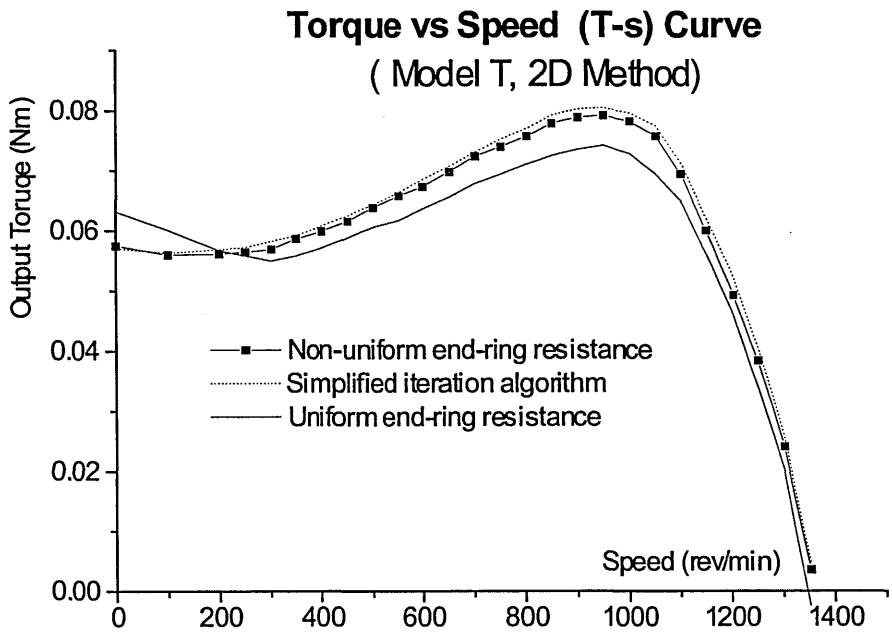

Fig. 4.12 Variation of output torque with speed (Model T)

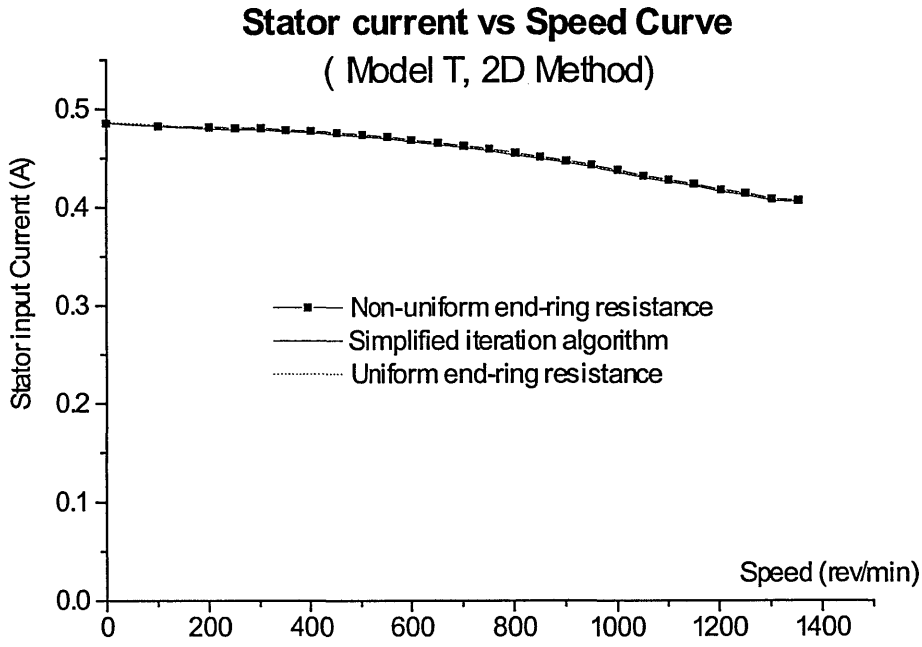

Fig. 4.13 Variation of stator current with speed (Model T)

The notable difference on the torque/speed performance of SPIMs resulting from the different end-ring models is due to the damping effect of end-ring resistance on the rotor

current harmonics. It is known that the end-ring resistance depends not only on the physical dimension but also on the distribution pattern of the end-ring current. For the machines with the same size end-ring, the end-ring resistance is different for the machines with different poles. The same end-ring presents a larger resistance for high-order rotor current harmonics [Williamson 1986]. Using a 3D time-stepping finite element method to study the effect of the end-ring [Kometani, 1996], it was also found that the ratios of the harmonic to the fundamental current of the rotor end-ring are reduced due to the effect of variable resistance on the harmonics. If the uniform end-ring resistance model is used, the damping action of the end-ring resistance on harmonic currents cannot be take into account. Therefore the torque obtained with the uniform end-ring resistance model may decrease because of over-estimating the harmonic current and torque.

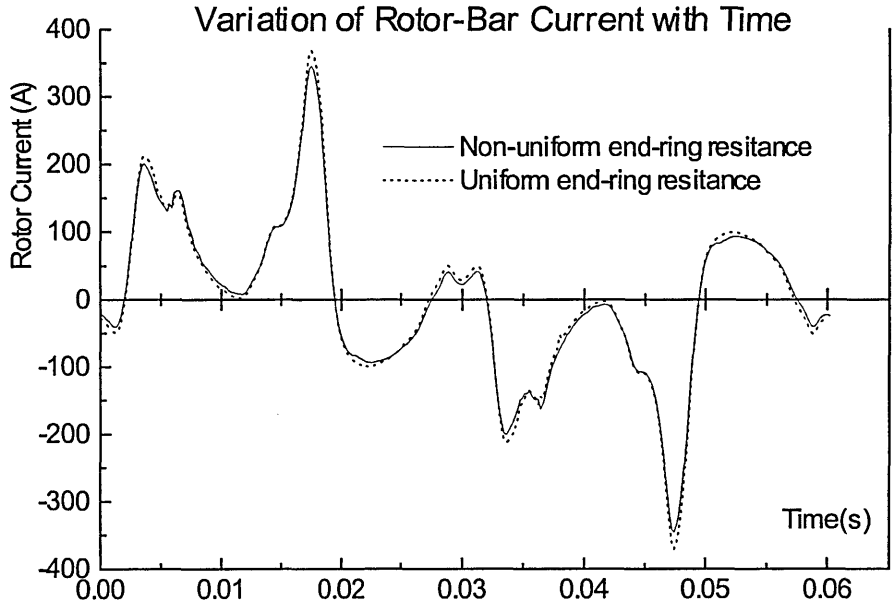

Fig. 4.14 Variation of rotor-bar current with time (Model T at 1000rev /min)

To check the effect of end-ring resistance on the harmonics, the variation of the rotor-bar current with time was studied. Fig.4.14 shows the difference between the results obtained using different end-ring models. In order to know harmonic distribution of the rotor bar current, the DFT analysis is applied. The major harmonic components obtained by the non-uniform end-ring resistance model are compared with those by the uniform end-ring resistance model. The variation of each harmonic is given in Table 4.4. Additionally, the

total harmonic distortion (THD) and the distortion factor (DF) for the different model were also calculated and are given in Table 4.5. The definition and methods of calculating THD and DF are given in Chapter 5.

Table 4.4 Harmonic components variation for the two different end-ring resistance models (Model T at 1000rev /min)

	Frequency(Hz)	Variation(%)
Fundamental(Forward)	16.6	+7.13
Fundamental(Backward)	83.1	-4.34
3^{rd} order (Forward)	49.8	+5.83
3^{rd} order (Backward)	149.5	-4.62
5^{th} order (Forward)	116.3	-12.8
5^{th} order (Backward)	216.0	-4.95
7^{th} order (Forward)	182.7	+1.6
7^{th} order (Backward)	282.4	-3.9
9^{th} order (Forward)	249.2	-3.98

* The result of the uniform end-ring resistance model is set as the criterion

Table 4.5 The THD and DF of rotor current for different end-ring resistance models

	THD	DF
Uniform end-ring resistance model	3.3070	0.1107
Non-uniform end-ring resistance model	3.1353	0.1050

From Table 4.4 and Table 4.5, it can be seen that, by using non-uniform end-ring resistance model, the fundamental forward component is increased and the harmonics in the rotor current are weakened. These results prove that the damping effect of end-ring on higher order harmonics can be taken into account by using the non-end-ring resistance model.

Nevertheless, if the harmonics are eliminated by a skewed rotor, the damping effect of the end-ring on the harmonics becomes small. Fig.4.15 shows the comparison of output

torque between the different end-ring models by using the 2D multi-slice finite element method. The differences between the three models are not as significant as under non-skew condition. Therefore, for normal three-phase induction motors in which most of the harmonics have been eliminated, the torque results are still in the acceptable accuracy range even if the non-uniform end-ring resistance is not considered.

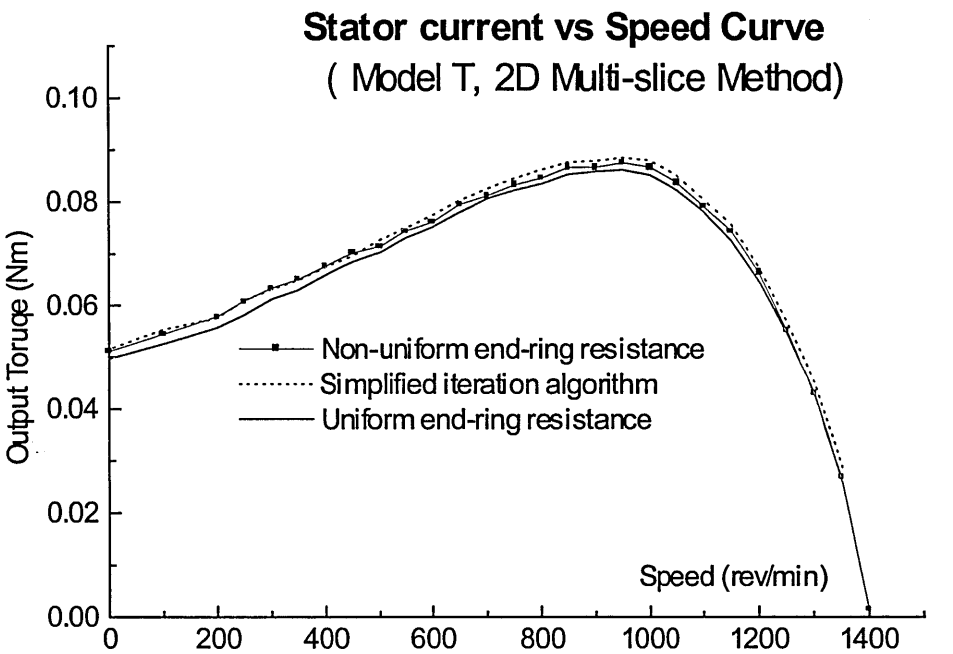

Fig. 4.15 Variation of output torque with speed (Model T)

4. 4 Verifying the 2D multi-slice FE Model of SPIM by Experiment

In order to verify the validity of the 2D multi-slice finite element model with non-uniform end-ring resistance described in the previous section, in this section this model is applied to evaluate the steady state performance and to simulate the transient process of two different designed SPIMs, Model T and Model R, which are both 220V, 50Hz, 50W, 4-pole. Since the number of rotor bars of both motors is not an integer in a quarter model (Model T has 26 rotor slots and Model R has 22), the basic finite elements meshes, which are manually generated, shown in Fig. 4.16 have to span a full pole pitch in both models used.

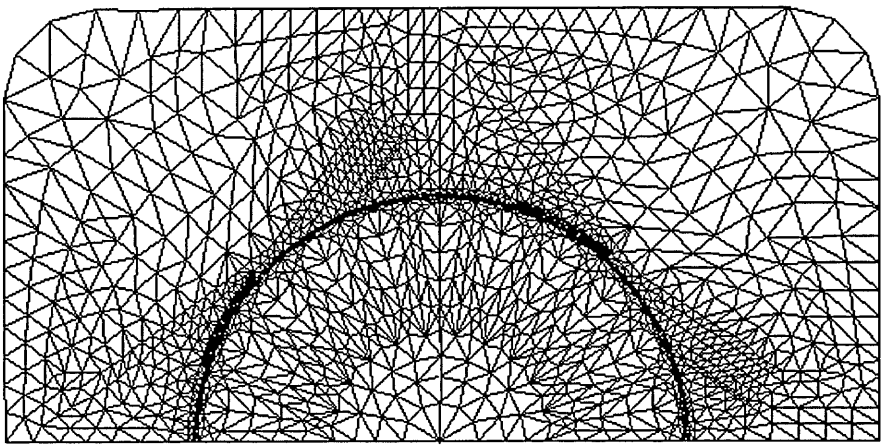

Fig. 4.16a Finite elements mesh of Model R
(1427 nodes, 2764 elements, skew 56 electrical degree)

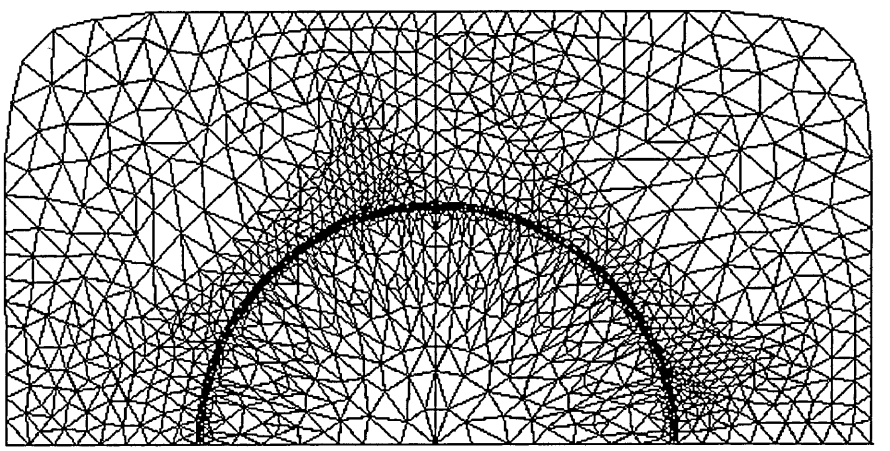

Fig. 4.16b Finite elements mesh of Model T
(1709 nodes, 3322 elements, skew 48 electrical degree)

To measure both steady and transient performances, a PC-based data acquisition system was employed whose principle will be introduced in Chapter 7.2. With this test rig, the signals of the supply voltage, the stator current, the rotor speed and mechanical torque are all fed into a PC. The sampling rate of the current and voltage is 5KHz. In the test rig, the torque and speed are converted into DC voltage signals by using a torque/speed transducer mounted on the same shaft of the SPIM. To eliminate resonance and other forms of interference coming from the coupling of mechanical elements, a low-pass filter was introduced in the torque signal conditioning circuit in the transducer. The cut-off

frequency of the filter is set at 1kHz.

With the multi-slice FE model, the variation of the flux distribution variation along the axial direction of the motor due to the skewed rotor can be clearly observed in the flux plot of three slices in one simulation time. The difference between each slice shown in Fig. 4.17 can be considered as useful evidence for proving the necessity for the multi-slice model.

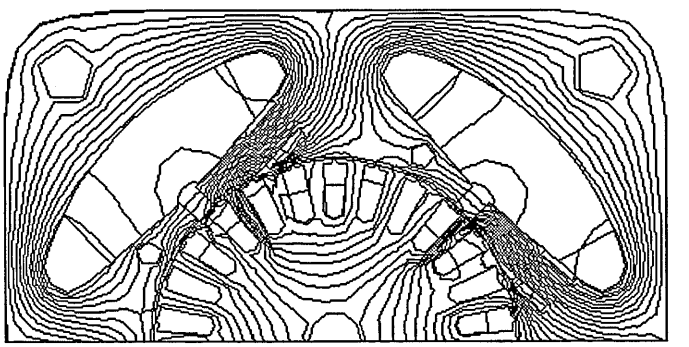

a) 1st Slice

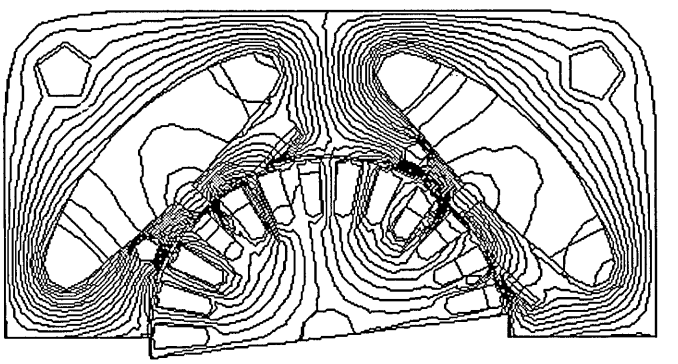

b) 2nd Slice

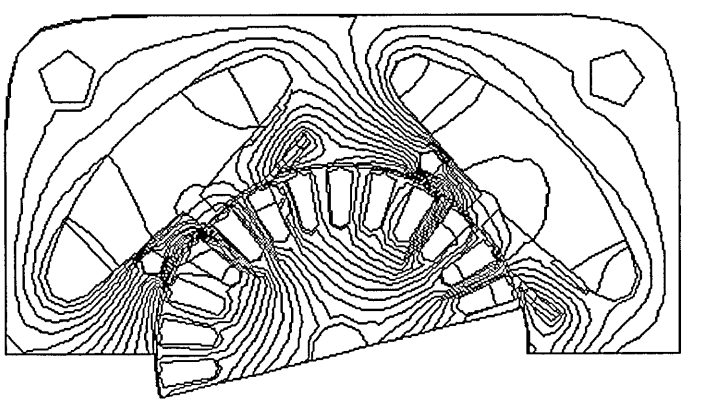

c) 3rd Slice

Fig. 4.17 Computed flux distrubion under locked-rotor state (Model T)
($\omega t = 262.7^{o}$, U=-308.6V, i_C= 0.645A, I_{S1}=-258.9A, I_{S2}= -263.4A)

As well as the information about the flux distribution, the external characteristics, such as the torque, currents of the stator coil and shaded-rings, are usually of more concern to the designer. To estimate the accuracy of the 2D multi-slice approach, a 2D model ignoring the skew of the rotor conductors was also applied to both model T and model R.

First, the current and torque variations with time under locked rotor conditions obtained by the different models are shown in Fig. 4.18 and Fig. 4.19. Because the simulating programs are time-stepped and switched on at zero voltage point, the switch transient phenomena can be clearly observed in the first few cycles in Fig. 3-5. Although Williamson [1981] suggested there was no twice-line-frequency pulsating torque in the starting point, in our result the pulsating torque can be observed when the switch transient disappears.

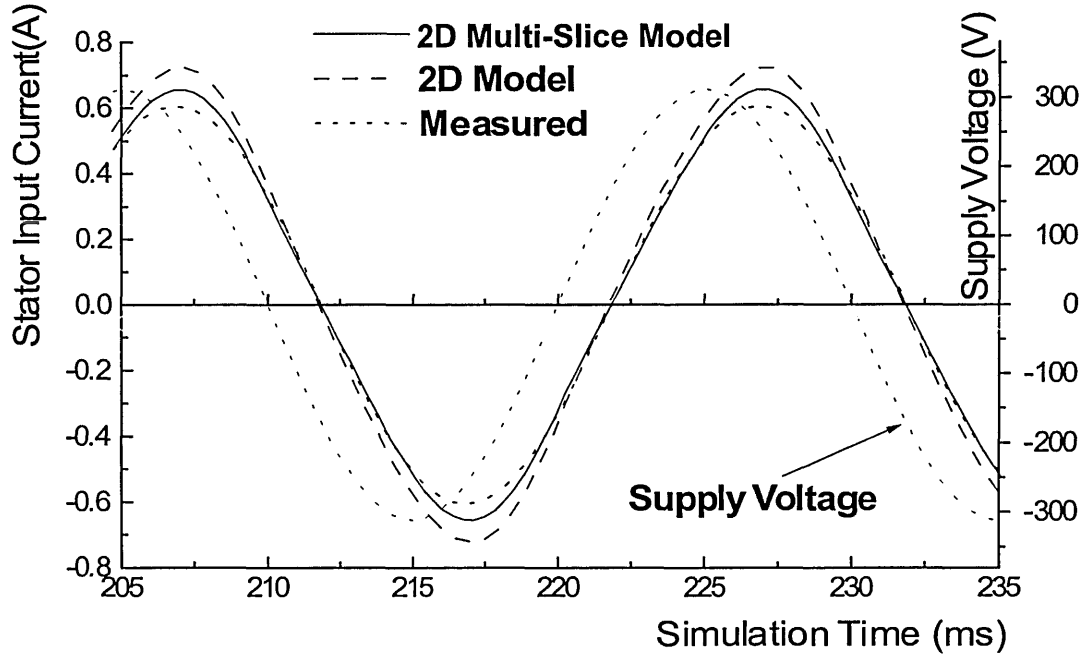

Fig. 4.18 Waveforms of stator current with time under locked rotor condition (model T)

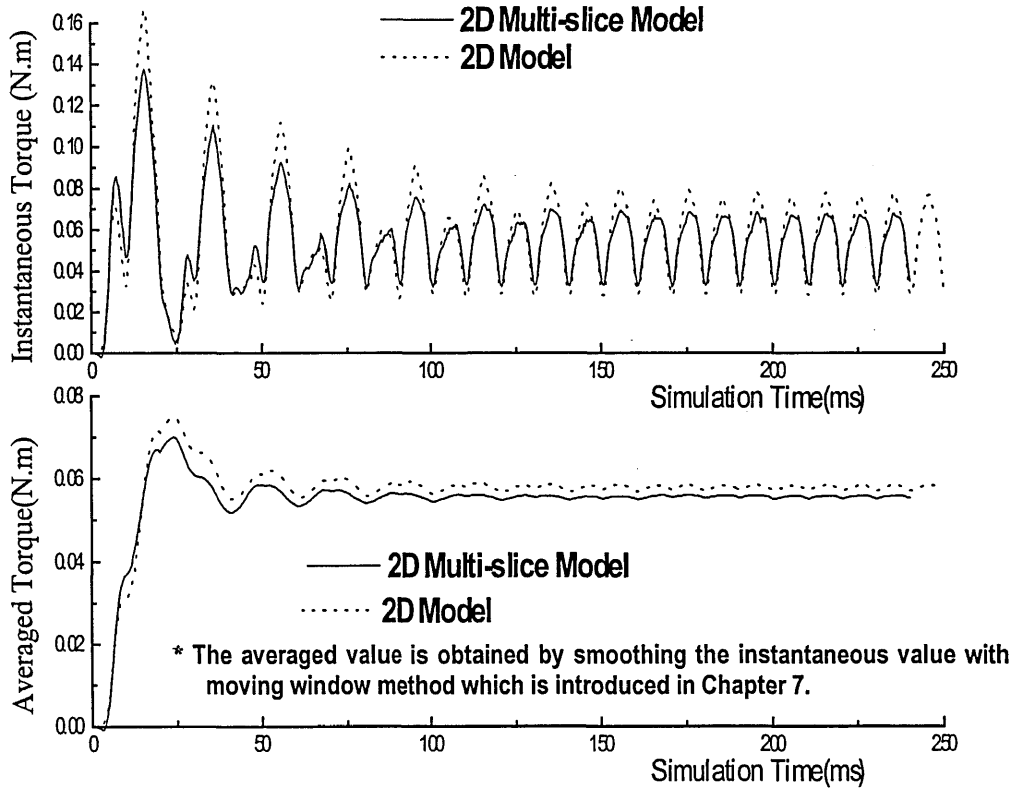

Fig. 4.19 Waveforms of torque with time under locked rotor conditions (Model T)

Since the result obtained with the time-stepping method is the instantaneous value, to calculate the steady torque as read by a normal torque measurement meter, the instantaneous torque is averaged by a moving window with fixed length 20ms. The detail of the moving window averaging method can be found in Chapter 7. It can be seen in Fig. 4.19 that the averaged torque tends to stable after several cycles. The same averaging procedures can also be applied to currents except that the currents are the averaged value of root-mean-square. With the simulations at different speeds, the current and torque variations of SPIMs with speed in the steady state are obtained. The results are shown in Fig. 4.20 and Fig. 4.21, along with experimentally measured characteristics.

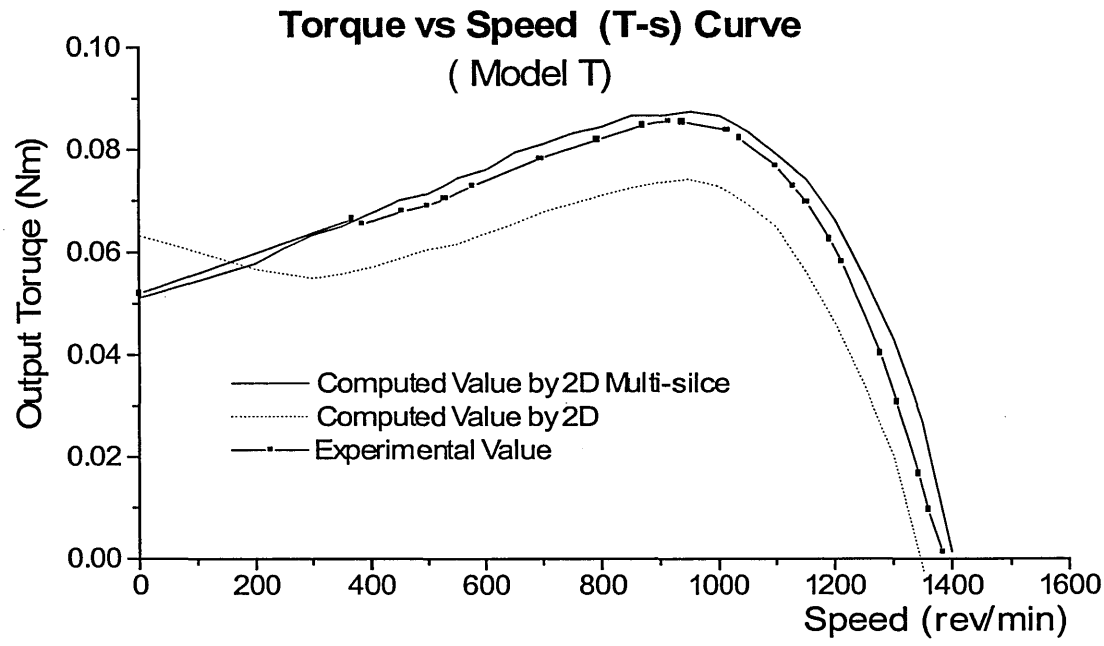

Fig. 4.20a Output torque variation with different speed in the steady state (Model T)

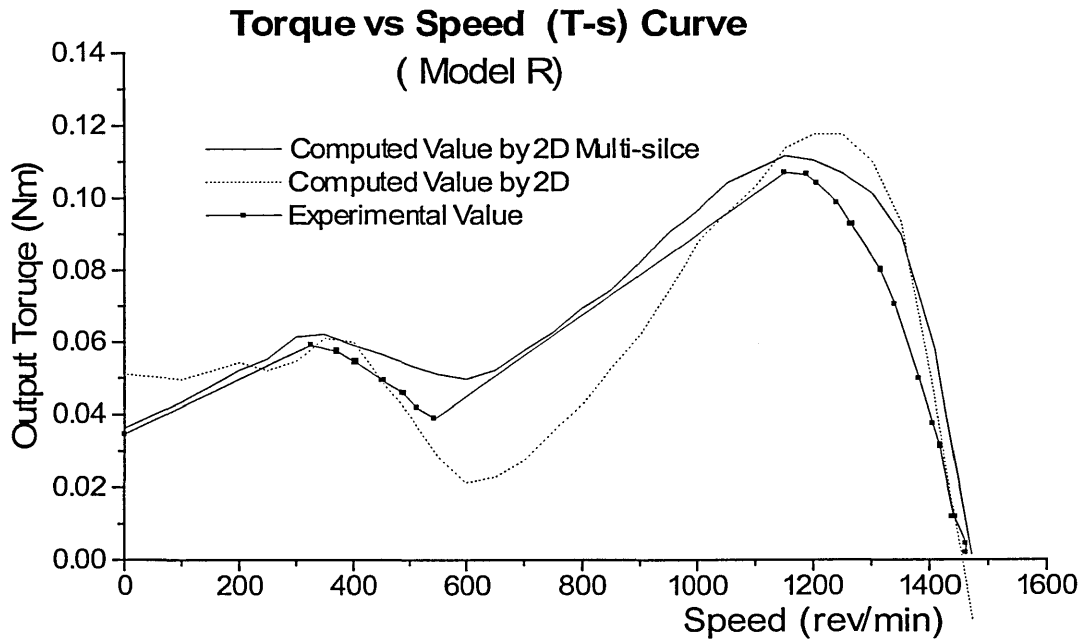

Fig. 4.20b Output torque variation with different speed in the steady state (Model R)

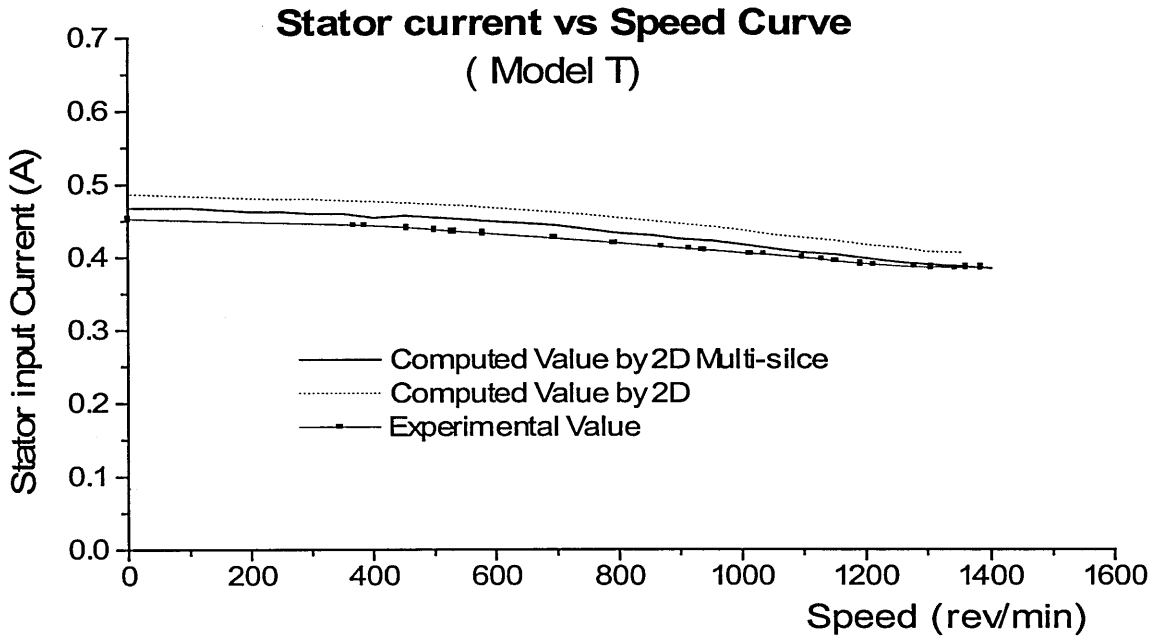

Fig. 4.21a Stator input current variation with different speed in the steady state (Model T)

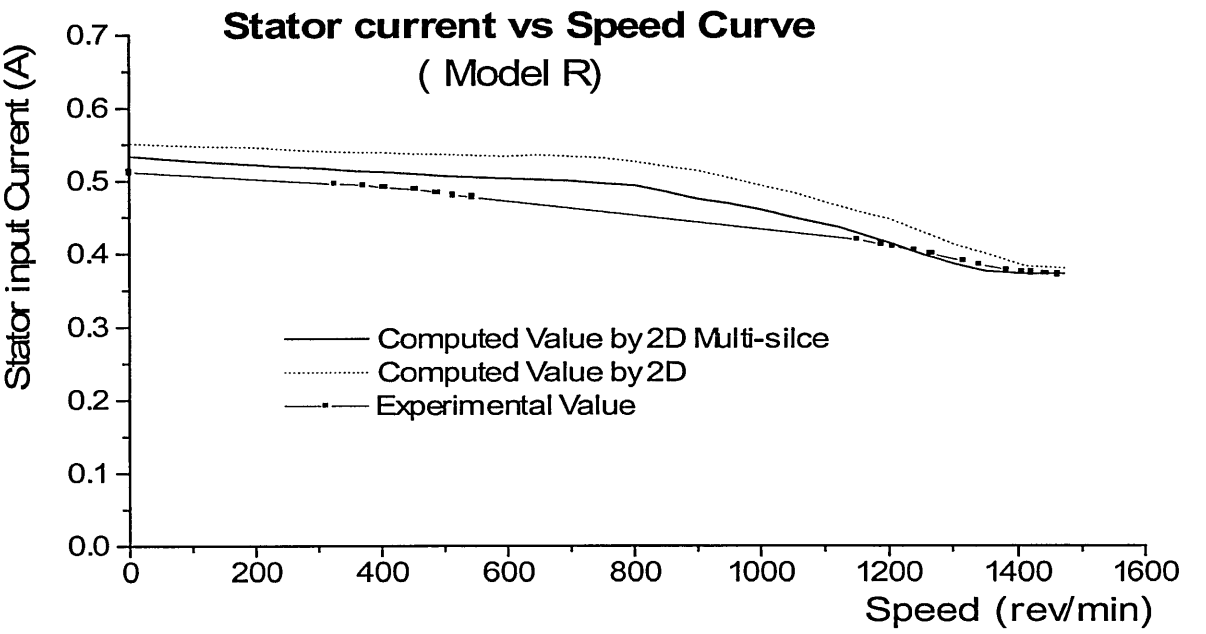

Fig. 4.21b Stator input current variation with different speed in the steady state (model R)

The results shown in Fig. 4.20 and Fig. 4.21 confirm that the 2D multi-slice model produces a better simulation result than the conventional 2D modelling.

Besides the steady performance, the transient performance during the starting process of Model T was studied as well. The variation of the stator current, the shaded-ring current, the torque and speed under free acceleration conditions with no-load are shown in Fig.4.22 to Fig. 4.26. The supply voltage is switched on randomly at the 50^{O} point on wave. Since the direct experimental verification of the shaded-ring current is not available, only the simulation result is shown in Fig. 4.23.

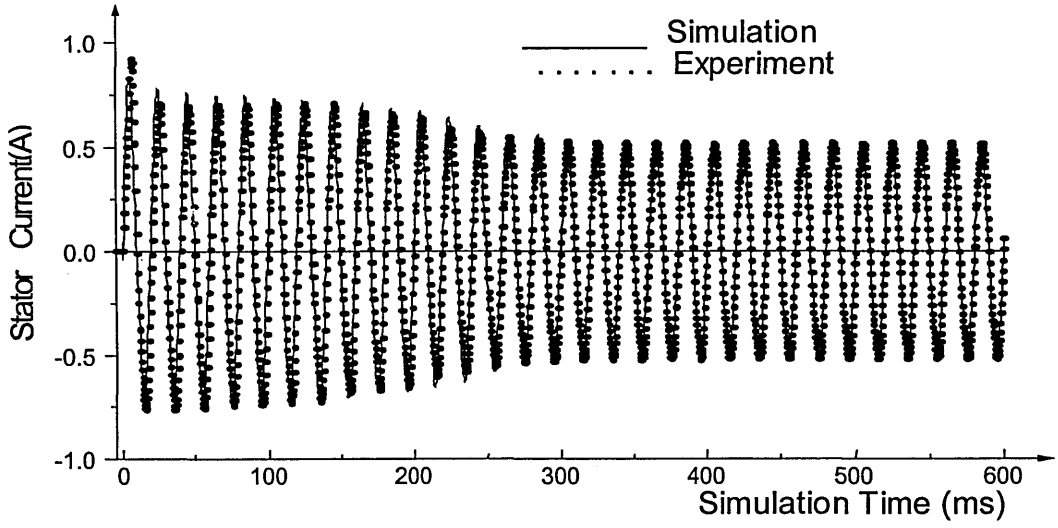

Fig. 4.22 Stator Current /Time curve (Model T)

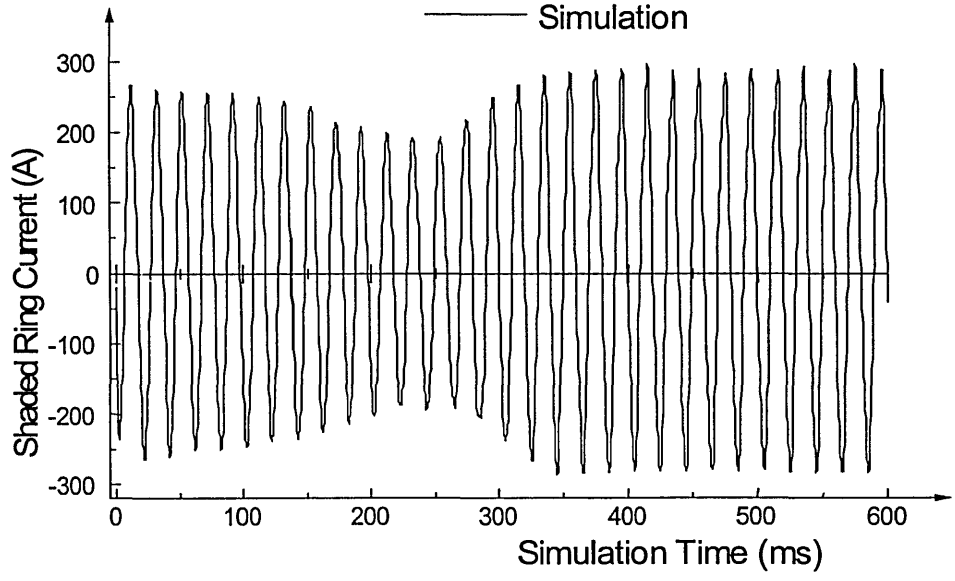

Fig. 4.23 Shaded-ring Current /Time curve (Model T)

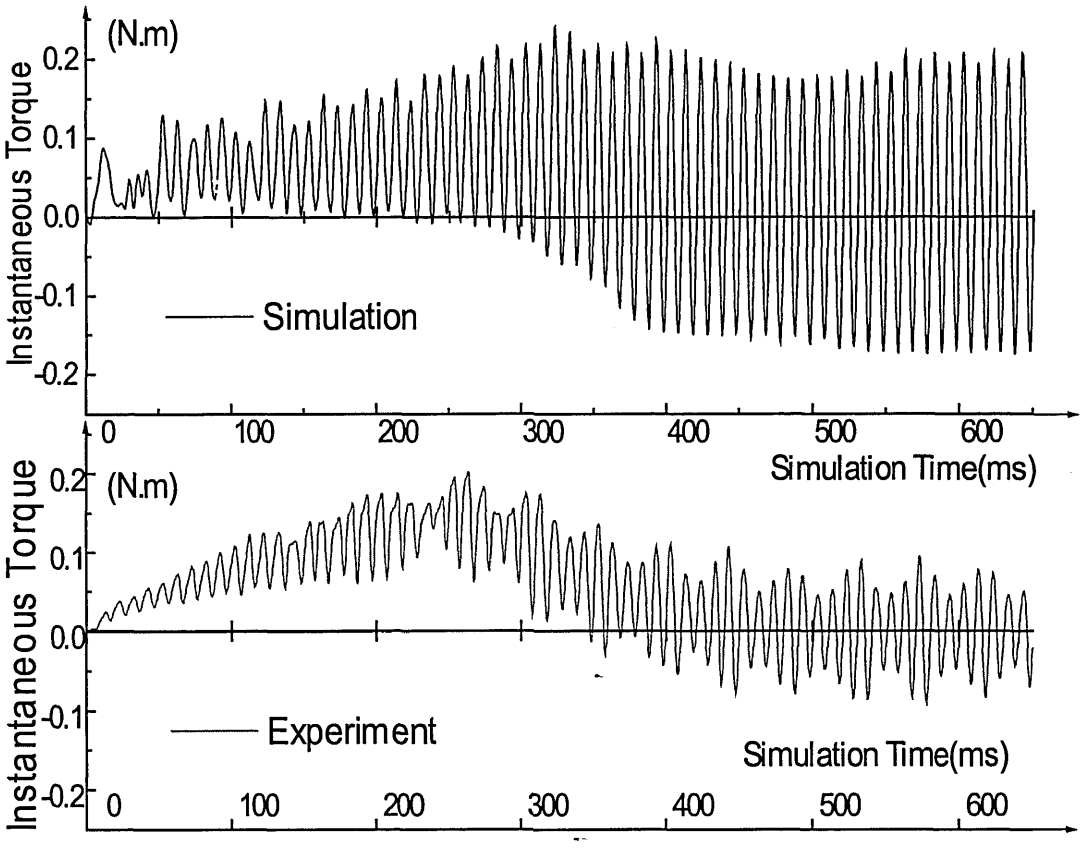

Fig. 4.24 The Instantaneous Torque /Time curve (Model T)

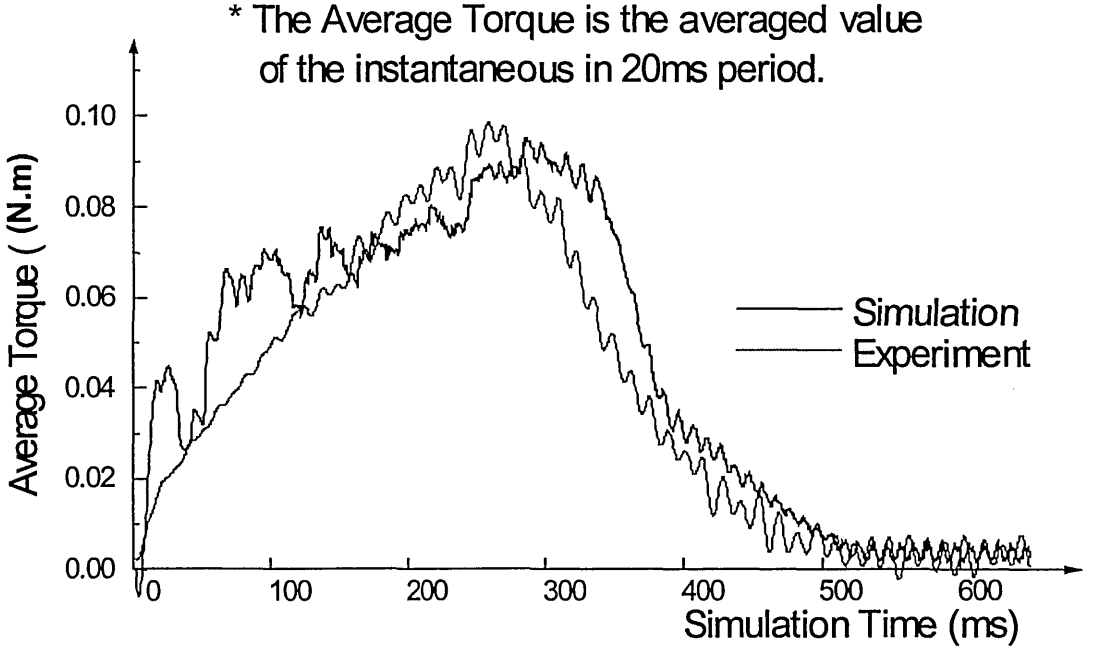

Fig. 4.25 The Averaged Torque /Time curve(Model T)

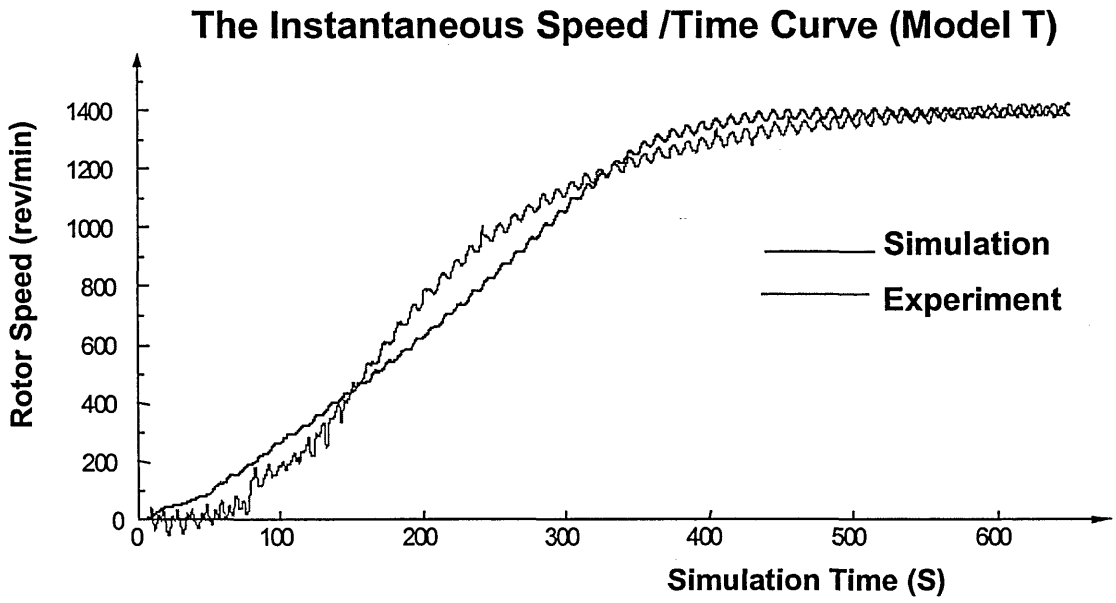

Fig. 4.26 The Instantaneous Speed /Time curve(Model T)

Like other forms of induction motors, the speed of SPIMs sometimes need to be variable in a certain range. The simplest method of speed variation is to adjust the supply voltage. This is easily implemented by using the phase-control scheme with a triac or a pair of thyristors. The control circuit is shown in Fig. 4.27

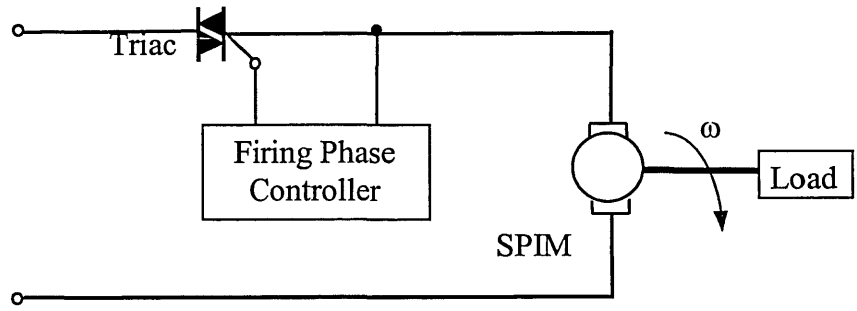

Fig. 4.27 A full-wave voltage phase-control circuit for SPIMs

However, phase-control tends to make the performance analysis of SPIMs more complicated. This is because, besides the abundant space harmonics caused by the asymmetrical stator winding and the non-uniform air gap, the discontinuous source

voltage and input current will introduce time harmonics as well. Lock [1984,1987] presented a step-by-step numerical method of solving the basic differential equation of the rotor circuit. With this method, the air gap irregularities, the skew rotor and the asymmetry stator winding could be taken into account. However the saturation is still neglected and the MMF of the air gap is drawn out directly from the air gap profile. Therefore, for the close-slot rotor or higher saturation, the accuracy of Lock's method is not satisfactory. This disadvantage can also be seen in his results. For the proposed method in this study, both the saturation and the non-sinusoidal supply condition are readily included.

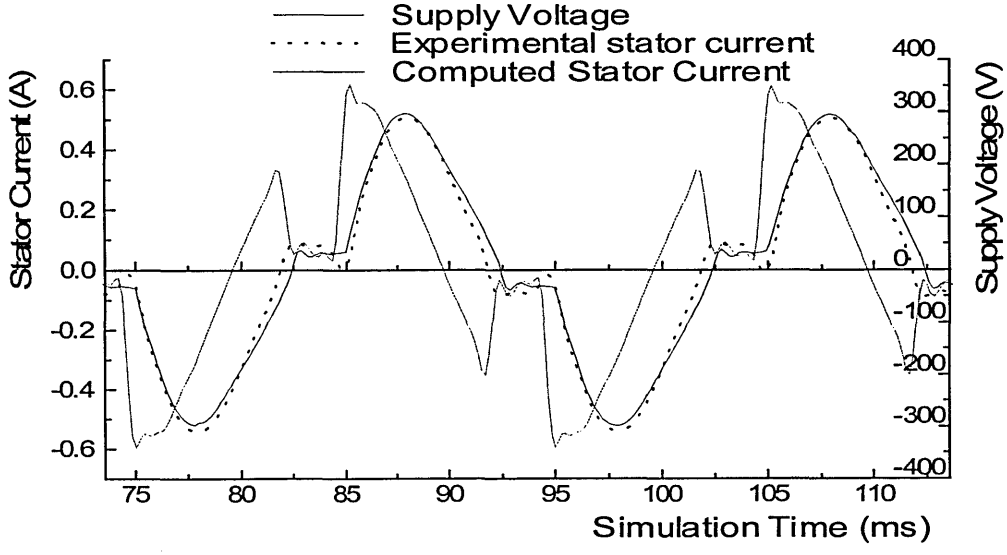

Fig. 4.28 Waveforms of stator current with time under locked rotor condition (Model T)

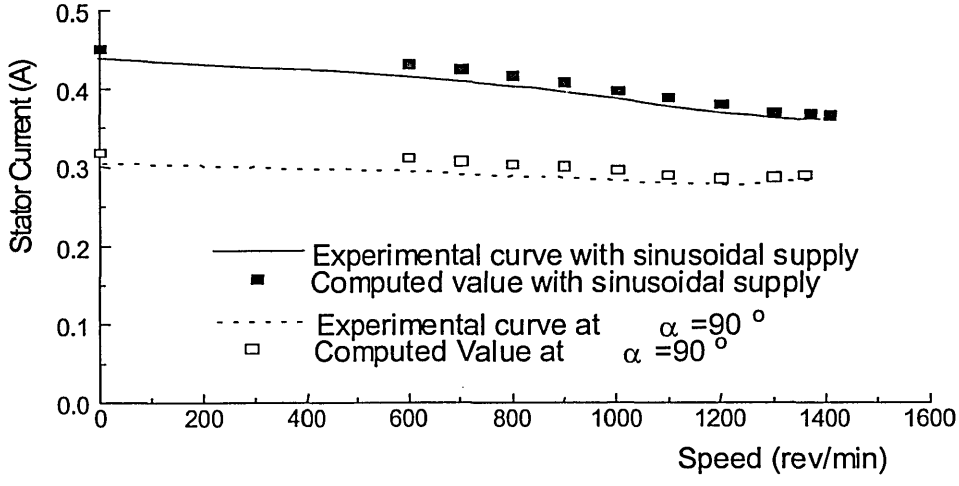

Fig. 4.29 Stator input current variation with speed in the steady state (Model T)

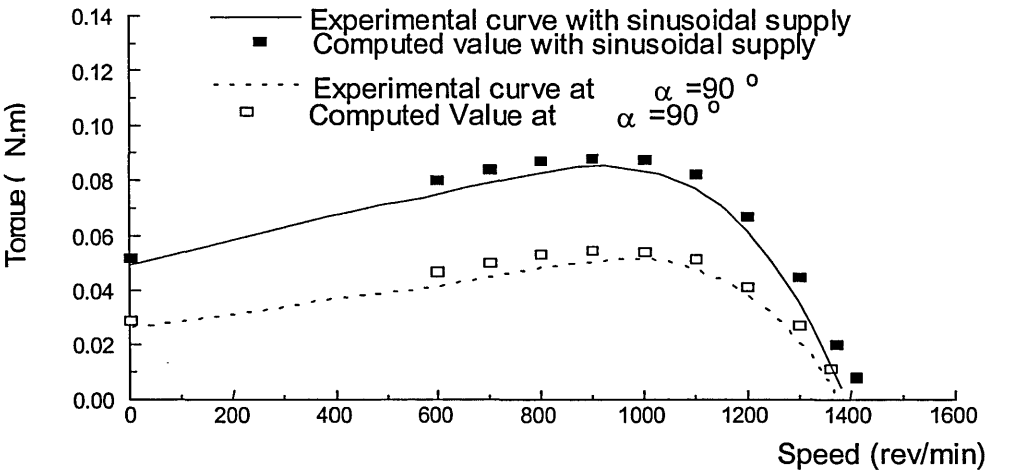

Fig. 4.30 Output torque variation with speed in the steady state (Model T)

From the results presented in this section, it is shown that:

1) with the proposed 2D multi-slice FE model, the skewed rotor, the saturation and the skin effect can all be included directly in the system equation. The rotor end-ring has also been considered;
2) the non-sinusoidal quantities, such as supply voltage, stator current and flux density, can also be properly represented;
3) the accuracy of the results for both the steady and transient state was proved to be very high. Therefore, this technique can replace the more expensive 3D modelling.

4. 5 Conclusion

For the conventional 2D finite element model, the effect of skewed rotor was presented by the skew reactance and the end-ring were roughly taken into account by using the

uniform lumped resistance. In order to improve the accuracy of the finite element model of SPIMs, a 2D multi-slice time-stepping finite element model with the non-uniform end-ring resistance has been proposed in this chapter.

In order to consider the effect of skew, the skewed rotor of SPIMs was divided into a series of un-skewed sections accordingly in the 2D multi-slice model developed. The governing field equations of the multi-slice model for SPIMs has been derived in this chapter. Additionally, the external circuit equations have been coupled with the field equation directly, therefore, the main performances of SPIMs can be obtained once the system equation is solved. By using the time-stepping model, the proposed 2D multi-slice eddy-current FE model can be used to consider all the effects of the skewed rotor, the skin effect, the saturation and the non-sinusoidal quantities directly.

On the other hand, by studying the electric field of the end-ring with the finite element model, it was found that the equivalent end-ring resistances between any two adjacent rotor bars were uneven along the circumferential direction and they changed in a large scale with the variation of the current distribution in the end-ring area. In the conventional 2D finite element model, a uniform end-ring resistance model was usually used to consider the effect of the end-ring. Consequently, the harmonics of rotor currents were always over-estimated because the fact that the end-ring presenting a different resistance to each order harmonic could not be taken into account by using the uniform end-ring resistance model. Thus, the necessity of the non-uniform resistance model was proved in this chapter. Since the end-ring resistance depends on the rotor-bar currents distribution, the procedure for calculating the end-ring resistance was coupled with the magnetic field computation for SPIMs. In order to reduce the computing cost due to coupling end-ring resistance calculation with magnetic field computation, a simplified iteration scheme has been studied. Compared with an ordinary iteration algorithm, the simplified method can keep the result within an acceptably accurate range while its cost in time is significantly reduced. The computing cost of the simplified method is nearly the same as that of the normal time-stepping method with uniform resistance model.

To confirm the validation of the proposed 2D multi-slice finite element model of SPIMs, two different design motors have been investigated. Both the steady state and transient

state were studied. The comparison between the experimental and the computed results showed that the proposed model was superior to the normal 2D finite element model concerning the accuracy of the SPIMs' performance analysis.

5 EFFECT OF PARAMETER VARIATION ON PERFORMANCE OF SPIMS

5. 1 Introduction

It has been demonstrated that the performance characteristics of SPIMs evaluated using the multi-slice finite element model gives good agreement with the test results. In consequence, the effect of parameter variations on the performance of SPIMs, which motor designers usually show more interest in, can be investigated more accurately with this analysis tool developed in previous chapters.

For SPIMs, the starting torque, the maximum torque (breakdown torque), the output power, the input current and efficiency are usually considered as the main performance criteria. According to the existing knowledge for the induction motor design, the essential design parameters for these characteristics can be divided into the following categories:

- stator geometry and stator winding, including turns and winding resistance
- shaded-ring, including shaded-pole arc, resistance of shaded-ring
- rotor resistance
- air gap profile and air gap length
- pole-bridge
- skew
- number of rotor slots and closed-slot rotor

With different equivalent circuit models, many researchers have presented their results on performance changes due to the variation of the design parameters mentioned. Focusing on the starting performance, Trickey [1936] examined the influence of several essential design variables including rotor resistance, shaded-ring resistance, shaded-pole arc and air gap length using his original equivalent circuit model of SPIMs. Thereafter, Butler and Wallace [1969] investigated the effect of major design features, namely, the number of stator winding turns, the total pole arc, the shaded-pole arc, the shaded-ring conductance and the resistance of rotor-bar. Williamson and Breese [1977,1978] studied the effect of various air gap profiles on the characteristics of reluctance-augmented SPIMs. The effect of rotor resistance on both steady state and transient performance was the focal point in Osheiba's paper [1991]. By using optimisation technology, Yokozuka [1983] reported the variation of characteristics with the changes in the equivalent circuit parameters. In Miles' paper [1985], four different equivalent circuit models were used to examine the effect of shaded-arc and shaded-ring resistance on the starting torque of SPIMs. By using a constant saturation factor, S_{fm}, to take the saturation into account, Faiz [1995] studied the effect of air gap length on the performance of this kind of motor.

In fact, these published papers using the equivalent circuit model mainly focused on the first three categories of design parameters. As to the remaining four categories of design parameters, which are closely related to local saturation and harmonics, their effect can be estimated accurately only when the saturation and harmonics are properly taken into account. However, the equivalent circuit models can not satisfy such a demand, so only a few papers studying the effect of the air gap profile [Williamson, 1977, 1978] touched upon these areas by means of traditional methods. With the 2D multi-slice time-stepping FE model, saturation and harmonics can all be taken into account accurately, hence the influence of all the design parameters on SPIMs' performance is able to be properly examined. Therefore, the effect of design parameters belonging to the remaining four categories is studied in this chapter, including air gap profile, the pole-bridge, the skew, the number of rotor slots and the shaded-pole arc.

Additionally, in order to learn the effect of parameter variation on the field harmonics and current harmonics, a harmonic analysis method based on the time-stepping FE method is

first introduced before the detail of the results on predicted performance with varying parameters is given.

5. 2 Harmonic Analysis Based on FE Method

Owing to the stator construction, with its concentrated wound coils fixed around salient poles, the air gap magnetic field distribution of SPIMs contains a great number of spatial harmonics. Consequently, a set of harmonics is induced in the rotor-bar currents. Both the magnetic field spatial harmonics and the rotor-bar current time harmonics play the very important roles on the motor performances. Fig.5.1 shows the torque component resulting mainly from the fundamental and dominate harmonic components (both forward- and backward rotating components) in a 4-pole SPIM.

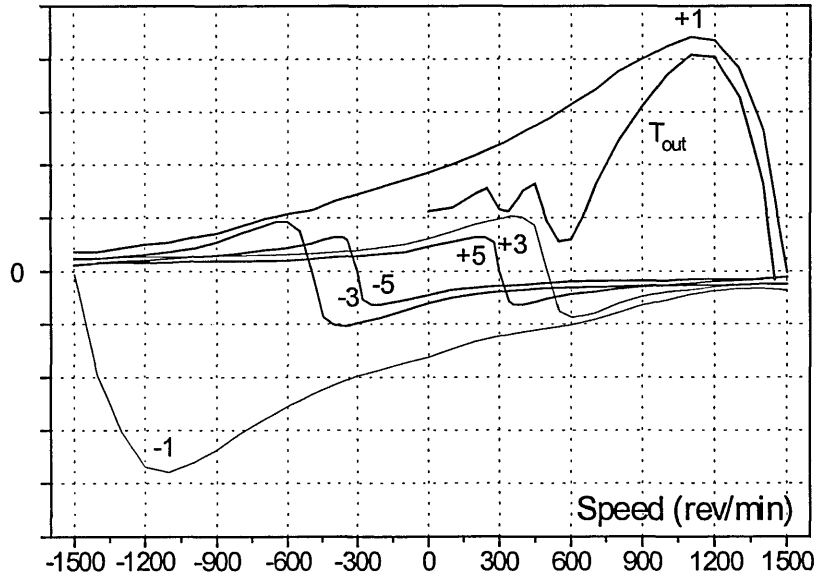

Fig. 5.1 Fundamental and harmonic torque components (forward- and backward rotating) and the resultant characteristic of a 4-pole SPIM.

In order to reduce the effect of the harmonics, the designer usually tries various methods

which include adding a pole-bridge, changing the shaded-arc, using a closed-slot rotor or employing different skew angles. To verify the validation of the designs, harmonic analysis is necessary. Based upon the linear superposition principle, the conventional harmonic analysis and corresponding equivalent circuit models may yield the correct results only when the iron lamination is unsaturated. Although the flux density in most parts of SPIMs is not high, for some particular areas, e.g. pole tip, pole-bridge and slot-bridge of the closed-slot, the flux density may still reach a considerably higher value. Since the higher-order harmonics are significantly affected by local saturation, to study their effect, the saturation of rotor and stator must be considered properly. However, such a demand is beyond the capability of normal harmonic analysis methods and equivalent circuit models.

Instead of equivalent circuit methods, the time-stepping eddy-current FE method is used to estimate the performance of SPIMs in the study, so saturation, eddy-current and the skin effects can be taken into account accurately. Because the time-stepping FE method is a numerical method, the flux density in the air gap of SPIMs is only obtained at each time point. Although the flux density distribution can be drawn as in Fig. 5.2 at each time step, the amplitude of each harmonic component and its variation with time are still unknown. Sadeghi [1995] used a Trajectory (Locus) plotting to describe the fundamental and higher-order components, but he did not indicate how to distinguish each harmonic component from the results of the time-stepping finite element method. On the other hand, in his model, the sampling points for air gap flux density are too few to recognise the higher-order components, e.g. the fifth- or seventh-order component. Additionally, the effect of switching transients has not been excluded in Sadeghi's result.

Therefore, an improved method of harmonic evaluation for the time-stepping finite element model has been proposed in this research. Using this method, after the field is solved by the time-stepping finite element model, the amplitude of the fundamental and the higher-order harmonics are obtained by applying a Discrete Fourier Transform (DFT). Consequently, the variation of the harmonics with time may be visualised. For the different designs, the effect of design parameters on each harmonic component of the air gap MMF and rotor-bar current can be studied directly.

With the time-stepping FE method, the flux distribution in the middle of the air gap at each time-step at a certain speed can be obtained (Fig. 5.2a). Sampling each element in the air gap with a small constant spatial step, a total of N sampling points of flux density along the rotor are then produced. The DFT operation is applied to these sample points as shown:

$$X(k)=\sum_{n=1}^{N} x(n)\cdot e^{-j\frac{2\pi(k-1)(n-1)}{N}} \qquad 1\le k\le N. \tag{5.1}$$

The relations between the coefficient X(k) of DFT and the Fourier coefficients, a_0, $a(k)$ and $b(k)$, in the continuous Fourier transform

$$x(n)=a_0+\text{sum}\sum_{k=1}^{N/2} a(k)\cos(\frac{2\pi k\cdot\theta(n)}{N\Delta\theta})+b(k)\sin(\frac{2\pi k\cdot\theta(n)}{N\Delta\theta}) \tag{5.2a}$$

are

$$a_0=\frac{2X(1)}{N},\ a(k)=\frac{2\cdot real(X(k+1))}{N},\ b(k)=\frac{2\cdot imag(X(k+1))}{N}, \tag{5.2b}$$

where $x(n)$ is a discrete signal sampled at step time point t_k with angular spacing $\Delta\theta$. $\theta(n)$ is the spatial angle of the n^{th} sample. The amplitude of k^{th} order component can be calculated by using the following equation:

$$F_k=\sqrt{a(k)^2+b(k)^2}=X(k+1)\frac{4.0\cdot conj(X(k+1))}{N^2}. \tag{5.3}$$

Thus, the amplitude of the fundamental and higher-order spatial harmonics at time step t_k can be obtained and shown in (Fig. 5.2b).

Since the amplitude of the fundamental and higher-order spatial harmonics at different time steps are known after applying FFT analysis, joining them together in time sequence, the amplitude variations of the fundamental and higher-order spatial harmonics with time can be found and are shown in Fig. 5.3. Unlike the poly-phase induction motor, the strength of the fundamental rotating magnetic field varies as the SPIM's rotor spins. The variations with time of the fundamental component and the third- and fifth-order spatial harmonics are redrawn accordingly in Fig. 5.4. It can be seen that the fundamental component of the air gap magnetic field varies with a frequency of 100Hz (one cycle time is 0.01s) which is twice that of the AC supply voltage. Therefore, the electromagnetic torque, whose magnitude depends on the amplitude of the air gap flux density, varies

twice in one source AC cycle. In other words, the instantaneous torque of SPIMs is always a twice-line-frequency pulsating torque.

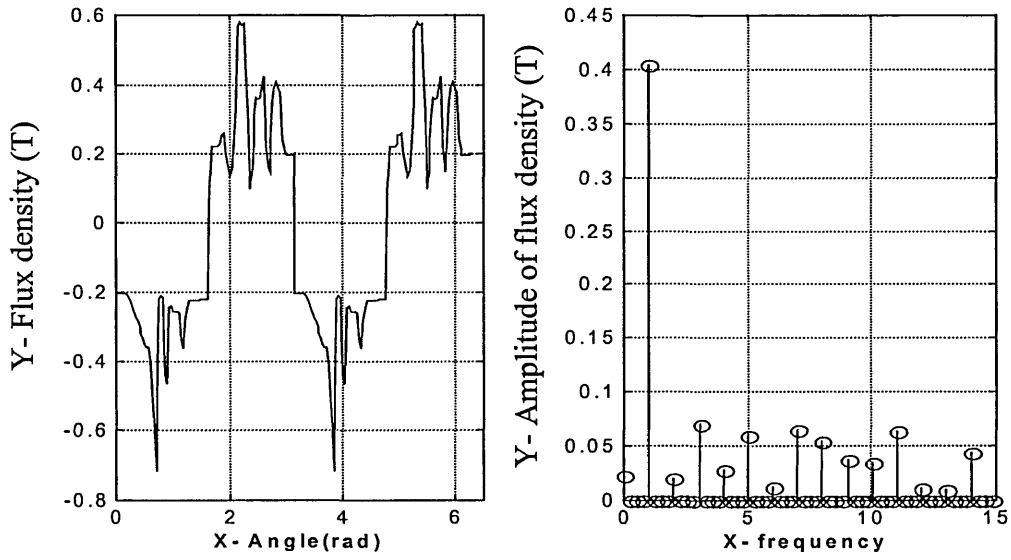

Fig. 5.2 a) Flux density distribution in the air gap b) Spatial harmonic distribution

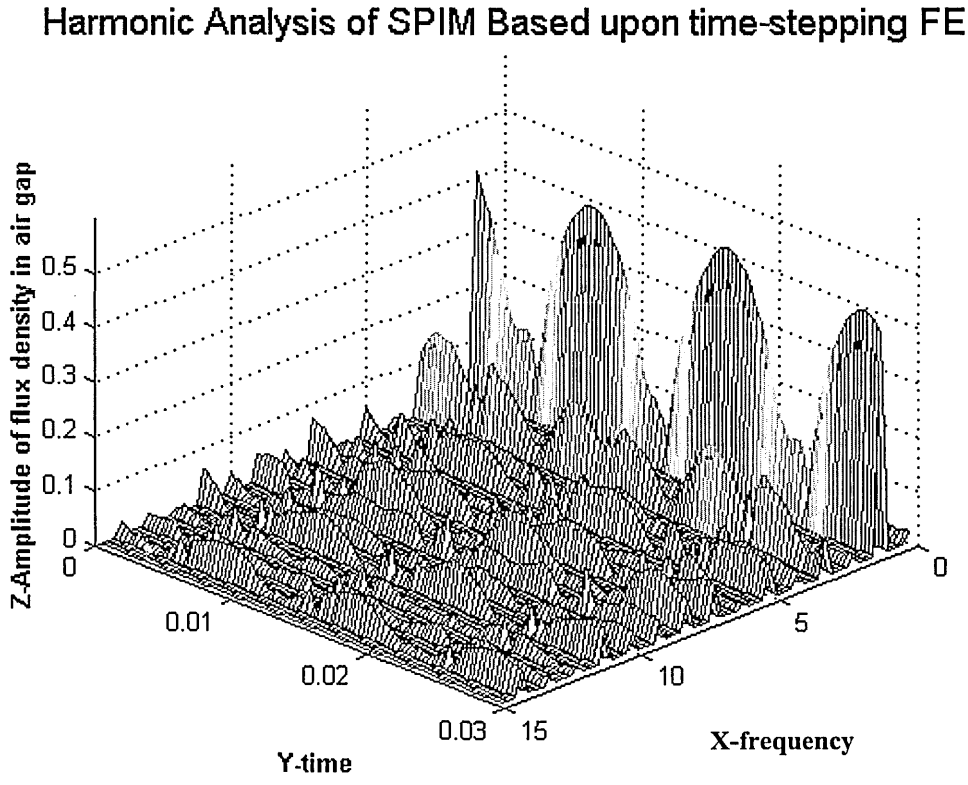

Fig. 5.3 Spatial harmonic distribution and their variation with time

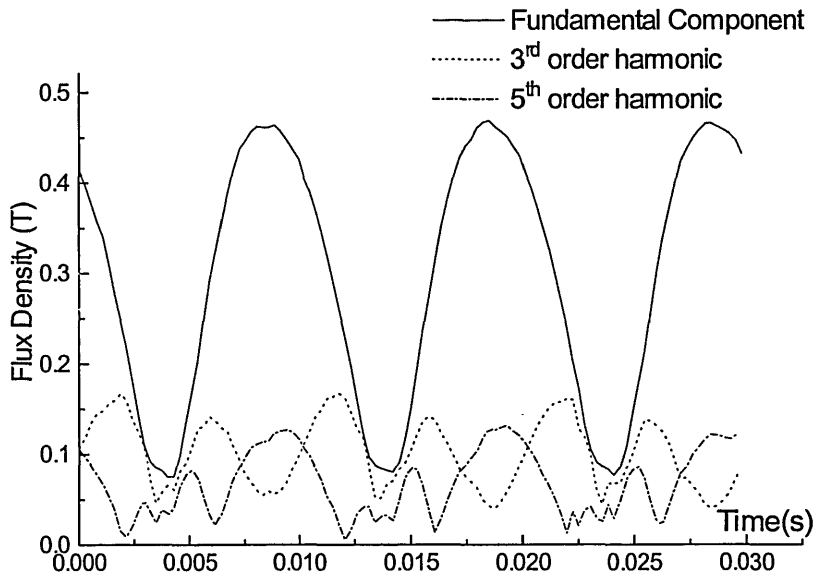

Fig. 5.4 Variation of fundamental and higher-order spatial harmonics with time (Model R, skew=1.5slot, 600 rev/min)

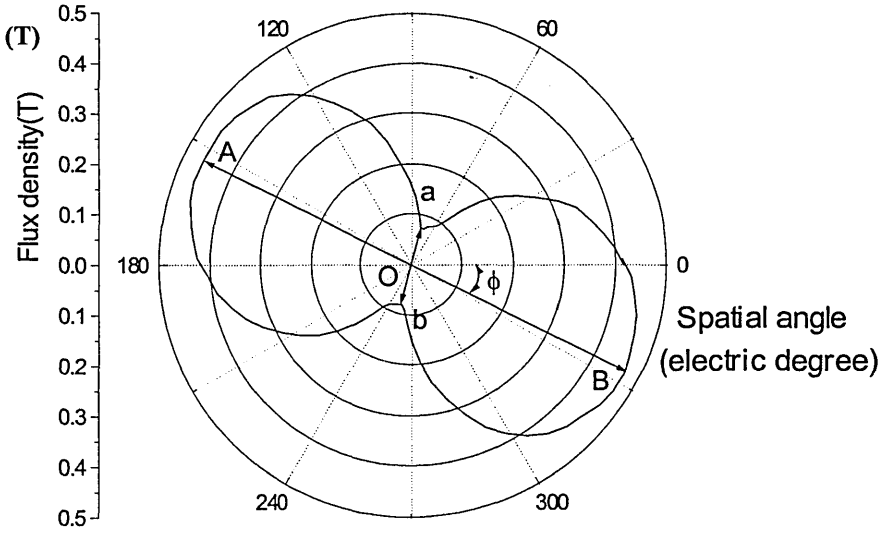

Fig. 5.5 Trajectory (locus) plotting of the fundamental component of the magnetic field in the air gap of a SPIM (Model R, skew=1.5, 600rev/min)

The variation of the rotating field of SPIMs can also visualised by using a variable rotating phasor vector. The trajectory (locus) plotting which show the track of the extremity of the phasor arrow can be obtained by transferring the time co-ordinate into

the corresponding spatial co-ordinates. The locus plotting of the fundamental component of Fig. 5.4 is shown in Fig. 5.5. The angular position of the field is represented by the angular position, ϕ, and the strength of the field is represented by the length of the phasor OB. For the SPIMs, the locus of the phasor of the fundamental field is approximately an ellipse whose the minor axis (neutral axis, *ab*) drops quite notably due to the salient-pole structure of the stator.

From the viewpoint of the revolving-field theory, the variable rotating magnetic field of a single-phase induction motor may be mathematically substituted by two uneven rotating fields which have same speed and opposite directions of rotation. These two rotating fields named forward-rotating (direct-rotating) field and backward-rotating (counter-rotating) field accordingly are usually described by two oppositely rotating phasors (vectors). With locus plotting of Fig. 5.5, these two equivalent rotating phasors can be estimated. Assuming the amplitudes of forward- and backward-rotating fields are B_f and B_b, they can be approximately calculated using the following equations:

$$\begin{aligned} B_f &= (L_{AB} + L_{ab})/4 \\ B_B &= (L_{AB} - L_{ab})/4 \end{aligned} \tag{5.4}$$

where L_{AB} is the length of the major axis (longitudinal axis) and L_{ab} is the length of the minor axis (neutral axis) of the elliptic rotating field.

In order to increase the output torque and to reduce the pulsating torque, the forward field component should be increased as the backward one is reduced. Thus, one aim of adjusting the design parameters of the main winding and shaded-ring, such as the shaded-arc and shaded-ring resistance, is to change an elliptical rotating magnetic field to a circular one. The locus plotting of Fig. 5.5 can be used to reflect the effect of the change in parameters on the rotating fields.

For each higher-order harmonic, its variable rotating field can also be divided into the forward- and backward-rotating components and two components can also be distinguished in the locus plotting. But, more conveniently, the total harmonic distortion (THD), the distortion factor (DF) and the distortion factor of an individual harmonic (DF_n) are used to estimate the magnitude ratio between higher-order harmonics and the

fundamental component in the air gap flux distribution. The THD, DF and DF_n are defined as follows.

$$\begin{cases} \text{THD} = \dfrac{1}{V_1}\left(\sum_{n=2}^{\infty} V_n^2\right)^{\frac{1}{2}} \\ \text{DF} = \dfrac{1}{V_1}\left(\sum_{n=2}^{\infty}\left(\dfrac{V_n}{n^2}\right)^2\right)^{\frac{1}{2}} \\ \text{DF}_n = \dfrac{V_n}{V_1 n^2} \end{cases} \tag{5.5}$$

where V_1 and V_n are the amplitude of the fundamental and the n^{th} order spatial harmonic at each time step. Their variation with time is plotted in Fig. 5.6:

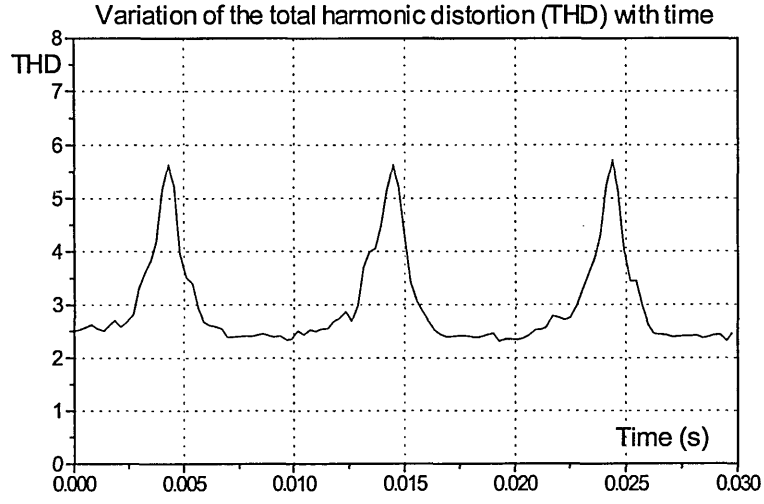

Fig. 5.6a) THD

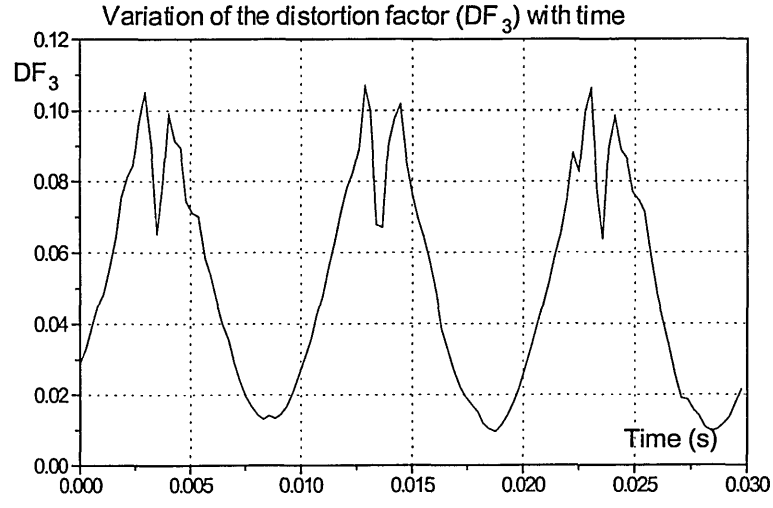

Fig. 5.6b) DF_3

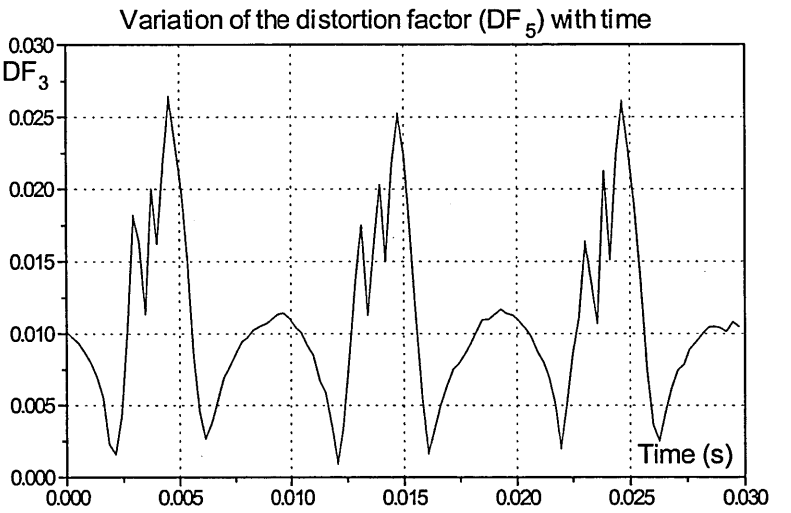

Fig. 5.6c) DF_5

Fig. 5.6 Spatial harmonic distortion variation with time

By comparing the Fig. 5.4 and Fig. 5.6, it is found that the peaks of THD, DF_3 and DF_5 always appear when the fundamental component drops into a valley. At this moment, the rotating field goes through the area between a shaded-pole and the following main pole, and the pattern of the field waveform becomes more irregular and changes very rapidly.

If the V_1 and V_n are averaged first over a cycle of the supply source and then substituted into (5.5), the average value of THD, DF_3 and DF_5 can be obtained. Compared with the instantaneous values, the average values are more sensitive to the overall effect of the design parameters on harmonics, and are used more frequently.

Although the harmonic analysis discussed above focuses on the rotating magnetic field in SPIMs, the same analysis tool can also be used to analyse the spatial harmonics in the distribution of the rotor-bar currents as well as the time harmonics in each bar current.

5. 3 Pole-Bridge and Skew

The pole-bridge and the skew are usually regarded as two main means to reduce the effect of harmonics. The advantage of using the pole-bridge is that the amplitude of harmonics

in the air gap can be reduced. Unlike skew, the effect of the pole-bridge is not definite yet. Some researchers have found that the pole-bridge improves the performance of the motor, but others disagree. Because the equivalent circuit model is not able to handle the saturation on the pole-bridge, the effect of the pole-bridge is usually studied with experimental methods. With the 2D muti-slice FE Method, the effect of the pole-bridge is ready to be investigated accurately. So, in this section, the performance with or without a pole-bridge for two different motor designs is calculated.

Fig. 5.7a illustrates a SPIM's construction with a solid, permanent bridge between two main poles[Veinott, 1959]. In this case, the stator core is made up of two pieces(part I & II). The pole sides are straight and parallel, and it is easy to install stator windings with this construction. Another kind of construction, in which the stator is only one piece, is shown in Fig. 5.7b. To build the pole-bridge, several slices of silicon-steel sheet are inserted between the two pole tips after the stator coils and shaded-rings are installed. With this construction, the pole-bridge is easy to install or uninstall according to the motor performance. Therefore, the second kind of construction is more widely used and is studied in this research. To simulate the different reluctivity along the different directions in the silicon-steel sheet and to express the fine gap between the slices, a small air gap (0.05mm – 0.1mm), shown in Fig. 5.7c, was used to separate the pole-bridge into two parts. A performance comparison for motors with or without a pole-bridge is shown in the following figures.

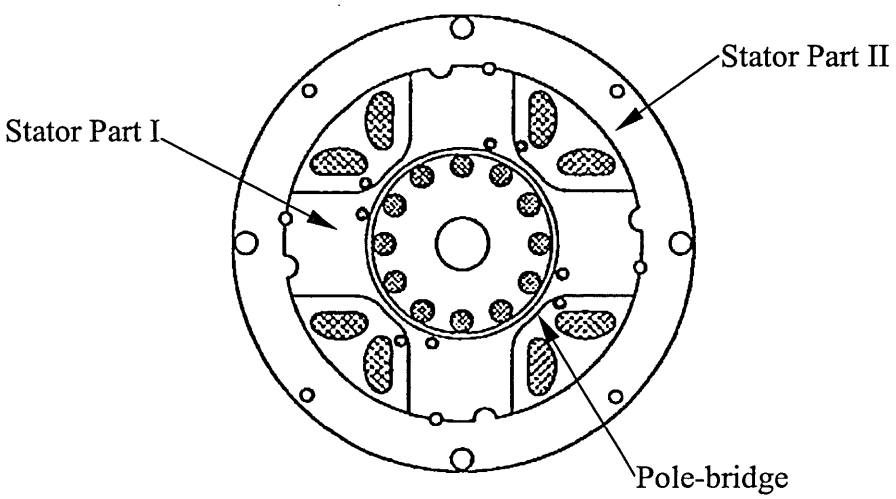

Fig. 5.7a SPIM with Pole-bridge (two-piece stator)

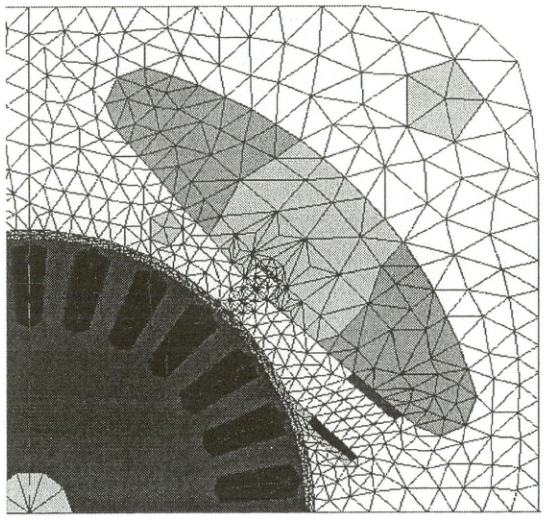

Fig. 5.7b Mesh of SPIM with pole-bridge (one-piece stator)

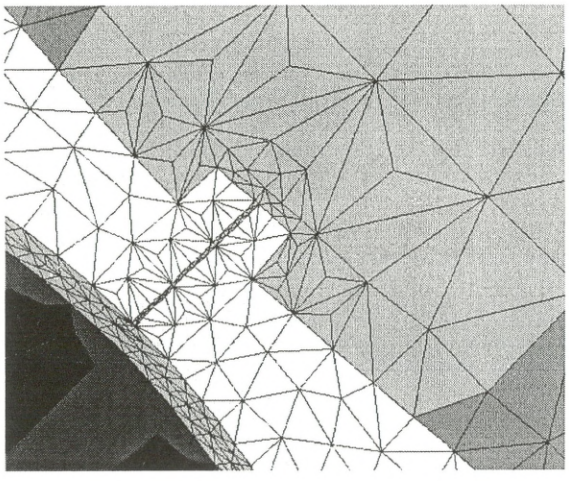

Fig. 5.7c Mesh detail of pole-bridge

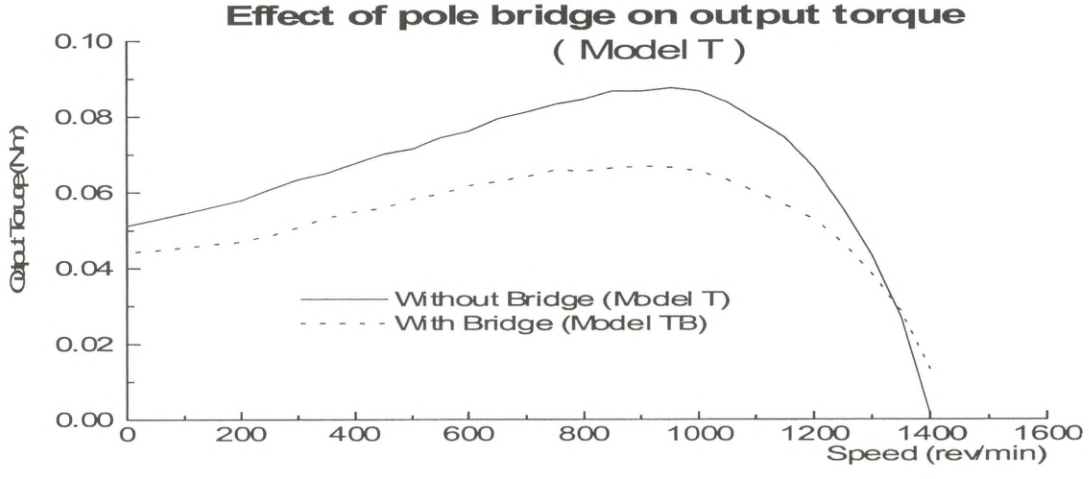

Fig. 5.8a) Torque versus speed

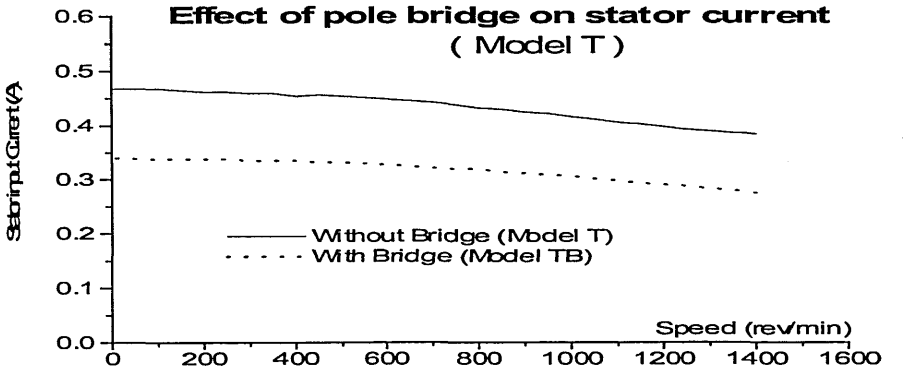

Fig. 5.8b) Input current versus speed

Fig. 5.8 Computed effect of pole-bridge on the SPIM performance (Model T)

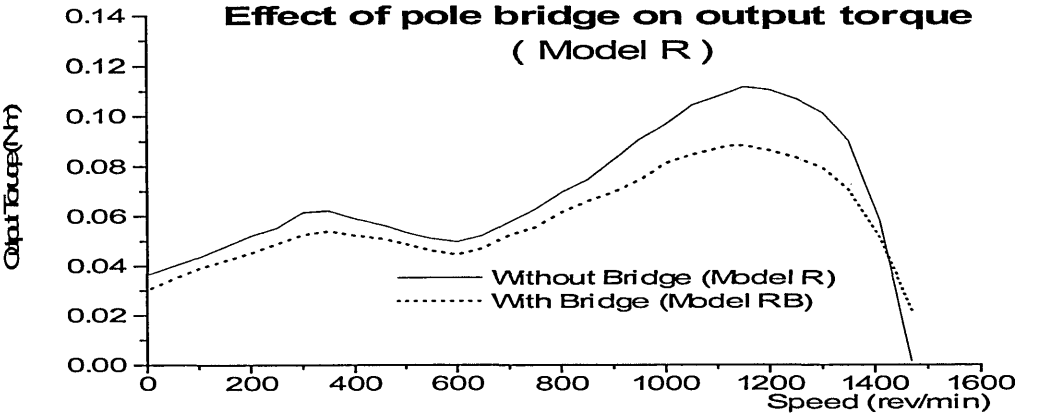

Fig. 5.9a) Torque versus speed

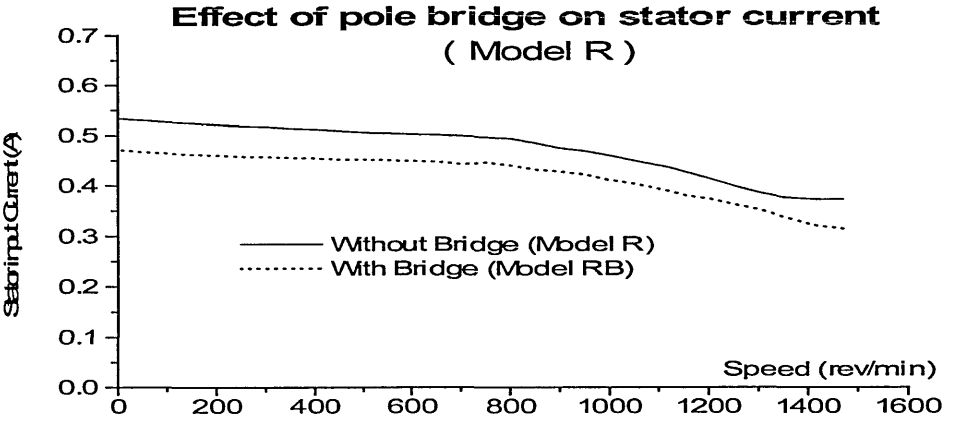

Fig. 5.9b) Input current versus speed

Fig. 5.9 Computed effect of pole-bridge on SPIM performance (Model R)

In Fig. 5.9a, the calculate result shows that the torque/speed curve becomes smooth when the pole-bridge is present. The torque dip due to the the third harmonic is improved with respect to its breakdown torque, but the magnitude of the torque is not increased compared with the output torque of the motor without the pole-bridge. It is seen that, for the whole speed range, the torque of the motor with the pole-bridge is decreased significantly. The same situation can also be observed for Model T in Fig. 5.8a.

To illustrate the effect of the pole-bridge on the third harmonic, the third harmonic variation of Model T for the two cases (with or without a pole-bridge) was studied at a speed of 600 rev/min. At this speed, which is just over the synchronous speed of the third harmonic (500 rev/min), the flux density of the third harmonic reaches the maximum value, and the torque produced by the third harmonic is near to its maximum value as well. The amplitude variation of the flux density of the third harmonic with time is shown in Fig. 5.10. In Fig. 5.10a, for the case with the pole-bridge, the amplitude of the third harmonic can be seen to decrease significantly. But in Fig. 5.10b, the harmonic distortion of the third harmonic, DF_3, which expresses the the amplitude ratio between the third harmonic and the fundamental, has not been reduced with the pole-bridge because the magnitude of the fundamental flux density is also decreased significantly for the motor by using the pole-bridge.

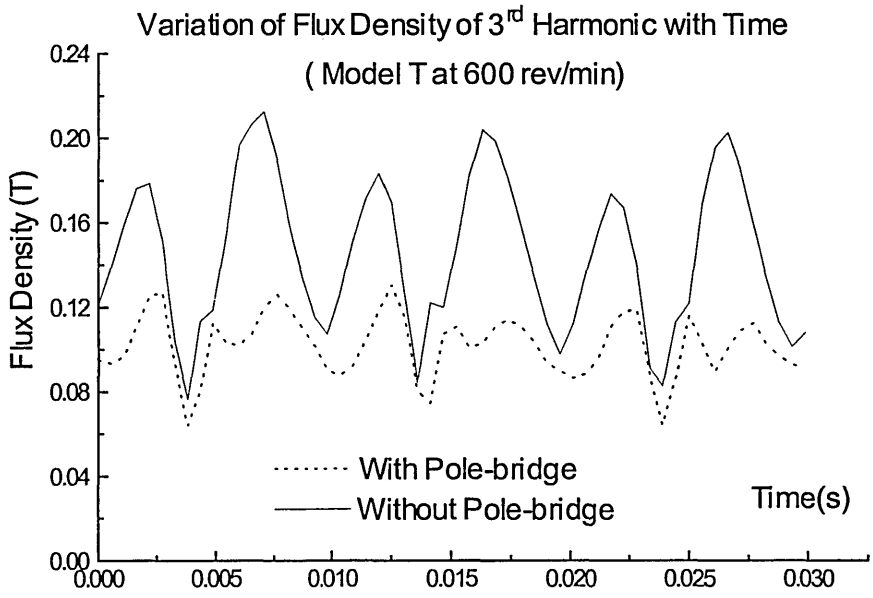

Fig. 5.10a) flux density

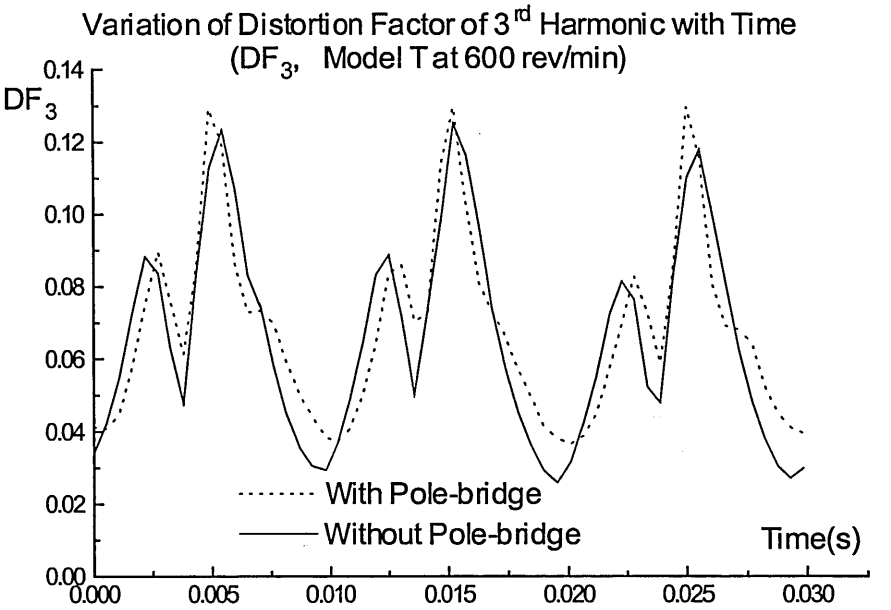

Fig. 5.10 b) DF_3

Fig. 5.10 The 3rd harmonic comparison between the motors with or without a pole-bridge

Additionally, although the magnitude of each harmonic has been reduced significantly by using a pole-bridge, the averaged harmonic distortion factors of the 3rd-, 5th- and 7th-order harmonics (DF_3, DF_5, DF_7) and the total harmonic distortion (THD) of the motor without the pole-bridge are still smaller than that of the motor with the pole-bridge, which indicates that the harmonic effect has not be reduced by using the pole-bridge. The detail of each harmonic distortion factor is shown in Table 5.1.

Table 5.1 Comparison of spatial harmonic distortion for two cases (with or without pole-bridge); Model T at 600 rev/min

	DF_3	DF_5	DF_7	THD
with pole-bridge	0.5534	0.3247	0.2241	1.8803
without pole-bridge	0.5174	0.2470	0.2154	1.6468

Therefore, although the value of the torque of the third harmonic is decreased due to the significant reduction in the flux density of the third harmonic, the total torque at the speed

of 600 rev/min can not be increased because the amplitude of fundamental torque is reduced as well due to the presence of the pole-bridge. The same conclusion can also be drawn from the viewpoint of the equivalent circuit model. Since the presence of the pole-bridge results in a significant increase in the leakage of the main pole flux, the reactance of the stator coil leakage which includes the reactance of the pole-bridge leakage becomes bigger, consequently, the rotor current in the equivalent circuit reduces and the output torque drops as well.

As to the two motors studied, the advantages of using the pole-bridge cannot be clearly observed except that the input currents are reduced a lot as using the pole-bridge.

The skewed rotor is always adopted as the main mean of reducing harmonics in SPIMs. For SPIMs, because the dominant harmonic present is the third-order, a torque dip near 600rev/min where the third-order harmonic reaches its peak in the opposite direction to the fundamental torque can usually be observed in the torque/speed curve. The periodical spatial length of the third harmonic is one third of the length of fundamental, 120 electrical degree. To eliminate the third harmonic torque completely, the skew angle should be 120^{o} (elec), at which the total inductive electromotice force (emf) of the third harmonic is reduced to zero in one rotor bar. However, such an excessive skew is unacceptable because of the difficulties of manufacture and the drastic reduction of the fundamental rotor emf. Usually the skew angle is below 60^{o} (elec).

To exam the effect of a skewed rotor on the charteristics of SPIMs, two different designs of SPIMs with different skew angles were investigated.

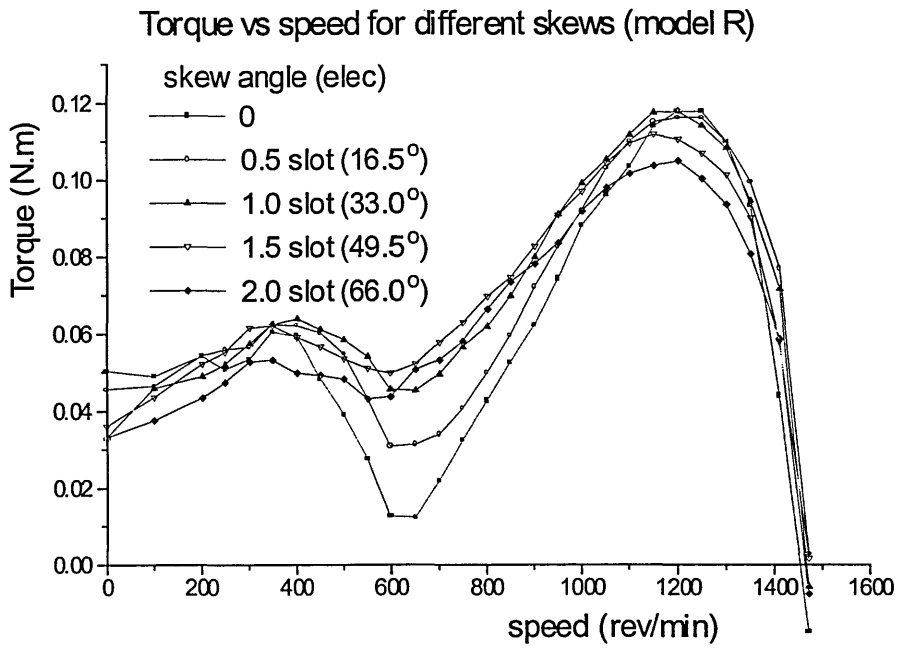

Fig. 5.11a) Torque versus speed

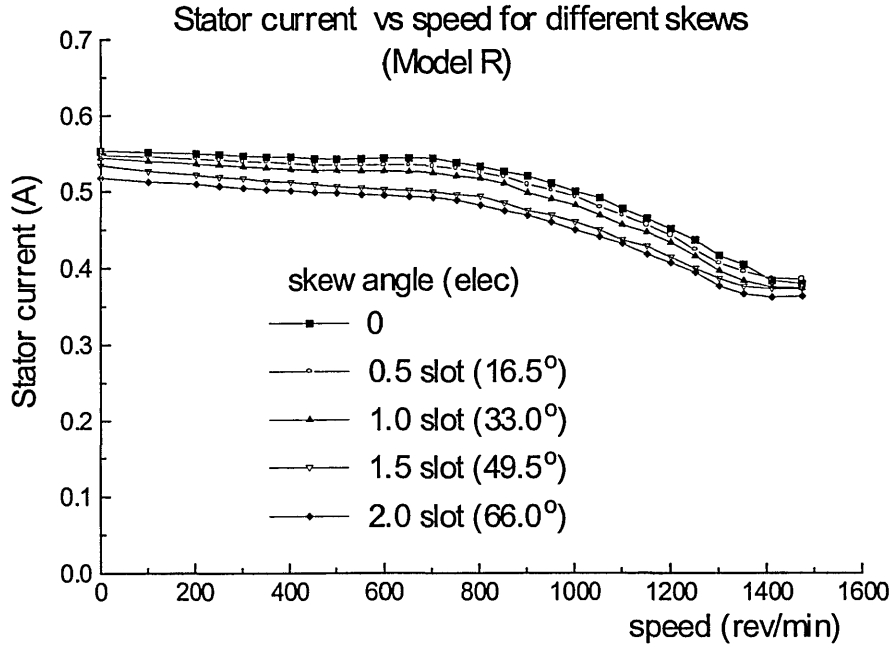

Fig. 5.11b) Input current versus speed

Fig. 5.11 The effect of different skew angles (Model R)

The torque/speed characteristics of Model R for different skew angles are shown in Fig5.11a. The torque dip is smoothed greatly by using a bigger skew angle, so the advantage of using the skew is clearly shown here. To check the effect of skew on the

spatial harmonics of magnetic field, the total harmonic distortion (THD) and the distortion factor of the third, fifth and seventh harmonics (DF_3, DF_5, DF_7) were calculated for two different skew angles and are shown in Table 5.2. It is found that, with a skewed rotor, the waveform of the magnetic field in the air gap tends to be more sinusoidal because of the magnitude reduction of the main spatial harmonics.

Table 5.2 Comparison of spatial harmonic distortion for different skew angles (Model R at 600 rev/min)

	DF_3	DF_5	DF_7	THD
skew = 0	0.3789	0.2533	0.1930	1.6770
skew =1.5 slot	0.3390	0.2322	0.1746	1.5119

As a result of the decrease of the spatial harmonics, the time harmonics of rotor current is also notablely decreased. In Table 5.3, the fifth and seven-order time harmonics, both forward (+5, +7) and backward (-5, -7) component, are significantly reduced because the skew angle (50^O elec) is very near their periodical spatial length. The other higher oerder ones are also reduced considerably.

Table 5.3 Variation of the rotor current harmonics of skewed rotor (skew =1.5 slot) compared with the non-skewed rotor (Model R, 600 rev/min)

	Frequency(Hz)	Variation(%)
Fundamental(Forward)	30.0	-10.5
Fundamental(Backward)	70.0	-13.6
3^{rd} order (Forward)	10.0	-38.1
3^{rd} order (Backward)	110.0	-41.2
5^{th} order (Forward)	50.0	-63.6
5^{th} order (Backward)	150.0	-77.9
7^{th} order (Forward)	90.0	-60.5
7^{th} order (Backward)	190.0	-79.7
9^{th} order (Forward)	130.0	-17.9

* The result of the no skew motor is set as the criterion

However, the disadvantage of using the skewed rotor is also shown in Fig. 5.11a. As the skew angle increases, the maximum ouput torque at speed of 1200rev/min is reduced. The gap of the maximum torque between the unskewed curve and the 2.0 slots skewed curve is notable in Fig. 5.11a. This is because using the skewed rotor can also reduce the amplitude of the fundamental emf, as it does the higher order harmonic emf. In Table5.3, the decrease of both the forward (+1) and backward (-1) fundamental conponent of the induction rotor current can be seen when the bigger skew angle is used. Consequently, for the motor with a skewed rotor, the fundamental components of the torque are decreased compared with the machine wihout skew.

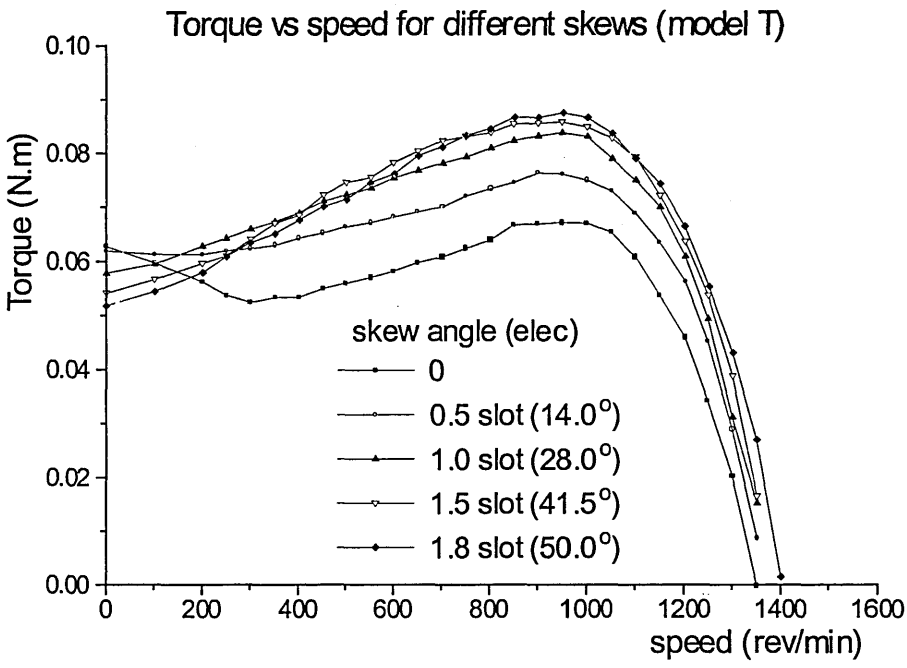

Fig. 5.12 a) Torque versus speed

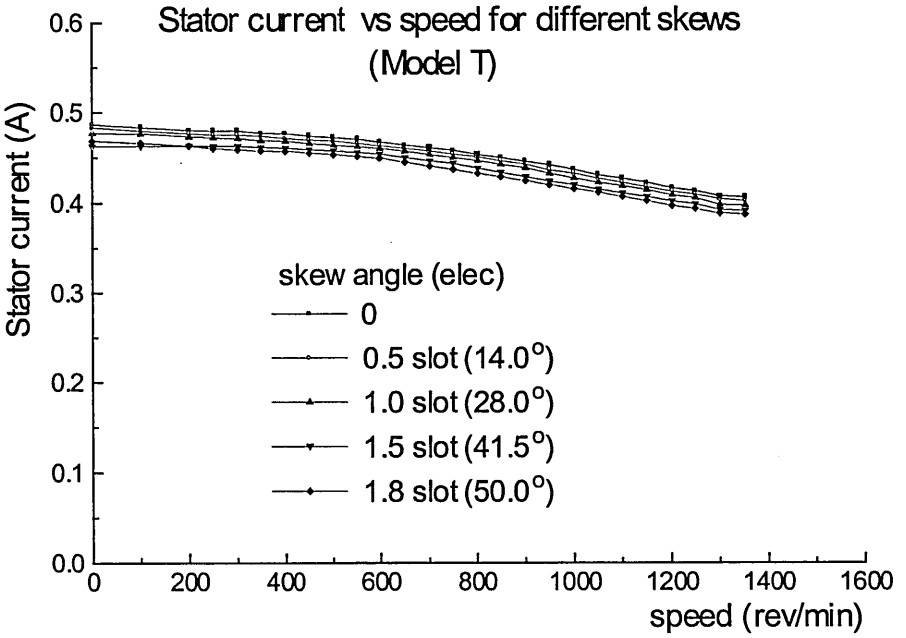

Fig. 5.12b) Input current versus speed

Fig. 5.12 The effect of different skew angles (Model T)

By contrast, in Fig. 5.12a, the results of Moled T show a contradictory case, in which the maximum (breakdown) torque is improved when the skew angle increases. The different effect of skew on the maximum torque between the two motors results from the different break-down speed at which the maximum torque occurs. For the Model R, the maximum torque occurs at speeds above 1200 rev/min. At this speed, the negative torque due to all the higher-order harmonics and the backward fundamental (-1) is not significant. the total output torque is mainly decided by the fundamental torque. Once the forward fundamental rotor current is reduced with the skew, the total torque decreases considerablely . However, for the Model T, its maximum torque occurs between 800 and 1000 rev/min. At such a speed, the negative torque due to the higher-order harmonics and the backward fundamental is quite notable. For example, the third harmonics (+3) reaches its maximum negative torque at 600rev/min. If the third harmonic current flowing in the rotor-bar can be eliminated, its negative torque may be reduced significantly. Although, the fundamental torque is also reduced when skewed rotor is used, the total output torque near a speed of 900rev/min can be increased. So the maximum torque is not always be reduced by using the skewed rotor.

Table 5.4 Variation of the rotor current harmonics of 1.5 slot skewed rotor compared with 0.5 slot skewed rotor (Model T, 900 rev/min)

	Frequency(Hz)	Variation(%)
Fundamental(Forward)	20.0	-10.3
Fundamental(Backward)	80.0	-10.9
3rd order (Forward)	40.0	-43.9
3rd order (Backward)	140.0	-38.9
5th order (Forward)	100.0	-81.9
5th order (Backward)	200.0	-86.8
7th order (Forward)	160.0	-80.4
7th order (Backward)	260.0	-81.2
9th order (Forward)	220.0	-64.1

* The result of the 0.5 slot skewed motor is set as the criterion

Additionally, in Table 5.3 and Table 5.4, it is seen that the amplitudes of both the forward (+1) and backward (-1) fundamental of the rotor current are reduced almost evenly at different speeds by using the skew. In other words, the field strength of the forward and backward components of the rotating magnetic field is decreased equally. Consequently, the amplitude of the pulsating torque, which is the result of the ellipsoidal rotating field, cannot be changed significantly by using different skew angles. This result can be used to explain the phenomenon found by Williamson [1981]. In Williamson's report, the experimental results indicated that the amplitude of the pulsating torque could not be notably changed when the rotor design parameters, such as the skew angle and the resistance of rotor bar, are modified.

5. 4 Effect of the Air Gap Profile

If the radial air gap length is increased under one pole tip of a single-phase motor, a starting torque whose direction is from the big air gap to the small air gap can be obtained at standstill state. SPIMs which rely on this principle to increase the starting torque are

termed reluctance-augmented SPIMs. The asymmetrical flux due to the step air gap increases the difficulty of using an analytical model. The well known research result of the effect of the air gap profile variation on SPIMs' performance was published by Williamson [1977,1978] who used an analytical model for direct solution of the air gap field equations. However, the saturation and space harmonics were not considered properly with his model, especially when the closed-slot is adopted in the rotor.

In this research, in order to investigate the effect of the air gap profile on SPIMs' performance, the 2D multi-slice FE method was applied to a designed SPIM with a closed-slot rotor (Model R). Since the step air gap is the most common form of profile used in the reluctance-augmented SPIMs, this kind of air gap profile is considered in this section. For the step air gap shown in Fig. 5.13, the step length and its height are two variable geometric factors. The length of step air gap, α, is usually measured in electrical degrees, and its height can be described with the parameter K, which is the ratio between the air gap length under the step air gap and that under other parts of the air gap.

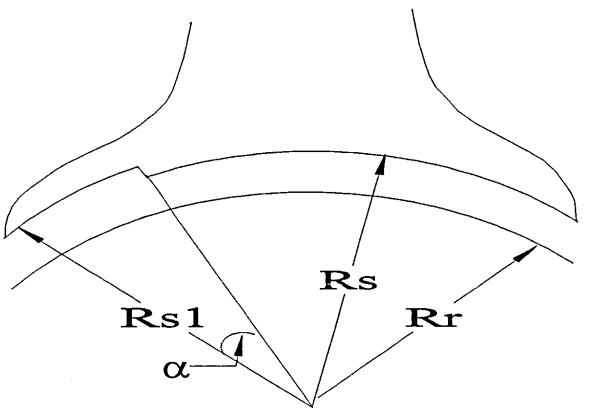

Fig. 5.13 Step air gap geometrical parameters

Fig. 5.14a) and b) illustrate the variation of torque/speed and current/speed characteristics of the machines with a constant air gap ratio, K. By adjusting the ratio K, the variation of torque/speed and current/speed are shown in Fig. 5.15 and Fig. 5.16.

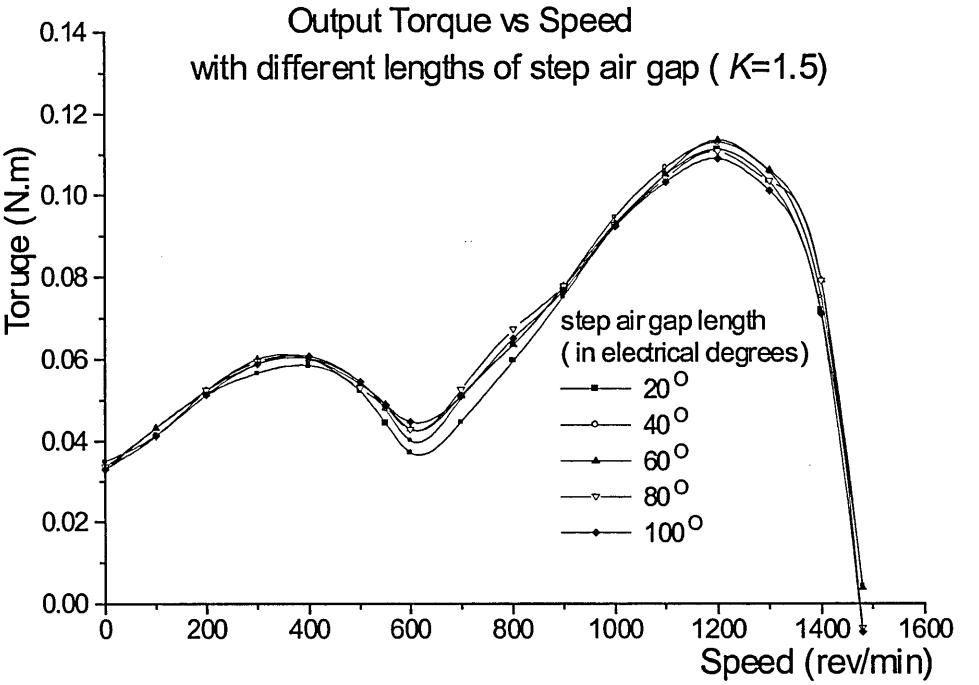

Fig. 5.14a) Torque versus speed

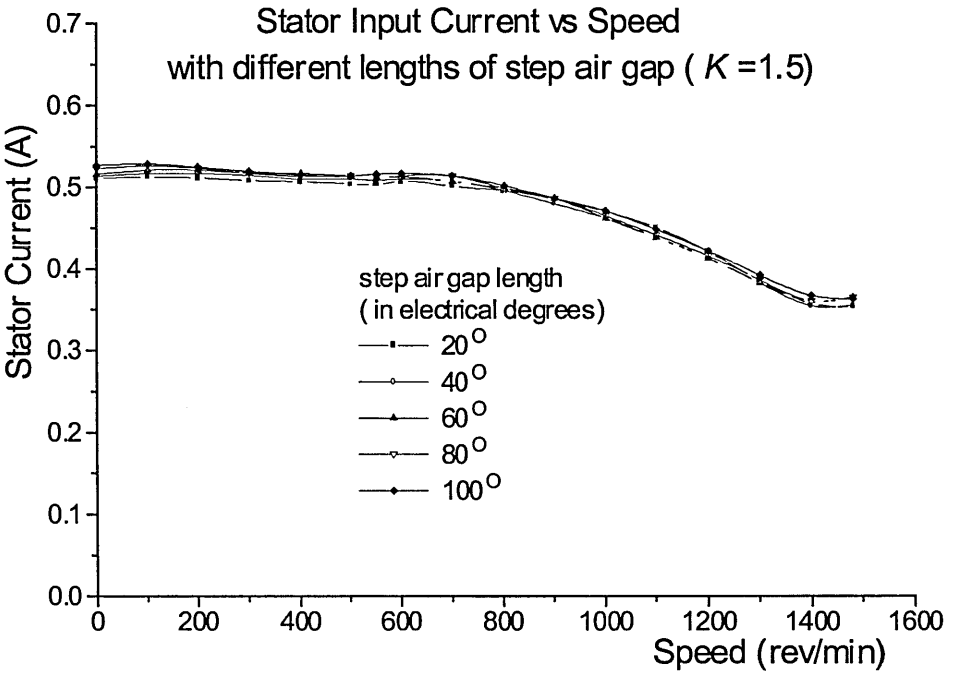

Fig. 5.14b) Current versus speed

Fig. 5.14 Effect of variation in step length with constant air gap ratio, K=1.5

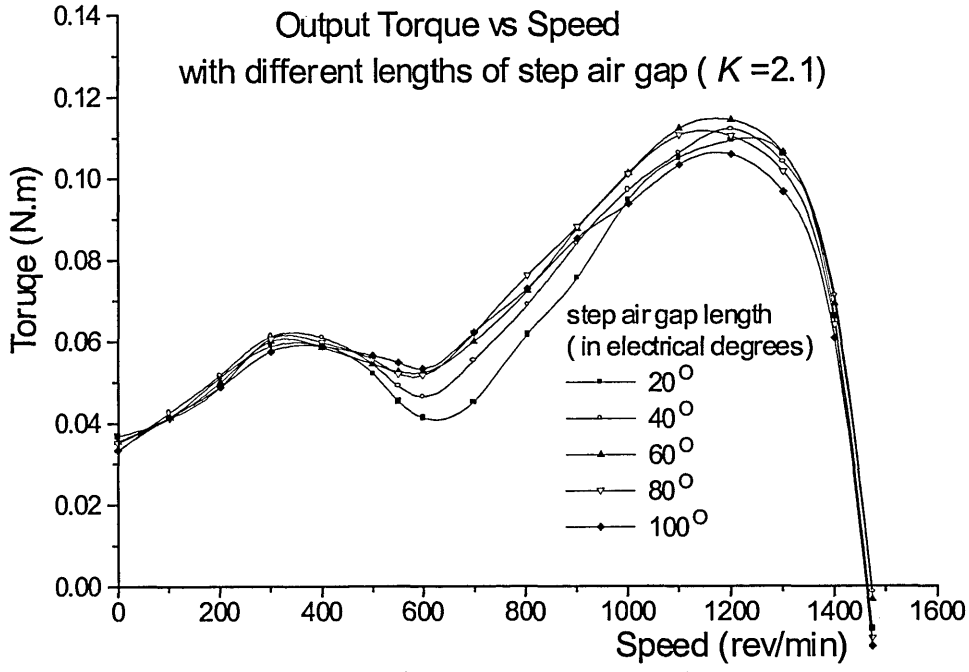

Fig. 5.15a) Torque versus speed

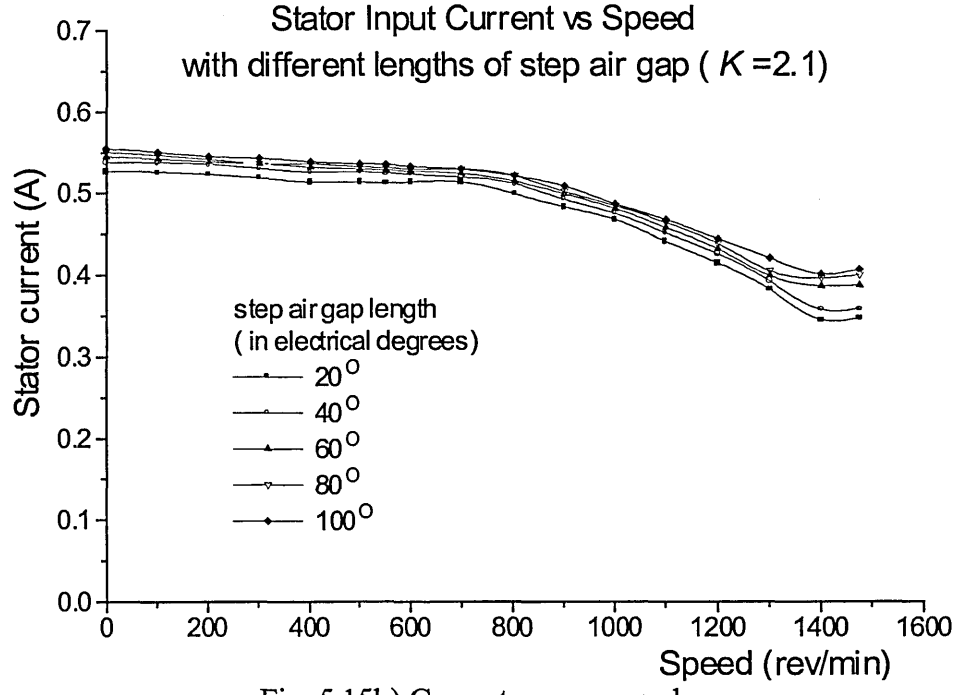

Fig. 5.15b) Current versus speed

Fig. 5.15 Effect of variation in step length with constant air gap ratio, K=2.1

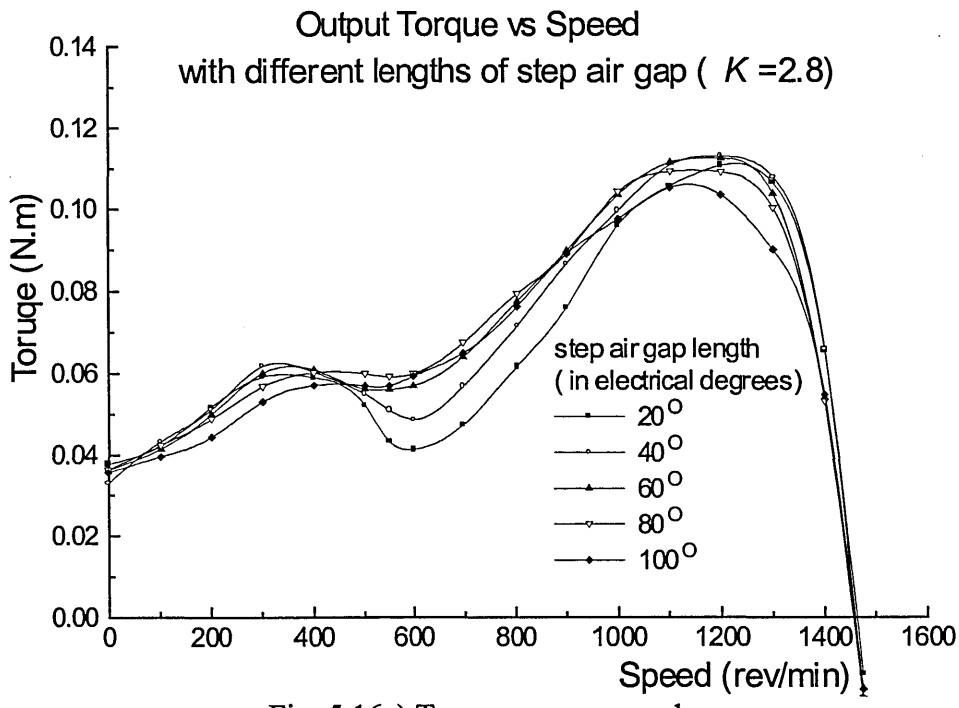

Fig. 5.16a) Torque versus speed

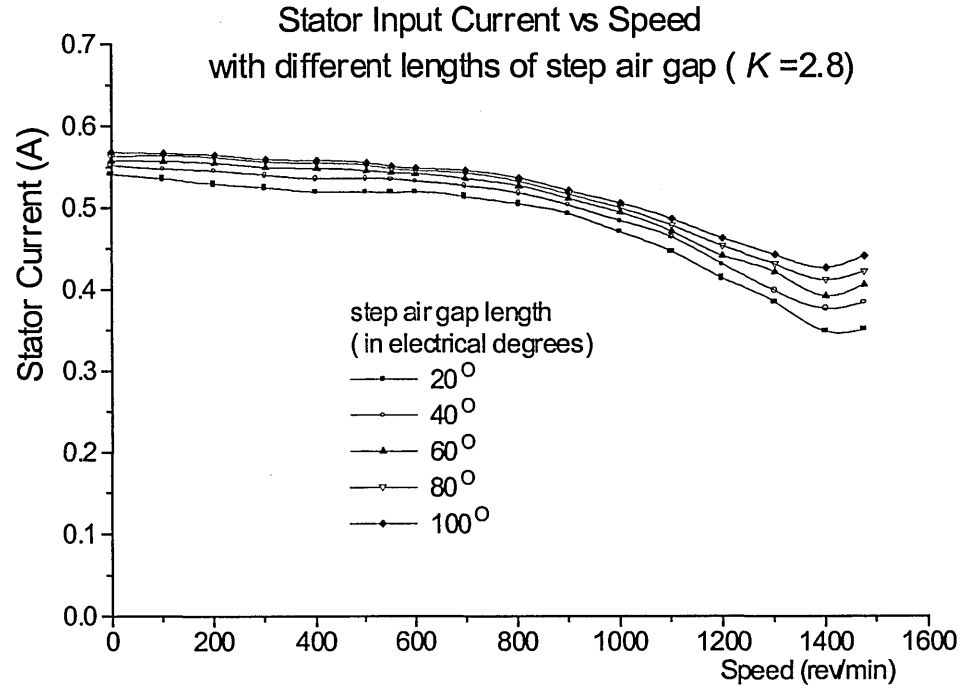

Fig. 5.16b) Current versus speed

Fig. 5.16 Effect of variation in step length with constant air gap ratio, K=2.8

Although in Williamson's result [1981] the reluctance effect can be used to increase the starting torque by up to approximately 40%, the starting torque improvement due to the

reluctance augmentation for closed rotor slot is not significant and cannot be clearly read in Fig. 5.14 to Fig. 5.16. Therefore, for different air gap ratios and lengths, the variation of starting torque is redrawn in Fig. 5.17a. From this figure, following conclusions can be drawn.

1) The maximum increase of the starting torque resulting from using the step air gap is about 18%.
2) There is no starting torque improvement when the air gap length equals 40°.

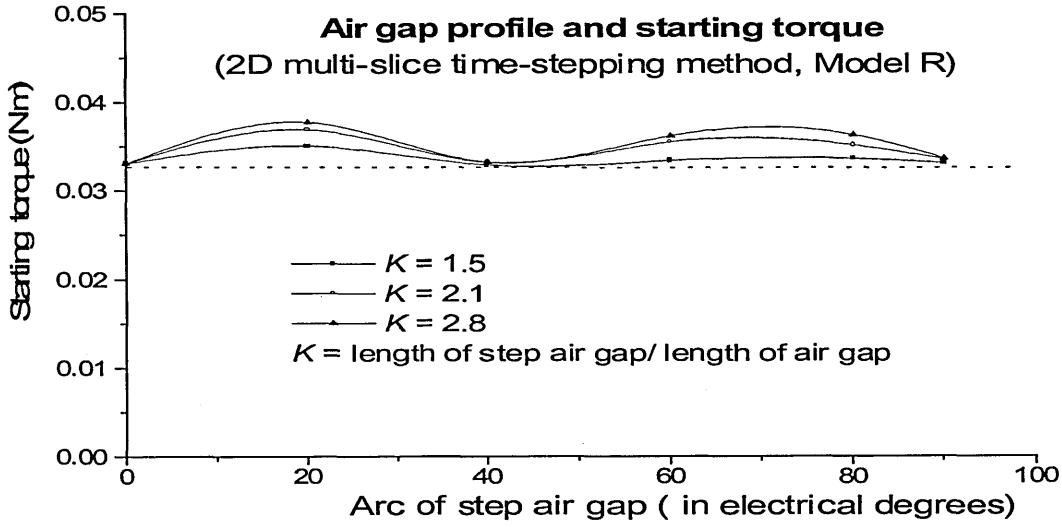

Fig. 5.17a) Using 2D multi-slice time-stepping method,

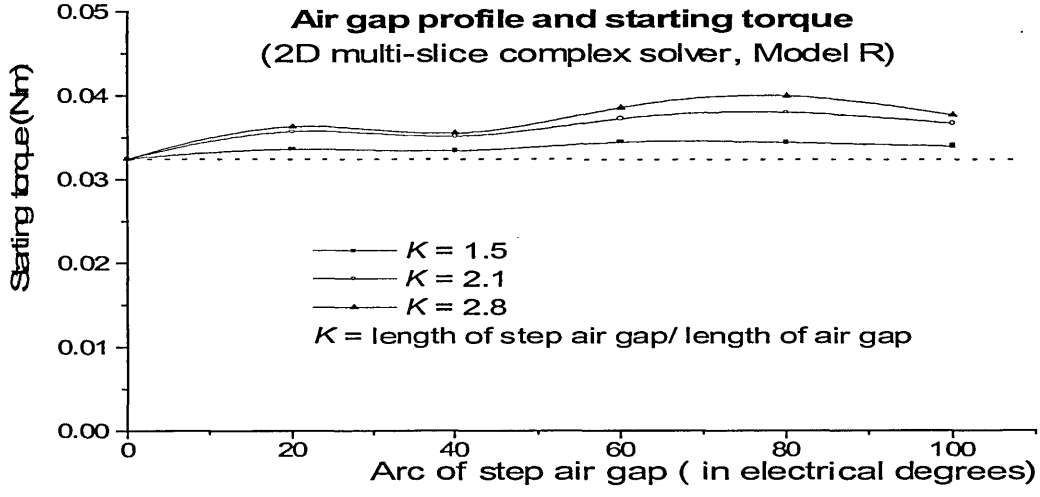

Fig. 5.17b) Using 2D multi-slice complex solver

Fig. 5.17 Variation of starting torque with different step air gap

Since the flux distribution and the harmonic components are changed when the air gap shape is modified, the curves shown in Fig. 5.17a can be considered as the combining results of harmonic and reluctance augmentation. To exclude the effect of harmonics on the starting torque, the variations of starting torque is calculated by the complex solver (explained in the next chapter), which assumes all the currents and the field variables vary sinusoidally with time at the fundamental frequency. The results are shown in Fig. 5.17b. Although there is still a slight torque dip at 40°, the torque increase due to the reluctance effect is much more significant compared with the results obtained with the time-stepping method. The variation of reluctance torque with the step air gap length shown in Fig. 5.17b is similar to Williamson's result obtained without considering the harmonic effect.

Unlike the effect on the starting torque, the effect of the step air gap on the torque dip near the one-third synchronous speed is clearly observed from Fig. 5.14 to Fig. 5.16. In particular, when air gap length is between 60° and 80° and K = 2.8, the torque dip is removed significantly. Using a step air gap, the length of the equivalent uniform air gap increases. Consequently, the magnitude of the third harmonic is reduced depending on the length and the width of the step air gap because the third-order harmonic, as well as other higher-order harmonics, is sensitive to the length of the air gap and can be significantly reduced with the large air gap length. Table 5.5 shows the variation of spatial harmonic distortion for different lengths of step air gaps. It is seen that higher-order harmonics for large step air gaps are smaller than those for small step air gaps.

Table 5.5 Comparison of spatial harmonic distortion for different lengths of step air gaps (Model R at 600 rev/min)

	DF_3	DF_5	DF_7	THD
K=2.8, α= 20°	0.4037	0.2855	0.2639	1.8506
K=2.8, α= 100°	0.3900	0.2126	0.1889	1.6883

As to the stator current, the variation of the stator starting current with the length of step air gap is not notable. But at the synchronous speed, the increase of the stator current

becomes very significant when the length of step air gap is increased. This can also be regarded as the result of the equivalent uniform air gap increase due to the large air gap since a large air gap requires a bigger exciting current and the exciting current is the dominant part of the stator input current at synchronous speed.

5. 5 Effect of Number of Rotor Slots and Closed-Slot Rotor

For the normal three-phase or single-phase induction motor, there are abundant literatures on how to select a proper slot number for the stator and rotor. To give all known references in this area would require too much space. Most of these references tell what kind of the combinations of stator slots and rotor slots are inferior. Usually, these design rules are obtained from the experimental investigations and the manufacturing experience. In order to learn the effect of different combinations of stator and rotor slots, a precise calculation on the effect of the harmonics always requires, however this is beyond the ability of the conventional equivalent circuit. .

For the SPIMs which have a salient stator, there was no papers giving details for choosing number of rotor slots. The books on machine design [Veinott, 1959; Heller, 1977] suggest that the number of rotor slots for a normal single-phase motor can also be adopted for the SPIMs. As for the 4-pole SPIMs, Veinott gave a list of recommend slot numbers that are 22, 26 and 30. In this section, these three numbers of rotor slots are examined under the condition that the total area of all the slots is the same for the different designs. The same condition is used to adjust the number of rotor slots in order to simplify the whole pole-pitch mesh to a half pole-pitch mesh for finite element analyses [Williamson, 1982].

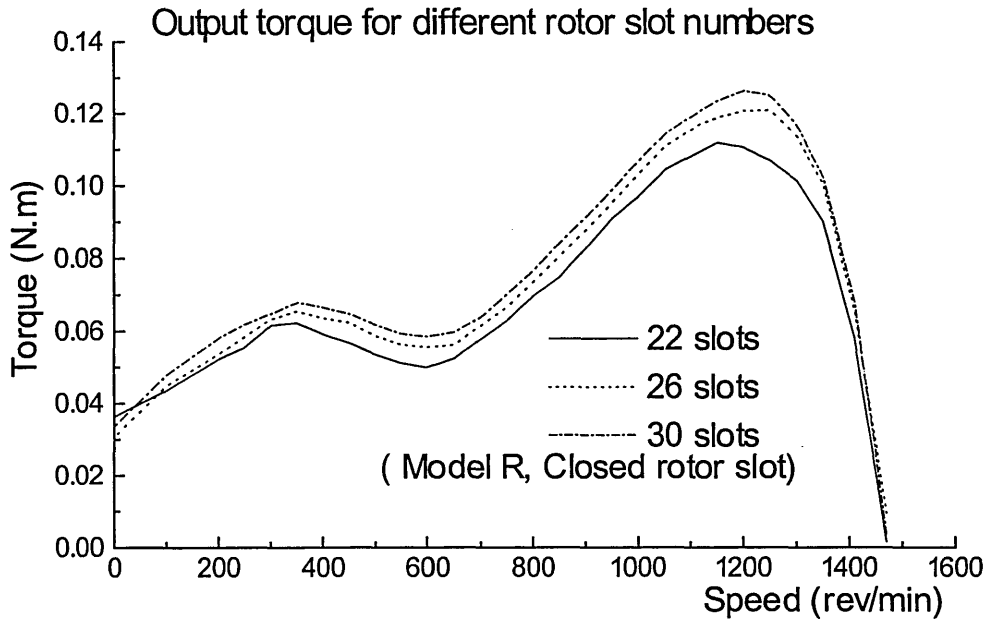

Fig. 5.18a) Model R, closed rotor slot (T_{SB} =0.15mm)

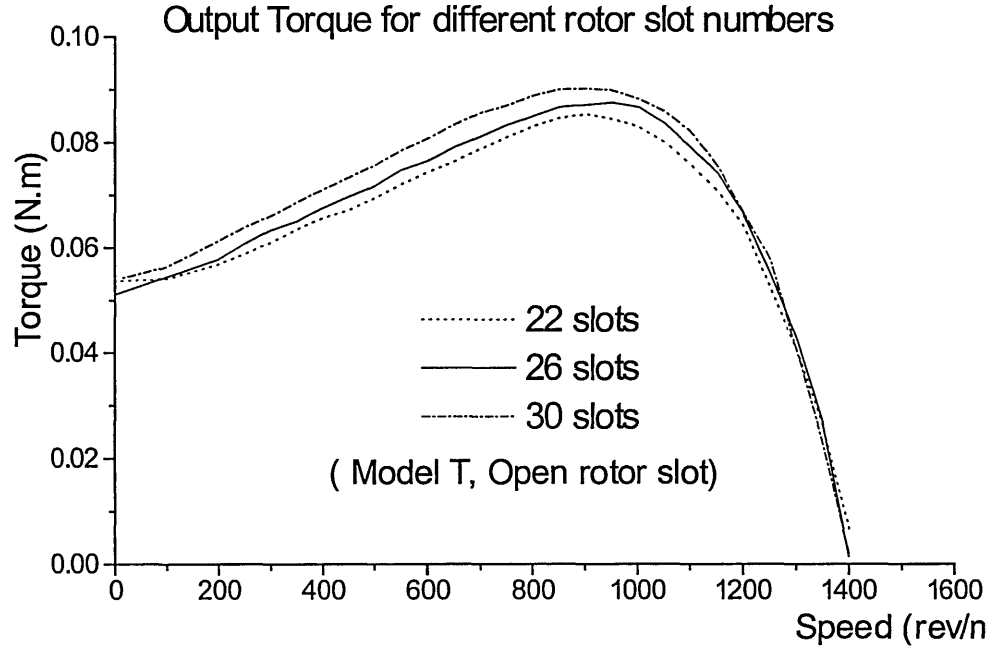

Fig. 5.18b) Model T, open rotor slot

Fig. 5.18 Comparison of output torque for different numbers of rotor slots

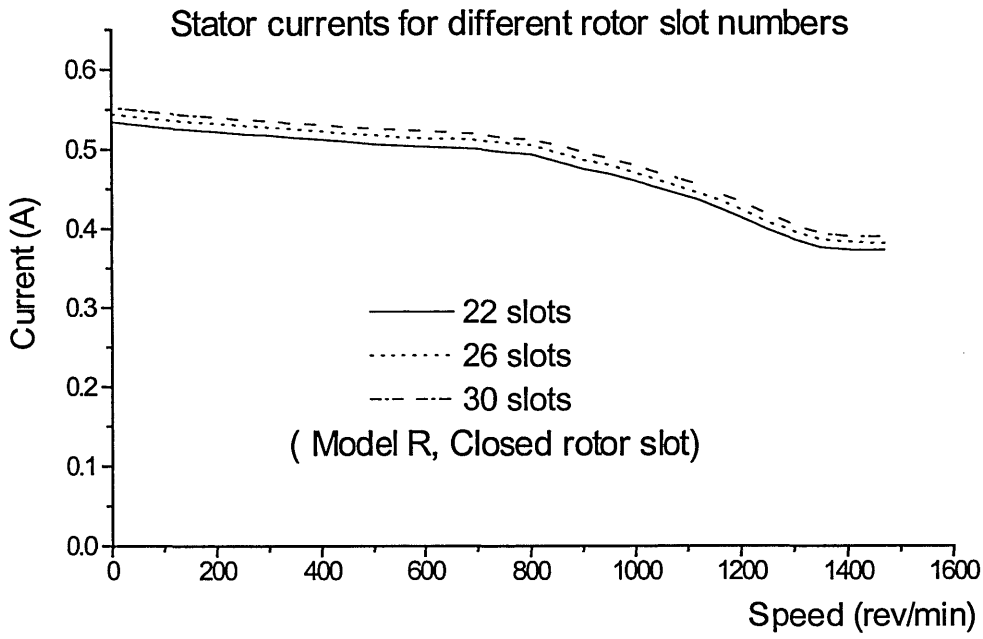

Fig. 5.19a) Model R, closed rotor slot (T_{SB} =0.15mm)

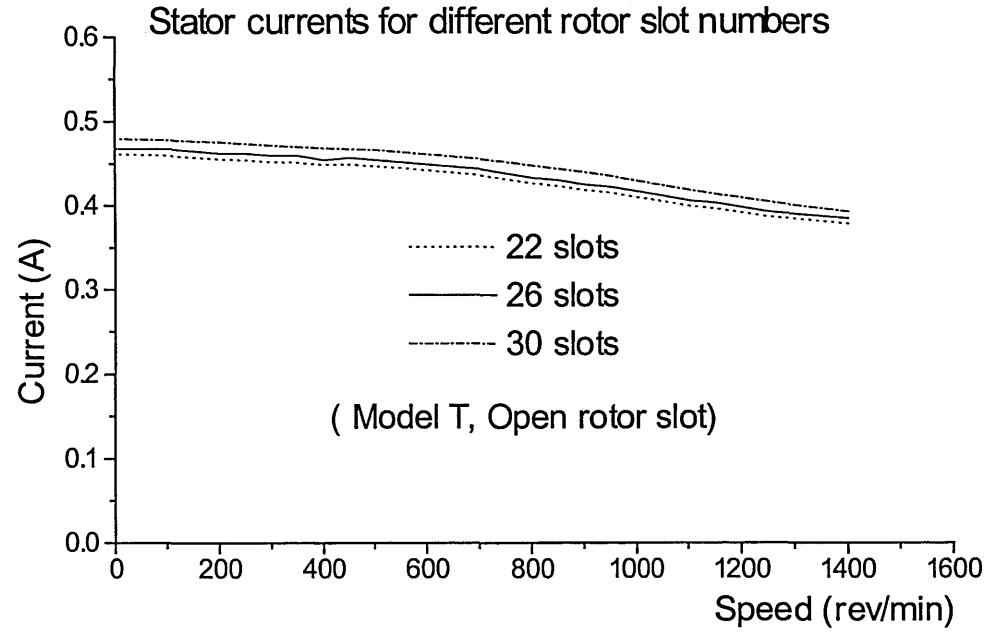

Fig. 5.19b) Model T, open rotor slot

Fig. 5.19 Comparison of stator currents for different numbers of rotor slots

The Fig. 5.18a and Fig. 5.18b present comparison of the torque variation with speed for different numbers of rotor slots. Although a large number of rotor slots gives an

advantage in terms of the ouput torque, especially for the maximum torque, the different slot numbers cannot change the shape of the torque/speed curves notably. For example, the torque dip near 600 rev/min in Model R occurs for all three slot numbers; however, the torque dip due to the third harmonic does not appear in Model T when using the same three slot numbers. In fact, another two unusual rotor slot numbers, 24 and 28, were also investigated in this study, and the results for the calculated torque did not show a greater difference compared with the torque curves for the above three rotor slots. It was considered that the spatial harmonic distribution in the air gap of a SPIM was mainly decided by the stator design because the salient pole is always used, consequently, the choice of the rotor slot number cannot make the harmonics change significantly if the number of rotor slots was large enough.

Besides the rotor slot number, using the closed-slot rotor shown in Fig. 5.20 is another issue of SPIMs design. For the normal poly-phase induction motor, introducing a closed-slot rotor can significantly reduce the effect of harmonics and noise although it may increase the slot leakage and therefore decrease the output torque. However, since the slot-bridge for the closed-slot is usually the most saturated part in of the machine, employing a slot leakage reactance model to calculate the effect of slot-bridge in a normal equivalent circuit cannot lead to a precise result. There was no guide rule on the closed-slot rotor given in previous published papers or books for SPIMs analysis and design. Therefore, in this section, the difference on motor performance between closed-slot and open-slot were studied. Fig.5.21 shows the comparison of the torque and current variation for a closed-slot rotor and an open-slot rotor.

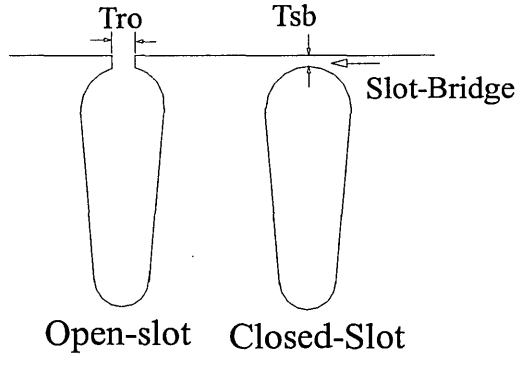

Fig. 5.20 Constructure of open- and closed-slot

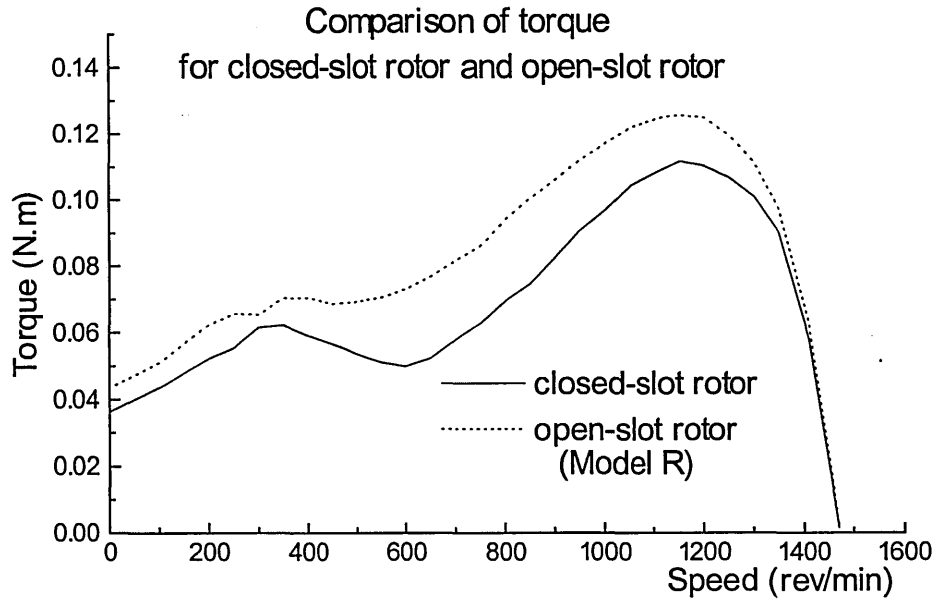

Fig. 5.21a) torque versus speed curve

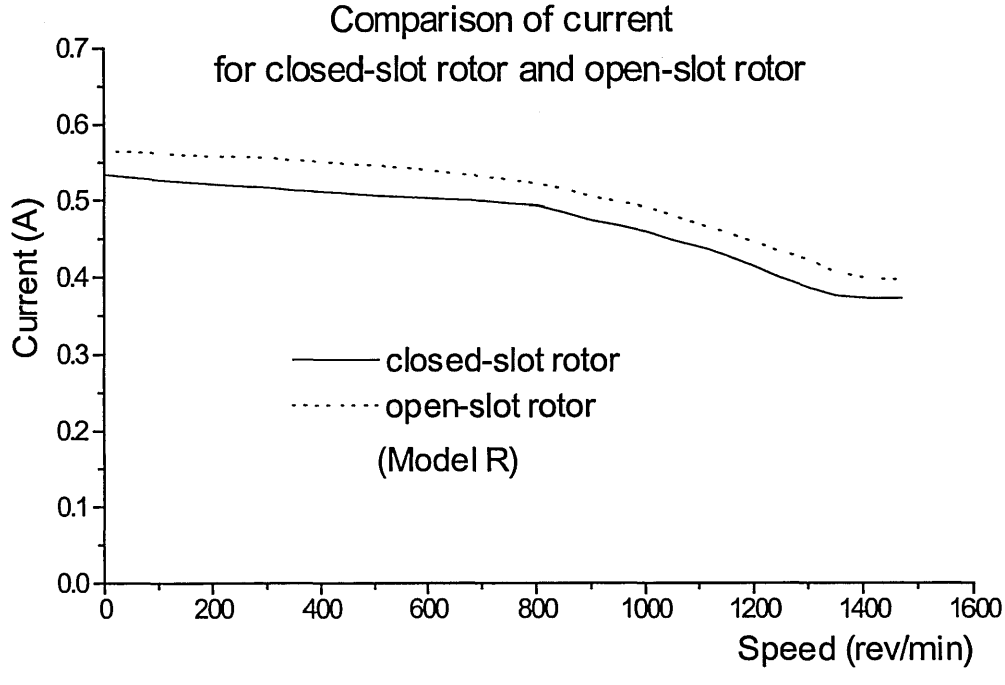

Fig. 5.21b) current versus speed curve

Fig. 5.21 Comparison of the torque and current variation with speed for closed-slot rotor (T_{SB} =0.15mm) and open-slot rotor (Model R).

It is seen that, in the most of the torque/speed curve, the model with the open-slot rotor produces a greater output torque than the model with the closed-slot rotor does. To examine the differences between the two designs, the magnetic field at 600 rev/min was calculated and harmonic analysis results for both the air gap field and rotor-bar current are given in Table 5.6, Fig. 5.22 and Table 5.8 accordingly.

Table 5.6 Comparison of spatial harmonic distortion between closed- and open- rotor slot (Model R at 600 rev/min)

	DF_3	DF_5	DF_7	THD
Closed-rotor slot	0.3390	0.2322	0.1746	1.5119
Open-rotor slot	0.4551	0.2935	0.2118	2.0885

In Table 5.6, the machine with the closed-slot rotor has smaller harmonic distortion factors for all the main harmonics, which indicates that the spatial harmonic in the air gap field may be notably reduced by using the closed-slot. Therefore, the magnetic field gets a better waveform using the closed-slot rotor.

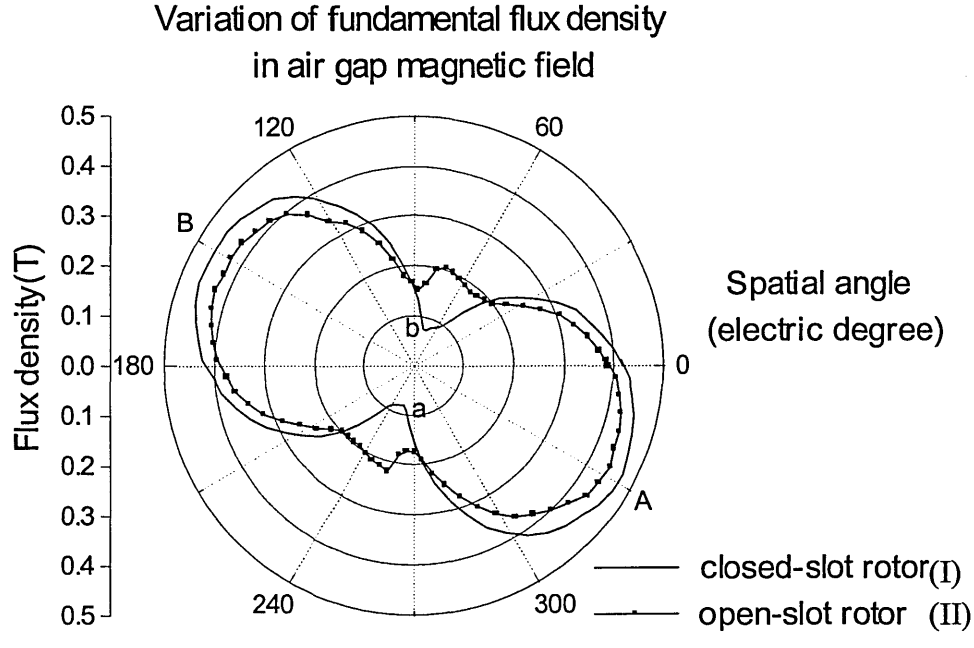

Fig. 5.22 Comparison of the variation of the fundamental flux density in the air gap for open-slot rotor and closed-slot rotor at 600 rev/min (Model R)

In Fig. 5.22, It can be seen that the maximum magnitude of the fundamental flux density of motor I using the closed-slot is greater than that of motor II using the open-slot. However, the minimum value of the fundamental flux density of motor I using the closed-slot is much smaller compared with motor II using the open-slot. To check the influence of the slot design on the rotating magnetic field, the flux densities of the forward- and backward-rotating field were calculated and shown in Table 5.7. It was found that motor I with the closed-slot had a weaker forward-rotating field and a stronger backward-rotating field compared with motor II with the open-slot. Therefore, the motor using the closed-slot rotor may produce less torque output accordingly.

Table 5.7 Comparison of the flux densities of the forward- and backward-rotating field for closed- and open- rotor slot (Model R at 600 rev/min)

	L_{AB}	L_{ab}	B_f(T)	B_b(T)
Closed-rotor slot	0.95	0.17	0.28	0.195
Open-rotor slot	0.86	0.36	0.305	0.125

Table 5.8 Variation of the rotor current harmonics of closed-slot rotor (T_{SB} =0.15mm) compared with open-slot rotor (Model R, 600 rev/min)

	Frequency(Hz)	Variation(%)
Fundamental(Forward)	30.0	-20.3
Fundamental(Backward)	70.0	-21.5
3rd order (Forward)	10.0	-20.6
3rd order (Backward)	110.0	-44.1
5th order (Forward)	50.0	-14.4
5th order (Backward)	150.0	-49.0
7th order (Forward)	90.0	-12.0
7th order (Backward)	190.0	-38.2
9th order (Forward)	130.0	+79.0

* The result of the open slot rotor is set as the criterion

Additionally, due to the existence of the slot-bridge, part of the fundamental flux in the air gap only passes though the slot-bridge and comes back to the stator directly without

linking the rotor bar, so the total flux linking both stator coil and rotor-bar circuit is decreased. From the point of view of the flux leakage, the closed-slot increases the leakage of the rotor slot significantly. Consequently, the magnitude of the fundamental of the induced rotor-bar current is reduced, which can be seen in Table 5.8. Hence the output torque shrinks as well. The scale of leakage increase depends mainly on the saturation scale of the slot-bridge and the thickness of the slot-bridge. If the flux density in the air gap is very high, e.g. 0.7T - 0.9T in effective value, and slot-bridge is very thin, e.g. 0.2mm, the flux density in the slot-bridge of the closed-slot becomes highly saturated. Thus the slot leakage will not increase significantly compared with the open-slot rotor. Unfortunately, for SPIMs, the effective value of the air gap flux is usually below 0.5T, so the slot-bridge may become highly saturated only if the thickness of the slot-bridge is very small. However, a small thickness of slot-bridge, e.g. less than 0.1mm, is too difficult to be secured during manufacturing.

Generally, it is not suggested that the design of SPIMs employs a closed-slot rotor. Such a conclusion is also verified by Model T when the torque comparison between closed-slot and open-slot is shown in Fig. 5.23.

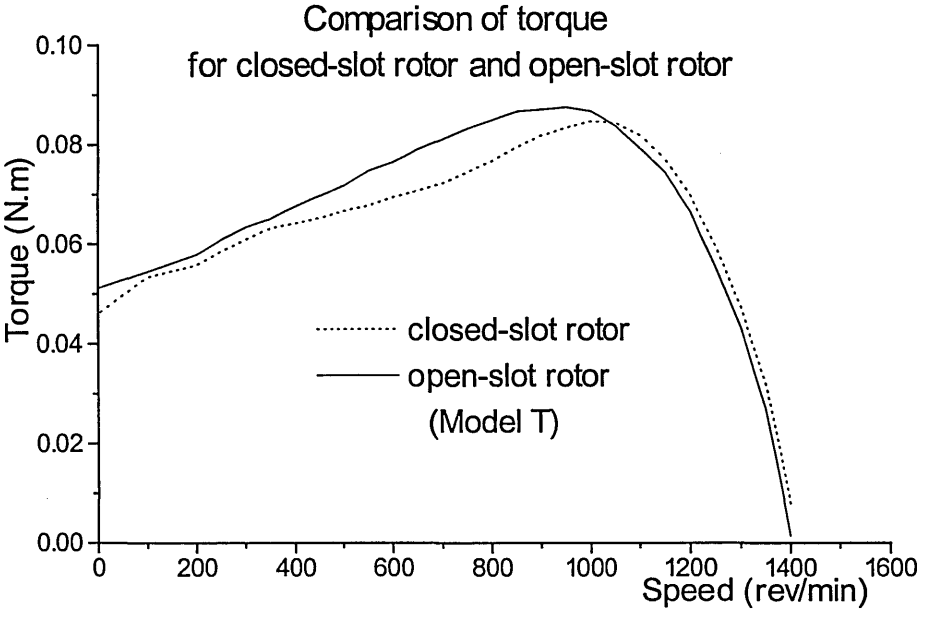

Fig. 5.23 Comparison of the torque variation with speed between closed-slot rotor (T_{SB}=0.1mm) and open-slot rotor (Model T).

5. 6 Effect of Shaded-Pole Arc

The shaded-pole arc has been discussed in several previous papers. Trickey [1936] claimed the best overall ratio for the shaded-pole arc against the total arc face was between 0.25 and 0.5. When the motor is designed for continuously running, the value 0.3 is often chosen. If the maximum starting torque is the only design goal, a bigger value – up to 0.5 – is required. According to the curve describing the torque variation against shaded-pole arc given by Moczala [1987], the best shaded-pole arc for the starting torque and the breakdown torque is between 30 and 60 electrical degrees. In Butler's paper [1969], 40 electrical degrees was recommended as the best shaded-pole arc to obtain the maximum starting torque and breakdown torque under a given temperature-rise condition.

In this study, three SPIM models with the different shaded-pole arcs of 20°, 40° and 60° were meshed and their performances were calculated with the proposed 2D multi-slice FE method. Fig. 5.24 shows the torque variation with speed for different shaded-pole arcs. It is seen that the 40° shaded-pole arc gives both the maximum starting torque and breakdown torque. In Fig. 5.25, the input current variations are presented. It is also found that the 40° shaded-pole arc produces the lowest input current for the whole speed range. In order to examine the effect of different shaded-pole arcs on the rotating field, the locus plotting of the fundamental components for the 20° and 40° shaded-pole arc designs are drawn under the locked-rotor condition and shown in Fig. 5.26. In Fig. 5.26 the phase angle difference between the two cases can be clearly seen and it is found that the forward-rotating fundamental component of the 40° shaded-pole arc is bigger than that of the 20° design. Consequently, a bigger starting torque and the breakdown torque are obtained by using the 40° shaded-pole arc.

Although the angle of the shaded-pole arc for the best starting and breakdown torque may not be exactly 40° and, for the different SPIM designs, the best angle may vary slightly. It is believed that the 40° shaded-pole arc can deliver a satifactory performances for the usual design.

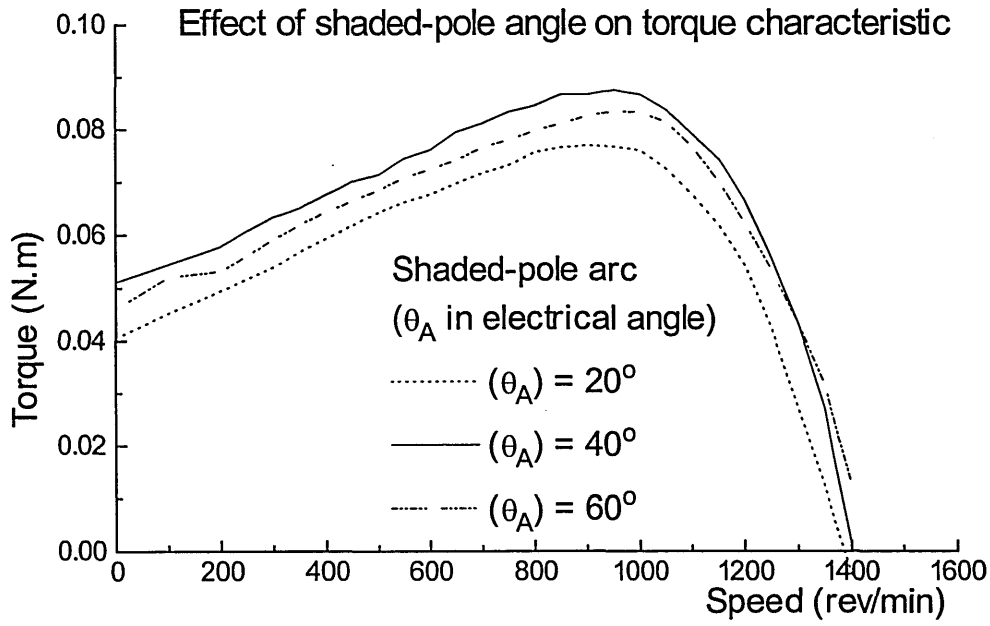

Fig. 5.24 Comparison of the torque variation with speed for different shaded-pole arcs (Model T).

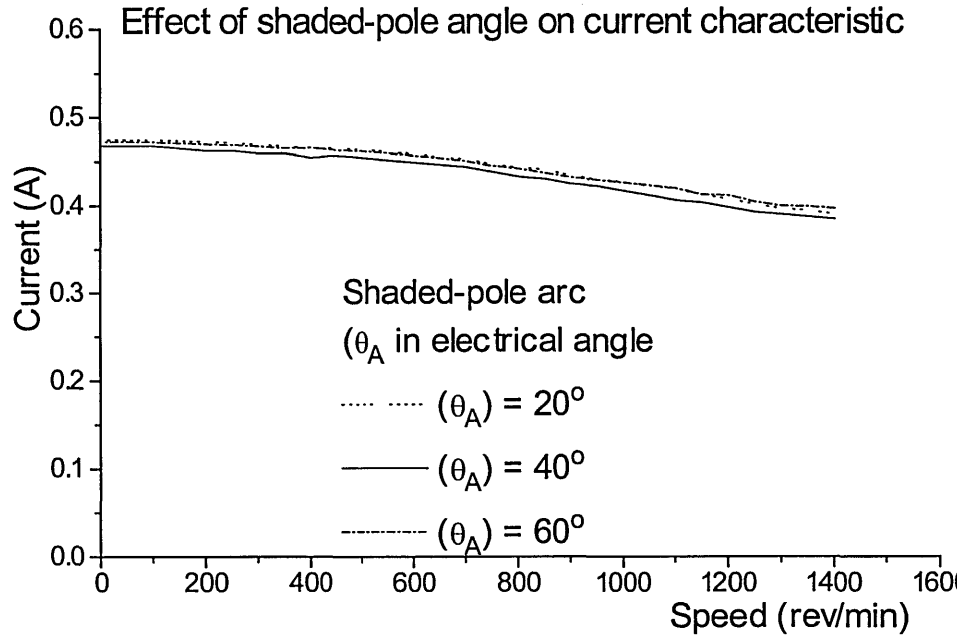

Fig. 5.25 Comparison of the stator current variation with speed for different shaded-pole arcs (Model T).

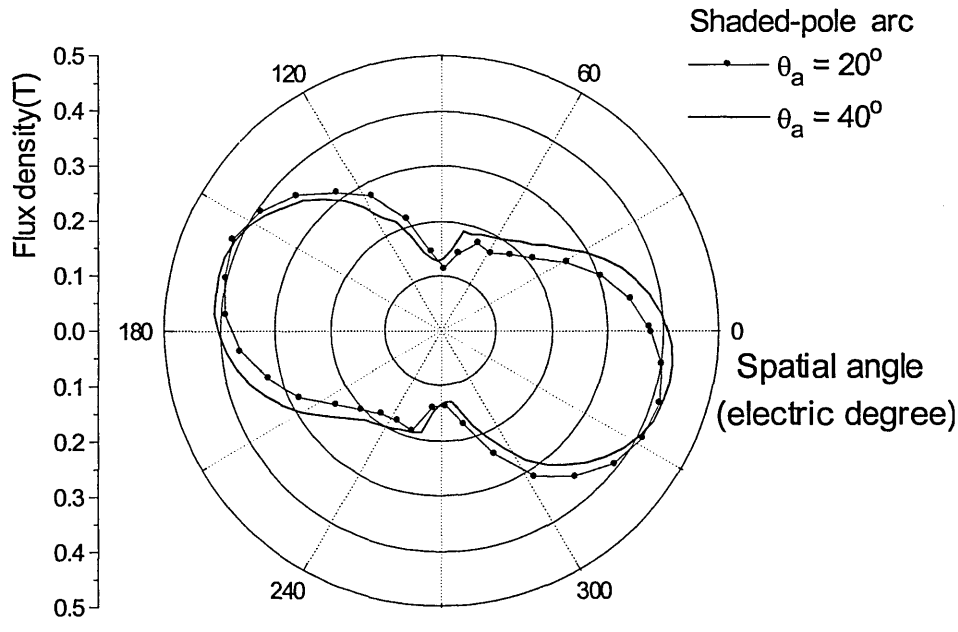

Fig. 5.26 Locus plotting of the fundamental component for 20° and 40° shaded-pole arc designs at zero speed (Model T).

5. 7 Conclusion

The two-dimensional multi-slice finite element model, a highly accurate tool for electrical machine analysis, was developed in the previous chapters and was ready for applying to SPIMs design analysis. Therefore, the focus of this chapter was on using the developed finite element tool to investigate the effect of the design parameters' variation on SPIMs' characteristics, especially on the torque performance.

Before examining the effect of varying parameters on the SPIMs' performance, a harmonic analysis method based on the time-stepping FE method directly was first introduced. Using this method, the amplitude of the fundamental and the higher-order harmonics was refined from the air gap flux distribution calculated by the time-stepping finite element model, and the variation of all harmonic components with time was therefore visualised. Hence, the total harmonic distortion (THD) and the distortion factor

(DF) could be adopted to measure the magnitude ratio between higher-order harmonics and the fundamental component in the air gap field. As a result, the effect of the design parameters on each air gap MMF harmonic can be studied directly. Certainly, The same analysis method can also be used to estimate the time harmonics in the rotor-bar current which has a direct relationship with the output torque.

With the aid of the proposed harmonic analysis tool and the finite element method, several design parameters, including the air gap profile, the pole-bridge, the skew, the number of rotor slots, the closed-slot rotor and the shaded-pole arc, were investigated in this chapter and the following conclusions can be drawn from the study.

1. Using the pole-bridge increases the leakage of the main pole flux quite significantly, therefore, the output torque will decrease accordingly. The improvement in the flux waveform of the air gap field is very limited using the pole-bridge.

2. The skew is the essential parameter for reducing the harmonic current in the rotor-bar, although it cannot change the flux waveform of the air gap magnetic field notably. The skew angle of SPIMs is larger than that of normal three-phase or other kinds of single-phase induction motors. The effect of skew on maximum torque depends on each particular design. Usually, a skew angle between 40 and 60 electrical degree is a suitable angle for both the maximum torque and starting torque.

3. The step air gap can help improve the starting torque, but its effect is not significant for a small SPIM with closed-slot rotor. However, a large step air gap presents some benefit in removing the torque dip due to the third order harmonic and it can also eliminate other higher-order spatial harmonics.

4. A large number of rotor slots gives an advantage in terms of the ouput torque, especially the maximum torque, but changing the slot number cannot change the shape of the torque/speed curves significantly. The number of rotor slots does not have a significant effect on the spatial harmonics of the air gap field.

5. Although the closed-slot rotor can reduce the spatial harmonics, it is not suitable for SPIMs because the rotor slot leakage will increase quite significantly and the forward-rotating field may be decreased.

6. The best shaded-pole arc is about 40 electrical degree. With this shade-pole angle, both the starting torque and maximum torque can be kept within a suitable range.

The performance of a SPIM depends on the combination of a set of design parameters. All the above conclusions are suitable for usual situation. For a specific design, the influence of design parameters on the machine's performance may be slightly different. For designing a SPIM for a particular specification, the most difficult problem is to choose the proper value for each design variable. For such a problem, an optimisation program is of great help.

6 OPTIMUM DESIGN OF SPIMS BASED UPON DIRECT FINITE ELEMENT METHOD

6. 1 Introduction

A general optimisation problem can be formulated as follows: find the values of m variables $x_1, x_2, x_3, \ldots x_m$, denoted for brevity by x, which satisfy the given constrains, a set of given equations or/and inequalities, and optimise (minimise or maximise) the objective function $f(x)$ [Walsh, 1975; Ratschek, 1988]. Since the problems of minimising $f(x)$ and maximising $-f(x)$ are equivalent, the optimisation problem can be generalised as:

$$\min_{x \in R^m} f(x) \tag{6.1}$$

subject to

$$g_i(x) \le 0 \qquad i = 1, \cdots, k,$$
$$h_i(x) = 0 \qquad i = k+1, \cdots, r,$$

where R^m denotes the m-dimensional space formed by the optimisation variable vector $\{x\}$.

In the vector notation this general problem is written as

$$\min_{x \in R^m} f(x) \quad s.t. \quad g(x) \le 0, \quad h(x) = 0 \tag{6.2}$$

where $g(x) = \{g_1(x), g_2(x), \ldots g_k(x)\}^T$ and $h(x) = \{h_{k+1}(x), h_{K+2}(x), \ldots h_r(x)\}^T$.

If there are no constraints ($r = 0$), the problem is said to be unconstrained, otherwise, it is

said to be constrained. The optimal design of an electrical motor is usually a constrained problem. The constraints of the electromagnetic devices are always inequality constraints including the geometrical structure, the electromagnetic performance and other design demands.

The optimisation procedure adopted in this study, which was based upon the direct FE analysis, can be described with the flow chart of Fig 6.1. From the flow chart, it is clear that the search algorithm and the analysis tool are two key issues of the optimisation. In the optimisation procedure, the search algorithm takes charge of deciding the optimisation strategy or search direction, while the analysis tool is used to calculate electromagnetic performance of SPIMs from which the optimisation objective function can be evaluated. For the optimisation problem of SPIMs, both parts are the focus of the study.

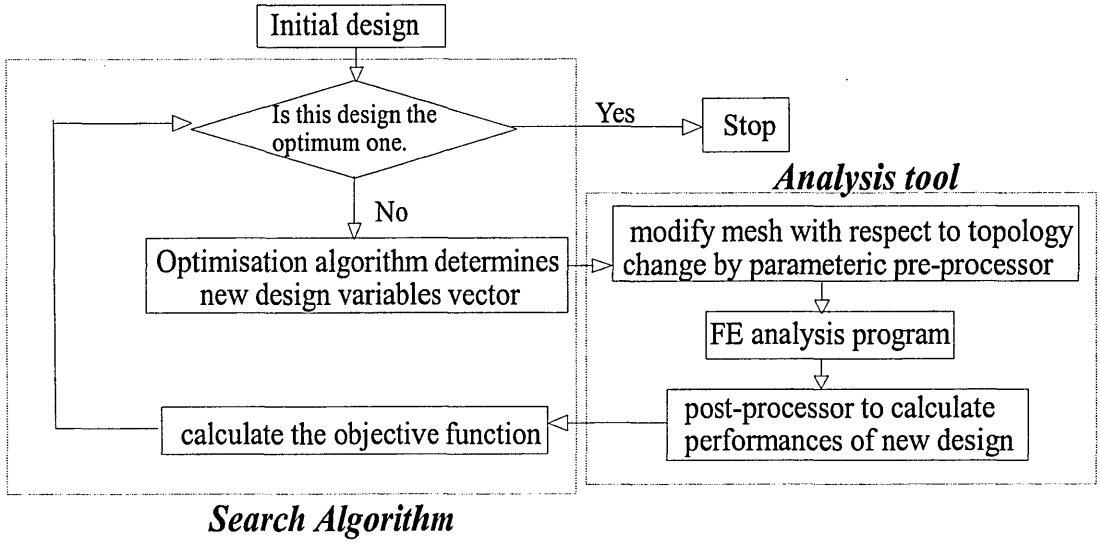

Fig 6.1 The procedure of a general optimisation

In this chapter, the different optimisation methods are investigated first, among which two different popular methods, the Genetic Algorithms and the modified Hooke–Jeeves' method, are introduced in detail. Based upon these two methods, a more efficient and reliable hybrid optimisation method is studied. Then, to produce the different meshes required by the FE analysis program when the machine geometry is changed, a partial auto-remesh program driven by the geometrical design parameters is developed.

Additionally, in order to save the computing time costs, a multi-slice sinusoidal approximation (fixed–mesh) FE model is employed to calculate the electromagnetic performance of SPIMs. To verify the validity of the approximation FE model under locked-rotor conditions, the calculated results obtained with this model are compared with that of the time-stepping method and the experimental results. In the final section of this chapter, the proposed optimisation program combined with the sinusoidal approximation FE model is applied for the optimisation design of SPIMs, and the maximum starting torque is set as the optimisation object.

6. 2 Improved Hybrid Optimisation Method

For the optimisation of SPIMs, there is a variety of optimisation algorithms available. The normal optimisation methods, which have been used for the design of electromagnetic devices, are classified in the following categories.

- Deterministic methods (Hooke-Jeeves' method, Powell's Method, Steepest Decent method, Quasi-Newton algorithm) [Li, 1990; Kamper, 1996; Brisset, 1998; Williamson, 1996; Brandstater, 1998]
- Stochastic method (Evolution strategies, Genetic Algorithms, Simulated Annealing and Monte Carlo method) [Simkin, 1992; Hameyer, 1996; Hameyer, 1994; Bianchi, 1998; Uler, 1996; Salujian, 1998]
- Artificial intelligence method (Artificial Neural Networks and Expert system) [Mohammed, 1992; Lowther, 1993; Rong, 1994; Dym, 1991]
- Enumerative methods
- Hybrid method [Messine, 1998; Kim, 1998; Mohmmed, 1998]

Normally, the performance of optimisation search algorithms can be judged by two big issues: the convergence speed and the global optimisation.

The deterministic method has been available for a long time [Walsh, 1975]. It has a rich theory, and many excellent numerical methods and recipes are available. Most deterministic methods, such as the Steepest Decent method, the Gradient method and the Quasi-Newton algorithm, involve numerical differentiation to determine the direction of the search for the optimum. For those deterministic methods relying on differentiation, the sensitivity analysis of design parameters, which is the derivative of objective function with respect to a design variable, is the most important one. Some researchers have formulated their optimisation problems in terms of design variables and their derivatives directly [Brisset, 1998; Park, 1995]. However, for the optimisation problems of electromagnetic devices design, it is always very difficult to calculate the derivatives of the design parameters directly because some design variables only have discrete values, e.g. turns of the stator winding and coil layers, and the relationships between the optimisation objective and the design variables are highly non-linear. To avoid this trouble, other kinds of deterministic methods (such as the Hooke–Jeeves' method and the Powell's method) that do not need the derivatives of the objective function have been applied for electrical machine design. The greatest benefit of the deterministic method is its fast convergence speed compared with other kinds of search algorithms. However, these methods are usually considered as local optimisation method, which means that the global optimisation in the whole feasible area can not be secured.

Nowadays, more importance has been attached to the stochastic methods that can secure the global optimisation result. With the stochastic methods, the variation of the objective function due to random variation of the design variables can be accepted with a probability and certain rules. The most widely used stochastic methods are the Simulated Annealing and the Genetic Algorithms.

Simulated Annealing (SA) comes from the analogy with metallurgical annealing. In metallurgical annealing, the metal is heated near its melting point and then is cooled down slowly [Simkin, 1992; Hameyer, 1994, 1996]. The essence of this procedure is that the global energy function of the metal will eventually reach a minimum value. The basic idea of SA is to provisionally change a single randomly selected variable of the system at a time. If the change resulted in a lower overall global system energy, the change would

then be accepted. If the change resulted in a higher global energy of the system, then this change would be accepted with a probability. Since the stability of the optimisation progress cannot be always achieved, an improved simulated annealing method was developed by Uler and Mohammed [1996]. This improved method separates the search track and the update sequence by using two arrays to record the state, one for the current global state of the network and another for the global state of the current minimal energy.

The genetic algorithm is one of the most up-to-date optimisation technique and it has been mentioned frequently in recent publications on optimisation problems [Bianchi, 1998; Uler, 1996; Salujian, 1998]. It is a search procedure emulating the mechanism of natural selection and genetics. GAs use probabilistic transition rules. Compared with other traditional optimisation methods, GAs are different due to the fact that: (1) GAs operate on a group of points in the search space simultaneously rather than on just one point, (2) they work with a coded string representing the parameters instead of the parameter itself. The GAs share the same advantages and disadvantages of all the stochastic methods. They work well with non-linear multi-dimension optimisation problems and could successfully avoid any local optimums. However, GAs require a long computing time. It is commonly considered that GAs exhibit fast and good convergence rate only at the beginning of the searching process, but once the search procedure evolves with time, the convergence rate becomes extremely slow.

During the past years, the Artificial Neural Networks (ANNs) have been applied to many engineering problems ranging from search operations in optimisation to auto-mesh for FE analysis [Mohammed, 1992; Lowther, 1993]. The ANNs are massively parallel interconnected networks of simple adaptive neural elements. After they have been trained with a variety of different designs, the ANNs can reflect the high non-linear relationship among design parameters and the performances of the electromagnetic devices by adjusting the parameters of each element. Therefore, once a new design demand is fed in, the trained ANNs can yield an optimal design. Besides relying on the proper structure of neural network, the validation of ANNs method also depends on the training data given in advance. Compared with other optimisation methods, the trained ANNs can produce the optimum design at very high speed, but the procedure of training will take a considerably long time.

Like the ANNs, the expert system is also a knowledge-based optimisation method. Since the problem of representing expert's knowledge is still unsolved, this kind of method has not achieved great success in optimisation design of electromagnetic device [Rong, 1994; Dym, 1991].

Generally speaking, the deterministic methods have the fastest convergence speed while they suffer from the limitation of the local optimisation. To the frequently used stochastic methods, like Genetic Algorithms, the slow convergence speed hinders it from applying on the FE based optimisation although they can get the global optimum design. Therefore, the hybrid methods, which combine the stochastic methods with one of the deterministic methods, are utilised to help the numerical optimisation models escape from the local minimum or to improve the convergence speed of the stochastic methods. In this study, an improved hybrid method based on an efficient integration of the GAs and modified Hooke-Jeeves method is proposed. The detail of the proposed method is introduced in this section.

6.2.1 Genetic Algorithms.

Genetic algorithms have been successfully applied to optimisation problems in many areas. The important work of Holland [1975] sets up the fundamental of the GAs which is popularised by Goldberg's book [1989]. Although GAs have been known since 1975, the first papers in literatures applying GAs in electromagnetic were only published in 1994 [Vasconcelos, 1994; Uler, 1994]

The GAs act on a set of possible solutions, usually referred to as a population of individual. All optimisation variables of these individuals are encoded into the form of genetic code, the chromosome. The technique for the encoding solution may vary from problem to problem and from genetic algorithm to genetic algorithm, and probably no method works best for all problems. However, in most studies of using GAs, the encoding

is carried out using the binary string. Compared with other encoding method, the binary encoding is easy to be applied and the scale difference among each variable disappears. Therefore, this technique was adopted in our study.

Using the binary encoding, a real optimisation variable is discretized and is represented by a string of binary character $A = a_L a_{L-1} a_{L-2} \cdots a_3 a_2 a_1$. The string length L is decided by the precision required for parameter representation. For a variable x, which is bounded between x_{min} and x_{max}, the string length L can be calculated with the given discretization precision, x_{step}, by the following equation.

$$L = \text{int}(\log_2 \frac{(x_{\max} - x_{\min})}{x_{step}} + 1). \tag{6.3}$$

On the contrary, once the binary string is known, the parameter value can be decoded by using the equation (6.4). Some examples of coding and decoding between binary string and parameter value are given in Table 6.1,

$$x = x_{step} \sum_{i=1}^{L} a_i \cdot 2^{i-1} + x_{\min} \tag{6.4}$$

Table 6.1 Example Of coding and decoding between binary string and parameter value

Boundary of x	Discretized Step	String Length	Value x	Binary String
[10, 138]	2	7	124	0 1 1 1 1 0 0 1
			80	0 1 0 0 0 1 1
[1.2, 7.6]	0.1	5	6.0	1 1 0 0 0
			4.7	1 0 0 1 1

1 0 1 1 0 1 1 0 0 0 1 1 1 0 1 0 1 1 ..... 0 1 1 1 1 1 0 0 0 1 1 1 1 0 1 0 1

$L_1 = 6$	$L_2 = 5$	$L_3 = 7$	$L_{n-2} = 4$	$L_{n-1} = 8$	$L_n = 5$
var 1	var 2	var 3	var n-2	var n-1	var n

Fig 6.2 Multi-parameter code costruction

When there are several optimisation variables, they can be represented by a single binary

string. In the string, the first variable takes the initial L_1 position, the second takes the next L_2 position, and etc. The picture in Fig 6.2 shows a string with n optimisation parameters.

Once all the optimisation variables have been encoded, the GAs is ready to be applied. The algorithmic description of a genetic algorithm shown in Fig 6.3 describes most genetic algorithms, but different researchers have implemented this description in different ways.

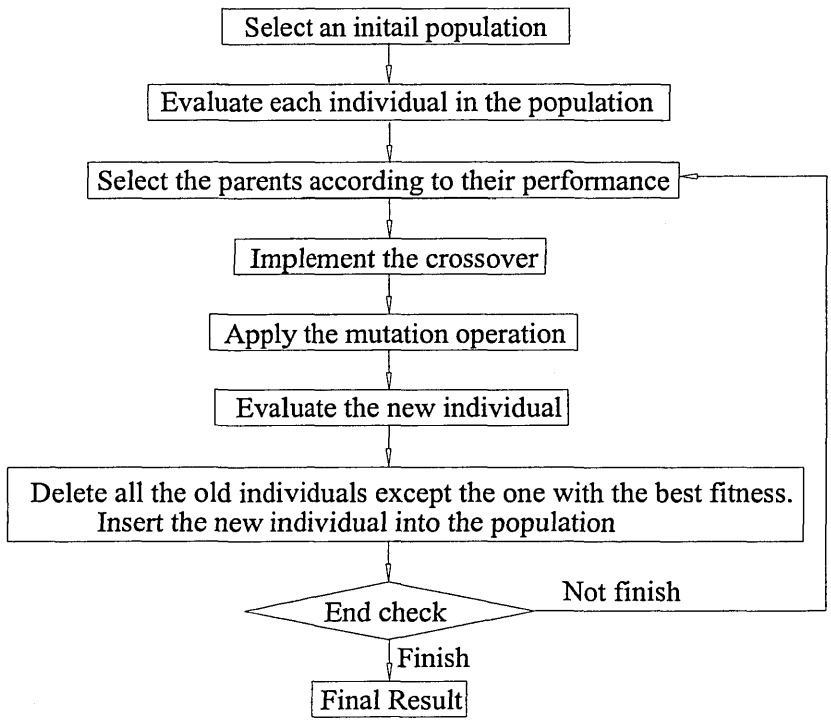

Fig 6.3 Flow chart of the Genetic Algorithms

In the flow chart of Fig 6.3, there are three fundamental operations involved in the GAs search process, which are the parent selection, the crossover and the mutation. The combination of these three operations is usually called reproduction.

The purpose of the parent selection is to give more reproductive chances, on the whole, to those individuals that are most fit. In the other words, the stronger individuals have more chance to survive. The strength of each individual is measured by the fitness. In most situations, the fitness function is closely related to the objective function and often

coincides with it. Using the fitness, one commonly used implement is the roulette wheel parent selection. The roulette wheel parent selection procedure can be described by three main steps,

1) Sum the fitness of all the individuals in one generation. The final summation is called total fitness;
2) Generate a random number, N_{rondom}, between 0 and the total fitness;
3) Return the individual whose fitness, adding to the fitness of all the preceding population member, is greater than or equal to N_{rondom}.

Table 6.2 shows an example of parent selection with a population of six chromosomes.

Table 6.2 Examples of roulette wheel parent selection

Individual Number	1	2	3	4	5	6
Fitness	2	12	8	6	20	16
Running Total	2	14	22	28	48	64

Random Number (N_{rondom})	5	32	56	15	44	21
Individual Chosen	2	5	6	3	5	4

Although the new individual is chosen randomly with the roulette wheel parent selection, each parent's chance of being selected depends directly on its fitness. The individual with higher fitness has more chance to be promoted. In the Table 6.2, the 5^{th} individual, who has the highest fitness, is selected twice while the 1st individual has been excluded due to its lowest fitness.

The operation of the crossover occupies a special place in heart of the Genetic Algorithms. Without the crossover operation, the Genetic Algorithms do not exist. In nature, crossover occurs when two parents exchange parts of their corresponding chromosomes. In the genetic algorithm, crossover recombines the binary string of two parent chromosomes to make two children. A conventional crossover operation is called

one-point crossover. Using this method, the chromosomes of the two children are produced by swapping parts of the two parents chromosomes after a randomly selected point. Fig 6.4 shows two examples of the one-point crossover.

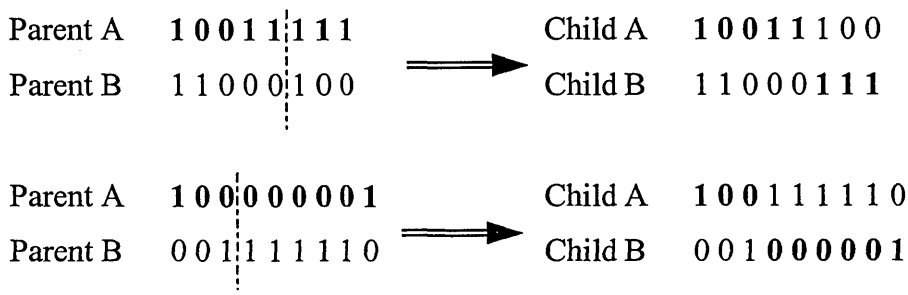

Fig 6.4 Two examples of one-point crossover.

An important feature of the one-point crossover is that it can generate children that are totally different from their parents. The second example among the above figure shows such a case.

Besides the one-point crossover, another important crossover method is called the uniform crossover. With the uniform crossover, each bit position of the two children gets the value from either father's or mother's chromosomes randomly. Fig.6.5 gives an example of the uniform crossover operation. For each bit position on the parents, the template indicates which parent will contribute its value in that position to the first child. The second child receives the bit value in that position from another parent. Each bit of the template is decided randomly when the crossover operation occurs.

Parent A	1 0 1 1 0 1 1 1 1 1
Parent B	0 1 1 1 0 0 0 1 0 0
Template	1 1 0 0 0 0 1 1 0 1
Child A	1 0 1 1 0 0 1 1 0 1
Child B	0 1 1 1 0 1 0 1 1 0

Fig 6.5 Example of the uniform crossover.

Compared with the one-point crossover, the location of encoding of a feature on a chromosome is irrelevant to the uniform crossover and the operation of crossover of the uniform crossover is more global. In this study, the uniform crossover operation is used.

The operation of the crossover is not always applied to every pair of parents selected. Only the parents who pass the test of the crossover probability will be applied with the operation. In the test, a random number, normally between [0, 1], is generated and compared with the given crossover probability. The crossover occurs only when the number is less than the crossover probability. For the parents who do not pass the test, their children's chromosome is as same as one of their parents. For the one-point crossover, this probability is set between 0.6 and 0.7. For the uniform crossover, 0.5 is recommended.

Unlike the crossover, the mutation operation changes only one bit each time in a chromosome string. During the mutation operation, each chromosome in the population is checked bit by bit. For each bit, a random number between [0, 1] is generated, this number is compared with the assumed mutation probability. If the number is less than the given probability, the value of bit is reversed, so 1 is changed into 0 or vice verse. Table 6.3 contains three chromosomes with 4 bit length in mutation operation.

Table 6.3 Mutation operation with mutation probability $p_m = 0.06$.

Old Chromosomes	Random Numbers	New Bit	New Chromosomes
1 0 1 1	.781 .152 .678 .290	-	1 0 1 1
0 1 1 0	.812 .523 .487 .009	1	0 1 1 1
1 0 0 1	.052 .171 .784 .390	0	0 0 0 1

The mutation operation shown in Fig 6.3 is called the Jump Mutation. Although the mutation operation only randomly change a bit in a chromosomes, the chromosomes can still be modified significantly when the bit changed happens to be the left-side bit of a parameter string.

Another kind of mutation operation named Creep Mutation, which only increases or decreases one step size for the chosen parameter, is also widely used. Using the Creep Mutation, the chromosomes standing for a set of design parameters is decoded first, then each parameter rather than the bit of chromosome in the Jump Mutation is checked with mutation probability. If the random number for a parameter is less than the given probability of the Creep Mutation, this parameter is increased or decreased randomly.

Normally, the mutation probability of the Jump Mutation is much bigger than that of the Creep Mutation. For the Jump Mutation, the typical mutation probabilities set for two methods, p_{jump_M} and p_{creep_M}, are calculated as:

$$p_{Jump\_M} = \frac{1}{Npopsize}$$
$$p_{Creep\_M} = \frac{Nchroms}{Npopsize * Nparamts} \tag{6.5}$$

where *Npopsize* is the number of total individuals in the population, *Nchroms* denotes the bit length of the chromosomes and *Nparamts* is the number of total design parameters.

The end check is another issue of the conventional genetic algorithm. There is no direct evidence to show when the global optimisation is found by the genetic algorithm. The following criteria are commonly used.

1) *Number of generation*: This is the simplest case, but how does one know which number of generation is suitable for a particular problem? To secure the global optimisation, a big enough number is always defined. This is one reason why the genetic algorithm is so time-costly.

2) *Average fitness in a generation*: In this case, the procedure of the genetic algorithm stops the search when the average fitness reaches a certain figure. Using this criterion can not secure the global result either, but in engineering design, a set of better designs are also very important. For this method, the difficulty lies in that the designer should know how far the optimisation can go.

3) *Difference of the best fitness among a set of generations*: With this criterion, the search of genetic algorithm stops when the value of the best fitness is not stable or changes very little in several generations. This criterion will lose its sensitivity to the problem whose global result is difficult to be found. Another similar criterion is the difference of the average fitness among a set of generations.

So far, the GAs are only discussed for searching the unconstrained objective function. However, for the optimisation of electrical machines, the inequality constraints due to the performance requirement and the geometric limitation always exist. To deal with the constrained problem, the modification of the fitness calculation is normally used. For each individual, the solution is checked to see whether any constraints are violated. If not, the parameter set is assigned the fitness value corresponding to the objective function evaluated. If the constraints are violated, the solution is infeasible and therefore no fitness is given. This method is very similar to the Penalty method used in the deterministic optimisation methods.

6.2.2 Modified Hooke–Jeeves Method

Besides its fast convergence speed, the modified Hooke-Jeeves method does not need differentiation and it only relies on the value of objective function. Consequently, it is suitable to solve the problems, which include the discrete optimisation variables, and it has been successfully used for the different optimisation problems of designing electrical machine [Li, 1990].

According to Li's method, the procedure of the modified Hooke–Jeeves method is mainly made up of two search operations, the exploratory moves and the pattern moves. In the exploratory moves, from the initial point, $X^{(k-1)}$, the value of each optimisation variable is increased and decreased with a given step size. By checking the variation of the objective

function, the best current point, $X^{(k)}$, is chosen among the previous point and the two exploration points. When all the optimisation variables have been investigated, the exploratory move is completed. Then, the pattern move, which indicates the move along the direction from previous point to current point, is executed and the new pattern point, $X^{(k+1)}$, is obtained. In the modified Hooke-Jeeves method, after arriving the pattern point $X^{(k+1)}$, a new pattern move is initiated without any exploratory move, which is different from the conventional Hooke-Jeeves method.

The detail of the procedure can be described as follows [Li, 1990].

1) Define the initial point $X^{(k-1)}$ which must be in the feasible region. The largest step size, which is different for each optimisation variable, is adopted.
2) Perform exploratory search for all optimisation variables to find current point $X^{(k)}$.
3) Execute pattern move. $X^{(k+1)}= X^{(k)}+\alpha(X^{(k)} -X^{(k-1)})$. Where α is an acceleration factor.
4) Set $X^{(k-1)}= X^{(k)}$.
5) Perform the tests for feasibility and improvement. Is objective function at $X^{(k+1)}$ decreased?
   If yes, $X^{(k)}= X^{(k+1)}$, go to step 3. Otherwise, go to the next step
6) Is the current step size the smallest one?
   If yes, stop, the optimisation design, $X^{(k)}$, has been reached. Otherwise, reduce the step size, then go to step 2.

In the above procedure, every point after the pattern move or the exploratory move is checked with the constraints to see whether the point is feasible or not. Hence, once the initial point is in the feasible region, the optimisation result can be secured to meet the constraint conditions.

If the initial point does not meet the constraints of optimisation, two options can usually be token. With the first one, a design parameter vector formed by randomly selecting the value of each variable in the given range is used as a trial point. If all the constraints are

satisfied, the optimisation search is launched from this feasible point, otherwise, go on to chooses another different point. This process usually takes a very long time to get a feasible initial point. With the second approach, a penalty function is introduced to the original objective function, and then the objective function is varied into the form of equation 6.6 [Walsh, 1975];

$$\min_{x \in R^m} \left(f(\mathbf{x}) + r_i \sum_i \frac{w_i}{[g_i(x)]^2} \right) \qquad (k = 1,2\ldots) \tag{6.6}$$

where $r_k > 0$ for all k when $g_i(x) > 0$, and $w_i > 0$ for all i. The w_i is a positive weighting factor that remains fixed throughout the optimisation, while the r_k decreases from one iteration to the next. Once the feasible initial point is achieved, $r_k = 0$, and the objective function reverts to the original one. The computing cost of the second method is superior to the first one.

In this study, the second method was chosen in the optimisation program developed.

6.2.3 Hybrid Global–Local Search Method

In order to overcome the drawback of low convergence rate of the GAs, much attention has been paid recently to the hybrid methods in which the deterministic methods and the GAs are combined and employed at different stages of the search [Vasconcelos, 1997; Fanni, 1999]. Generally, the GAs are used initially to locate the possible region of the solution containing a global minimum or maximum. Once this region is judged to be found, the search by the genetic algorithm is stopped and the deterministic method is launched from the refined initial vector of variables. In this way the global optimisation can be achieved rapidly. However, this kind of hybrid method suffers from the major difficulty of finding the moment to switch the search from the genetic algorithm to the deterministic method. It stands to reason that the global optimisation can be achieved in this way only when the region that includes the global solution has been bracketed first.

Therefore, an error in the estimation of this transition can lead to failure in reaching the final solution with the global maximum or minimum [Vasconcelos, 1997].

In this study, an improved hybrid global-local search method combining the niching GAs with a modified Hooke–Jeeves method was presented as the design tool for the SPIMs. The procedure of the proposed hybrid method, which works by co-ordinating the activities of the global search and the local search, is shown in Table 6.4 using pseudo-code.

Table 6.4 Outline of the Hybrid Global-Local Search Method

	Randomly select the starting population
Global search (Niching GAs)	Repeat evaluate the fitness of each individual implement niche on population perform parent selection and crossover apply mutation (jump and/or creep) until (fitness improvement is very little)
Local search (Direct Search)	apply the deterministic search from the chosen individuals
	Terminate if maximum generation is reached Otherwise go back to the Global search

In every global-local search iteration, the niching genetic algorithm is invoked first to explore the region of the global optimisation. Its efficiency is monitored by measuring the fitness improvement during the latest T_G generations with (6.7),

$$eff_G = \frac{1}{T_G - 1} \sum_{i}^{i_0} \frac{f_{Best}^{i} - f_{Best}^{i-1}}{f_{Best}^{i}} \qquad (i = i_0 - T_G + 1) \tag{6.7}$$

where f_{Best}^{i} is the best fitness at generation i_0.

The global search is repeated until the eff_G is smaller than a given small positive number. Then, a sequence of multiple local searches is launched. Within the latest population of GAs, the individual whose fitness is over the average value is chosen as the improved initial point of the local search. The local search proceeds until either a local optimisation is found or a maximum number of times T_L is exceeded. The local search result whose fitness is better than the best individual of the latest generation will be used to replace the original one, and the global search is resumed. This global-local search iteration is repeated until the stop criterion is reached.

Using such a proposed algorithm, some local optimisations can be found rapidly after the local search is invoked. If the normal GAs are used as the global search tool, when it is restarted again, the population will soon climb to one of the sub-global peaks, distributing most of the individuals near the top of this peak. Although the mutation operation can distribute the individuals into other search region, the search process will take a very long time and requires a big mutation probability. To overcome this drawback, the niching method is adopted in this paper [Goldberg, 1989]. With the niching method, the competition among the different sub-domains is reduced in the individual selection. Thus, a stable sub-population is able to form around each peak in the search domain. In other words, when the optimisation procedure is completed, besides the global optimisation, several better solutions can also be identified by the niching GAs.

A practical scheme that directly uses the fitness sharing to realise the niching is described by Goldberg [1989]. In this scheme, the fitness of each individual is shared among some individuals before the selection. The shared fitness $f_s(x)$ of each individual is calculated with the prior fitness $f(x)$ and the total sharing function $\sum_j^N s(d(x_i, x_j))$ as:

$$f_S(x_i) = \frac{f(x_i)}{\sum_j^N s(d(x_i, x_j))}. \tag{6.8}$$

In (6.8), the sharing function between the two individuals, x_i and x_j, is determined by their distance function $d(x_i, x_j)$:

$$s(d(x_i,x_j)) = \begin{cases} 1-(\dfrac{d(x_i,x_j)}{\delta_{Share}})^{\alpha}, & if \quad d \le \delta_{Share} \\ 0, & otherwise \end{cases} \tag{6.9}$$

where the α is a constant with respect to the shape of the sharing function. For the triangular sharing function used, $\alpha = 1$. The δ_{Share} in (6.9) is the sharing distance. All the distances used in (6.9) are all normalised with following equation,

$$d(x_i,x_j) = \sqrt{\sum_{k=1}^{N}\left(\frac{x_i^k - x_j^k}{x_{k,\max} - x_{k,\min}}\right)^2} \tag{6.10}$$

where N is the total number of the optimisation variables, and the $x_{k,max}$ and $x_{k,min}$ are the two boundary limits allowed for variable k.

The algorithm of local search used is the modified Hooke–Jeeves method which is a kind of direct search method, in which the derivatives of objective function are not needed. For each local search, the boundary of the search area for variable k from initial point i is determined as,

$$Boundry(x_i^k) = x_{i,initial}^k \pm \beta(x_{k,\max} - x_{k,\min}) \tag{6.11}$$

where the constant β, whose value is between 0.05 and 0.15, is decided according to the sensitivity of the variable k to the objective function. If the changes in the variable greatly influence the objective function, a small value of β is used, otherwise, it takes a bigger value.

In order to avoid the local search repetition in the same region, after each local search stops, the area defined by the boundary of each local search is marked. For the next local search, if the initial point drops into these marked regions, the local search will not be launched. The obtained optimisation of the respective area will be considered as the local optimum result in this area. Thus, the whole search area is reduced gradually and the total number of objective function calculations can be further reduced.

6.2.4 Test Problem

Before it is employed in the optimal design of a SPIM, the proposed optimisation algorithm is put to the test by solving an ideal mathematical problem in order to evaluate its performance. A simple two-dimensional function *f(x,y)* is chosen as a test bed. The two variables x and y are in the close interval [0, 10]. The function displayed in Fig 6.6 consists of five peaks (centre $c_i = (cx_i, cy_i)$, radius r_i and height d_i). Its function value can be described as:

$$f(x,y) = \begin{cases} \dfrac{d_i}{r_i^2}\bar{r}^2\left(\dfrac{\bar{r}_i^2}{r_i^2} - 2\right) + d_i & \text{for } \bar{r}^2 \le r_i^2 \\ 0 & \text{otherwise} \end{cases} \tag{6.12}$$

where $\bar{x} = x - cx_i$, $\bar{y} = y - cy_i$, $\bar{r}^2 = \bar{x}^2 + \bar{y}^2$, and c_i = {(2.0, 8.0), (3.0, 4.0), (5.0, 7.0), (7.0, 8.5), (7.0, 4.0)}, r_i = {1.5, 2.5, 1.0, 0.75, 3.0}, d_i = {2.0, 4.4, 3.0, 4.5, 4.0}. The global maximum is at (7.0, 8.5) and has a value of 4.5. Because the area of the second highest peak is much larger than that of the global peak and its peak value 4.4 is very close to the global maximum, the global peak is very difficult to find when a small population size is adopted.

The convergence characteristics of the niching genetic algorithm with the different population sizes are shown in Fig 6.7 compared with the results of the proposed hybrid algorithm. In Fig 6.7, the convergence speed of the hybrid method is much faster than that of normal niching GAs. Besides, with the proposed hybrid algorithm, the global peak can still be reached even in the situation of a small population size. Therefore, the reliability of the proposed hybrid GAs is improved for the small population size.

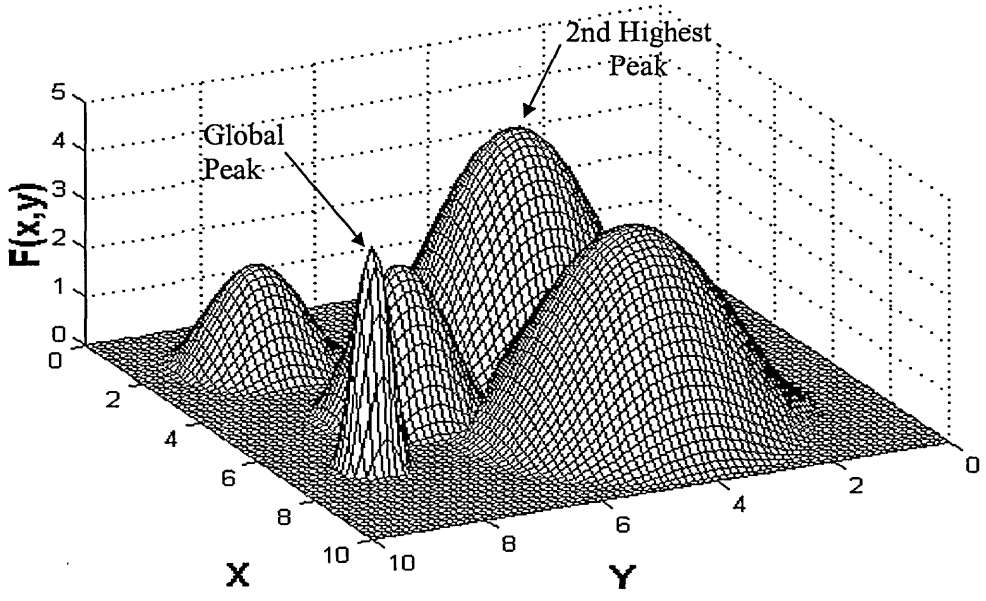

Fig 6.6 The testbed function f(x,y) shown in the top view.

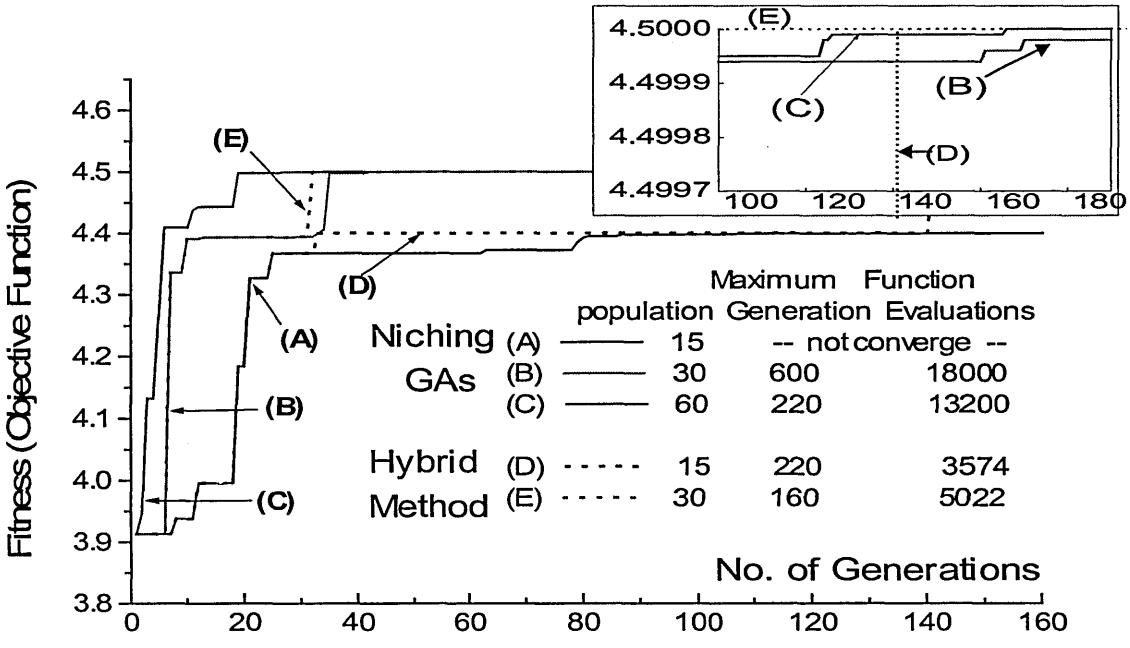

Fig 6.7 Comparison of convergence characteristic between two methods

(For all the cases shown here, the uniform crossover is used, the crossover probability = 0.5, the mutation probability = 1/population, $\delta_{Share} = 0.1$, $Tg = 6$.)

6. 3 Optimisation Variables And Parametric Pre-processor

For the SPIMs, there are a number of design parameters affecting the performance of the motors, but there is no chance to consider all these parameters as optimisation variables since it makes the scale of optimisation problem too big to be solved. Therefore, before employing the optimisation, the number of optimisation variables should be reduced as much as possible to increase the efficiency of optimisation procedure and the possibility of finding the optimisation goal. Based on the analysis of the effects of design parameters on machine performance in the former chapter as well as on the results of sensitivity analysis [Sadghi, 1995], three categories of design variables of the SPIM, which include (1) turns of stator coil, (2) rotor slot shape and (3) step air gap shape, are chosen as the variables in the optimisation. Because the shape parameters of rotor slot and step air gap are involved, the geometrical design of the SPIMs will be varied when these parameters are modified. Hence, a new mesh corresponding to the change of geometrical parameters should be generated automatically for the FE analysis program.

At present, there are no existing technique which can automatically create a new FE mesh depending only on the design parameters. Although some researchers are working on the parametric or automatic pre-processor for the FE method, the result is still very complicated and it only suits the simple structures of electromagnetic device [Hameyer, 1996, Mohmmed, 1998]. The popular way to auto-mesh for shape optimisation is called the point control method [Mohmmed, 1992, Park, 1995]. Fig 6.8 shows a case of using such a method for the optimisation of rotor slot shape. Its procedure can be described by two steps: 1) creating a initial FE mesh manually, 2) moving the selected control point with respect to the sharp variation. This method has two limitations: 1) to get a good geometrical (shape) description, a large amount of control nodes is needed; 2) when the scale of the geometrical change becomes bigger, the mesh may be distorted greatly.

In this study, the partial parametric pre-processor depending on a few key design parameters (Table 6.5) has been developed. With this method, the mesh of rotor slot and step airgap can be decided by several key geometrical parameters shown in Fig 6.9 and Fig 6.10 As to the SPIMs, the slot shape is not as complicated as that of middle or large capability 3-phase induction motor. The shape of the usually used rotor slot can be

accurately described by using the key geometrical parameters shown in Fig 6.9. So the general model of rotor slot with 17 design parameters proposed by Williamson [1996] is not necessary for the SPIMs. The procedure of the pre-processor is shown in the flow chart of Fig 6.11.

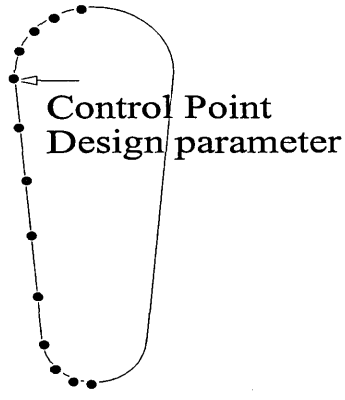

Fig 6.8 Point control scheme

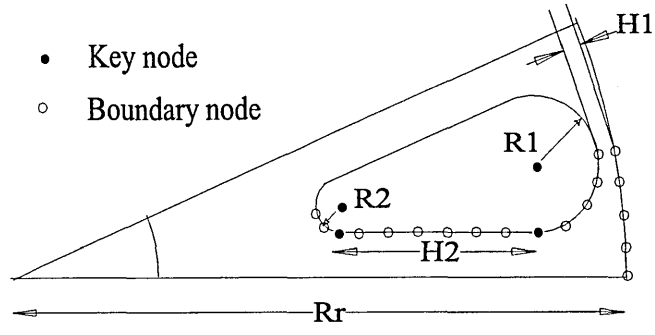

Fig 6.9 Rotor geometrical and control parameters

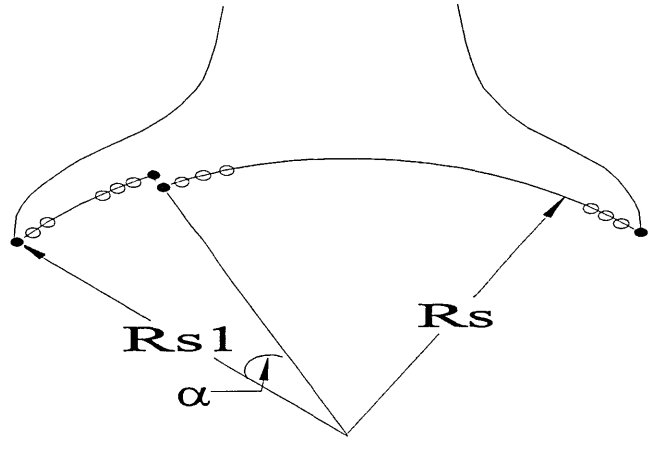

Fig 6.10 Step air gap geometrical and control parameters

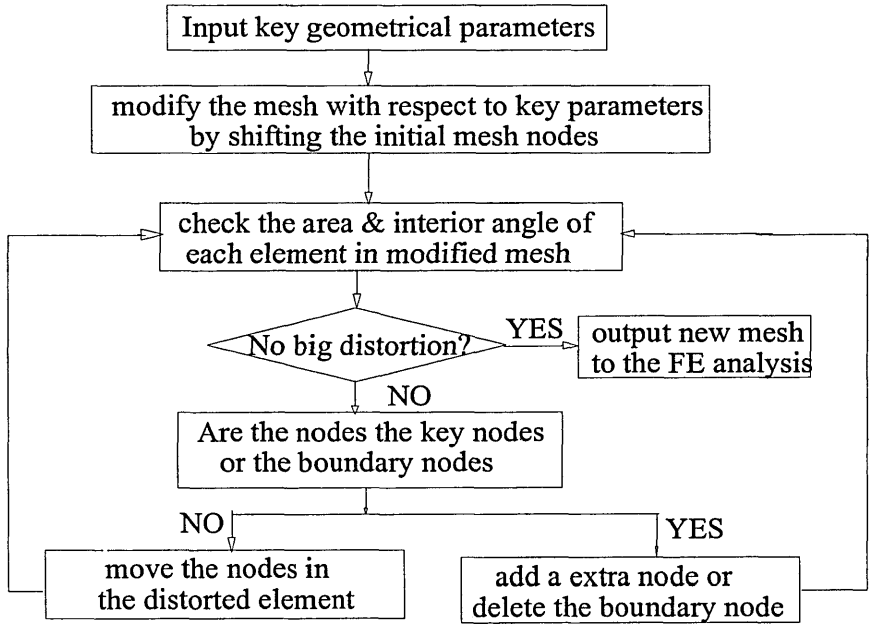

Fig 6.11 Flow chart of pre-processing

Using the proposed pre-processor program, when the search algorithm modifies the geometrical parameters of SPIMs, both key nodes and the boundary nodes are moved to the new co-ordination position decided by the changed geometrical parameters. Then, the other nodes, which are connected with the key nodes or the boundary nodes in the initial mesh, are shifted correspondingly. To avoid the too big mesh distortion, the area and three interior angles of each triangle element in the modified mesh is checked. If the size of the checked element is too big, the element is broken into three new elements by introducing a new node at the centroid. If the minimal interior angle of the triangle is smaller than the given limitation, such as 10^{o}, the relevant vertex is moved to enlarge the interior angle. The pre-processing program will be terminated when all the modified elements satisfy the condition of distortion.

Therefore, with the proposed scheme for the pre-processor, the mesh distortion can be reduced when the geometrical parameters vary in a big scale. Additionally, the number of final optimisation variables become only nine, which is much less than the normal optimisation FE model for electrical machines. It leads to significant reduction of

computing time cost. The nine optimisation variables for the SPIMs used in this study are shown in Table 6.5.

Table 6.5 Optimisation variables for the SPIMs

Variables	Meaning of the Variables
Rr (mm)	Outer radius of rotor
H1 (mm)	Thickness of mouth of close slot
R1 (mm)	Radius of upper half circle of rotor slot
H2 (mm)	Length of middle part of rotor slot
R2 (mm)	Radius of lower half circle of rotor slot
Skew (slot)	Skewed angle of rotor bar
α (^{o})	Angle of step air gap
Rs1 (mm)	Radius of step air gap
Turns (turns)	Turns of stator coil

6. 4 Multi-Slice Fixed-Mesh Model of SPIMs

In order to obtain a reliable optimisation result, the accurate evaluation of the SPIMs performances is another vital point. If the performance calculation is not accurate enough, the optimisation objective function will mislead the optimisation search to a wrong direction. For this reason, the FE methods rather than the conventional equivalent circuit models are used more in electrical machine optimisation recently. Besides the demands of high accuracy, the fast speed is another essential requirement for the program that computes the objective function. Generally, three kinds of FE model are used for the optimisation problems of electromagnetic devices, which are:

1) Simplified FE model (single-slot model) combined with equivalent circuit [Williamson, 1996]
2) Fixed-mesh (sinusoidal approximation) model [Salujian, 1998; Park, 1995]

3) Moving-mesh (time-stepping) method [Kamper, 1996]

Among these three models, the first one is easy to be used, but the effect of the magnetic saturation can not be considered properly and the skewed effect can only be taken into account by means of a skew factor in equivalent circuit. Additionally, due to the salient pole structure, the SPIMs cannot be simplified to a single-slot model unless the geometry of the stator is not considered as the optimisation variables. As to the moving-mesh model, which has been successfully used to analyse the performances of SPIMs in the former chapters, it is considered as the most accurate model among these three models. With this model, all the field quantities can be of non-sinusoidal time variation and the instantaneous reluctivity is used rather than time-average one. However, against its advantages, the main disadvantage of the moving-mesh model is that it requires a massive calculating time. Therefore, it is seldom used as the analysis tool to evaluate the objective function in optimisation design.

The fixed-mesh sinusoidal approximation model is the earliest form of the FE models for induction motors [Tandon, 1983; Luomi, 1986; Arkkio, 1987]. This model employing rotor meshes that are stationary with respect to the stator mesh is developed primarily for the calculating the performance of sinusoidal-excited machines at a constant speed. The main assumption of this model is that all currents and fields variables vary sinusoidally in time, thus the calculation becomes easy when the complex variable is used. As discussed in the former chapters, the time variation of fields in SPIMs is practically never sinusoidal. Therefore, it is considered that the accuracy of fixed-mesh model is lower than that of the moving-mesh model for the machines with significant MMF harmonics. But in some circumstances, such as the starting, the result of the fixed-mesh is still acceptable since the harmonic current in the rotor-bar is not significant under the rotor-locked situation. The waveforms of the rotor current obtained by means of the time-stepping method are shown in Fig 6.12. Except for the distortion in the first two cycles due to the switching transients, the current waveform is almost the sinusoidal variation.

By using the Discrete Fourier Transform analysis, the harmonic distributions of two models under rotor-lucked state are obtained in the frequency domain. In Fig 6.13, it is found that the fundamental component in rotor-bar currents are dominant, especially for

the Model T. Hence, the variation of rotor current can be assumed sinusoidal without big difference compared with real current and the complex model can therefore be applied directly.

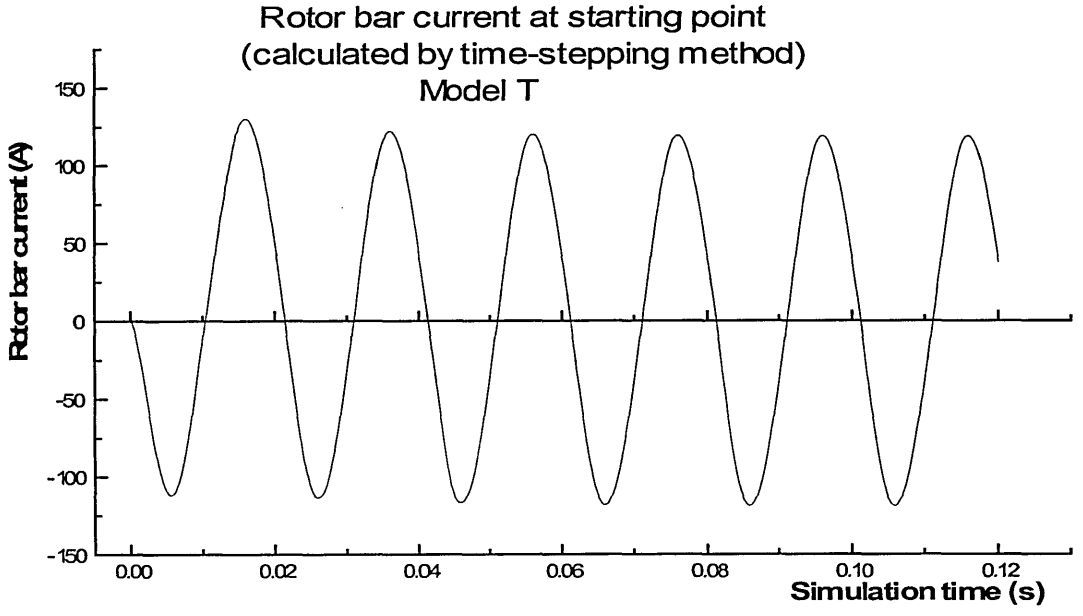

(a) Model T

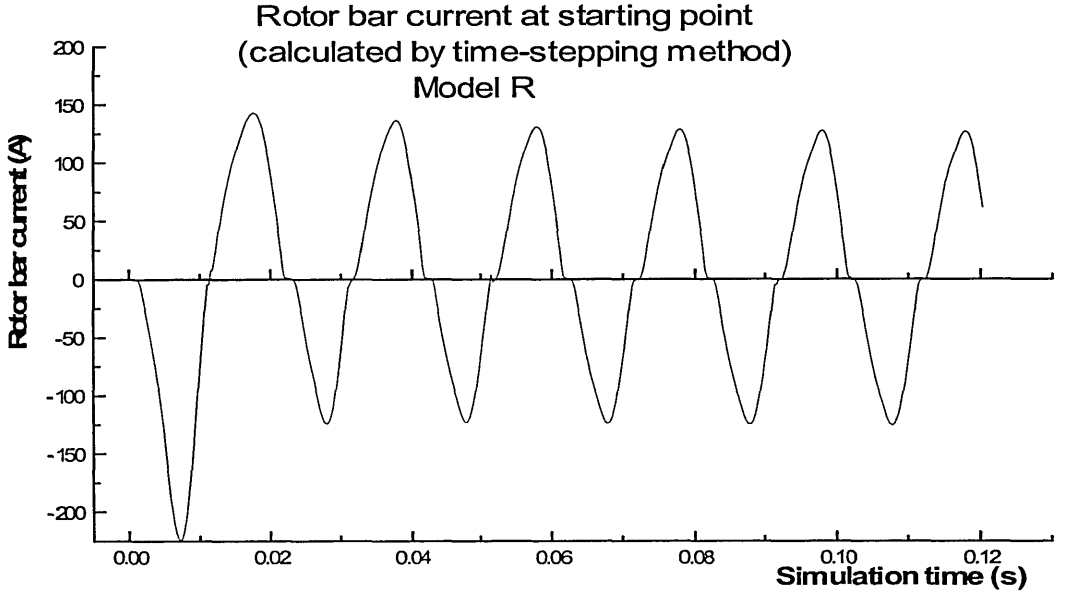

(b) Model R

Fig 6.12 Waveform of rotor-bar current obtained with time-stepping method at starting

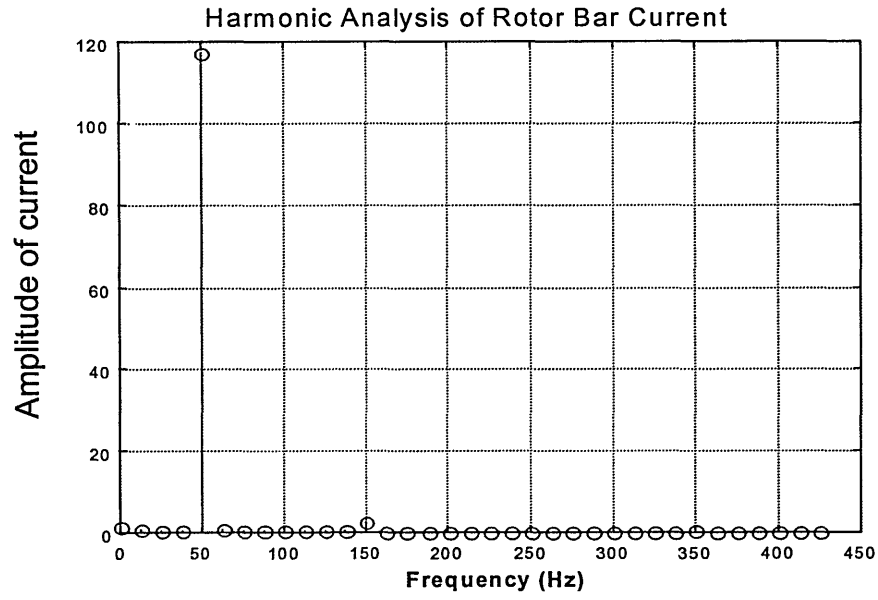

(a) Model T

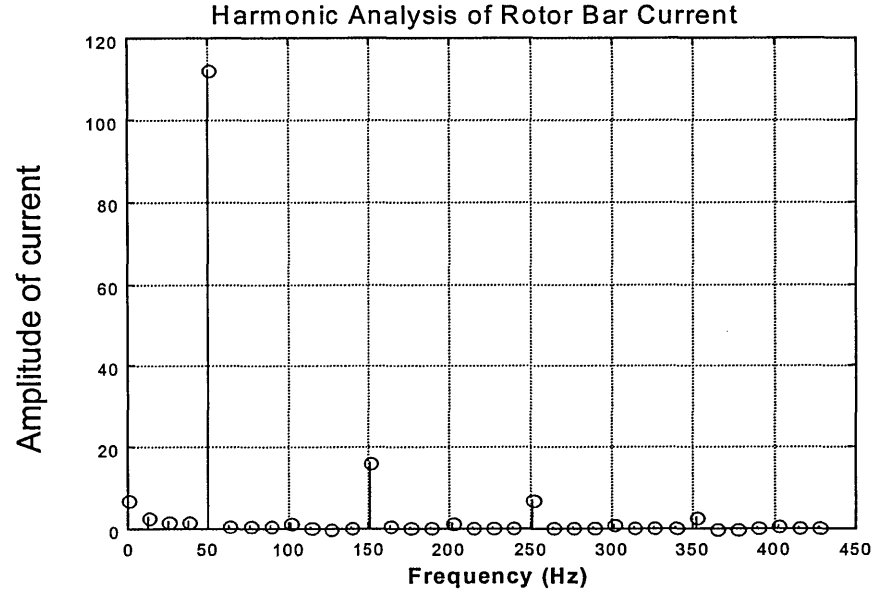

(b) Model R

Fig 6.13(a, b) Time harmonic distribution in rotor-bar current at starting

In fact, the crucial factor for applying the fixed-mesh model is that the computation time can be reduced radically compared with the time-stepping method. Therefore, once the validity of the sinusoidal approximation FE model has been approved, the fixed-mesh model is the first choice for the SPIMs analysis. To consider the effect of the skewed

rotor, 2D multi-slice technique was also applied.

With the fixed-mesh model, the field solution of the rotor is carried out in the fixed reference frame, in which all quantities are assumed to vary at slip-frequency. Thus, with the eddy-current FE model, the current following in the rotor bars can be related to the magnetic vector potential via the following equations:

$$J_b = \sigma\left(\frac{V_b}{l} - js\omega A\right). \tag{6.13}$$

where ω is the angular supply frequency, and the s is the per unit slip. At starting s =1, thus, the 2D electromagnetic field of each slice S_i can be described as

$$\frac{\partial}{\partial x}(\nu\frac{\partial A^{Si}}{\partial x}) + \frac{\partial}{\partial y}(\nu\frac{\partial A^{Si}}{\partial y}) = J_C^{Si} + J_S^{Si} + \sigma\left(\frac{V_b^{Si}}{l} - j\omega A^{Si}\right). \tag{6.14}$$

All the symbols of the variables in (6.14) have the same meaning defined in (4.2) except that they are all in the form of the complex vectors.

For the non-linear situation, the reluctivity, ν, in (6.14) varies with time according to the magnitude of the flux density in the iron core. Because the approximation of sinusoidal time variation is reasonable only when calculating effective values in steady state, it is necessary to define the reluctivity as a function of effective value of the flux density. There are an unlimited number of possibilities to define an effective reluctivity. The definition showing the best result for the effective value of current, torque and other machine characteristics is the best definition in that special case. Results computed with various effective reluctivity definitions have been compared with the result of a time-stepping method by Luomi [1986]. The best agreement with time-stepping method is obtained by following effective reluctivity definition.

$$\nu_{eff} = \frac{1}{T}\int_0^T \frac{H(t)}{\hat{B}\sin(\frac{2\pi}{T}t)}dt \tag{6.15}$$

where T is the period of an AC cycle, and $\hat{B}$ is the peak value of flux density. In this equation, it is assumed that the flux density varies sinusoidally, the magnetic field strength $H(t)$ is calculated from the magnetisation curve of the material according to the

flux density at time point t. Therefore, the effective reluctivity is obtained as the time average of the ratio of the field strength and the flux density.

Since the reluctivity of the non-linear ferromagnetic material used for the stator and rotor core is flux density dependant, the value of reluctivity for each element is determined by the absolute value of the flux density which is unknown before the field equation is solved. Because ν, a real value reluctivity, is not differentiable with respect to the complex node value, the Newton–Raphson method can not be applied directly. If S. Williamson's method [1982] is adopted, the real part and imaginary part of the complex vector potential are separated and each part are differentiable against the reluctivity, ν. However, the number of system equations will be enlarged twice bigger than that of the original complex model. Meanwhile the symmetric will be lost if the eddy-current model is employed. So, in this study, the non-linear complex equation (6.14) is solved by using direct iterative process. With the so called 'Chord Method' [Tandon, 1983], the reluctivity of each element is modified in each iteration by

$$\frac{1}{\mu^{n+1}} = \frac{1}{\mu^n} + \alpha\left(\frac{1}{\mu^{n+1}} - \frac{1}{\mu^n}\right) \tag{6.16}$$

where n denotes the nth iteration and α is an under-relaxation factor ranging from 0.1 to 0.4. In this study α =0.22. The iterative process is terminated after the following convergence criterion is satisfied.

$$\varepsilon = \frac{1}{N}\sum_{i=1}^{N}\left|\frac{A_i^{n+1} - A_i^n}{A_i^n}\right| \le 10^{-4} \tag{6.17}$$

Referring to the discussion in the chapter 3, the external circuit equations of stator coils, shaded-rings and rotor bars can be deducted similarly. The final equation is shown as follows.

$$i_C(R_C + jwL_C) + Nsl_z^{Si}\sum_{i=1}^{m}\beta_i^{C,Si}\left\{\sum_{i=1}^{N} j\omega A^{Si}N_j\right\}d\Omega^{Si} = V_C \tag{6.18}$$

$$i_S(R_S + jwL_S) + l_z^{Si}\sum_{i=1}^{2}\beta_i^{S,Si}\left\{\sum_{i=1}^{N} j\omega A^{Si}N_j\right\}d\Omega^{Si} = 0 \tag{6.19}$$

$$\{\mathbf{I_b}\} = \{\mathbf{I}_b^{S1}\} = \{\mathbf{I}_b^{S2}\}\ldots = \{\mathbf{I}_b^{Ms}\}$$

$$= \frac{-1}{R_e + jwL_e}\left(\frac{1}{2}[\mathbf{M}]^T[\mathbf{M}]\sum_{Si=1}^{Ms}\{\mathbf{V}_b^{Si}\}\right) \tag{6.20}$$

$$= \frac{\{\mathbf{V_b^{Si}}\}}{R_b^{Si}} - \sum_{bar,i}\beta_i^b\frac{\Delta_e}{3}j\omega\mathbf{A_i^{Si}}$$

After the field equation and external circuit equation are solved, the motor electromagnetic torque can be derived with the Maxwell stress tensor method. The average torque in a cycle may be written as

$$T = \sum_{Si=1}^{Ms}\frac{\mathrm{Pr}\,l_z^{Si}}{2\mu_0}\int_{\Gamma}\mathrm{Re}\left(\mathbf{B}_r^{Si}\times(\mathbf{B}_n^{Si})^*\right)d\Gamma \tag{6.21}$$

where μ_o is the air permeability and Γ an arbitrary arc with a radius r and an angle $2\pi/P$ in the air gap, $\mathbf{B_r}$ and $\mathbf{B_n}$ are the tangential and normal component of the flux density. The l_z is length of rotor, and the P is the number of pole.

Finally, the locked-rotor characteristics, the current and the torque, computed for the designed motor using the time-step method and the sinusoidal approximation are given in Table 6.6.

Table 6.6 Comparison of the locked-rotor characteristics between the time-step method and the sinusoidal approximation

Machine		Time-stepping method	Sinusoidal approximation	Experimental results
Model T (open slot)	Stator current (A)	0.459	0.460	0.455
	Shaded-ring current (A)	135.6	137.5	-----
	Starting torque(N.m)	0.0510	0.0522	0.0516
	Power Factor	0.764	0.741	0.78
Model R (close slot)	Stator current (A)	0.533	0.555	0.515
	Shaded-ring current (A)	75.40	75.1	-
	Starting torque(N.m)	0.0355	0.0366	0.0346
	Power Factor	0.750	0.740	0.76

6. 5 Optimisation Design for Maximum Starting Torque

In order to examine the validity of proposed hybrid optimisation algorithm and the simplified finite element model, an actual optimisation design for a 4-pole, 50W, 230V, 50Hz, SPIM (Model R) was investigated in this study.

For this optimisation problem, the maximum starting torque, $Torq_S$, was set as the optimisation objective. Other characteristics of SPIMs including the starting current, the current density in the rotor-bar and shaded-ring as well as the flux density in the iron core were considered as the constraints which were taken into account by using the penalty function method. Thus, the fitness function for the genetic algorithm is defined as

$$F(x) = \begin{cases} Torq_S & \textit{All the constraints are satisfied} \\ \varepsilon & \textit{Otherwise} \end{cases} \tag{6.22}$$

where ε is a small positive number. As to the local search, the objective function is changed to $1/F(x)$ in order to meet the requirement of the modified Hooke–Jeeve's method in which the objective function is minimised.

The Fig 6.14 shows the shape of the initial design of Model R which transforms into the final shape shown in Fig 6.15 after optimisation. In order to show the shapes of the internal parts, the field distribution is removed from Fig 6.14. After optimisation, the turns of stator coil, the rotor-bar area and the angle of step air gap are all decreased. The details of optimisation parameters either before or after optimisation are compared in Table 6.1. It is seen that the starting torque is significantly increased. The validity of the optimisation model can be proved with the result.

Table 6.1Table 2: Optimisation Result of SPIM

Variables	Search Space	Initial	Optimised
Rr (mm)	[22.5, 22.9]	22.90	22.90
H1 (mm)	[0.09, 0.49]	0.29	0.09
R1 (mm)	[1.00, 2.40]	2.03	2.15
H2 (mm)	[4.00, 10.00]	8.08	8.60
R2 (mm)	[0.50, 1.20]	0.86	1.05
Skew (slot)	[0.5, 2.5]	1.50	1.00
α (°)	[0.0, 52.0]	25.0	0.00
Rs1 (mm)	[23.1, 24.3]	23.85	24.00
turns (turns)	[480, 860]	730	694
Objective Function: Starting torque (N.m)		$3.66*10^{-2}$	$5.324*10^{-2}$

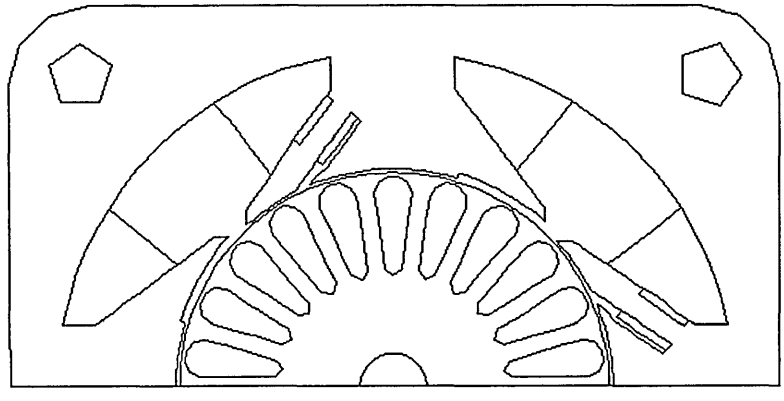

Fig 6.14 Initial design shape of Model R

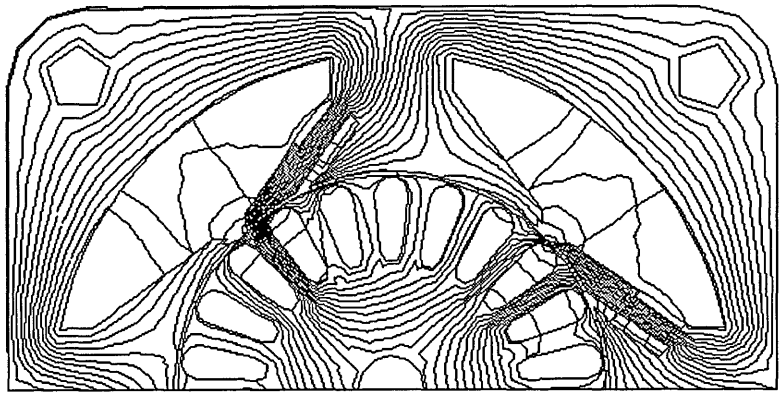

Fig 6.15 Flux distribution of final design (u=220V)

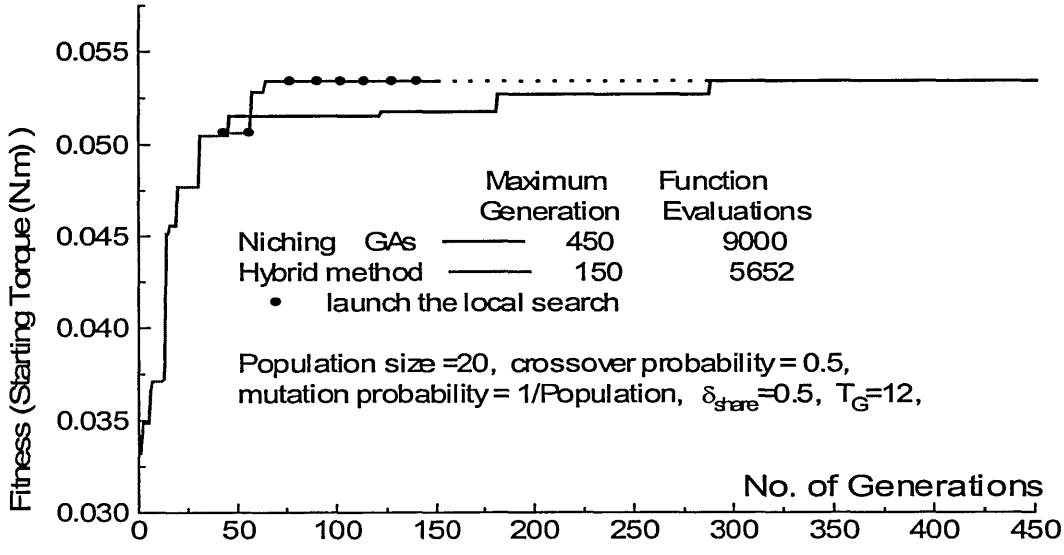

Fig 6.16 Comparison of convergence performance between two methods for the optimisation design of SPIMs.

The comprison of optimisation procedure between the normal genetic algorithm and the proposed hybrid method is shown in Fig 6.16. The superiority on covergence speed of the proposed method can be seen form theFig 6.16.

In the optimisation design, α, the angle of the step air gap shown in Fig 5-4 is reduced from 25 degrees in the starting design to 2.7 degrees. The reluctance augmentation, a

main means of increasing the starting torque, was not used in this particular design. To explain this phenomenon, some new models with different angles of step air gap based on optimisation design were meshed and investigated. The starting torque of the designs with the step air gap was increased more or less, but the current density of rotor bar, one of design constraints, was beyond the given limitation. In fact, for the given optimisation design, the current density almost reaches the boundary of the feasible area. Although the reluctance augmentation can still be used to increase the starting torque in this design, adjusting other design parameters can produce better result under the defined design constraints. Therefore, validity and efficiency of the developed optimisation model were further proved.

6. 6 Conclusion

As mentioned in the previous chapter, the characteristics of SPIMs depended on many design parameters. When it needs to be designed to meet given specifications, the SPIMs always present a formidable difficulty in choosing suitable parameters. Although the performances of SPIMs can be calculated accurately with the multi-slice finite element model, a lot of effort in adjusting and matching the design parameters are still required to achieve a good motor design even by an experienced engineer. Therefore, the automatic optimisation design for SPIMs is very necessary even if it is more challenging.

At the beginning of this chapter, different optimisation methods were compared. Then, two popular methods, the Genetic Algorithms and the modified Hooke–Jeeves' method, were examined in detail. Based upon these two methods, a more efficient and reliable hybrid optimisation method was proposed.

With the proposed hybrid method, the genetic algorithm and the deterministic method were invoked alternatively according to the variation of the best fitness. Because it could avoid local optimum solutions and it gave a fast convergence rate at the beginning of the optimisation searching procedure, the genetic algorithm was employed first. Once the variation of best fitness tended to stop improving with time, a set of local searches were brought into play to find out the local optimum results with the improved initial starting condition. After the local searches were finished, the new individuals were used as parents to reproduce again with the genetic algorithm method. Such a global–local search iteration was repeated until the value of the best fitness stopped improving for several generations. In order to avoid the search process converging to a certain local optimum solution, the Niching technique was adopted in the genetic algorithm's search. Using such a hybrid global–local search method, the major difficulty of deciding when to switch from the genetic algorithm to local search in the normal hybrid methods has been avoided. The global optimum was secured while the convergence rate was improved much compared with the conventional GA. The validity of the proposed hybrid method was first proved by an ideal mathematical problem.

In order to obtain a more accurate analysis tool, the finite element method was adopted to calculate the performance of SPIMs. Since the finite element method requires different meshes when the geometry of SPIMs is changed, a partial auto-remesh program driven by the geometrical design parameters has therefore been developed. With this auto-remesh program, the number of the optimisation variables was reduced notably.

Due to the fact that the time-stepping method costs so much in computing time, it is nearly impossible for it to be used in the optimisation problem of normal electrical machine design. A multi-slice sinusoidal approximation (fixed–mesh) FE model was therefore employed to reduce the computing time cost. The validity of the sinusoidal approximation model was verified under the locked-rotor condition by comparing the calculated results of the fixed-mesh FE model with that of the time-stepping method and the experimental results.

Finally, the improved hybrid optimisation program and the sinusoidal approximation FE

model were applied to the design of SPIMs setting the maximum starting torque as the optimisation object. When the optimisation procedure finished, the objective function, the starting torque of the optimised SPIM, was improved quite significantly. Meanwhile, the proposed hybrid search algorithm had a higher convergence speed compared with the normal genetic algorithm. The validity and the efficiency of the developed optimisation model were therefore proven by the actual example of the SPIMs design.

7 MEASUREMENT OF SPIM PERFORMANCE

7. 1 Introduction

From the designer's perspective, it is important to implement the motor performance tests in order to know the motor's capability and to verify the current designs. Performance tests for the SPIMs fall into three major areas, which are [Veinott, 1986; Zimmerman, 1983]:

- Steady state load test: This test is carried out to obtain the performances of the motor with various loads, giving a set of performance characteristics under different rotating speeds, such as input power, input current, efficiency and power factors at either rated or various supply voltages.

- Transient test: A speed-torque test may be taken to determine the accelerating characteristics of the motor, to look for possible cusps and valleys or to diagnose the action of the starting process.

- Thermal capability and losses tests: From these tests, the rise of temperature at a determined load can be known and different types of losses, which are named as mechanical losses, iron losses and copper losses, need be determined separately in the most cases.

For the SPIMs, the torque capability of a motor from the starting point to breakdown point is probably one of the least predictable areas with the normal equivalent circuit design methods, and it is also one of the most difficult areas to be measured. Therefore, the torque-speed characteristic measurement is one of interesting points in this chapter.

To date, a number of measurement techniques have been developed. The traditional means [Veinott, 1986] including dynamometer, rope and pulley and torque table methods have serious limitations in accuracy due to motor heating, motor vibration and operator judgement, and they usually require hours to complete. For a large motor, the variation in load for the steady state load test and transient test is difficult to obtain. Especially, with this kind of method, the problem of measuring torque-speed curve from the locked-rotor point to breakdown point is still unsolved. Therefore, researchers try to use different alternatives, and numerous methods are now available [Nystuen, 1976; Holt, 1981; Zimmerman, 1983; Plunket, 1985; Andria, 1986; Lipo, 1986; Christiansen, 1989; Ojo, 1990; Szabados, 1990]. All these new methods are mainly computer-based. Compared with the traditional method, the heating effects are virtually eliminated due to the fact that the actual testing only lasts for a few seconds after the motor is started, and the human error in reading and recording test data is also eliminated.

For the dynamic shaft torque measurement, there are two main measurement methods, the direct one and the indirect one.

The direct methods in which both the torque and the speed sensors are involved are usually considered to be adopted first [Nortan, 1989; Plunket, 1985; Penman, 1996]. For the dynamic test, the speed and quality of the torque sensor and the accessory electronic-circuit response must match the dynamics of the transient process. Among the various transducers, the following two are claimed as having good dynamic characteristics.

- The rotary transducer with strain-gage sensor and contactless excitation and signal transmission [Penman, 1996].
- The cylindrical transducer with inductive torque sensor.

Owing to their relatively small mass, the transducers do not practically affect the dynamic behaviour of the tested motors. In addition, these two kinds of transducers have a wide measuring range. However, in direct method, the torque transducer has to be mounted as a part of the rotational system while the problem can be the space needed for its mounting. For laboratory research, this problem can in general be avoided. On the other hand, the cylindrical transducer is partly sensitive to the stress of the rotation axis, and the double-element coupling is required if the supported installation is used.

The indirect methods only requiring a speed sensor have been reported recently, which can be divided into following categories.

- Acceleration method [Hoffman de Visme, 1968; Christiansen, 1989; Szabados,1990]
- Acceleration method combined with the use of input voltage and current[Andria,1986]
- Methods using search-coils and input current [Holt, 1981; Lipo, 1986; Ojo, 1990]

Among these three methods, the first is used as a standard method of determining the torque-speed curve according to IEEE standards [1978]. Using this method, the rotor is started without load after it has been rotated manually in the reverse direction against the rotation when the motor is switched on. The instantaneous acceleration at each time point is determined by differentiating the speed signal. The torque at the respective speed is given by calculating the acceleration using the moment of inertia of the rotational parts. If the moment of the inertia is unknown, the relative torque versus time is obtained. The absolute value of the torque needs to be re-scaled from the starting torque or breakdown torque measurement. Accurate measurement of the speed and determination of its first derivative, the acceleration, are crucial for this method. Previously, several methods to measure the velocity of rotating parts have been reported. Older methods [Hoffman de Visme, 1968] are based upon the analogue principles, which generally suffers from low resolution and severe background noise. A recent digital method to obtain angular velocity is given with a fairly complex sensing method by Chistiansen [1989]. Using a

fast data acquisition system to sample the output of a DC tachometer, Szabados [1990] developed an adaptive window-size average filtering and numerical differential algorithm to remove undesired extraneous signals from obtained coarse data digitally. With this method, the accuracy of machines characteristics over the complete range of speed can be preserved.

The accuracy of the acceleration method is highly dependent on the accuracy of the speed measurement.

As to the second method, proposed by G. Andria [1986], instead of the re-scaling of the relative torque obtained from the starting process, the stator flux component and the electromagnetic torque are calculated from the sampling of input voltages and currents. The total moment of inertia is identified by comparing the calculated torque with the acceleration derived from the speed signal. The drawbacks of this method are that the iron loss in the rotor and stator is neglected and that the different degrees of saturation of various machine parts are ignored. The result of this method is dependent on the size, type, saturation degree and rotor skin effect of the tested motor. To obtain an accurate result, the design and construction parameters may be needed while an ideal method should regard the tested induction motor or other mechanical system elements as a black box.

The final method incorporating a search-coil and the input current, which is considered as the best method for measuring the transient electromechanical torque [Ojo, 1990], is practically applicable only in prototype factory testing. Its application will result in a complete dismantling of the motor and the mounting of search-coils with the stator slots is extremely dedicate and tedious, especially for high-voltage motor. For the small motor, like SPIMs, the space for the search-coil is difficult to be found. This method is rarely used in normal practice.

In this research, using a cylindrical torque/speed transducer, a PC-based data acquisition system has been developed in order to measure the performance in both the steady state and transient state. To measure the variation of output torque with time, the direct method was employed. In the following section, the detail of the test rig is first explained. Using

this test rig, two different designs of SPIMs have been tested under both steady state and transient states. The results of tests are given in the last section.

7. 2 Computer-Based SPIMs Measuring Rig

In this research, to study both steady state and transient state performance of SPIMs, a PC–based measuring rig has been developed. This test rig whose main structure is shown in Fig. 7.1 includes the following elements:

- Power supply and meters
- Torque/Speed measuring unit (includes Torque/Speed transducer and display unit)
- Eddy-current Brake
- Computer-based data acquisition system
- Motor tested

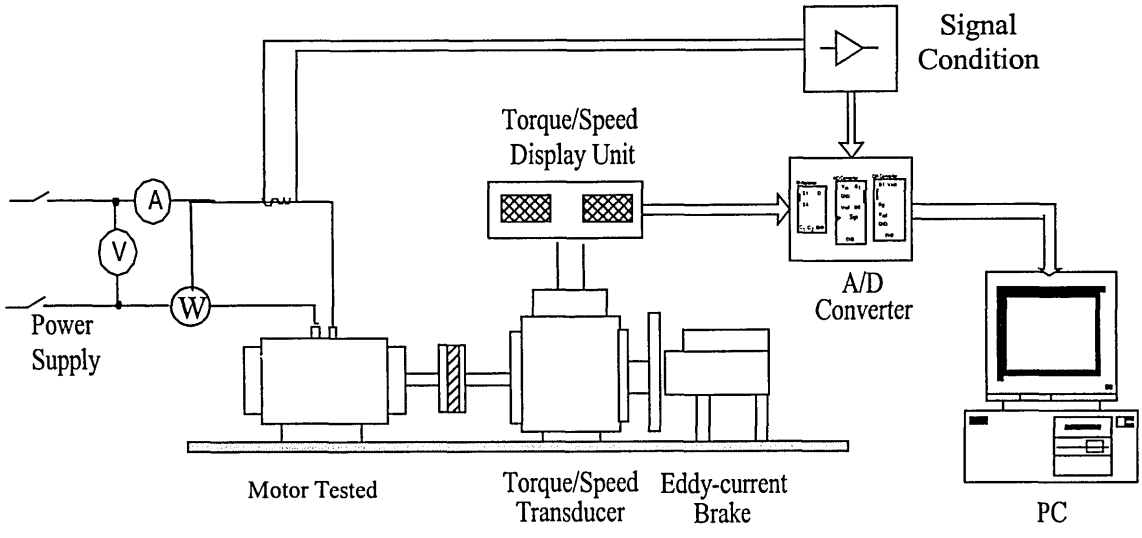

Fig. 7.1 Structure of the computer-based SPIM measuring rig

There are two kinds of signals measured in this test rig: electrical signals and mechanical signals. In the steady state, the electrical signals including supply voltage, input current and input power are easy to be read directly through the conventional AC current meter, voltage meter and wattmeter. Compared with the electrical signals, mechanical signals including output torque and rotation speed are more difficult to measure. In our test rig, a torque/speed transducer with built-in electronic conditioning circuits is employed to convert the mechanical signals into the electrical signals. With additional combined torque/speed display unit designed for the torque/speed transducer, the output torque and rotation speed can be read directly. Thus, with these meters, the stator current, input power, power factors, output torque, speed and the different kinds of loss can be known directly or calculated indirectly.

By changing the applied coil current of the eddy-current brake and therefore the load of the tested motor, the motor rotation speed can be changed. Hence, the motor performance variation with speed can be monitored. In addition, in order to make the motor speed stable from breakdown torque to the starting point, the slope of the curve of the brake torque versus the speed must be greater than that of the motor output torque variation with the speed, which can be described as:

$$\frac{dT_B}{dn} > \frac{dT_M}{dn} \tag{7.1}$$

where T_B is the brake torque, T_M denotes the output mechanical torque and n is the rotor speed in rev/min.

Since all the signals, voltage and torque etc., are transferred into the computer-based data acquisition (DAQ) system during the test as well as in the steady state, the result data can be obtained through the computer-based DAQ system. To record the transient state performances, the meters and display unit become useless, therefore the computer-based data acquisition system is the only means to be used. The data acquisition system is divided into two parts, hardware and software. The hardware includes transducer, signal conditioning, DAQ board and computer (shown in Fig. 7.1).

7.2.1 Transducer

Transducer is used to change physical phenomena into electrical signals. Normally, the transducer for the electrical signal is very simple. A transformer can be used as voltage transducer, and a small series resistance (0.1- 0.5 Ohm) can be used as the current transducer. However, for the mechanical signals, the transducer becomes little more complex. In our testing rig, the torque transducer is an inductive torque transducer operating on the basis of a voltage transformer having a variable coupling factor. Its main structure is shown in Fig. 7.2.

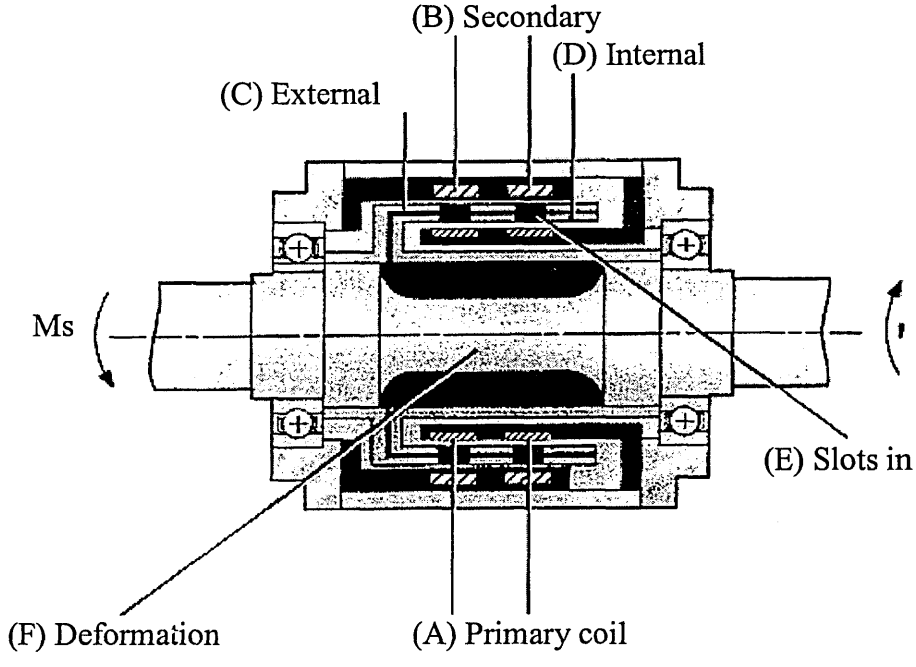

Fig. 7.2 Main structure of torque/speed transducer [Instruction Manual,1997]

The primary and secondary coils of transformer (Fig. 7.2 Refs. A and B) are separated by two concentric cylinders (Fig. 7.2 Refs. C and D), each cylinder having finely position slots (Fig. 7.2 Refs. E). The cylinders are connected to the torque measuring shaft, the external cylinder to one side of the shaft's deformation zone (Fig. 7.2 Ref. F) and the internal cylinder to another side of deformation zone. When no torque is applied to the shaft, the slots in both cylinders fail to overlap resulting in a total screening (no induction)

between the primary and secondary coils. As the torque applied to the shaft is increased, the deformation zone undergoes an increasing angular deformation. This causes an increasing overlap between the slots in the cylinders and hence an increasing induction between two transformers coils. In this way, when the primary coils are excited by a sinusoidal voltage signal, the transformer secondary coils produce a voltage signal whose magnitude is dependent on the applied torque [Instruction Manual, 1997].

Each primary coil of the transformer consists of two equal windings mounted in series. It is excited by a signal having a frequency of 20 kHz produced by the transducer's built-in electronics. In addition, a constant current is supplied to the primary coils. By monitoring the terminal voltage of the primary coils under zero-torque condition, the temperature of the unit can be determined. Each secondary coil consists of two windings in phase opposition. This allows the mechanical phase shift between the two cylinders to be determined. The secondary coils produce proportional (dynamic) voltage signal corresponding to the measured torque.

The speed transducer is incorporated in the torque transducer housing to measure the rotational speed. This transducer is mounted so as to face a toothed part of rotor and produces 30 pulses per revolution. The same transducer is used to determine the rotational direction of the shaft. The minimum speed measurable is 50rev/min, and the minimum speed for detection of rotation direction is 20 rev/min.

7.2.2 Signal Conditioning

Usually the output signal of transducer is low level signal and not suitable for DAQ board. To the PC30FA, the used DAQ board in the test rig, the full scale of input signal is –5V to +5V DC or –10V to +10V DC. So before the signal transfers to the DAQ board, the signals must be conditioned to match the input signal specification of the DAQ board.

Signal conditioning is used to amplify low-level signal to high level, isolate high voltage, filter background noise in the signals and excite the transducers.

The torque transducer unit uses a built-in electronics to carry out torque/speed signal conditioning. The torque conditioning chain is based on a carrier frequency system containing a synchronous demodulator. This chain also contains a low-pass filter (second order Butterworth type) which can be set by the user by positioning micro-switches which are built into the transducer. The filter is used to eliminate the resonance and other forms of interference coming from the chain of mechanical elements (driving machine, couplings, etc.) and the torque-measuring shaft. Since the harmonics in the studied motor are considered up to the 17^{th} order, the cut-off frequency of the built-in filter is set at 1kHz.

The exciting voltage (20-32V DC) for torque/speed transducer is supplied by the additional combined RPM & Torque Monitor (the display unit). The output torque and speed signal are conditioned by the built-in circuit and the signal can be obtained at the auxiliary output socket of the display unit. Both signals ranging from –10V to +10 V DC, which equal to the maximum input range of the DAQ board, can be transferred into the DAQ board directly.

Due to the fact that the transformer is used as a voltage transducer, the maximum range of input signal for the DAQ board can be easily satisfied by choosing the primary/secondary turns ratio. Obviously, the output signal from the secondary coil is isolated from the high voltage input in the primary coil.

The input stator current of the tested motor is usually less than 1A. Since a 0.5 Ohm shunt resistance was connected in series within the stator circuit as a current transducer, the voltage across the resistance, the output signal of current transducer, is less than 0.5V. Therefore, this signal should be amplified. The conditioning circuit used for current signal is shown in Fig. 6-3. In order to isolate the DAQ board from the high voltage, an AC input opto-isolator was used in the circuit.

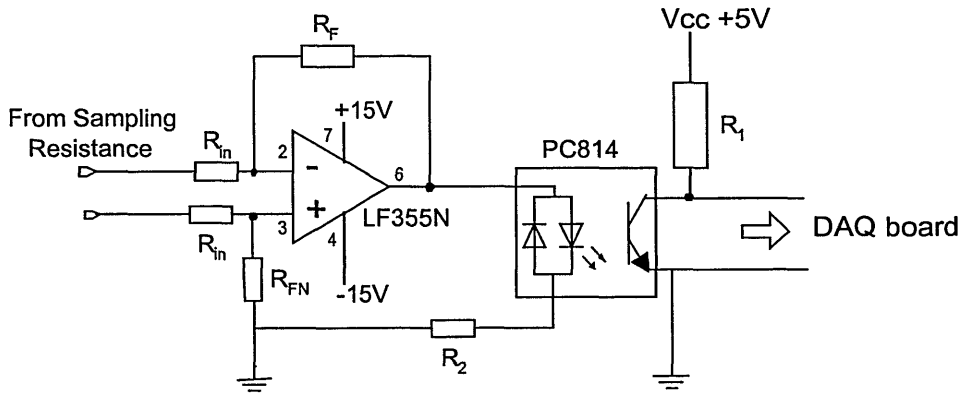

Fig. 7.3 Conditioning circuit for stator input current signal

7.2.3 DAQ Board

The DAQ board used in the rig is a PC30FA, a 12 bit analogue and digital I/O board and it can be plugged into any slot of PC/AT or compatible computer. This board supports 16 single or 8 differential A/D inputs. The A/D throughput rate can be chosen between 100kHz and 330kHz. Additionally, The PC30FA features software programmable gain. The gain of each of the 16 input channels can be independently set to 1, 10 100 or 1000.

The block diagram in Fig. 7.4 highlights the major elements contained in the board and their relationship. There are four subsections shown as follows:

(a) Analogue/Digital (A/D) sub-system
(b) Bus interface
(c) Timing and Control
(d) Digital Input/Output (I/O)
(e) Digital/Analogue (D/A) sub-system

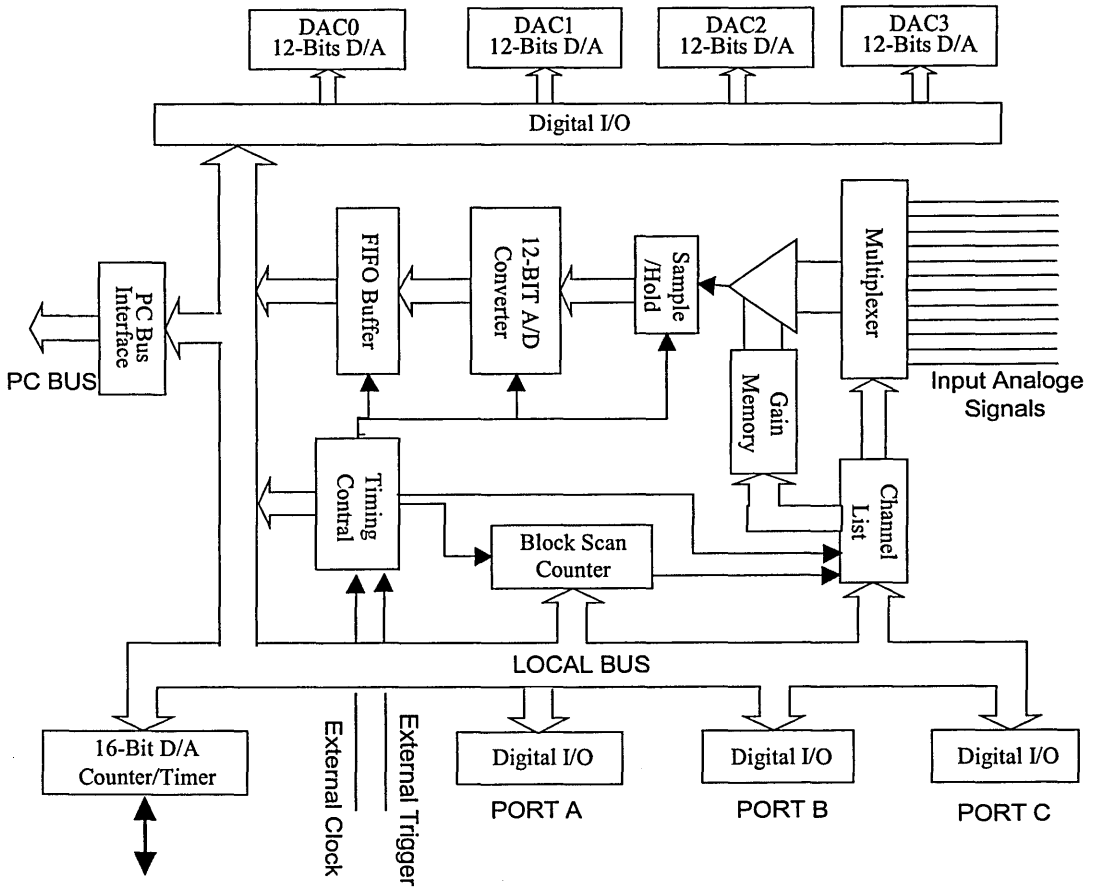

Fig. 7.4 Major elements of the PC30-FA board [EDR User Manual, 1996]

In the PC30-FA board, the A/D sub-system contains several separate components [EDR User Manual, 1996]:

- **Input Multiplexer**. The multiplexer selects one of 16 single ended or 8 differential input channels to be converted from analogue to digital form. In differential mode, two multiplexer switches per channel are used, and the A/D converter measures the difference between the high and low input lines of each channel. Therefore, it can reject the common mode noise that can not be avoided with single ended connection. In the testing rig, the differential input mode is used.

  The measuring channel is selected by a channel address obtained from the channel list. The channel list contains a sequential list of channel to be converted. When the end of list is reached, the A/D loops back to first channel in the list.

- **Programmable Gain Amplifier**. The programmable gain amplifier is used to amplify the analogue signal from the multiplexer. The gain is automatically selected by the gain code stored in the board's memory

- **Sample and Hold Unit**. This unit holds the analogue signal from the selected input channel steady during the A/D converter's conversion process. Normally, there are three sampling /hold modes which are Normal Mode, Burst Mode and Simultaneous Mode. Fig.7.5 shows the space between samplings taken from channel 0, 1, 2 and 3 on the PC30-FA at 5kHz in different modes.

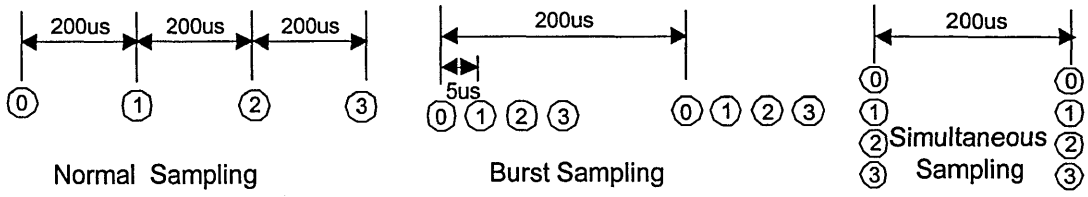

Fig. 7.5 Three Sampling/Hold Mode

For the PC30-FA board, only normal mode and burst mode are supported. Thus, only one channel's signal is input to convert on each strobe and there is a time delay between the two sampling processes. To minimise the time delay, the burst sampling mode is adopted.

For torque and speed, because they change at a very slow rate compared with the sampling rate, the sampling time delay can be omitted. For the current and the supply voltage signals, the sampling rate is set to 5kHz, which means an interval time between two samples is 0.2ms. Since in burst sampling mode, the time delay only costs 0.005ms which is much less than the sampling interval time. Therefore, even for fast changing signals, such as current and voltage, the sampling time delay can be ignored.

- **A/D Converter**. The A/D converter performs the actual A/D conversion. An A/D

conversion is begun by an A/D strobe that is generated by the timing and control section.

- **FIFO buffer**. The FIFO (First In First Out) buffer is temporary store for converted results. The FIFO stores data while PC is dealing with other functions. The FIFO can store up to 16 samples. By changing memory buffer, the PC30-FA board can perform DMA (Direct Memory Access) into entire memory of the PC without break.

The bus interface is responsible for the following three functions

- The decoding of the board's base address, which is done by setting a DIP switch. The base address of the board is set at 0300H
- The generating interrupts under one of the following register selectable condition:
    1) The end of each A/D conversion.
    2) The end of DMA block.
    3) On each pulse from the uncommitted counter/timer
- The generation of DMA signal.

The timing and control sub-section is used for generation of the A/D strobe, and it also contains an uncommitted counter/timer which is responsible for the signal generation, or as a frequency or plus period counter.

7.2.4 Software

DAQ hardware without software is of little use and DAQ hardware with poor software can be even worse. To avoid low-level, complicated detail of hardware programming while preserving high performance, the PC30-FA board provides the user with an easy-to-

understand software which is used to directly program the registers of the DAQ hardware and to manage its operation and its integration with computer sources. With this driver software, the user's application can be written in any of several popular languages, such as C/C++. The application program can run under DOS, Windows 3.1 and Windows 95. According to the need of our data acquisition system, C running under the DOS is used in this system.

To input the converted data to computer, a proper transfer mode should be selected. To the PC30- FA board, three modes, which are Polled IO mode, Interrupts Mode and DMA mode, can be used. Using the Polled IO, the CPU continually monitors the DAQ board waiting for conversion to complete. Once each conversion has completed the data is read by CPU and stored in memory. So Polled IO method requires the full attention of CPU and can not be done in the background. In the Interrupt Mode, the board operation can be done in the background. Once the DAQ board generates an interrupt if an A/D conversion completes, the CPU suspends other currently executing programs and calls the interrupt service routine to read data from the board and store it in memory. When the interrupt service routine is finished, the other programs can resume. The first two modes are normally employed for low speed applications (sampling rate <10 kHz). Although these two modes can satisfy the application, a more efficient and reliable way, DMA mode, is adopted. The DMA mode requires very little work on part of the CPU and supports the maximum transfer rate of the board. In this mode, the PC's DMA controller is programmed to transfer data from the A/D board to memory without going through the CPU.

The flow chart of the data acquisition program using the PC30-FA board is shown in Fig. 7.6.

Besides the user application, a commercial software package named LABVIEW can also be used in the data acquisition system as a digital storage scope combined with the DAQ board.

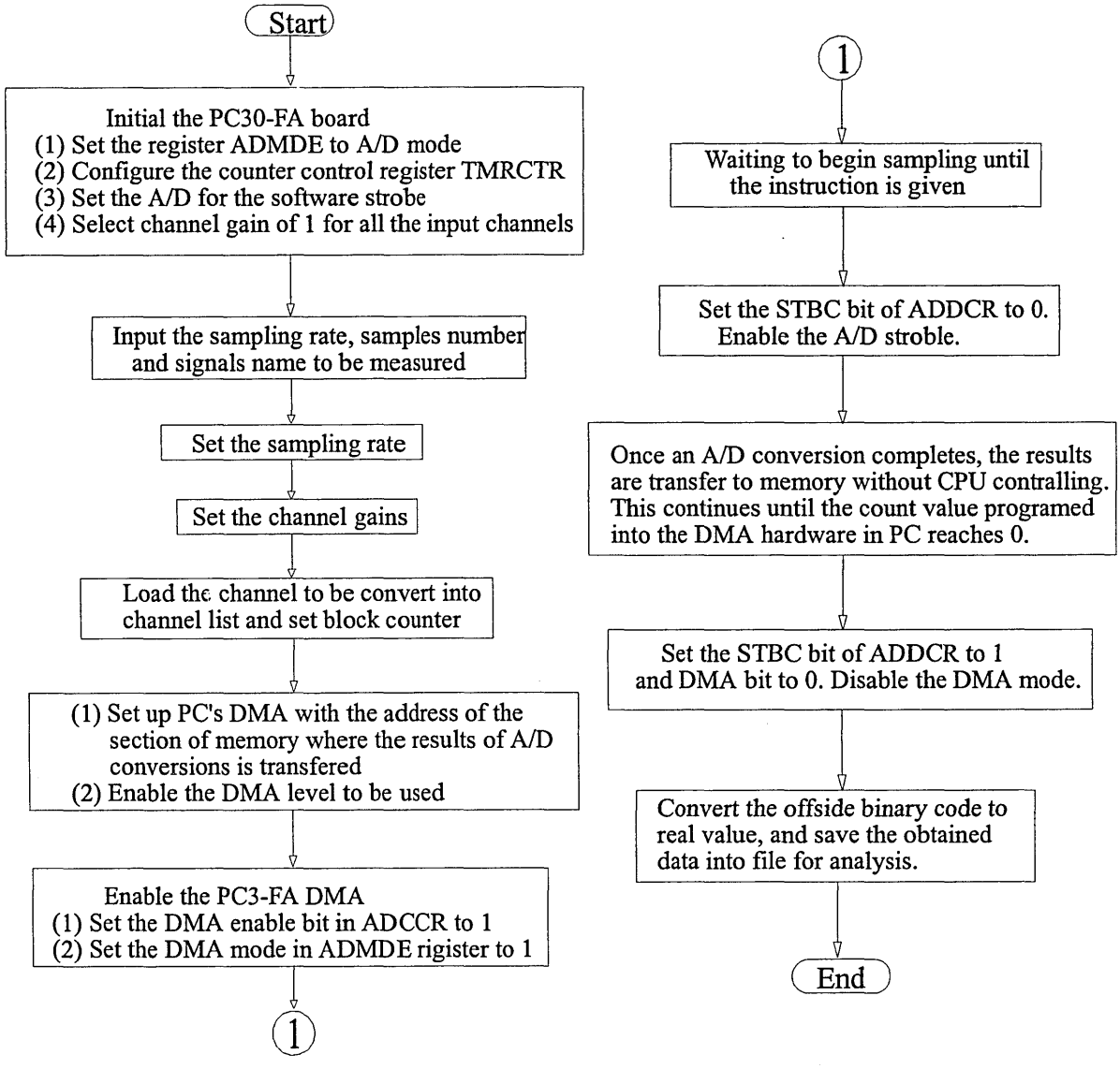

Fig. 7.6 Flow chart of data acquisition program with PC30-AF

7. 3 Experimental Results

7.3.1 Steady State Characteristics

With the measuring rig, the steady state performance of two different designs of the 220V, 50Hz, 50W, 4 pole SPIM, Model R and Model T, are studied.

First, the steady state torque/speed characteristics of the Model R and the Model T under the 220V, 200V, 180V, 160V and 140V voltage supply are measured. The results measured are compared in Fig.7.7 to Fig. 7.9

For the Model R, its torque drops much faster than that of the eddy-current brake at 500-1100 rev/min, which means equation (7.1) cannot be satisfied, so there are no testing points in this region for the Model R. From this case, the disadvantage of steady state measurement method can be seen.

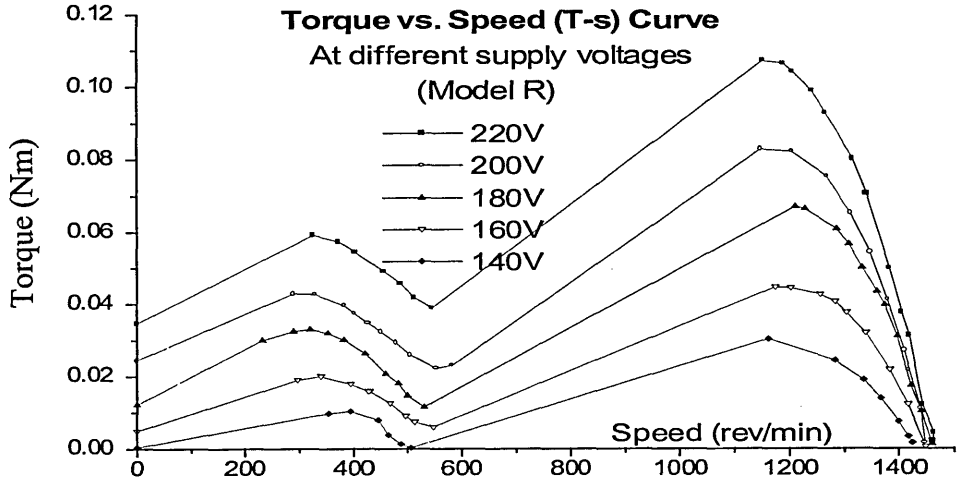

Fig. 7.7a Torque/speed variation with speed under different supply voltages (Model R)

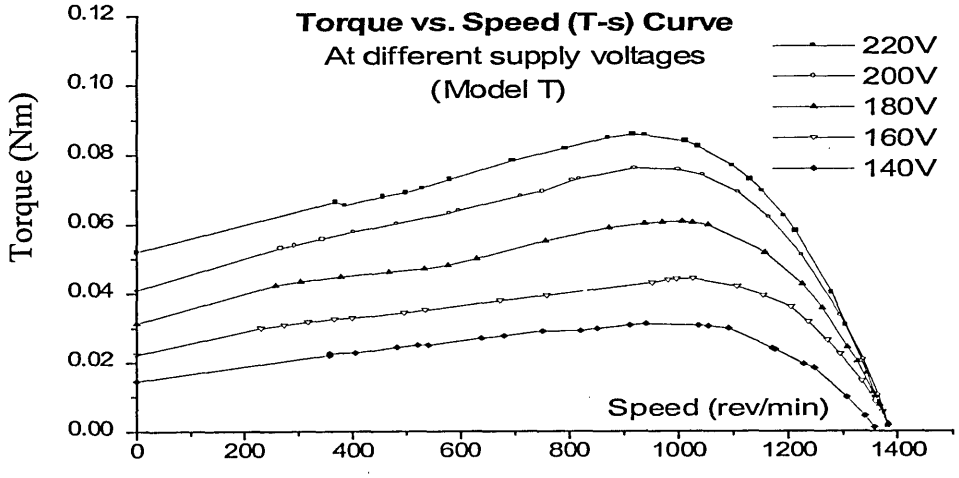

Fig. 7.7b Torque/speed variation with speed under different supply voltages (Model T)

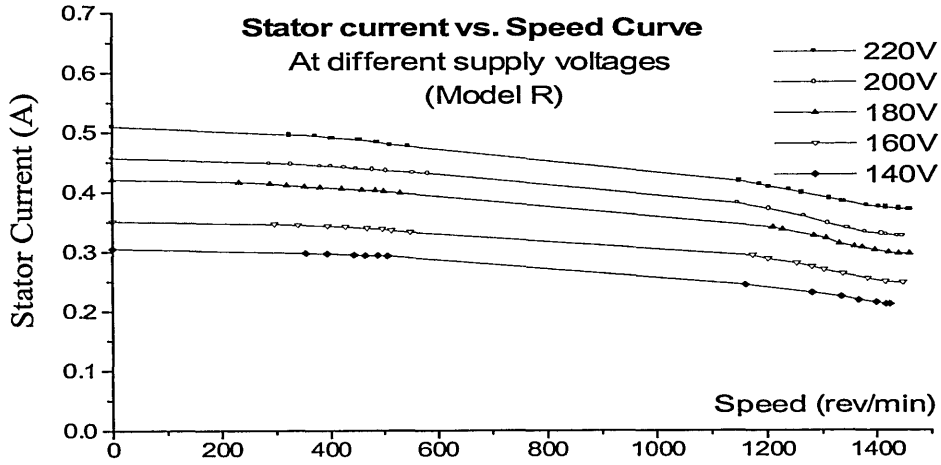

Fig. 7.8a Input stator current variation with speed under different supply voltages (Model R)

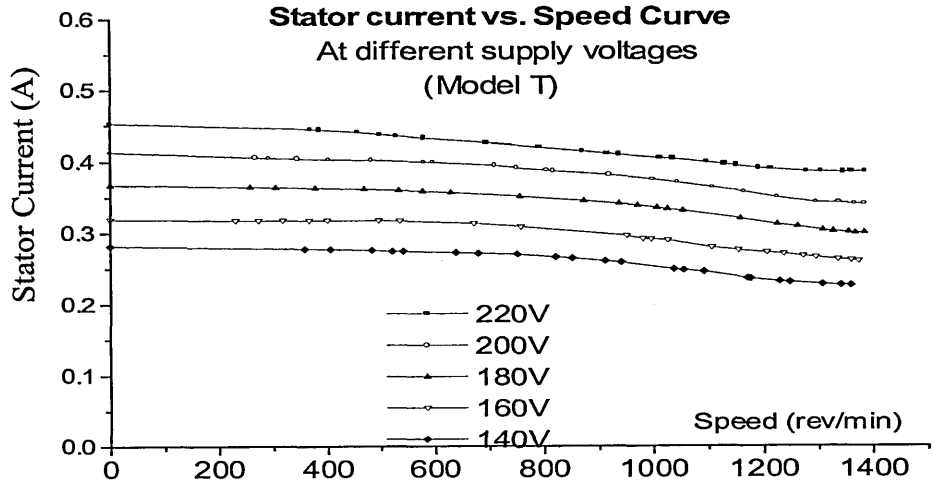

Fig. 7.8b Input stator current variation with speed under different supply voltages (Model T)

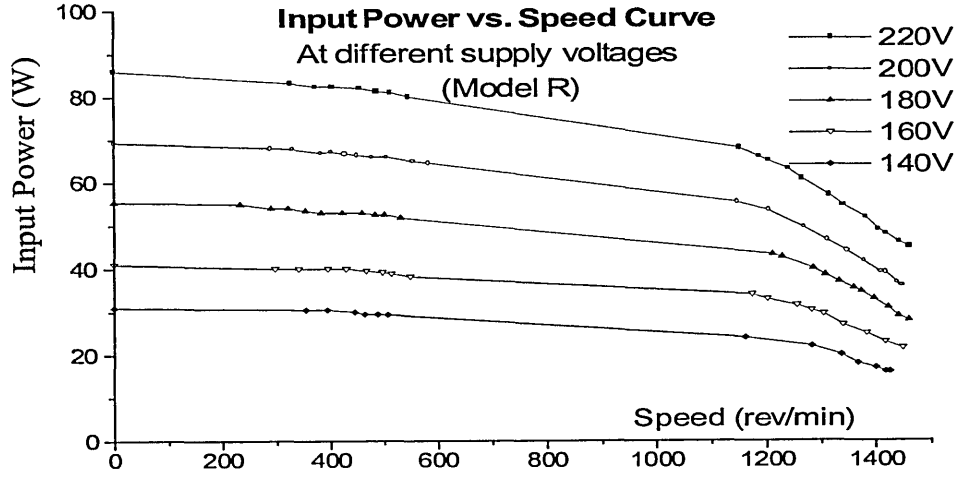

Fig. 7.9a Input power variation with speed under different supply voltages (Model R)

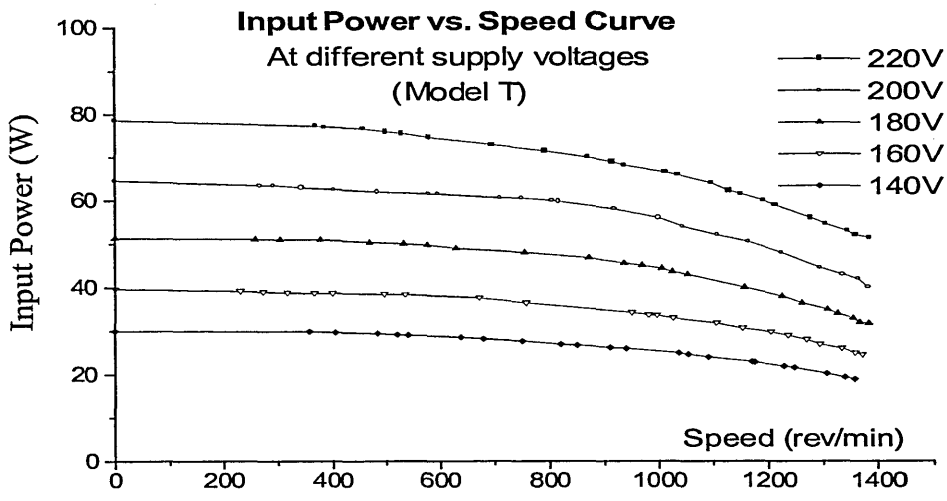

Fig. 7.9b Input power variation with speed under different supply voltages (Model T)

Comparing the performances between the two different designs, we can find that

1. the Model R has the higher breakdown torque than the Model T does, therefore the Model R can produce higher output power.

2. a big torque drop occurs with the Model R during the speed area of 400-600 rev/min due to the effect of third-order harmonic, indicating that the third-order harmonic plays the most important role compared with other higher-order harmonics. No observed torque drop can be seen on the torque-speed curve of the Model T which has a bigger air gap. The length of air gap of the Model T is 0.7mm.

3. the starting torque of the Model T is higher than that of the Model R although the step air gap is adopted in the Model R.

With the test results for torque, input current and power, the output mechanical power, the efficiency and the power factors can be calculated and shown from Fig. 7.10. to Fig. 7.12.

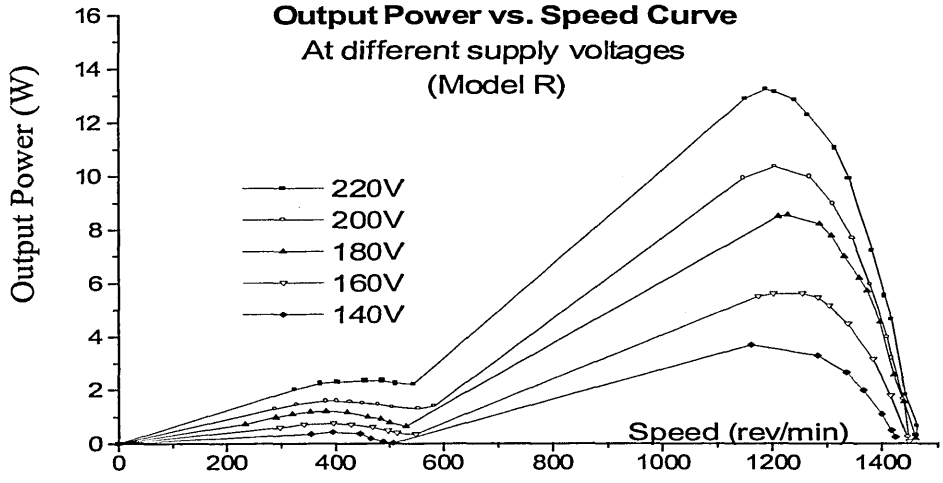

Fig. 7.10a Output power variation with speed under different supply voltages (Model R)

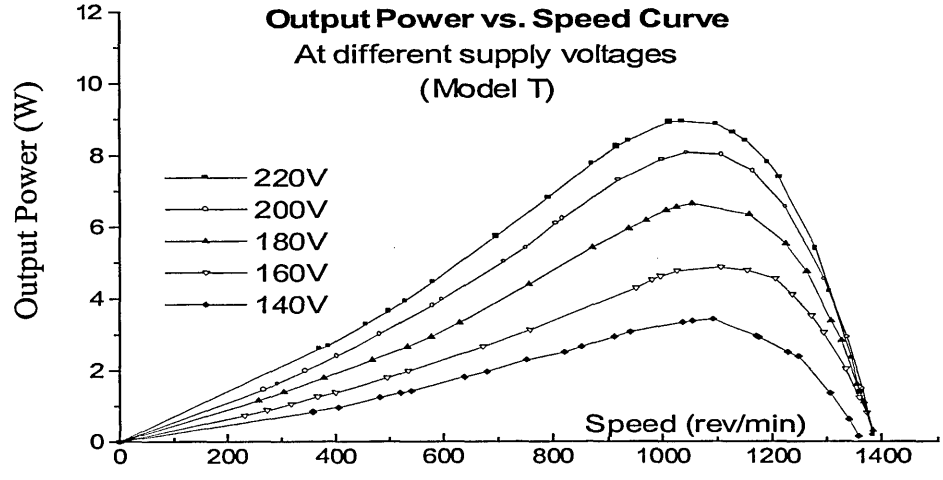

Fig. 7.10b Output power variation with speed under different supply voltages (Model T)

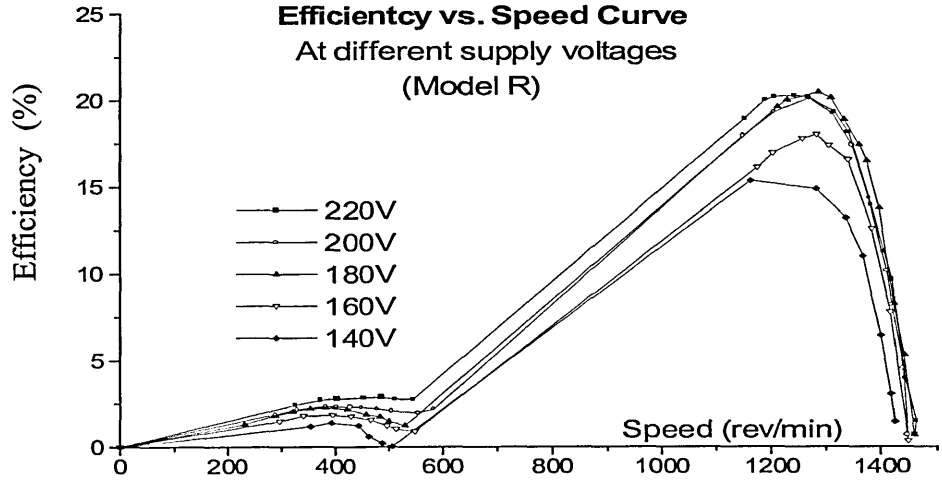

Fig. 7.11a Efficiency variation with speed under different supply voltages (Model R)

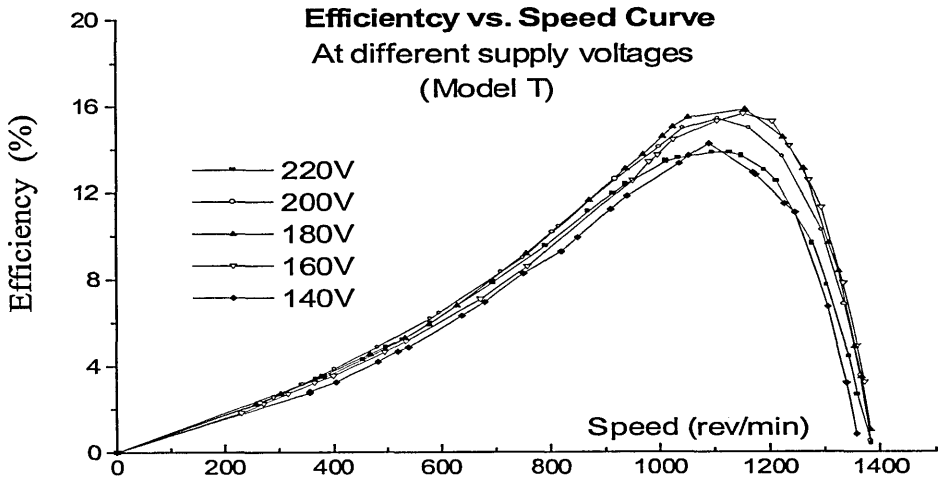

Fig. 7.11b Efficiency variation with speed under different supply voltages (Model T)

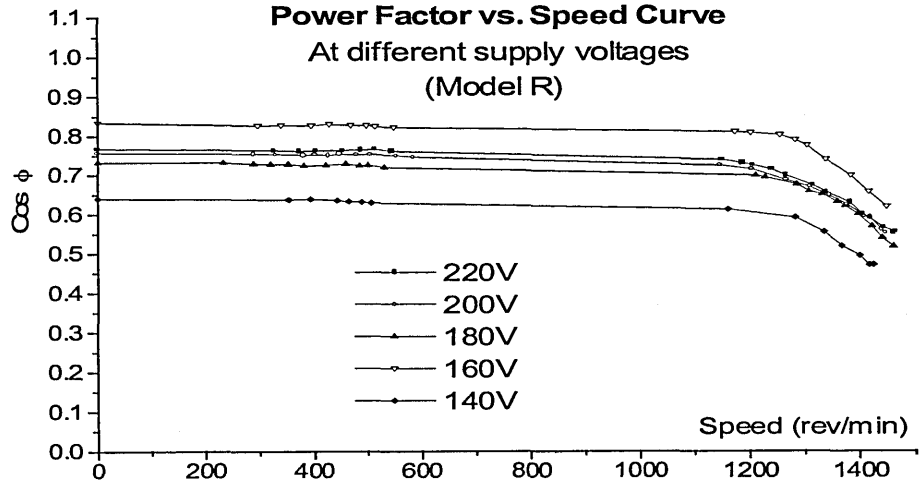

Fig. 7.12a Power Factors variation with speed under different supply voltage(Model R)

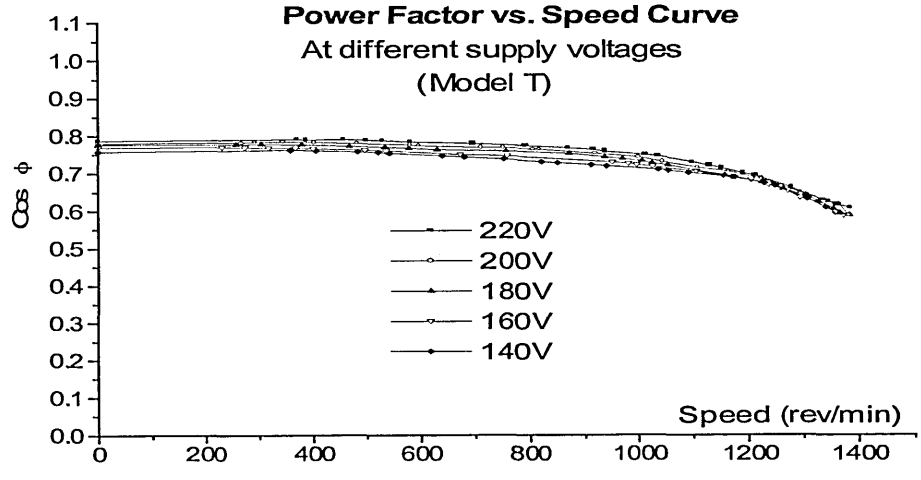

Fig. 7.12b Power Factors variation with speed under different supply voltages (Model T)

To learn the thermal capability of the tested motor, the temperature rise test is employed by measuring the increase of stator resistance according to the follwing equation.

$$T = (\frac{R_{hot}}{R_{cool}} - 1) * (235 + t) \tag{7.2}$$

where T = total temperature increase in °C above the surrounding temperature t

R_{hot} = hot stator resistance

R_{cool} = cool stator resistance when the temperature of the coil equals to the surrounding temperature t.

In temperature test, a switch which connects either the supply source or the digital resistance meter was used, so the stator resistance of the tested motor can be obtained immediately once the switch is connected to the digital resitance meter. The process of resistance measuring lasts only several seconds, therefore the temperature rising procedure can be considered as a continuous procedure. To prevent the metal base of test rig conducting away significant heat to affect the reading, several sheets of thick paper are put between the tested motor and mounted metal base. During the test, the output power of tested motor is held at a constant value of the maximum output by adjusting exciting current of the eddy-current brake.

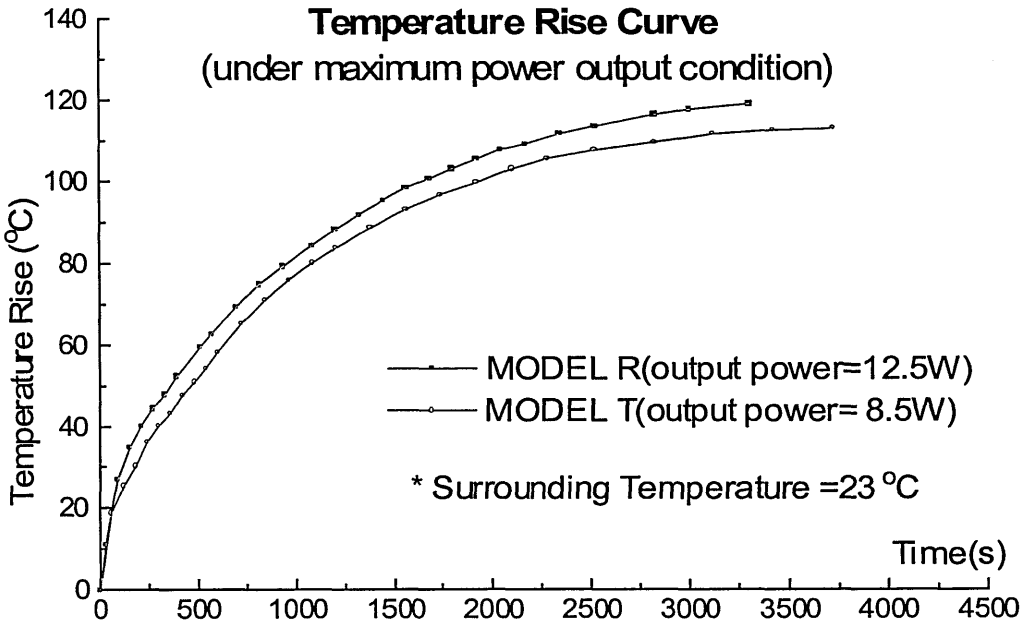

Fig. 7.13 Temperature variation with time under maximum output

7.3.2 Transient State Characteristics

In this section, in order to get the torque/speed characteristic during the transient state, the starting process of SPIM is carried out with the test rig. First, to know the effect of the switching angle of the supply voltage cycle on the tested motor, the motor is switched on 0, 20, 40, 60, 80 and 90 degrees of the voltage cycle. In order to obtain the exact starting angle on voltage cycle, a special equipment named 1-pole Point On Wave Switch has been used.

From the following figures of input current versus time at different switch angles, the difference of the transient procedure with different switch angles occurs only during the first one or two cycles. For the rest current cycles, no obvious difference can be observed. In the other words, the transient process due to the different swicthing angle disappears in the first two cycles.

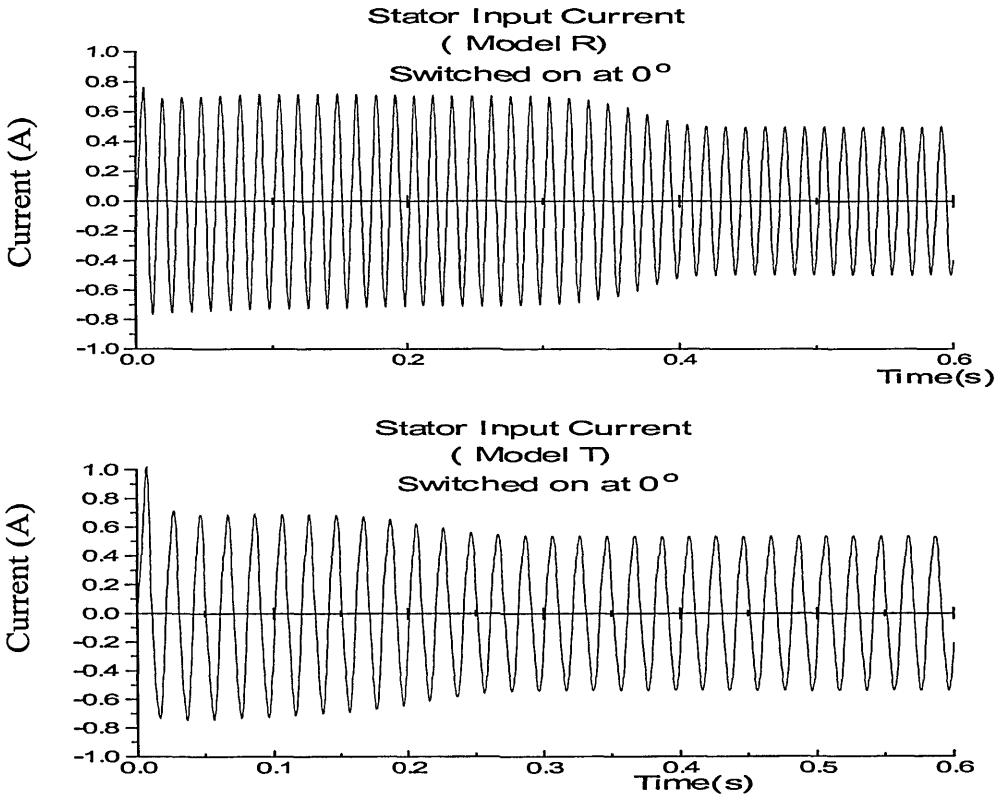

Fig. 7.14a Input current variation with time under starting
(Switch at 0 degree of supply voltage)

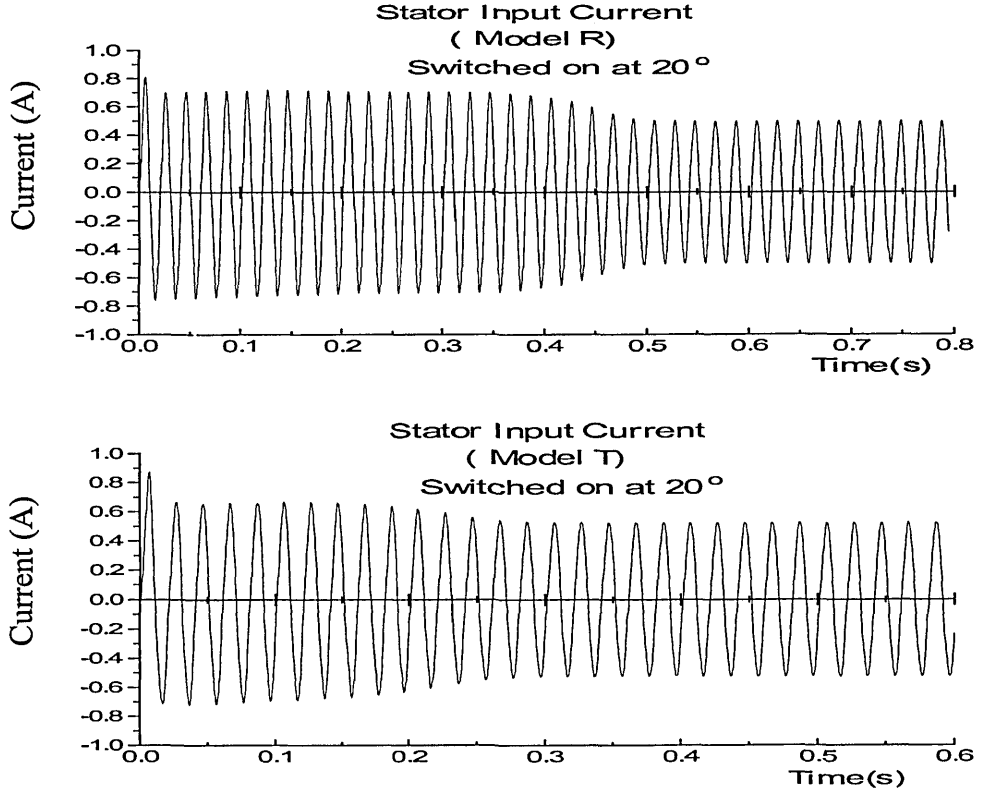

Fig. 7.14b Input current variation with time under starting
(Switch at 20 degree of supply voltage)

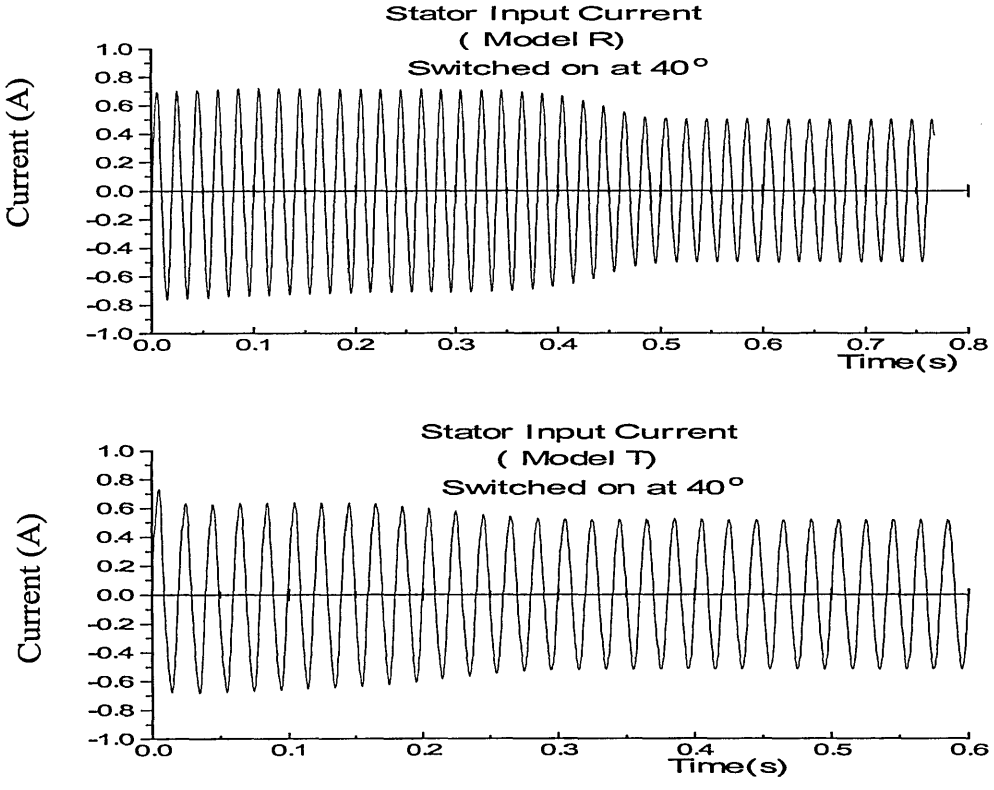

Fig. 7.14c Input current variation with time under starting
(Switch at 40 degree of supply voltage)

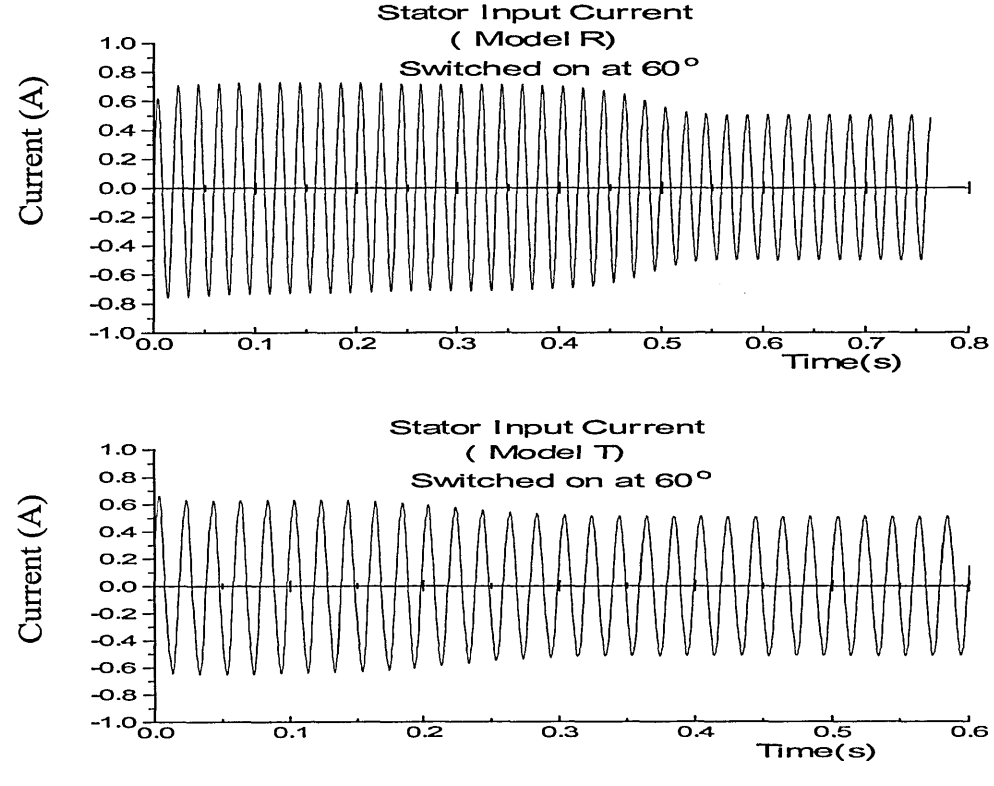

Fig. 7.14d Input current variation with time under starting
(Switch at 60 degree of supply voltage)

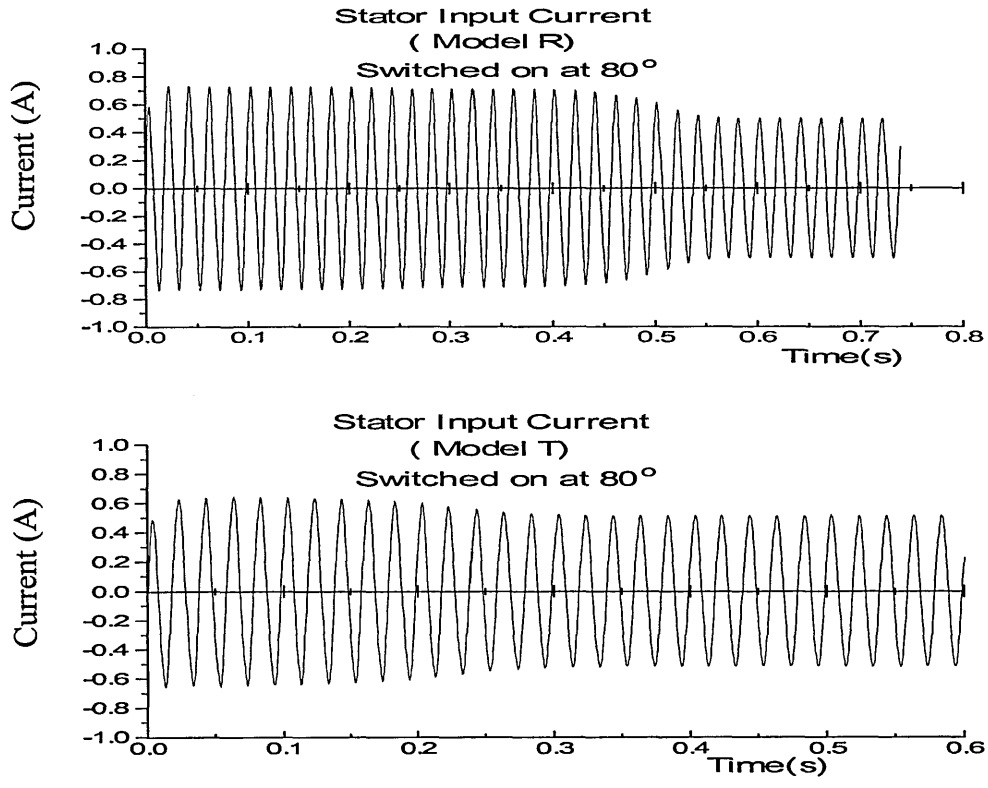

Fig. 7.14e Input current variation with time under starting
(Switch at 80 degree of supply voltage)

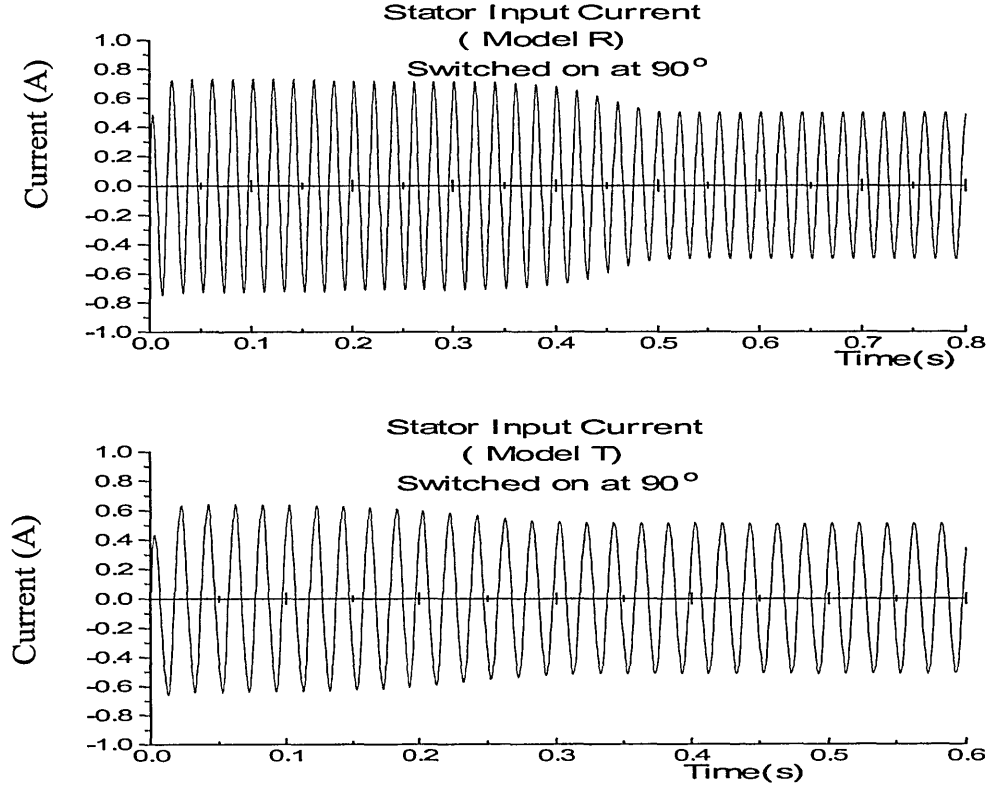

Fig. 7.14f Input current variation with time under starting
(Switch at 90 degree of supply voltage)

For the mechanical signals, like the torque and the speed signal, which change slower than the electrical signal, the different switch angles does not significantly effect the variation of torque and speed with the time. So, these two signals variation in the starting processing are shown here only with one situation of switching at 20 degree.

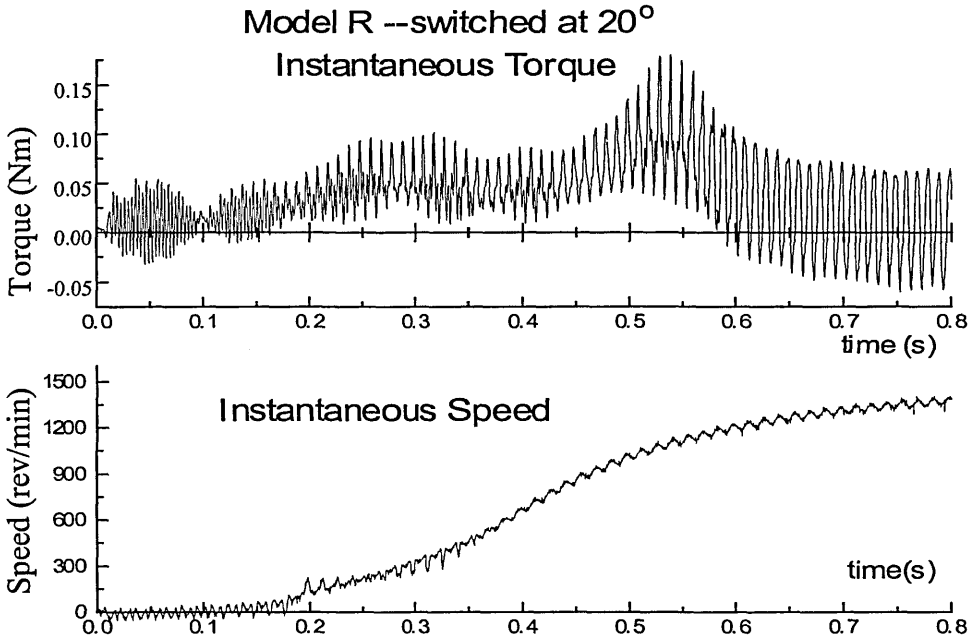

Fig. 7.15 Instantaneous torque & speed variation with time under starting (Model R)

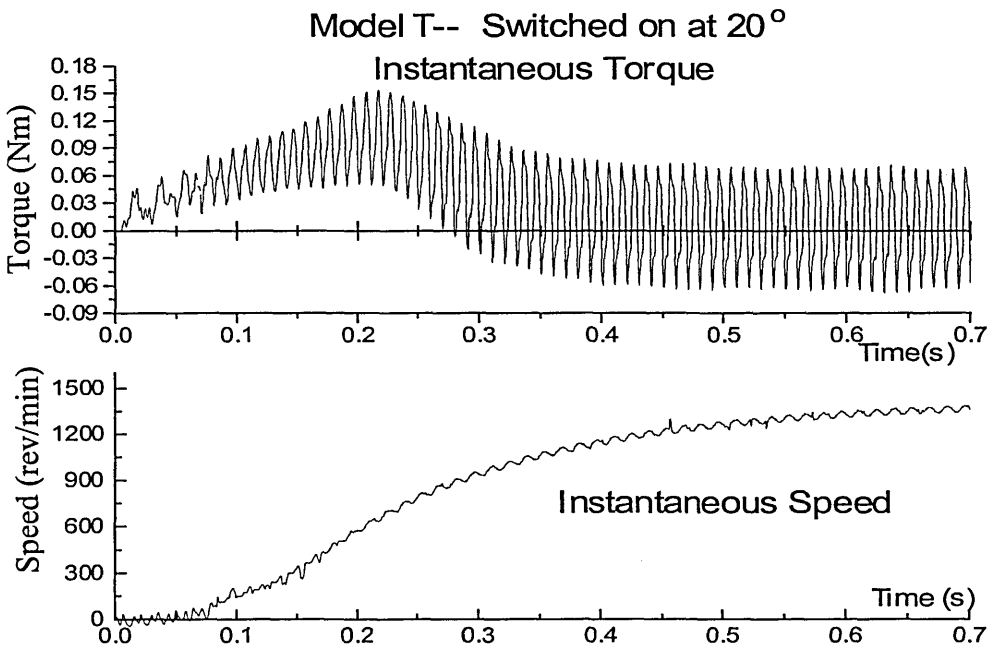

Fig. 7.15b Instantaneous torque & speed variation with time under starting (Model T)

In Fig. 7.15, the frequency of the output torque is two times higher than that of the source line. The twice-line-frequency pulsating torque appears over the whole range of speed including the starting point. With the increase of rotor speed, the amplitude of the pulsating torque increases as well.

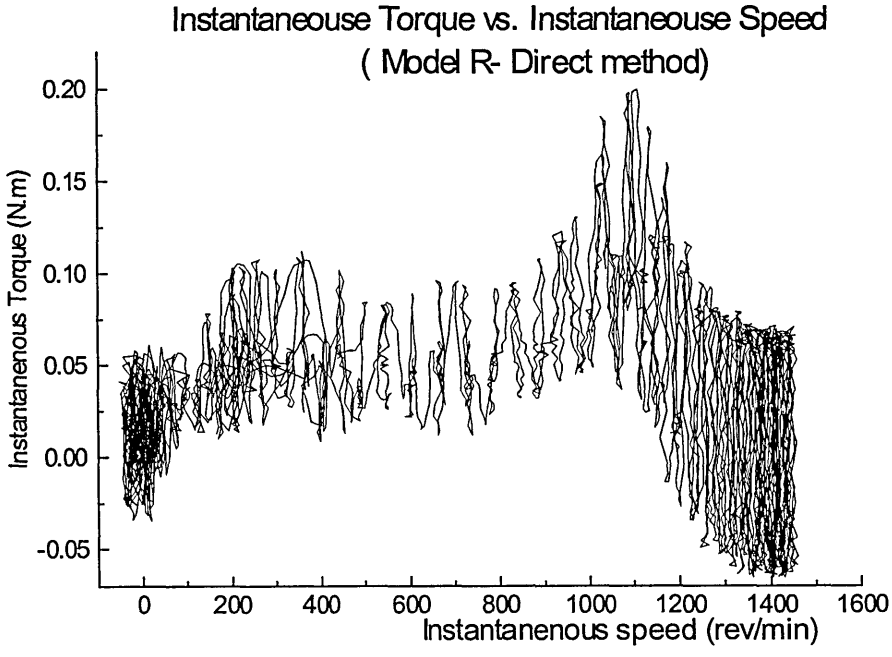

Fig. 7.16a Instantaneous output torque vs. speed with direct method(Model R)

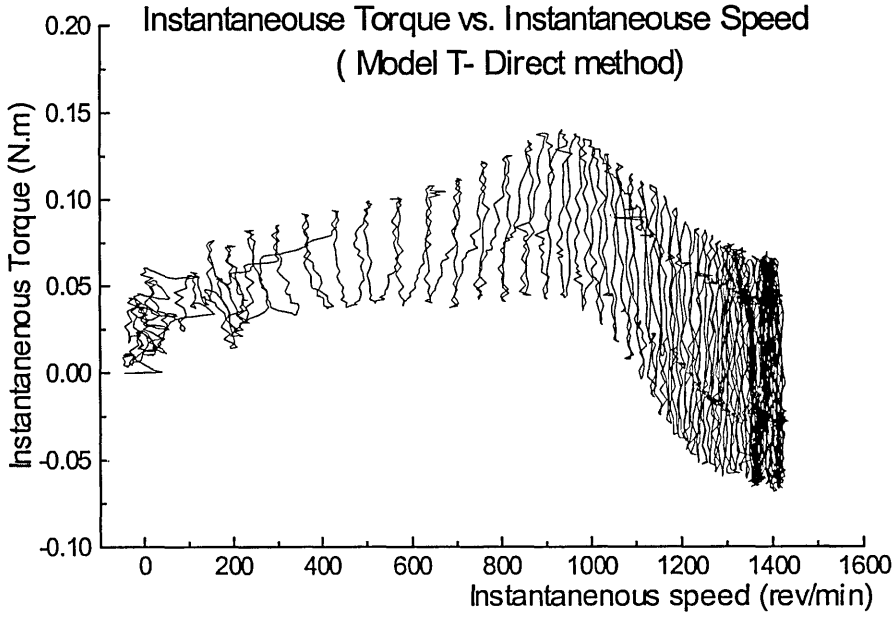

Fig. 7.16b Instantaneous output torque vs. speed with direct method(Model T)

From the instantaneous torque and speed variation with time, the relation between the torque and the speed can be drawn in Fig.7.16. Because the instantaneous torque of SPIMs varies at a twice-line-frequency, the instantaneous speed also shows a twice-line-frequency ripple accordingly. Therefore, at the different time point, the instantaneous torque of SPIMs may have a set of values under a certain speed. So, under the transient state, the relationship between instantaneous torque and the instantaneous speed is not mono-tropic and the torque at a given speed can not be decided from Fig. 7.16

To obtain the normal mono-tropic torque/speed curve sketched in the steady state, a moving-window average filter, whose window size is fixed at the cycle of supply voltage (0.02s), is applied to both instantaneous torque and the instantaneous speed. The principle of the moving-window smoothing method can be explained by the Fig. 7.17. Using such a smoothing method, the smoothed value is obtained by averaging the instantaneous value during the window-length period. The window moves one step each time and the step size is decided by the sampling step. For example, if the sampling rate is at 5kHz, the moving step is therefore 1/5K(s).

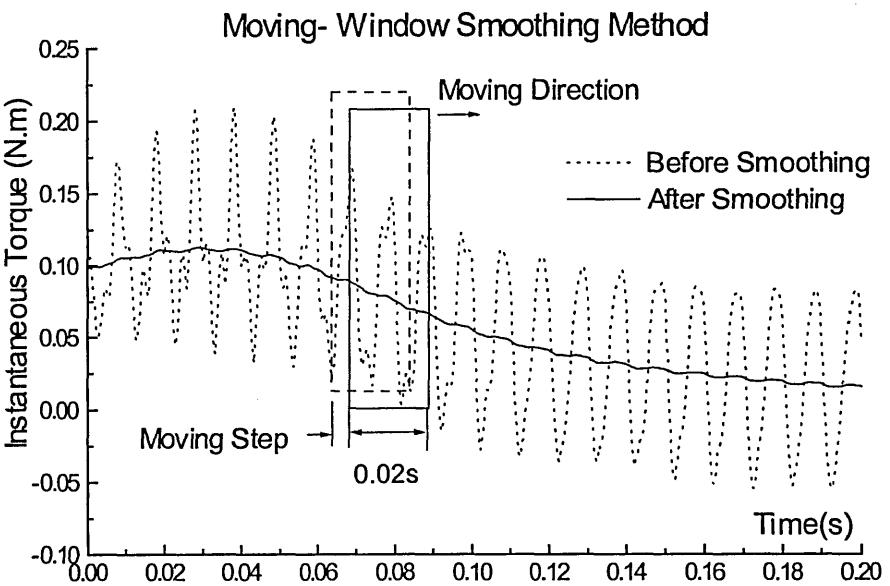

Fig. 7.17. The principle of moving-window method for smoothing the ripple.

After both instantaneous torque and the instantaneous speed are smoothed with the moving-window algorithm. The torque/speed curve obtained by direct method is

compared with the result measured under the steady state in Fig. 7.18.

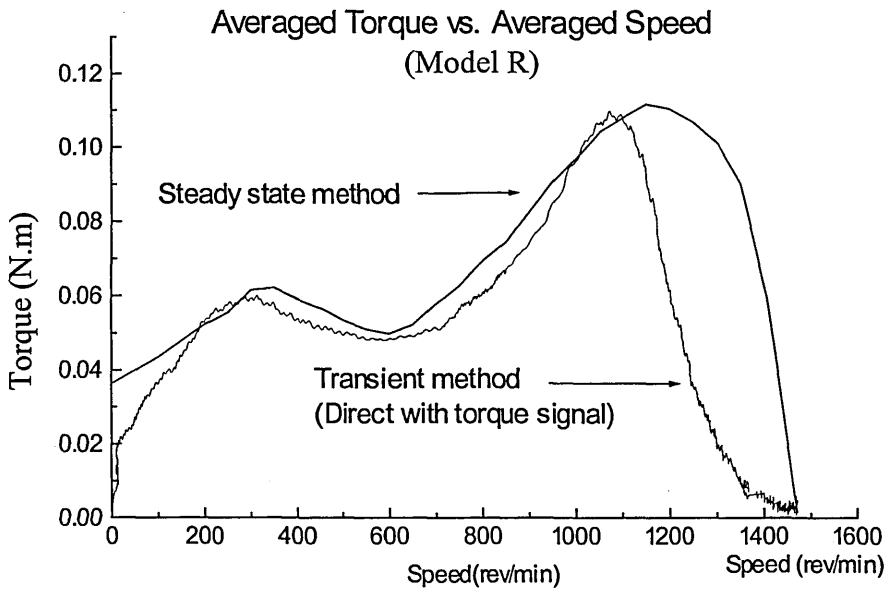

Fig. 7.18a, Averaged torque vs. speed with two different method (Model R)

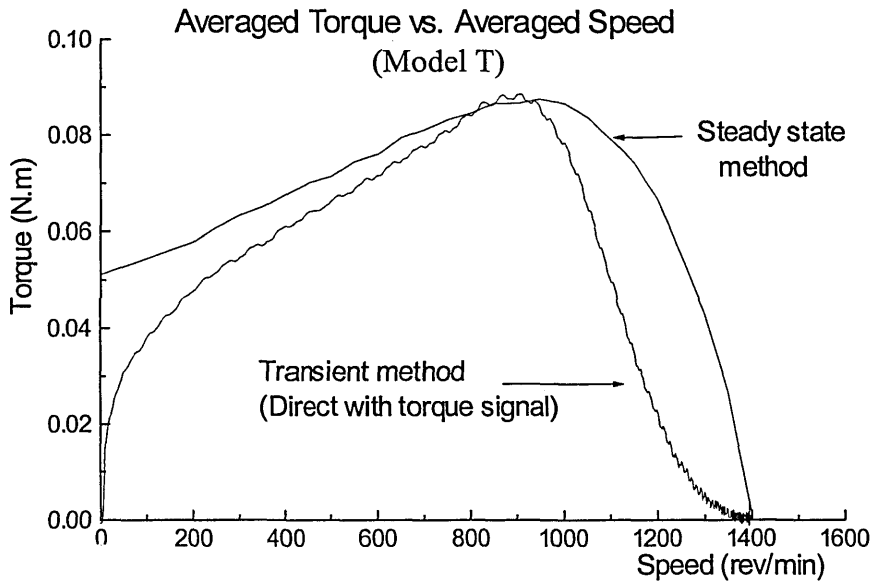

Fig. 7.18b, Averaged torque vs. speed with two different method (Model T)

Comparing the torque/speed curves obtained from the different ways, it is found that there exists a considerable gap between the result of transient method and the steady state measurement, especially in the starting area and high speed area. Although the maximum

torques gained by the two methods have the same magnitude, their corresponding speed is different. The difference on the torque-speed curve between two methods is mainly due to the following reasons.

1. The speed signal has a considerable time delay compared with the torque signal when measuring a dynamic procedure because the torque signal is set to be in advance of the speed one by the built-in electronic circuit. Although the torque/speed transducer has been modified by the manufacturer to improve the time response of the speed signal, the time delay still can not be eliminated.

2. The minimum measurable speed of the speed transducer is 50 rev/min. In low speed region, the dynamic accuracy of the speed transducer is reduced. Additionally, The built-in filter in the torque transducer decreases the magnitude of the high frequency component in the torque signal that is the significant part in the torque signal when the motor is suddenly started.

3. When the motor reaches a high speed, an error may be produced by using a fixed-size window to smooth the ripples. At high speed, the main assumption of the moving-window smoothing method that the rotor speed does not change significantly during the window-size period cannot be satisfied. Thus, at high speeds, the size of the moving-window should be reduced.

7. 4 Conclusion

In this chapter, both the hardware and the software of the PC-based data acquisition system developed were introduced in the detail. In order to remove the ripple of the instantaneous torque and the instantaneous speed, a moving-window average filter, whose window size was fixed at 0.02s, was applied.

With this PC-based measurement rig, the performances of SPIMs in different designs were measured. These two tested motors supplied much useful information to help the designer find the way to improve the starting torque, to reduce the effect of third order harmonic and to increase the maximum output power.

Using the test rig, the twice-line-frequency pulsating torque, a unique characteristic of SPIMs, can be measured dynamically. By measuring the magnitude of the pulsating torque, the effect of design parameters on the two rotating magnetic fields can be further studied.

Due to the time delay of the speed transducer, the result of the dynamic speed measurement is not satisfactory enough so far. Further research work should be focused on picking up the correct speed signal, and on the algorithm of smoothing the instantaneous torque and speed signals.

8 CONCLUSION AND FURTHER RESEARCH WORK

In this research, many fields have been involved ranging from the electromagnetic field theory, the numerical calculation to the different optimisation search algorithms. The main achievements of this research fall into three main areas: (1) developing the 2D multi-slice finite element model of SPIMs; (2) improving the optimisation search algorithm for the electrical motors design; (3) investigating the effect of the design parameter variations on SPIMs' characteristics.

1. The 2D multi-slice finite element model of SPIMs

As mentioned at the beginning of the thesis, the SPIMs are considered the most difficult induction motors to be analysed due to the asymmetrical windings, the non-uniform air gap and the abundant spatial harmonics in the field and the time harmonics in the rotor-bar current. In this thesis, based upon the finite element technology, a more accurate analysis model of the SPIMs, which is called the two-dimensional multi-slice time-stepping FE model, has been developed.

In this model, the time-stepping method has been used to consider the effect of the spatial harmonics and the time harmonics. In order to reduce the computing time required by the time-stepping technique, a variable step size method was adopted. By monitoring the

truncation error, which is the difference between the estimated value using Neville's algorithm and the backward difference method, the variation rate of the field is detected reliably. Therefore, a suitable step size can be determined accordingly

The most notable improvements on the 2D finite element model of the SPIMs lie in using the multi-slice technique and coupling the uneven end-ring resistance.

In the improved FE model, the multi-slice technique by which the skewed rotor was split into a series of unskewed slices has been introduced in order to consider the effect of a skewed rotor. With such a FE model, all the influence of the skewed rotor, the skin effect, the local saturation and the non-sinusoidal quantities can be considered directly. By coupling the external circuit equations with the field equations directly, the performance of a SPIM including current and torque can be obtained once the system equations are solved.

End-ring resistance was investigated by using the finite element model. It was found that the equivalent end-ring resistances between every part of adjacent rotor bars were decided by both the end-ring geometry size and the distribution of the end-ring current. The equivalent end-ring resistances are uneven along the circumferential direction and they change significantly with the variation of the current distribution in the end-ring area. Thus, an instantaneous non-uniform end-ring resistance model was proposed originally and coupled with the 2D multi-slice finite element model. With this non-uniform end-ring resistance model, the effect of the end ring on the harmonic currents flowing in the rotor bars can be considered properly. Furthermore, in order to reduce the computing cost due to coupling end-ring resistance calculation with magnetic field computing, a simplified iteration scheme was then studied. With this algorithm, the end-ring resistance calculated can be maintained in an acceptably accurate range.

2. *Optimisation design based upon the improved search algorithm and finite element analysis*

By combining the niching genetic algorithm with the modified Hooke–Jeeves' method, a

more efficient and reliable hybrid global–local search algorithm was presented. In this algorithm, the genetic algorithm and the deterministic method were invoked alternatively according to the variation of the best fitness. With this hybrid method, the global optimum could be obtained while the convergence speed was improved greatly compared with the conventional genetic algorithm. The validity and the efficiency of the developed hybrid search algorithm have been proven by the ideal mathematical function and the actual design of SPIMs

In order to improve the accuracy of the performance analysis for SPIMs, the finite element method was adopted to calculate the performance of SPIMs in the optimisation search procedure. A 2D multi-slice fixed–mesh (sinusoidal approximation) FE model was therefore developed. The validity of the sinusoidal approximation FE model was confirmed by the result of the time-stepping method and the experimental result under the locked-rotor circumstance. To modify the mesh with respect to the geometry change of the SPIMs, a partial auto-remesh program driven by the geometrical design parameters was also proposed. With the auto-remesh program the number of optimisation variables can be reduced notably, therefore the computing time of the optimisation search can be saved.

3. Investigating the effect of design parameter variations on the SPIMs' characteristics

With the 2D multi-slice FE model coupled with uneven end-ring resistance, the effect of the various design parameters can be studied more accurately. In this study, several design parameters, including the air gap profile, the pole bridge, the skew, the number of rotor slots, the closed-slot rotor and the shaded-pole arc, have been investigated. For these design parameters, it was difficult to study by the conventional equivalent circuit models or the normal 2D finite element model. Some suggestions about these design parameters were given after their effect had been discussed.

More importantly, in order to probe the effect of the different parameters on the SPIMs' performance, a harmonic analysis method based on the time-stepping FE method directly

was developed. Using this method, both the spatial harmonic in the air gap field and the time harmonics in the rotor-bar current can be refined from the results of time-stepping method. Therefore, the effect of the design parameters on both air gap MMF harmonics and rotor current harmonics may be investigated directly.

In addition to the above three main research work, a PC-based data acquisition system was built up as well. With this test rig, the SPIMs can be tested both in steady state and in transient state. The measured results were helpful for verifying the accuracy of the analysis models and could support useful information for performance improvement.

It is hoped that the work described in this thesis contribute to the current knowledge in the field of the SPIMs design and finite element method. However, there is still a lot of research to be done in the area concerned.

1) Three-dimensional finite element model for the SPIMs

Although with the proposed 2D multi-slice finite element model, a quite accurate result for SPIMs analysis can be achieved, the 3D-version model may offer an opportunity to investigate the electromagnetic field of the SPIMs thoroughly. The prior difficulty for the 3D analysis may result from the complicated 3D geometry and the huge amount of computing time. At present, most 3D models are normally used to analyse a machine partly, e.g. the end-ring and the overhang of stator windings. Therefore, how to create a 3D mesh with a simple algorithm and how to choose a proper potentials to reduce the number of unknowns is worthwhile to be further studied. Additionally, for normal machine designs, a simplified 3D model may be more suitable. Although some models have been proposed for the induction motor analysis [Ho, 1998], the simplified model for the transient performance analysis and the non-sinusoidal quantities still remains unsolved.

2) Approximate finite element model for the optimisation of SPIMs

In this study, the optimisation technology was only applied to improve the starting torque of the SPIMs. For the SPIMs which are designed and built for driving fans or pumps continuously, the demand on starting torque is not onerous and increasing the efficiency at the rated working point becomes more necessary. Although the proposed optimisation search algorithm can be used for any applications of motor design, there remains a doubt about the validity of the sinusoidal approximation model for SPIMs at the rated working point since the influence of harmonics has to be considered for SPIMs' analysis except for the rotor-locked state. Consequently, how to consider the harmonic effect with the fixed-mesh FE model needs to be studied further.

3) Construction variation of the SPIMs

The SPIMs may have the variety of construction, for instance, two shaded-rings per pole, the 'C' type asymmetrical stator and the two-piece stator punch [Moczala, 1998]. In this study, only the most popular construction has been investigated. Thus, by examining the different constructions of SPIMs, the effect of the structure variation can be learned and the knowledge will help the designer to choose the correct design for the different applications or to improve the current designs

4) Transient testing of the SPIMs

In this study, a PC-based data acquisition has been built up. However, due to the time delay on the speed signal, the dynamic torque/speed performance cannot be measured precisely. Therefore, the smooth torque/speed profile cannot be decided accurately during the starting procedure of the acceleration test. This problem can be solved by using other accurate speed transducers such as the optical encoder. Additionally, in order to obtain the smooth torque/speed curve, an adaptive window-size method is needed to smooth the twice-line-frequency pulsating torque and speed.

References

[1] Akbaba, M. & Fakhro, S. Q., 1996, "An improved computation technique of the inductance parameters of reluctance augmented shaded-pole motors using finite element method", ", *IEEE Trans. on Energy Conversion*, Vol. 7, No. 2, pp. 308-314,

[2] Andria, G., Aquila, A D. Salvators, L. & Savino, M., 1986, "Dynamic testing of induction machines by means of a digital system", *Proc. of the Conf. Of Electical Machines*, Munichen, pp484-487

[3] Arkkio, A., 1987, *Analysis of induction motors based on the numerical solution of the magnetic field and circuit equations*, ISBN 951-666-250-1, Helsinki

[4] Bianchi, N. & Bolognant, S., 1998, "Design optimisation of electric motor by genetic algorithm", *IEE Proc. Electric Power Application*, Vol. 145, No.5, pp 475-483

[5] Binns, K.J., Lawrenson, P.J., Trowbridge, C. W., 1992, *The Analytical and Numerical Solution of Electric and Magnetic Fields*, John Wiley & Son, UK.

[6] Boualem, B., Piriou, F, 1994, "Modelling of induction motor accounting for skewed slots effects", *Proceeding of Inter. Conf. on Electrical machine*, Paris, pp. 699-704

[7] Brandstater, B.R., Ring W., Magele, C.H. & Richter, R., 1998, "Shape design with great Geometrical deformations using continuously moving finite element nodes", *IEEE Trans. on Magnetics*, Vol. 34, No. 5, pp.2877-2880

[8] Brauer, J. R., Lee, S.H. & Chen, Q. M,, 1996, " Adaptive time-stepping in nonlinear transient electromagnetic finite element analysis", The Seventh Biennial IEEE Conference on Electromagnetic Field Computation, IEEE, New York, pp243

[9] Brisset, S., & Brochet, P., 1998, "Optimization of Switched reluctance motor using determinstic methods with static and dynamic finite element simulation", *IEEE Trans. on Magnetics*, Vol. 34, No. 5, pp.2853-2856

[10] Butler, O. I. & Wallace, A. K., 1969, "Effect of parameter changes on the performance of shaded pole motors", *Proc. IEE*, Vol. 116, No. 5, pp732-736

[11] Chang, S. S. L., 1951, " Equivalent circuits and their applications in designing shaded pole motors", *Trans. of AIEE*, vol. 70, pp690-699

[12] Chari, M. V. K. & Silvester, P., 1971, "Analysis of turbo-alternator magnetic fields by finite elements", ", *IEEE Trans. on Power Apparatus and Systems*, Vol.90, pp 454-464.

[13] Chedid, R. & Freris, L. L., 1994, "Magnetic-field analysis of Asymmetrical machines by finite element method", *IEE Proc. Gener. Transm. Distrib.* Vol.141, No. 1, pp 53-59

[14] Cheng, D. K., 1989, *Field and Wave Electromagnetics*, Addison-Wesley Publishing Company, Reading

[15] Christiansen, C. F., Battaiotta, R. & etc., 1989, "Digital measurement of angular velocity for speed control", *IEEE Trans. on Industry Electronic*, Vol. 36, No. 1, pp 79-83

[16] Coulomb, J. L. & Meunier, G., 1984, "Finite element implementation of virtual work priciple for magnetic or electric force and torque computation", *IEEE Trans. on Magnetics*, Vol. 20, No. 5, pp1894-1896.

[17] Coulomb, J. L., 1983, "A methodology for the determination of global electromechanical quantities from the finite element analysis and its application to evaluation of magnetic forces, torque and stiffness", *IEEE Trans. on Magnetics*, Vol. 19, No. 6, pp 2514-2519

[18] De Weerdt, R. & Belmans, R., 1995, "Squrrel cage inductance motor end effects using 2D and 3D finite element", *Proceeding of Conference on Electrical Machine and Drives*, pp62-66

[19] DeBortoli, M. J. & Salon, S.J., 1990, "Computation of forces and torque in electromagnetic devices using finite element method", *ICEM'90*, MTI,USA, pp699-705

[20] Desai, B. G. & Mathew, M.A., 1971, "Transient analysis of shaded pole motor", *IEEE Trans. on Power Apparatus and Systems*, Vol. PAS-90, No.2, pp 484-494

[21] Dym, C. L. & Levitt, R.E., 1991, *Knowledge-based system in engineering*, McGraw-Hill, USA

[22] Eastham, J. F. & Williamson, S., 1973, " Generalised theory of induction motors with asymmetrical air-gap and primary winding", *Proc. IEE*, Vol. 120, No. 10, pp 767-775

[23] EDR User Manual, 1996, *EDR software developers kits for Eagle Technology boards*, David Tinker & Eagle Technology

[24] Faiz, J., Feyzi M.R.& Ali-Abbasi, B., 1993, "Performance prediction and analysis of shaded pole induction motor considering asymmetrical flux distribution and saturation effect", *Proceeding of the 4th International conf. on Computational Aspect of Electromechanical Energy Conversion and Drives*, Montreal, pp183-188

[25] Fanni, A., Marchesi, M., Serri, A., & Usai, M., 1999, "Performance Improvement of a Hybrid Algorithm for Electromagnetic Devices Design", *IEEE Trans. Magnetics*, Vol.35, No.3, pp.1698-1701

[26] Gary, C. B. 1989, *Electrical Machines and Drive Systems*, Longman Seientific & Technical, England

[27] Goldberg, D. E., 1989, *Genetic Algorithms in Search, Optimization, and Machine Learning*, Addison-Wesley Publishing Company, Inc., Reading

[28] Guru, B. S., 1983, " Revolving-field analysis of Shaded-pole motor", *IEEE Trans. on Power Apparatus and Systems*, Vol. PAS-102, No.4, 1983, pp 918-927

[29] Hameyer, K. & Belmans, R., 1996, "Design and optimisation of electrotechnical devices", *Journal of Engineering Design*, Vol. &, No. 3, pp235-249,1996

[30] Hameyer, K. & Hanitsch, R., 1994, "Numerical optimisation of electromagnetic fields by stochastic search and MFC- model", *IEEE Trans. on Magnetics*, Vol. 30, No.5, pp.3431-3435

[31] Heller, B. & Hamata, V., 1977, *Harmonic Field Effects in Induction Machines*, Elsevier Scientific Publishing Company, Amsterdam

[32] Ho S. L. & Fu, W. N., 1997, "A comprehensive approach to the solution of direct-coupled multi-slice model of skewed rotor induction motors using time-stepping eddy-current finite element method", *IEEE Trans. on Magnetics*, vol. 33, pp2265

[33] Ho S. L. & Fu, W. N., 1998, "Review and future application of the finite element methods in induction motors ", *Electric Machines and Power System*, vol. 26, pp111-125

[34] Ho S. L., Fu, W. N. & Wong, H. C., 1997, "Application of automatics choice of step size for time stepping finite element method to induction motors" , *IEEE Trans. on Magnetics*, vol. 33, No. 2 pp1370-1373

[35] Hoffman de Visme, G., 1968, "Digital processing unit for evaluating angular acceleration", Electronic Engineering, Vol. 40 , pp183-188

[36] Holland, J. H., 1975, *Adaptation in Natural and Artificial System*, Ann Arbor, The University of Michigan Press

[37] Holt, T., 1981, "Measurement of electromagnetic air gap torque produced by a syschronous motor during starting", *IEEE Trans. on Power Apparatus and System*, Vol.100, No. 4, p.2058-2067, April, 1981

[38] IEEE standard 112-1978, *IEEE Standard Test Procedure for Poly-phase Induction Motors and Generators*, pp. 7-30

[39] Instruction Manual,1997, *Torquemaster- TM 200 Series*, Vibro-meter Company, Switzerland

[40] Jozsef, V. & Djura, B., 1997, "Analysis of the characteristics of single phase shaded pole induction motor with two short-circuited auxiliary phases", *IEEE Trans. on Energy Conversion*, Vol. 12, No. 4, pp 269-274

[41] Kametani, H., Sakabe, S., & Nakanishi, K., 1996, " 3D electro-magnetic analysis of a cage induction motor with rotor skew", *IEEE Trans. on Energy Conversion*, Vol. 11, No. 2, pp331-337

[42] Kamper, M.J., Van der Merwe, F.S., & Williamson, S., 1996, "Direct finite element design optimisation of the cageless reluctance synchronous machine", *IEEE Trans. on Energy Conversion*, Vol. 11, No. 3, pp. 547-553,

[43] Kim, M.K., Lee, C.G. & Jung, H. K., 1998, "Multiobjective optimal design of three-phase induction motor usiong improved evolution strategy", *IEEE Trans. on Magnetics*, Vol. 34, No. 5, pp.2980-2983

[44] Komeza, K., Pelikant,A., Tegopoulos, J. and Wiak, S., 1994, "Comparative Computation of force and torque of electromagnetic device by means of different formulate", *IEEE Trans. on Magnetics*, Vol. 30, No.5, pp3475-3479

[45] Kovacs, G., 1982, " Skin effect in the end of asynchronous motors'. *Proceeding of Conference on Electrical Machines*, Budapest, pp31-34

[46] Kron, G., 1950, " Equivalent circuits of the shaded pole motors with space harmonics", *Trans. of AIEE*, vol. 69, pp735-741

[47] Li, C., & Rahman, A., 1990, "Three-phase induction motor design optimisation using the modified Hoooke-Jeeves method", *Electirc Machines and Power System*, Vol. 18, pp1-12

[48] Lipo, T. A. & Chang, K. C., 1986, "A new approach to flux and torque-sensing in induction machines", *IEEE Trans. on Industry Application*, Vol.32, No. 4, pp.731-737

[49] Lock, K. S., 1984, "Transient analysis of the shaded pole motor by numerical solution of the basic performance equations", *IEEE Trans. on Power Apparatus and Systems*, Vol. PAS-103, No.9, pp 2691-2698

[50] Lock, K. S., 1984, "Analysis of the steady-state performance of the reluctance-augmented shaded pole motor", *IEEE Trans on Power Apparatus and System*, Vol. 103, No. 9, pp 2625-2632

[51] Lock, K. S., 1987, "Thyristor control of shaded-pole induction motors", *Electric Machines and Power Systems*, Vol. 13, pp185-193

[52] Lowther, D. A. & Dyck, D.N., 1993, "A density driven mesh generation guided by a neural network", *IEEE Trans. on Magnetics*, Vol. 29, pp.1927-1930

[53] Luomi, J., Niemenmaa, A. & Arkkio, A., 1986, "On the use of effectivities in magnetic field analysis of induction motors fed from a sinusoidal voltage source", *Proceeding of International Conference on Electrical Machines*, pp 707-709, Munich

[54] Matsubara, T., Ishihara, Y., Kitamura, S., etc., 1995, "Magnetic field analysis in shaded pole motor taking skewed slot effects into account", *IEEE Trans. on Magnetics*, Vol. 31, pp1916-1919

[55] McFee, S and Lowther, D. A., 1987, " ", *IEEE Trans. on Magnetics*, Vol. 23, No.5, pp3774

[56] Messine, F., Nogarede, B. & Lagouanelle, J., 1998, "Optimal design of electromagnetical actuators: A new method based on global optimisation", *IEEE Trans. on Magnetics*, Vol. 34, No.1, pp.299-307

[57] Miles, A. R., 1985, " The effect of machine geometry and materials on the starting torque of shaded-pole induction motor", *IEEE Trans on Industry Application*, Vol. 21, No. 4, pp 664-668

[58] Mizia, J., Adamiak, K., Eastham, A.R. & Dawson, G. E., 1988, "Finite element force calculation: comparison of method for electric machine", *IEEE Trans. on Magnetics*, Vol. 24, No.1, pp447-450

[59] Moczala, H., Draeger, J. & etc. 1987, *Small Electric Motors (English Version)*, IEE, ISBN 085296-921X. London

[60] Mohammed, O. A., Park, D. C., Uler, F.G. & Chen, Z., 1992, " Design optimisation of electromagnetic devices using artificial neural networks", *IEEE Trans. on Magnetics*, Vol. 28, No. 5, pp.2805-2807

[61] Mohammed, O.A. & Uler, F.G., 1998, "A hybrid technique for optimal design of electromagnetic devices using direct search and genetic algorithm" , *IEEE Trans. on Magnetics*, Vol. 33, No. 2, pp1931-1934

[62] Nondahl, T. A., 1981, " Equivalent circuit model for a shaded-pole induction motor 2. One shaded ring with a stepped air gap", *IEEE Trans. on Power Apparatus and Systems*, Vol. PAS-100, No.1, , pp 295-299

[63] Nortan, H., 1989, *Handbook of Transducers*, Prentice-hall Book Company, New York

[64] Nystuen, A. M., Knoop, D. E. & Loessel, M. C., 1976, "Automated Motor testing using a minicomputer", *IEEE Trans. on Industry Application*, Vol.12, No. 4, pp.349-353

[65] Ojo, J. O., Ostovic, V., Lipo, T. A. & White, J. C., 1990, "Measurement and computation of air-gap torque of salient pole synchronous motor", *IEEE Trans. on Energy Conversion*, Vol. 7, No. 1, pp 176-182

[66] Osheiba, A. M., Ahmed K. A. & Rahman, M. A., 1991, "Performance prediction of shaded pole induction motors", *IEEE Trans on Industry Application*, Vol. 27, No. 5, pp 876-882

[67] Park, S.B., LEE, H.B. & Hahn, S.Y., 1995, "Stator slot shape design of induction motors for iron loss reduction", *IEEE Trans. on Magnetics*, Vol. 31, No. 3, pp.2004-2007

[68] Penman, J. & Stavrou, A., 1996, " Broken rotor bars: their effect on the transient performance of induction machines" , *IEE Proc. of Electrical Power and Applications*, Vol. 143, pp.549-457

[69] Perret, R, & Poloujadoff, M., 1976, "Characteristics analysis of saturated shade-pole induction motors", IEEE Trans. on Power Apparatus and System, Vol. PAS-95,No. 4, pp 1347-1353

[70] Perret, R. & Poloujadoff, M., 1985, " Characteristics analysis of saturated shaded pole induction motors", *IEEE Trans on Power Apparatus and System*, Vol. 95, No. 4, pp 1347-1353

[71] Piriou, F. and Razek., A., 1990, "A model for coupled magnetic-electric circuit in electric machine with skewed slots", *IEEE Trans. on Magnetics*, vol. 26, pp1096-1100

[72] Plunket, A. B., Kelman, G. B. & Boyle, M. J., 1985, "Digital Techniques in the evaluation of high-efficiency induction motor for inverter drives", *IEEE Tran. on Industry Application*, Vol. 21, No. 2, pp.457-463

[73] Poloujadoff, M., 1982, " General rotating MMF theory of squirrel cage induction machines with non-uniform airgap and several non-sinusoidal distributed winding", *IEEE Trans. on Power Apparatus and Systems*, Vol. PAS-101, No.3, 1982, pp 582-591

[74] Press, W. H. 1992, *NUMERICAL recipes in FORTRAN: the art of scientific computing*, Cambridge University Press, UK

[75] Rajanathan C. B., Watson, B. J., 1996, " Simulation of a single-phase Induction motor operating in the motoring, generating and braking models", *IEEE Trans. on Magnetics*, Vol. 32, No.3, pp 1541-1544.

[76] Ratschek, H. & Rokne, J., 1988, *New Computer Methods for Global Optimization*, Ellis Horwood Limited, West Sussex, England

[77] Rogers, W. E., 1954, *Introduction to Electric Fields- a Vector Analysis Approach*, McGraw-Hill Book Company, Inc. New York, USA

[78] Rong, R. W. & Lowther, D. A., 1994, "Storage and Retrieval of solutions in the design of electromagnetic devices" , *IEEE Trans. on Magnetics*, Vol. 30, pp.3648-3651

[79] Sadeghi, H. & Richards, E. F., 1995, "Evaluation of space harmonic in the a 'C' type shaded pole motor and sensitivity study of its stalled torque with respect to its design parameyers", *Conf. Record of the 1995 IEEE 30th Industry Application and System*, pp759-766

[80] Salon, S. J., 1995, *Finite Element Analysis of Electrical Machines*, Kluwer Academic Publishers, Massachusetts, USA

[81] Salujian, L., Coulomb J. L. & Izabelle, A., 1998, "Genetic Algorithm and Taylor development of the finite element solution for shape optimisation of electromagnetic devices", *IEEE Trans. on Magnetics*, Vol. 34, No. 5, pp.2841-2845

[82] Shen, D. Meunier, G. & etc., 1985,"Solution of magnetic fields and electrical circuit combined problem", *IEEE Trans on Magnetics*, Vol. 21, No. 6, pp 2288-2291

[83] Shi, Z. W., 1997, "Computer Aided Design and construction of a multi-point position actuator system", PhD Thesis, University of Abertay Dundee

[84] Simkin, J. & Trowbridge, C.W., 1992, "Optimizing electromagnetic devices combining direct search method with simulated annealing", *IEEE Trans. on Magnetics*, Vol. 28, No.2, pp.1545-1548

[85] Smith, A.C., 1997, " Influnce on end-ring shape on induction motor performance", *Proceeding of IEE Conference on Electrical Machine and Drive*, pp143-147

[86] Strangas, E.G. & Theis, K.R., 1985, "Shaded pole motor design and evaluation using coupled field and circuit equations", *IEEE Trans. on Magnetics*, Vol. 21, pp1880-1882

[87] Stratton, J., 1941, *Electromagnetic Theory*. McGraw Hill, New York

[88] Szabados, B., Dableh, J. H., Findlay, R.D., etc., 1990, "Measurement of the torque-speed characteristics of induction motors using an improved new digital approach", *IEEE Tran. On Energy Conversion*, Vol. 5, No. 3, pp. 565-571

[89] Tandon, S. C., Armor A. F. & Chari, M. V. K., 1983, " Non-linear finite element fields computation for electrical machines and devices", *IEEE Trans. on Power Apparatus and System*, Vol. PAS-102, NO. 5, pp 1089-1095

[90] Tandon, S. C., Armor A. F. and Chari, M. V. K., 1983 "Non-linear finite element fields computation for electrical machines and devices", IEEE Trans. on Power Apparatus and System, Vol. PAS-102, NO. 5, pp 1089-1095

[91] Trickey, P. H., 1936, "An analysis of the shaded pole motor", *Trans. AIEE*, Vol. 55, pp 1007-1014

[92] Trickey, P. H., 1936, "Induction Motor Resistance Ring Width", *Trans. AIEE*, Vol. 55, pp 144-150

[93] Trutt, F. G., 1981, "Equivalent circuit analysis of shaded pole motor", *Electrical Machines and Electromechanics*, Vol. 6, pp 35-43.

[94] Tsukerman, I., 1995, "Accurate computation of 'Ripple Solution' on Moving Finite Element Meshes", *IEEE Trans. on Magnetics*, Vol. 31, pp1472-1475

[95] Uler, F.G, Mohammed, O.A. &.Koh, C.S., 1994, "Utilizing genetic algorithm for optimal design of electromagnetic devices" , *IEEE Trans. on Magnetics*, Vol. 30, No. 2, pp4296-4298

[96] Uler, G.F. & Mohammed, O. A., 1996, "Ancillary techniques for the practical implementation of Gas to the optimal of electromagnetic devices", *IEEE Trans. on Magnetics*, Vol. 32, No. 3, pp.1194-1198

[97] Vasconcelos, J., Krabenbuhl, L., Nicolas, L. & Nicolas, A., 1994, "Design optimisation using BEM coupled with Genetic Algorithm", *Proceeding of the 2nd IEE International conference on Computation in Electromagnetics* pp.60-63

[98] Vasconcelos, J., Saldanha, R., Krahenbuhl L., & Nicolas, A., 1997, "Genetic algorithm coupled with a deterministic for optimisation in electro-magnetics", *IEEE Trans Magnetices*, Vol.33, No.2, pp.1860-1863

[99] Vassent, E., Meunier, G. and Foggia, A., 1991, "Simulation of induction machines using complex magnetodynamic finite element method coupled with the circuit equations", IEEE Trans. on Magnetics, Vol. 27, pp4246-4249

[100] Veinott, C. G. & Martin, J. E., 1986, *Fractional and Sub-fractional Horsepower Electric Motors*, McGraw-Hill Book Company, New York, Forth Edition

[101] Veinott, C. G., 1959, *Theory and Design of Small Induction Motors*, McGraw-Hill Book Company, Inc,

[102] Walsh, G. R., 1975, *Methods of Optimisation*, John Wiley & Son, London

[103] Williamson S. & Breese, P., 1977, " Effect of air-gap profile variations on the performance of reluctance- augmented shaded pole motors", *Proc. IEE*, Vol. 124, No.10, pp 860-864

[104] Williamson S. & Breese, P., 1978 ," Evaluation of the reluctance- augmented principle in shaded –pole motors", *Proc. IEE*, Vol. 125, No.9, pp 831-835

[105] Williamson, S. & Begg, M. C., 1985, " Analysis of cage induction motors- a combined fields and circuit approach", *IEEE Trans. on Magnetics*, Vol. MAG-21, No. 6 pp396-2399.

[106] Williamson, S. & Begg, M. C., 1986, "Calculation of the Resistance of Induction Motor End Rings", *IEE Proc.*, Vol. 133, Part B, No. 2, pp 54 -60

[107] Williamson, S. & Breese, P., 1981, "Twice-line-frequency pulsating torque in shaded pole motors", *Electric machines and Electromechanics*, No. 6, pp. 67-78

[108] Williamson, S. & McClay, C. I., 1996, "Optimisation of the geometry of closed rotor slot for cage induction motors", *IEEE Trans. on Industry Application*. vol. 32, No. 3 pp 560-568

[109] Williamson, S. & Mueller, M. A., 1993, "Calculation of the impedance of rotor cage end rings", *IEE Proceedings*, Vol. 140, Part B, No. 1, pp 51 -60

[110] Williamson, S. & Ralph, J. W., 1982, "Finite–element analysis for non-linear magnetic fields problem with complex current sources", *IEE Proc.*, Vol.129, Pt. A, No. 6, pp 391-394

[111] Williamson, S. & Ralph, J. W., 1983, "Finite-element analysis of an induction motor fed from a constant-voltage source", *IEE Proc.*, Vol. 130, Part B, No. 1, pp 18 -24

[112] Williamson, S. Flack, T. J. & Volschenk, A. F., 1995, 'Representation of Skew in Time-Stepped 2-Dimensional Finite-Element Models of Electrical Machines', *IEEE Trans. on Industry Applications*, Vol.31, No.5, pp.1009-1015

[113] Yamazaki, K., 1997, "Modification of 2D non-linear time-stepping analysis by limited 3D analysis for induction machines", *IEEE Trans. on Magnetics*, vol. 33, No. 2, pp1694-1697

[114] Yamazaki, K., 1998, "A quasi 3D formulation for analyzing characteristics of induction motors with skew slot", *IEEE Trans. on Magnetics*, vol. 34, No. 5, pp3624-3627

[115] Yokozuka, T., 1983, "Optimum design of shaded-pole motors by means of 2-phase unsymmetrical component", *Proc. IEE*, Vol. 130, Part B. No. 5, pp 341-346

[116] Zimmerman, W. R. & Valentine, N., 1983, "Recent Testing Experience in a large motor test Facility", *IEEE Trans. On Industry Application*, Vol. 19, No. 5, pp.832-835

Appendix A
List of Papers Arising from the Research

In addition to the original research reported in the thesis the author has published several papers during the study. Here is the list of the papers.

1. D. Zhou and C. B. Rajanathan, May, 1999, "An Analysis of the Shaded Pole Induction Motor Taking Skew into Account", *Proceeding of International Magnetics Conference (Digest)*, Kyongju, Korea, pp216
2. D. Zhou, C. B. Rajanathan, September, 1999, "Performance Prediction of Thyrister-Controlled Shaded Pole Induction Motor Using Finite Element Method", *Proceeding of 34th University Power Engineering Conference*, Leicester, UK, pp 276- 280
3. D. Zhou, C. B. Rajanathan and A. T. Sapeluk, September, 1999, "Transient Simulation of the Shaded Pole Motor Based upon Multi-Slice Finite-Element Model", *IEE Proceeding of International Conference on Electrical Machines and Drives*, Canterbury, UK, pp180-183
4. D. Zhou, C. B. Rajanathan, A. T. Sapeluk and C. S. Ozveren, September 2000, "Finite Element Aided Design Optimisation of A Shaded-Pole Induction Motor for Maximum Starting Torque", *IEEE Trans on Magnetics*, pp 3351-3354

Appendix B

Design Details of Two SPIMs

In the research, two different designed Shaded Pole Induction Motors, Model R and Model T, were studied to confirm the validity of the proposed FE model. These two motors have been tested with the PC based test rig designed in this research, and the test results are given in chapter 6. The detail of design parameters is listed here.

Model R

220V, 50Hz, 50W, 4 poles

Turns of stator coil:	730 turn/pole (serial connected)
Diameter of the wire:	0.25mm
Resistance of stator winding:	118.5Ω (measured at 15°C)
Cross-section of shaded ring:	6.0mm x0.8mm (measured)
Cross-section of rotor end-ring:	6.14mm x13.1mm (measured)
Stack length:	18mm
Air gap length:	0.45mm
Skew angle:	28.0 degree

Model T

220V, 50Hz, 50W, 4 poles

Turns of stator coil:	730 turn/pole (serial connected)
Diameter of the wire:	0.25mm
Resistance of stator winding:	114.2Ω (measured at 15°C)
Cross-section of shaded ring:	8.0mm x0.8mm (measured)
Cross-section of rotor end-ring:	6.0mm x10.1mm (measured)
Stack length:	18mm
Air gap length:	0.7mm
Skew angle:	24.0 degree

As to the geometrical design parameters of two motors, please refer to following figures.

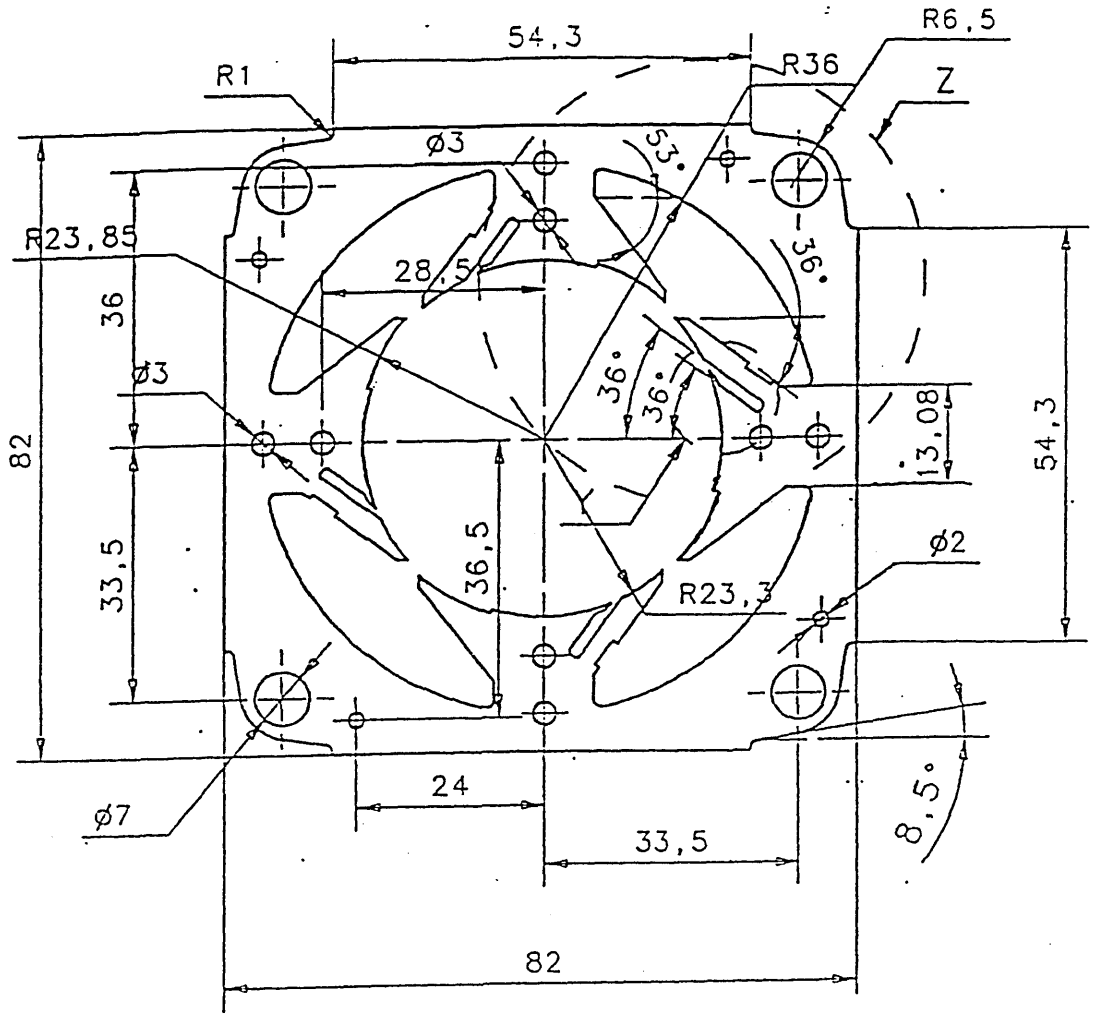

SCALE = 5:1

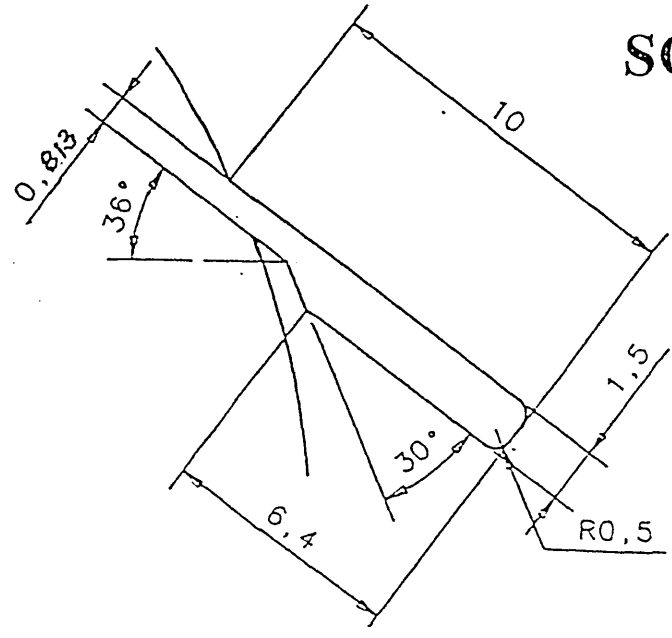

Model R -1

SCALE = 5:1

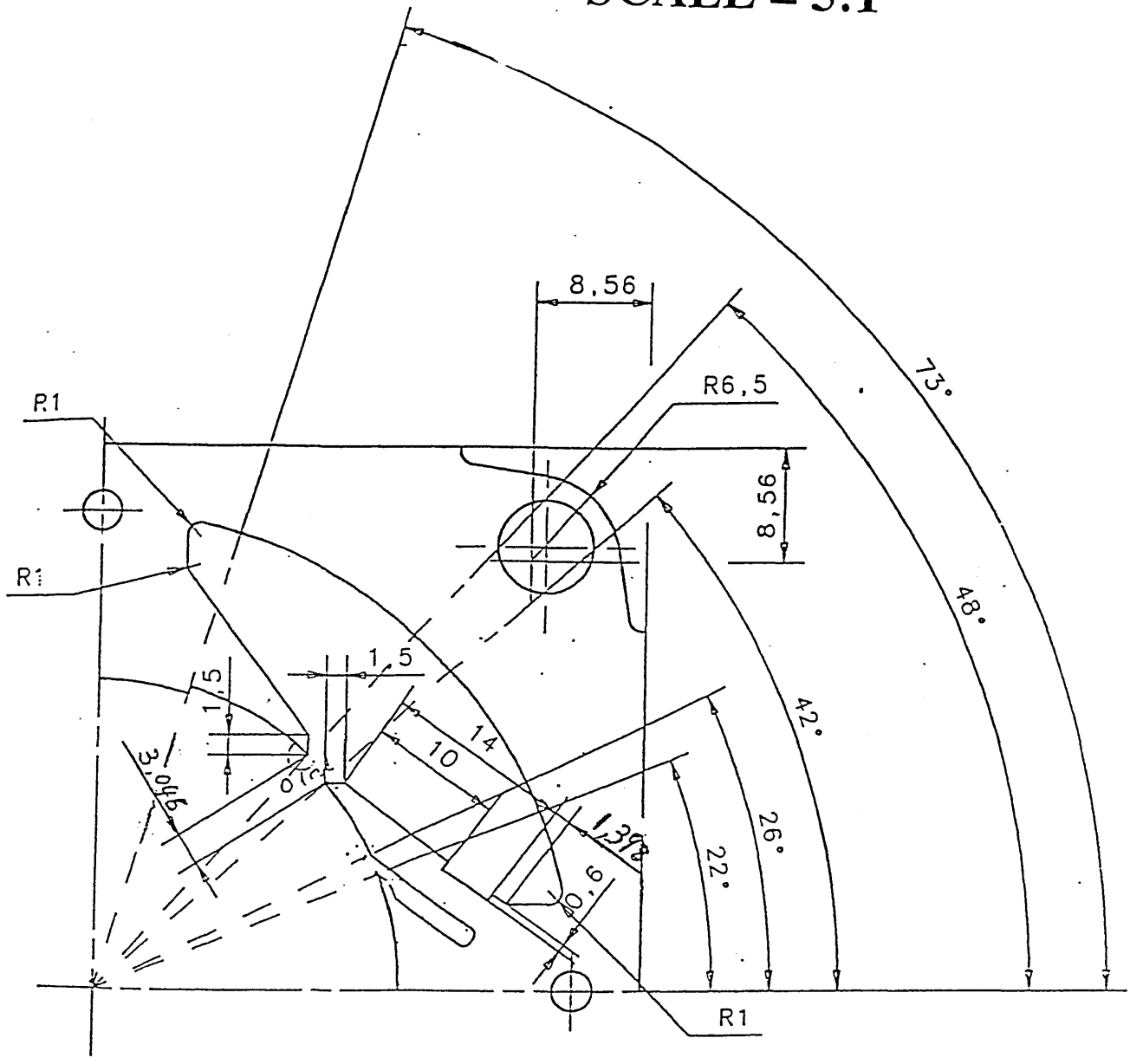

Model R -2

Slots = 22

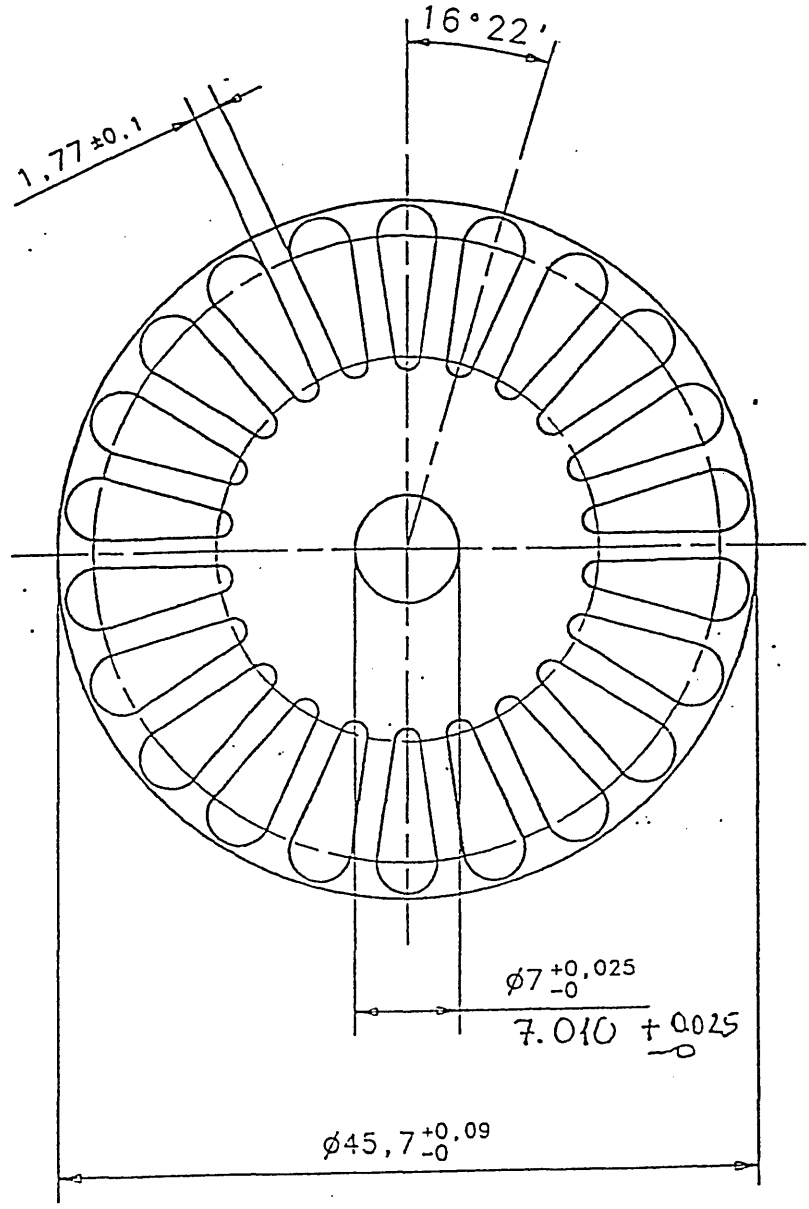

SCALE = 2:1

Model R -3

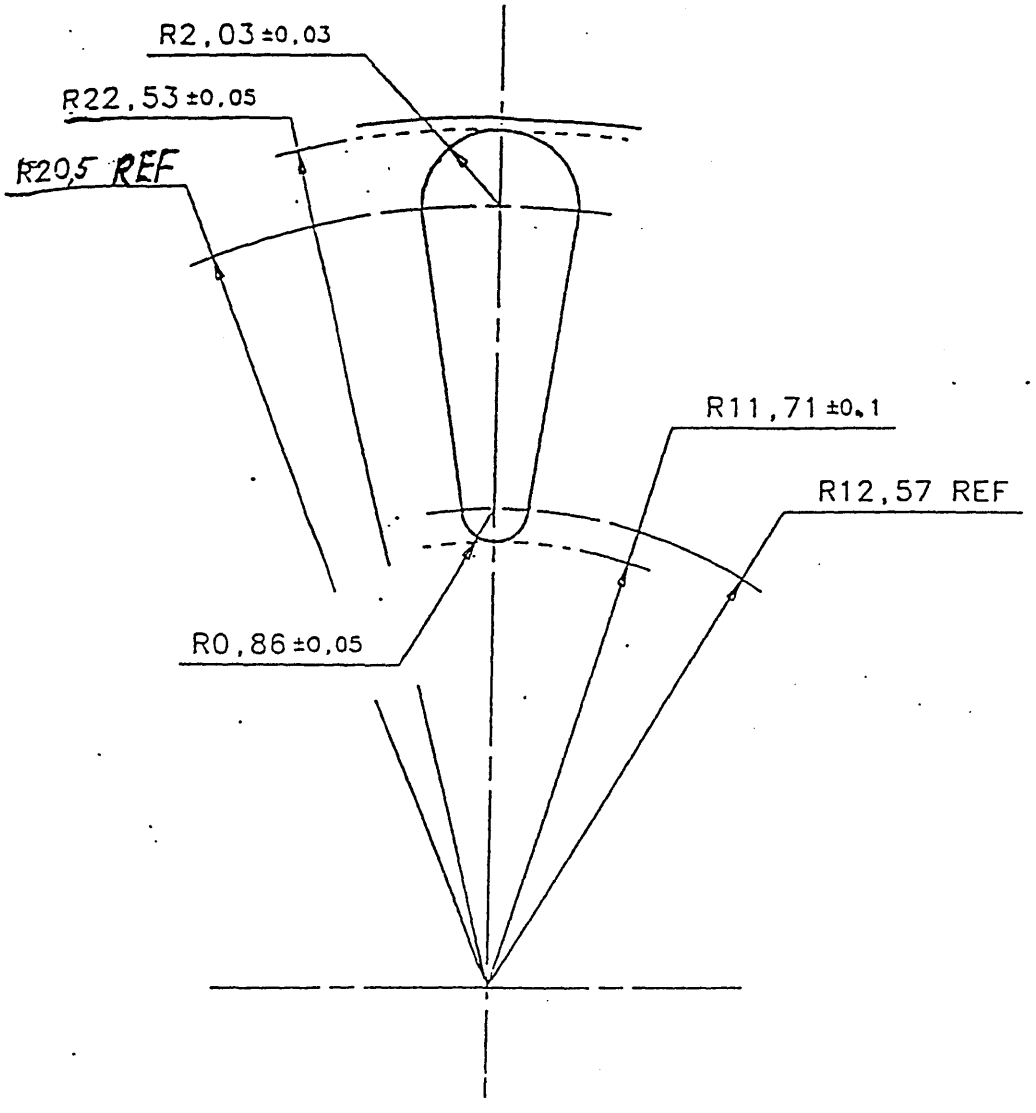

SCALE = 5:1

Model R -4

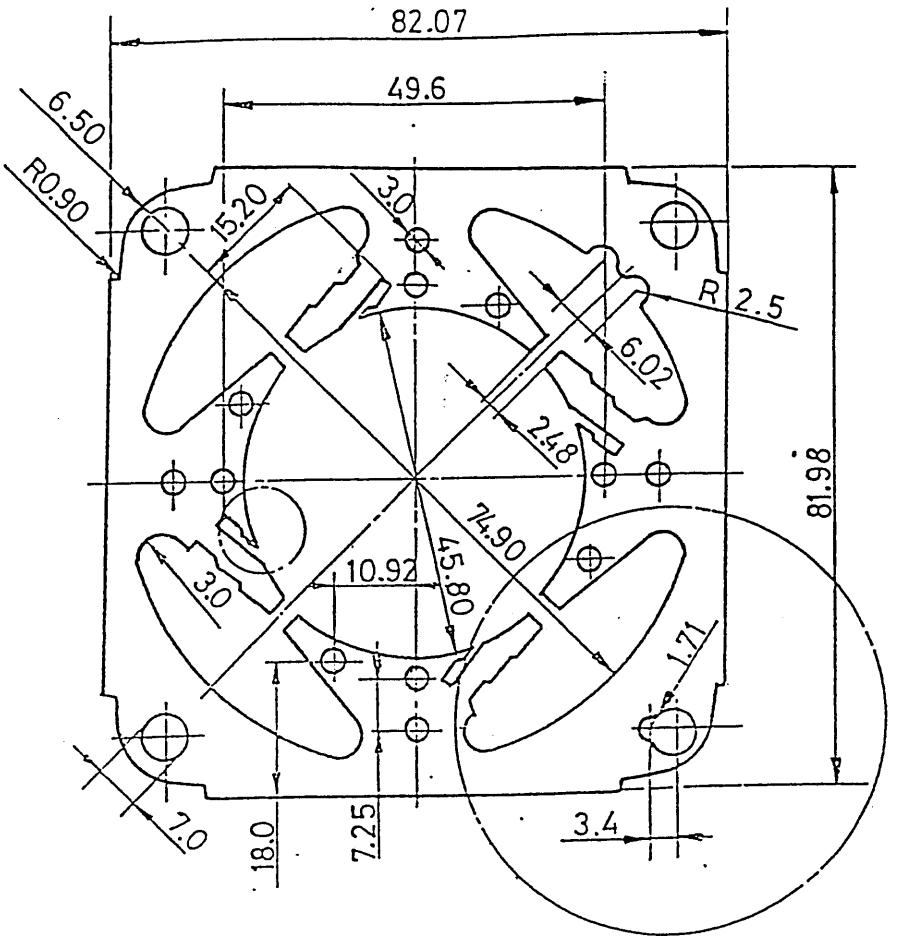

SCALE = 5:1

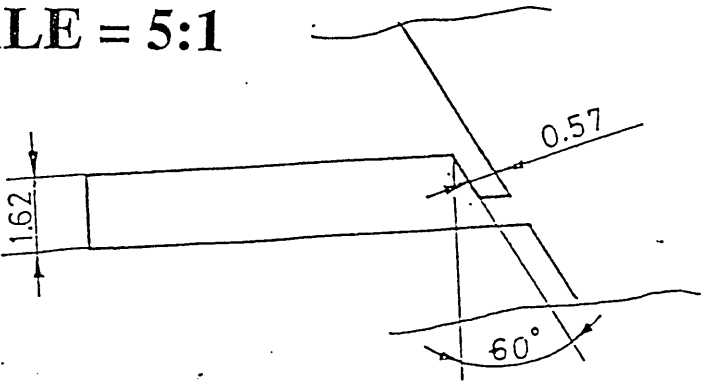

Model T -1

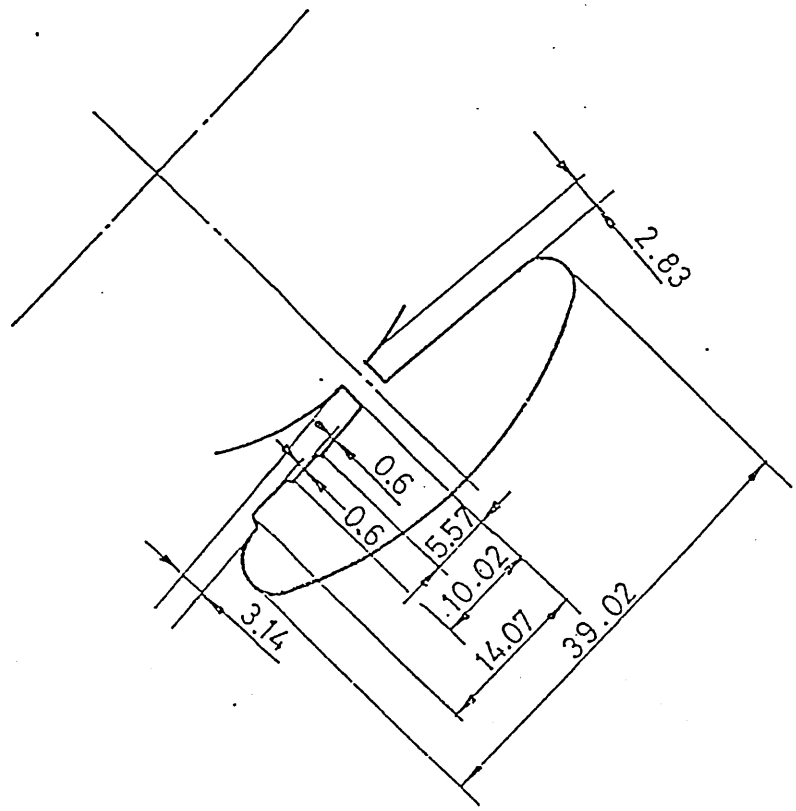

SCALE = 2:1

Model T – 2

SCALE = 2:1

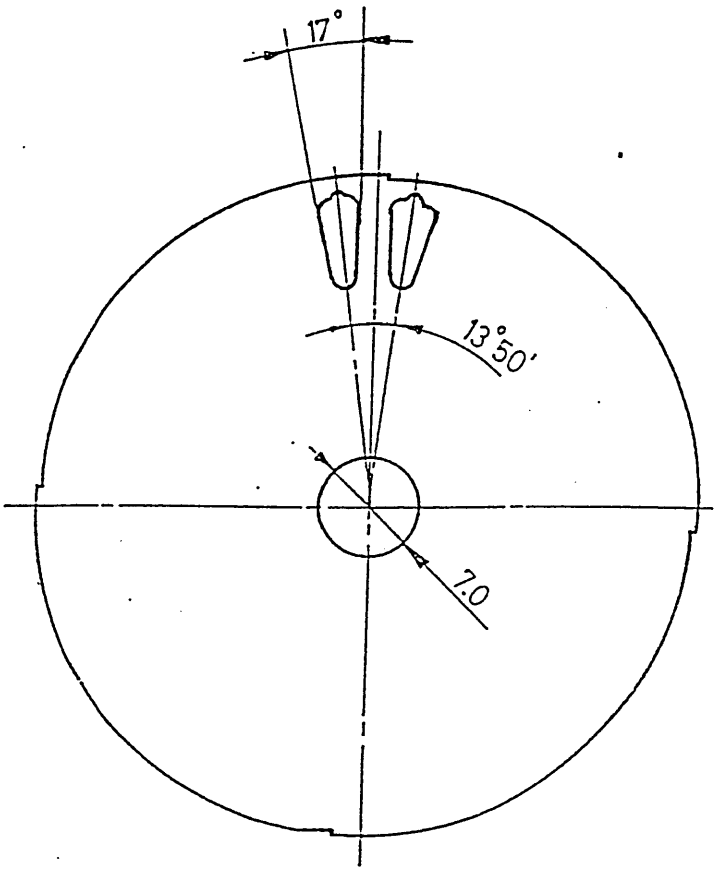

Slots = 26

Model T -3

SCALE = 5:1

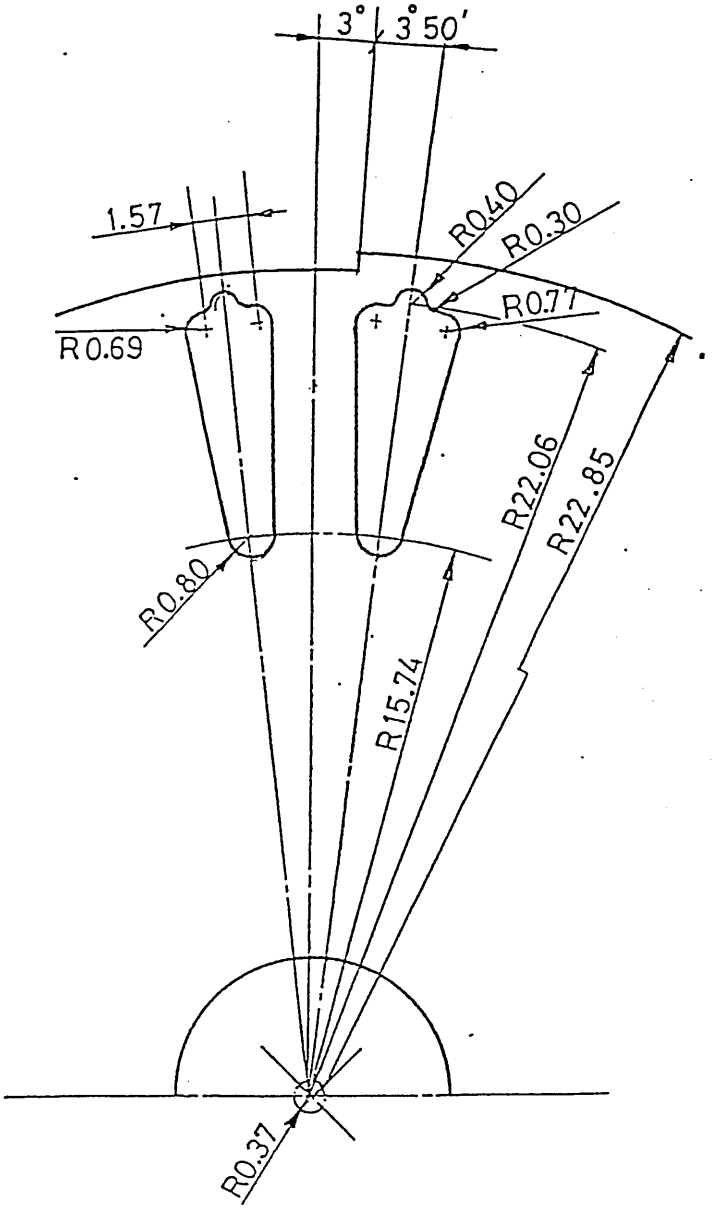

Model T -4